MODELING OF IN-PLANE AND INTERLAMINAR FATIGUE BEHAVIOR OF GLASS AND CARBON FIBER COMPOSITE MATERIALS

by

Timothy James Wilson

A thesis submitted in partial fulfillment
of the requirements for the degree

of

Master of Science

in

Mechanical Engineering

MONTANA STATE UNIVERSITY
Bozeman, Montana

January 2007

APPROVAL

of a thesis submitted by

Timothy James Wilson

This thesis has been read by each member of the thesis committee and has been found to be satisfactory regarding content, English usage, format, citations, bibliographic style, and consistency, and is ready for submission to the Division of Graduate Education.

Dr. Douglas S. Cairns

Approved for the Department of Mechanical Engineering

Dr. Christopher H.M. Jenkins

Approved for the Division of Graduate Education

Dr. Carl A. Fox

STATEMENT OF PERMISSION TO USE

In presenting this thesis in partial fulfillment of the requirements for a master's degree at Montana State University-Bozeman, I agree that the Library shall make it available to borrowers under rules of the Library.

If I have indicated my intention to copyright this thesis by including a copyright notice page, copying is allowable only for scholarly purposes, consistent with "fair use" as prescribed in the U.S. Copyright Law. Request for permission for extended quotation from or reproduction of this thesis in whole or in parts may be granted only by the copyright holder.

Timothy James Wilson

January 2007

ACKNOWLEDGEMENTS

I would like to thank a number of people for their help and support over the course of my thesis work: Dr. John Mandell, for providing me with this research opportunity and for his guidance over the course of this project; my committee members Drs. Douglas Cairns and Robert Bedaliance, for serving on my graduate committee; Daniel Samborsky, for providing me with countless hours worth of material test data; Ladean McKittrick and Tiok Agastra, for their help with the subtleties of MatLab and ANSYS; all of the faculty who have helped and instructed me during my time here at Montana State University; and all of my fellow graduate students who shared this experience with me.

I would also like to acknowledge the support that my mother and father, Barbara and James Wilson, have provided me with over the course of my educational career, and life as a whole. Also, I would like to thank my older brother, Chris, and younger sister, Katie, for there support. Finally, I would like to thank my girlfriend Amanda for her understanding over this seemingly never ending process.

TABLE OF CONTENTS

1. INTRODUCTION 1

Modeling of In-Plane Fatigue Behavior 2
Finite Element Analysis of Ply Drop Delamination.......................................4

2. MODELING OF IN-PLANE FATIGUE BEHAVIOR 7

Introduction to Materials 7
Fiberglass Laminate DD16, Axial Direction 7
Fiberglass Laminate QQ1, Axial Direction 8
Fiberglass Laminate QQ1T, Transverse Direction 8
Carbon/Glass Hybrid Laminate P2B, Axial Direction 8
Carbon/Glass Hybrid Laminate P2BT, Transverse Direction 9
Coupon Manufacture 9
Vacuum Assisted Resin Transfer Molding 9
Prepreg Layup 9
Coupon Design..11
Testing 13
Static Tests 13
Fatigue Tests 13
Test Results 17
Data Reduction 17
Static Results...17
Fatigue Models...19
95/95 Confidence Limits..20
Fits to Test Data 21
Fiberglass Laminate DD16, Axial Direction 23
Fiberglass Laminate QQ1, Axial Direction 34
Fiberglass Laminate QQ1T, Transverse Direction 36
Carbon/Glass Hybrid Laminate P2B, Axial Direction 38
Carbon/Glass Hybrid Laminate P2BT, Transverse Direction 40
Constant Life Diagrams...42
CLD for Fiberglass Laminate DD16, Axial Direction.....................................45
CLD for Fiberglass Laminate QQ1, Axial Direction.......................................47
Fiberglass Laminate QQ1T, Transverse Direction 49
Axial Carbon/Glass Hybrid Laminate P2B..51
Carbon/Glass Hybrid Laminate P2BT, Transverse Direction 52
Comparison of P2B and QQ1..53
Spectrum Loading 55

3. FINITE ELEMENT ANALYSIS OF PLY DROP DELAMINATION 61

TABLE OF CONTENTS - CONTINUED

Previous Work 62
Background 64
Geometry of Ply Drop Coupons 64
Element Properties 64
FEA Method for calculating G_I and G_{II} 65
Details of FEA Models 68
Element Sizing 71
Contact Elements 72
Angle of Taper 74
Composite Properties 76
Far-Field Strains 77
G vs. Load 78
Delamination Resistance of Composite Materials 78
Associated Experimental Study 82
Finite Element Results for Various Geometries and Materials 83
Ply Joint 83
Ply Joint, Carbon, Compression 85
Ply Joint, Carbon, Tension 87
Closed Form Approximation to Ply Joint 89
Ply Joint, Glass, Compression 90
Ply Joint, Glass, Tension 91
Central Ply Drop 93
Central Ply Drop, Carbon, Compression 93
Lay-Up Study, Central Ply Drop, Carbon, Compression 97
Central Ply Drop, Carbon, Tension 101
Internal Ply Drop 104
Internal Ply Drop, Carbon, Compression 105
Internal Ply Drop, Carbon, Tension 109
Internal Ply Drop, Glass, Compression 111
Internal Ply Drop Correlations 113
Associated Experimental Results 114
External Ply Drop 116
External Ply Drop, Carbon, Compression 117
Associated Experimental Results 123
External Ply Drop, Carbon, Tension 124
External Ply Drop, Glass, Compression 128
Associated Experimental Results 130
External Ply Drop, Glass, Tension 131
Comparison of G_{II} for Different Geometries 133

4. CONCLUSIONS 135

TABLE OF CONTENTS - CONTINUED

Modeling of In-Plane Fatigue Behavior 135
Finite Element Analysis of Ply Drop Delamination 136
Recommendations for Future Work 138
Modeling of In-Plane Fatigue Behavior 138
Grip Failures 138
High Cycle Fatigue Data 138
Multiaxial Fatigue Data 138
Low Cycle Fatigue Data 139
Stress Rupture / Residual Strength 139
Spectrum Loading Lifetime Predictions 139
Finite Element Analysis of Ply Drop Delamination 139
Experimental Program 139
Crack Growth Model Based on G Levels 140
Full Simulation 141
Substructure Testing and Analysis 142

REFERENCES 143

APPENDICES 147

APPENDIX A: MATERIAL TRANSITION DELAMINATION 148
Material Transition, Last Carbon Out 149
Last Carbon Out, Compression 150
Last Carbon Out, Tension 153
Material Transition, First Glass In 154
First Glass In, Compression 155
First Glass In, Tension 157
APPENDIX B: TAPERED PLY DROP STUDY 160
Project goals 161
Methodology 161
Coupon Manufacture 161
Coupon Testing 162
Scanning Electron Microscope Study 163
Experimental Results 164
Straight Internal Ply Drop, Tapered Ply Drop Study 168
Straight Internal Ply Drop, Tapered Ply Drop Study, Carbon, Tension 169
Straight Internal Ply Drop, Tapered Ply Drop Study, Glass, Tension 171
Straight Internal Ply Drop, Tapered Ply Drop Study, Carbon, Tension, Influence of Taper Angle 172
Straight Internal Ply Drop, Tapered Ply Drop Study, Glass, Tension, Influence of Taper Angle 173

TABLE OF CONTENTS - CONTINUED

Tapered Ply Drop 175
Tapered Ply Drop, Carbon, Tension 176
Tapered Ply Drop, Glass, Tension 178
Tapered Ply Drop, Carbon, Tension, Influence of Taper Angle 179
Tapered Ply Drop, Glass, Tension, Influence of Taper Angle 180
Experimental Observations 182
Numerical Observations 183
APPENDIX C: ADDITIONAL FEA RESULTS 186
Central Ply Drop 187
Glass, Compression 187
Glass, Tension 189
Internal Ply Drop 190
Carbon, Tension 190
Glass, Compression 192
Glass, Tension 194
External Ply Drop 198
Glass, Compression 198
Glass, Tension 200

LIST OF TABLES

Table Page

1. Vacuum Bagging Materials. 11

2. Fatigue Tests Run for Each Material. 14

3. Summary of Testing Equipment. 15

4. Number of Static and Fatigue Tests Performed. 17

5. Mean Static Properties. 18

6. Fit Parameters for Material DD16, Axial Direction (Fit to Fatigue Data Only, for Stresses which Produce Failure on the Order of 1000 cycles). 24

7. Fit Parameters for Material QQ1, Axial Direction (Fit to All Fatigue Data, Except Fit to Data for Stresses which Produce Failure above 10 Cycles (R = -1) and 500 Cycles (R = 0.5). 34

8. Fit Parameters for Material QQ1T, Transverse Direction (Fit to All Static and Fatigue Data). 36

9. Comparison of Residual Squared Values for Equation fits for Material P2B (Fit to All Static and Fatigue Data). 38

10. Fit Parameters for Material P2B, Axial Direction (Fit to All Static and Fatigue Data). 39

11. Fit Parameters for Material P2BT (Fit to All Fatigue Data). 41

12. Material Properties. 76

13. Results for Pure Mode I and II Delamination Tests. (The Prepreg is that Used for 0° Plies in the Current Study.) 80

14. Ply Joint, One Crack, Carbon, Compression, Maximum and Average G. 86

15. Ply Joint, 2 Cracks, Carbon, Compression, Maximum and Average G. 87

16. Ply Joint, 1 Crack, Carbon, Tension, Maximum and Average G. 88

LIST OF TABLES - CONTINUED

Table Page

17. Ply Joint, 1 Crack, Glass, Compression, Maximum and Average G. 91

18. Ply Joint, 1 Crack, Glass, Tension, Maximum and Average G..........................92

19. Central Ply Drop, 1 Ply Dropped Each Side,
Carbon, Compression, Maximum and Average G. 95

20. Central Ply Drop, 2 Plies Dropped Each Side, Carbon,
Compression, Maximum and Average G. 96

21. Central Ply Drop, Doubled Laminate Thickness Model,
2 Plies Dropped Each Side, Carbon, Compression,
Maximum and Average G. 97

22. Central Ply Drop, 1 Ply Dropped Each Side, Carbon,
Tension, Maximum and Average G. 102

23. Central Ply Drop, 2 Plies Dropped Each Side,
Carbon, Tension, Maximum and Average G. 103

24. Central Ply Drop, Doubled Model, 2 Plies Dropped
Each Side, Carbon, Tension, Maximum and Average G. 104

25. Internal Double Ply Drop, Carbon, Compression,
Both Cracks, Maximum and Average G. 107

26. Internal Ply Drop, Carbon, Compression, Lower
Crack Suppressed, Maximum and Average G. 108

27. Internal Ply Drop, Carbon, Compression, Upper
Crack Suppressed, Maximum and Average G. 109

28. Internal Ply Drop, Carbon, Tension, Both Cracks,
Maximum and Average G. 111

29. Internal Ply Drop, Glass, Compression, Both Cracks,
Maximum and Average G. 113

LIST OF TABLES - CONTINUED

Table Page

30. External Ply Drop, Carbon, Compression, Both Cracks, Maximum and Average G. 119

31. External Ply Drop, Carbon, Compression, Lower Crack Suppressed, Maximum and Average G. 120

32. External Ply Drop, Softened 45's, Carbon, Compression, Lower Crack Suppressed, Maximum and Average G. 121

33. External Ply Drop, Carbon, Compression, Upper Crack Suppressed, Maximum and Average G. 122

34. External Ply Drop, Softened 45's, Carbon, Compression, Upper Crack Suppressed, Maximum and Average G. 123

35. External Ply Drop, Carbon, Tension, Both Cracks. Maximum and Average G. 126

36. External Ply Drop, Carbon, Tension, Lower Crack Suppressed, Maximum and Average G. 127

37. External Ply Drop, Carbon, Tension, Upper Crack Suppressed, Maximum and Average G. 128

38. External Ply Drop, Glass, Compression, Both Cracks, Maximum and Average G. 130

39. External Ply Drop, Glass, Tension, Both Cracks, Maximum and Average G. 133

40. Last Carbon Out, Compression, Crack along Carbon Ply, Maximum and Average G. 151

41. Last Carbon Out, Compression, Into Glass, Maximum and Average G. 152

42. Last Carbon Out, Tension, Crack along Carbon Ply, Maximum and Average G. 153

43. Last Carbon Out, Tension, Into Glass, Maximum and Average G. 154

LIST OF TABLES - CONTINUED

Table Page

44. First Glass In, Compression, Crack along Glass Ply,
Maximum and Average G. 156

45. First Glass In, Compression, Crack into Carbon,
Maximum and Average G. 157

46. First Glass In, Tension, Crack along Glass Ply,
Maximum and Average G. 158

47. First Glass In, Tension, Crack along Ply, Maximum and Average G. 159

48. Carbon Coupon Logarithmic Fit Parameters, Percent Strain. 165

49. Glass Coupon Logarithmic Fit Parameters, Percent Strain. 167

50. Coupon Logarithmic Fit Parameters, Stress. 168

51. Internal Ply Drop, Tapered Ply Drop Study,
Carbon, Tension, Maximum and Average G. 171

52. Internal Ply Drop, Tapered Ply Drop Study,
Glass, Tension, Maximum and Average G. 172

53. Tapered Ply Drop, Carbon, Tension, Maximum and Average G. 178

54. Tapered Ply Drop, Glass, Tension, Maximum and Average G. 179

55. Central Ply Drop, 1 Ply Dropped, Glass,
Compression, Maximum and Average G. 188

56. Central Ply Drop, 2 Plies Dropped, Glass,
Compression, Maximum and Average G. 189

57. Central Ply Drop, 1 Ply Dropped, Glass,
Tension, Maximum and Average G. 189

58. Central Ply Drop, 2 Plies Dropped, Glass,
Tension, Maximum and Average G. 190

LIST OF TABLES - CONTINUED

Table Page

59. Internal Ply Drop, Carbon, Tension, Lower Crack Suppressed, Maximum and Average G. 191

60. Internal Ply Drop, Carbon, Tension, Upper Crack Suppressed, Maximum and Average G. 192

61. Internal Ply Drop, Glass, Compression, Lower Crack Suppressed, Maximum and Average G. 193

62. Internal Ply Drop, Glass, Compression, Upper Crack Suppressed, Maximum and Average G. 194

63. Internal Ply Drop, Glass, Tension, Both Cracks, Maximum and Average G. 196

64. Internal Ply Drop, Glass, Tension, Lower Crack Suppressed, Maximum and Average G. 197

65. Internal Ply Drop, Glass, Tension, Upper Crack Suppressed, Maximum and Average G. 198

66. External Ply Drop, Glass, Compression, Lower Crack Suppressed, Maximum and Average G. 199

67. External Ply Drop, Glass, Compression, Upper Crack Suppressed, Maximum and Average G. 200

68. External Ply Drop, Glass, Tension, Lower Crack Suppressed, Maximum and Average G. 201

69. External Ply Drop, Glass, Tension, Upper Crack Suppressed, Maximum and Average G. 202

LIST OF FIGURES

Figure Page

1. Ply Drop Photograph. 4

2. Delamination Crack in External Ply Drop. 5

3. Rectangular Coupon. 11

4. Dogbone Coupon..12

5. Waveform Definitions. 13

6. Waveforms for Common R Values. 15

7. Failed QQ1 Coupons; Upper: Compressive Failure;
Lower: Tensile Failure. 16

8. Typical Tensile Stress vs. Strain Diagrams for
Materials QQ1 and P2B. A: Axial Direction;
B: Transverse Direction...18

9. DD16, Axial Direction, Stress vs. Cycles to Failure,
95/95 Fit, R = 10 (Model Fit to Fatigue Data Only,
for Stresses which Produce Failure on the Order of 1000 cycles) 22

10. Compression Fatigue, Mean Power Law Fits
(Material DD16, Axial Direction). 25

11. Mixed Fatigue, Mean Power Law Fits
(Material DD16, Axial Direction). 26

12. Tensile Fatigue, Mean Power Law Fits
(Material DD16, Axial Direction). 26

13. Stress Rupture Data with Models
(Material DD16, Axial Direction). 27

14. Load Waveform, Stress Rupture Model; f = 5Hz, R = -2. 29

15. "Damage" per cycle, Stress Rupture Model;
f = 5Hz, R = -2 (Material DD16, Axial Direction). 30

LIST OF FIGURES - CONTINUED

Figure Page

16. Stress vs. Cycles to Failure, Stress Rupture Model;
R = 0.9 (Material DD16, Axial Direction). 31

17. Schematic of Anticipated Square Wave
Frequency Effects for Glass Reinforced Epoxy [14]. 33

18. Compression and Mixed Fatigue, Mean Power
Law Fits (Material QQ1, Axial Direction). 35

19. Tensile Fatigue, Mean Power Law Fits
(Material QQ1, Axial Direction). 35

20. Compression and Mixed Fatigue, Mean Power
Law Fits (Material QQ1T, Transverse Direction). 37

21. Tensile Fatigue, Mean Power Law Fits
(Material QQ1T, Transverse Direction). 37

22. Compression and Mixed Fatigue, Mean Power
Law Fits (Material P2B, Axial Direction). 39

23. Tensile Fatigue, Mean Power Law Fits
(Material P2B, Axial Direction). 40

24. Compression and Mixed Fatigue, Mean Power
Law Fits (Material P2BT, Transverse Direction). 41

25. Tensile Fatigue, Mean Power Law Fits
(Material P2BT, Transverse Direction). 42

26. Schematic of the relationship between S-N
Curves and Constant Life Diagrams [8] 43

27. Mean Axial Constant Life Diagram for Material DD16,
1 Hz Frequency. 45

28. Mean Axial Constant Life Diagram for Material DD16,
10 Hz Frequency. 46

LIST OF FIGURES - CONTINUED

Figure Page

29. 95/95 Axial Constant Life Diagram for Material DD16,
1 Hz Frequency. 46

30. 95/95 Axial Constant Life Diagram for Material DD16,
10 Hz Frequency. 47

31. Mean Axial Constant Life Diagram for Material QQ1. 47

32. 95/95 Axial Constant Life Diagram for Material QQ1. 49

33. Mean Transverse Constant Life Diagram for Material QQ1T. 49

34. 95/95 Transverse Constant Life Diagram for Material QQ1T. 50

35. Mean Axial Constant Life Diagram for Material P2B. 51

36. 95/95 Axial Constant Life Diagram for Material P2B. 52

37. Mean Transverse Constant Life Diagram for Material P2BT. 52

38. 95/95 Transverse Constant Life Diagram for Material P2BT. 53

39. Comparison of Materials QQ1 (Fiberglass) and
P2B (Carbon Dominated), Axial Direction,
Stress Constant Life Diagram. 54

40. Comparison of Materials QQ1 (Fiberglass) and
P2B (Carbon Dominated), Strain Constant Life Diagram. 55

41. WISPER and WISPERX Spectra Cycles
(Size of the Circle Indicates the Number of Cycles),
Showing the Truncation Line [8]. 57

42. Material DD16, Axial Direction, Mean Constant
Life Diagram, Frequency = 10Hz,
WISPERX Scale Factor = 416 MPa, Miner’s Sum = 1. 58

43. Stress Scale Factors Applied to the WISPERX Spectrum
to Achieve a Miner's Sum Equal to 1 (Mean Fit)..59

LIST OF FIGURES - CONTINUED

Figure Page

44. Strain Scale Factors Applied to the WISPERX Spectrum
to Achieve a Miner's Sum Equal to 1 (Mean Fit)...60

45. External Ply Drop Test Coupon. 64

46. Nodal Arrangement [28]. 65

47. ANSYS ‘kscon’ Crack Tip Elements..67

48. Internal Ply Drop, Showing Loads and Constraints...68

49. Percent Difference in Total G vs. Crack Length between
Displacement and Load Control in Internal Ply Drop Model. 69

50. Internal Ply Drop Model, Full Model, Showing
Extended Gauge Section. 69

51. Internal Ply Drop Model, Areas near Ply Drop..70

52. Internal Ply Drop, Carbon, Compression, Two 1 mm long Cracks,
G vs. Coupon Length..70

53. Internal Ply Drop Convergence Study, Total G vs. Number of Elements. 71

54. Internal Ply Drop Model, Exaggerated Crack Width...72

55. Coordinate System Adjustment Areas. 73

56. Internal Ply Drops, Two Plies dropped at each Location...................................74

57. Detail of Double Internal Ply Drops, Taper Angles Highlighted.......................75

58. Detail of Double Internal Ply Drops, Taper Angles Highlighted.......................75

59. Locations Where Strain Values are obtained in Models....................................77

60. Center Ply Drop, Carbon, Compression, 1 mm Crack,
G vs. Applied Stress Squared..78

LIST OF FIGURES - CONTINUED

Figure Page

61. Mixed-Mode Fracture of [0]10 E-glass/Isophthalic Polyester, Vinyl Ester and Epoxy, from Agastra (RTM molded, Fiber Volume Fraction about 0.35) [32]. 79

62. Mixed-Mode Fracture of Graphite Composite Materials [31]. 81

63. Schematic of Typical Ply Drop Coupon from Experimental Study. 82

64. Ply Joint, One Crack, $[\pm45_3/0_{13}/0^*_2]_S$. 84

65. Ply Joint, Two Cracks, $[\pm45_3/0_{13}/0^*_2]_S$. 85

66. Ply Joint, One Crack, Carbon, Compression. A: G vs. Crack Length; B: Far-Field Strain vs. Crack Length; Load = 559.2 MPa. 86

67. Ply Joint, 2 Cracks, Carbon, Compression. A: G vs. Crack Length; B: Far Field Strain vs. Crack Length; Applied Stress = 559.2 MPa. 87

68. Ply Joint, 1 Crack, Carbon, Tension. A: G vs. Crack Length; B: Far Field Strain vs. Crack Length; Applied Stress = 559.2 MPa. 88

69. Schematic for Ramkumar and Whitcomb's Strength of Materials Solution, where the Jointed or Dropped Ply has a Thickness t_p. 89

70. Ply Joint, 1 Crack, Glass, Compression. A: G vs. Crack Length; B: Far Field Strain vs. Crack Length; Applied Stress = 158.6 MPa. 91

71. Ply Joint, 1 Crack, Glass, Tension. A: G vs. Crack Length; B: Far Field Strain vs. Crack Length; Applied Stress = 158.6 MPa. 92

72. Central Ply Drop, Crack Location, Lay-Up: $[\pm45_3/0_{13}/0^*_1]_S$. 93

73. Central Ply Drop, 1 Ply Dropped Each Side, Carbon, Compression. A: G vs. Crack Length; B: Far Field Strain vs. Crack Length; Applied Stress = 548.5 MPa. 95

74. Central Ply Drop, 2 Plies Dropped Each Side, Carbon, Compression. A: G vs. Crack Length; B: Far Field Strain vs. Crack Length; Applied Stress = 548.5 MPa. 96

LIST OF FIGURES - CONTINUED

Figure Page

75. Central Ply Drop, Doubled Laminate Thickness Model,
2 Plies Dropped Each Side, Carbon, Compression.
A: G vs. Crack Length; B: Far Field Strain vs. Crack Length;
Applied Stress = 549.3 MPa. 97

76. Central Ply Drop, Carbon, Compression, Lay-Up Comparison.
A: Total G vs. Crack Length; B: G_I vs. Crack Length;
Applied Stress = 548.5 MPa. 98

77. Central Ply Drop, Carbon, Compression, Lay-Up Comparison.
A: G_{II} vs. Crack Length; B: Far Field Strain vs. Crack Length;
Applied Stress = 548.5 MPa. 99

78. Central Ply Drop, Carbon, Compression, Adjusted Lay-Up Comparison.
A: Adjusted Total G vs. Crack Length;
B: Adjusted G_I vs. Crack Length; Applied Stress = 548.5 MPa. 100

79. Central Ply Drop, Carbon, Compression, Adjusted Lay-Up Comparison,
Adjusted G_{II} vs. Crack Length; Applied Stress = 548.5 MPa. 100

80. Central Ply Drop, 1 Ply Dropped Each Side, Carbon, Tension.
A: G vs. Crack Length; B: Far Field Strain vs. Crack Length;
Applied Stress = 548.5 MPa. 101

81. Central Ply Drop, 2 Plies Dropped Each Side, Carbon, Tension.
A: G vs. Crack Length; B: Far Field Strain vs. Crack Length;
Applied Stress = 548.5 MPa. 102

82. Central Ply Drop, Doubled Model, 2 Plies Dropped Each Side,
Carbon, Tension. A: G vs. Crack Length;
B: Far Field Strain vs. Crack Length; Applied Stress = 549.3 MPa. 103

83. Internal Ply Drop, Crack Locations, $[\pm45_3/0_9/0^*_2/0_9/0^*_2/0_9/\pm45_3]$....................105

84. Internal Double Ply Drop, Carbon, Compression, Both Cracks.
A: Total G vs. Crack Length; B: G_I vs. Crack Length;
Applied Stress = 552.6 MPa. 106

LIST OF FIGURES - CONTINUED

Figure Page

85. Internal Double Ply Drop, Carbon, Compression, Both Cracks. A: G_{II} vs. Crack Length; B: Far Field Strain vs. Crack Length; Applied Stress = 552.6 MPa. 107

86. Internal Ply Drop, Carbon, Compression, Lower Crack Suppressed. A: G vs. Crack Length; B: Far Field Strain vs. Crack Length; Applied Stress = 552.6 MPa. 108

87. Internal Ply Drop, Carbon, Compression, Upper Crack Suppressed. A: G vs. Crack Length; B: Far Field Strain vs. Crack Length; Applied Stress = 552.6 MPa. 109

88. Internal Ply Drop, Carbon, Tension, Both Cracks. A: Total G vs. Crack Length; B: G_I vs. Crack Length; Applied Stress = 552.6 MPa. 110

89. Internal Ply Drop, Carbon, Tension, Both Cracks. A: G_{II} vs. Crack Length; B: Far Field Strain vs. Crack Length; Applied Stress = 552.6 MPa. 110

90. Internal Ply Drop, Glass, Compression, Both Cracks. A: Total G vs. Crack Length; B: G_I vs. Crack Length; Applied Stress = 156.9 MPa. 112

91. Internal Ply Drop, Glass, Compression, Both Cracks. A: G_{II} vs. Crack Length; B: Far Field Strain vs. Crack Length; Applied Stress = 156.9 MPa. 112

92. Internal Ply Drop, Compression, Both Cracks. A: Carbon and Glass at the Same Load (156.9 MPa); B: Carbon: Root of the Modulus Ratio Load (Equation 17), Glass: Regular Load, G_{II} vs. Crack Length. 114

93. Experimental Results for the Maximum Compressive Strain vs. Cycles to Failure for an Internal Ply Drop with Carbon or Glass 0's $[\pm45_3/0_9/0^*_2/0_9/0^*_2/0_9/\pm45_3]$ R = 10 [17]. 115

94. External Ply Drop, Crack Locations, $[\pm45_3/0^*_2/0_{27}/0^*_2/\pm45_3]$. 116

LIST OF FIGURES - CONTINUED

Figure Page

95. External Ply Drop, Carbon, Compression, Both Cracks.
A: Total G vs. Crack Length; B: G_I vs. Crack Length;
Applied Stress = 553.9 MPa. 118

96. External Ply Drop, Carbon, Compression, Both Cracks.
A: G_{II} vs. Crack Length; B: Far Field Strain vs. Crack Length;
Applied Stress = 553.9 MPa. 118

97. External Ply Drop, Carbon, Compression, Lower Crack Suppressed.
A: G vs. Crack Length; B: Far Field Strain vs. Crack Length;
Applied Stress = 553.9 MPa. 120

98. External Ply Drop, Softened 45's, Carbon, Compression,
Lower Crack Suppressed. A: G vs. Crack Length;
B: Far Field Strain vs. Crack Length; Applied Stress = 553.9 MPa. 121

99. External Ply Drop, Carbon, Compression, Upper Crack Suppressed.
A: G vs. Crack Length; B: Far Field Strain vs. Crack Length;
Applied Stress = 553.9 MPa. 122

100. External Ply Drop, Softened 45's, Carbon, Compression,
Upper Crack Suppressed. A: G vs. Crack Length;
B: Far Field Strain vs. Crack Length; Applied Stress = 553.9 MPa. 123

101. Experimental Results for the Maximum Compressive Strain vs.
Cycles to Failure for an External Ply Drop, 2 Plies Dropped, with
Carbon 0's [$\pm 45_3/0^*_2/0_{27}/0^*_2/\pm 45_3$], R = 10 [17]. 124

102. External Ply Drop, Carbon, Tension, Both Cracks.
A: Total G vs. Crack Length; B: G_I vs. Crack Length;
Applied Stress = 553.9 MPa. 125

103. External Ply Drop, Carbon, Tension, Both Cracks.
A: G_{II} vs. Crack Length; B: Far Field Strain vs. Crack Length;
Applied Stress = 553.9 MPa. 125

104. External Ply Drop, Carbon, Tension, Lower Crack Suppressed.
A: G vs. Crack Length; B: Far Field Strain vs. Crack Length;
Applied Stress = 553.9 MPa. 126

LIST OF FIGURES - CONTINUED

Figure Page

105. External Ply Drop, Carbon, Tension, Upper Crack Suppressed.
A: G vs. Crack Length; B: Far Field Strain vs. Crack Length;
Applied Stress = 553.9 MPa. 127

106. External Ply Drop, Glass, Compression, Both Cracks.
A: Total G vs. Crack Length; B: G_I vs. Crack Length;
Applied Stress = 160.0 MPa. 129

107. External Ply Drop, Glass, Compression, Both Cracks.
A: G_{II} vs. Crack Length; B: Far Field Strain vs. Crack Length;
Applied Stress = 160.0 MPa. 129

108. Experimental Results for the Maximum Compressive
Strain vs. Cycles to Failure for an External Ply Drop,
2 Plies Dropped, Glass 0's $[\pm45_3/0^*_2/0_{27}/0^*_2/\pm45_3]$, R = 10 [17]. 131

109. External Ply Drop, Glass, Tension, Both Cracks.
A: Total G vs. Crack Length; B: G_I vs. Crack Length;
Applied Stress = 160.0 MPa. 132

110. External Ply Drop, Glass, Tension, Both Cracks.
A: G_{II} vs. Crack Length; B: Far Field Strain vs. Crack Length;
Applied Stress = 160.0 MPa. 132

111. Comparison of Total G_{II} Values (G_{II} for both cracks, added together),
External, Internal, and Central Ply Drops, Carbon, Tension,
Two Plies Dropped. 134

112. Last Carbon Out, $[\pm45_2/0_1/0^*_1/0_8/0^\#_1]_S$. 149

113. Last Carbon Out, Compression, Crack along Carbon Ply,
A: G vs. Crack Length; B: Far Field Strain vs. Crack Length;
Applied Stress = 201.7 MPa. 151

114. Last Carbon Out, Compression, Into Glass,
A: G vs. Crack Length; B: Far Field Strain vs. Crack Length;
Applied Stress = 201.7 MPa. 152

LIST OF FIGURES - CONTINUED

Figure Page

115. Last Carbon Out, Tension, Crack along Carbon Ply,
A: G vs. Crack Length; B: Far Field Strain vs. Crack Length;
Applied Stress = 201.7 MPa. 153

116. Last Carbon Out, Tension, Into Glass,
A: G vs. Crack Length; B: Strain vs. Crack Length. 154

117. First Glass In, $[\pm45_2/0_1/0*_1/0_8/0^{\#}_1]_S$ 155

118. First Glass In, Compression, Crack along Glass Ply,
A: G vs. Crack Length; B: Far Field Strain vs. Crack Length;
Applied Stress = 563.6 MPa. 156

119. First Glass In, Compression, Crack into Carbon,
A: G vs. Crack Length; B: Far Field Strain vs. Crack Length;
Applied Stress = 563.6 MPa. 157

120. First Glass In, Tension, Crack along Glass Ply,
A: G vs. Crack Length; B: Strain vs. Crack Length. 158

121. First Glass In, Tension, Crack into Carbon,
A: G vs. Crack Length; B: Strain vs. Crack Length. 159

122. Electron Microscope Image showing both
Tips of a Tapered Ply Drop. 164

123. Comparison of 10° Tapered vs. Straight Ply Drops in Carbon
Prepreg Samples (Max Strain vs. Cycles to 6.4 mm Delamination). 165

124. Comparison of Tapered vs. Straight Ply Drops in Glass
Prepreg Coupons (Max Stress vs. Cycles to 6.4 mm Delamination). 166

125. Comparison of Tapered vs. Straight Ply Drops in Glass
Prepreg Coupons (Max Stress vs. Cycles to 6.4 mm Delamination). 168

126. Internal Ply Drop, Tapered Ply Drop Study,
$[\pm45_1/0_5/0*_3/0_5/0*_3/0_5/\pm45_1]$. 169

LIST OF FIGURES - CONTINUED

Figure Page

127. Internal Ply Drop, Tapered Ply Drop Study, Carbon, Tension.
A: Total G vs. Crack Length; B: G_I vs. Crack Length;
Applied Stress = 590.0 MPa. 170

128. Internal Ply Drop, Tapered Ply Drop Study, Carbon, Tension.
A: G_{II} vs. Crack Length; B: Far Field Strain vs. Crack Length;
Applied Stress = 590.0 MPa. 170

129. Internal Ply Drop, Tapered Ply Drop Study, Glass, Tension.
A: Total G vs. Crack Length; B: G_I vs. Crack Length;
Applied Stress = 156.9 MPa. 171

130. Internal Ply Drop, Tapered Ply Drop Study, Glass, Tension.
A: G_{II} vs. Crack Length; B: Far Field Strain vs. Crack Length;
Applied Stress = 156.9 MPa. 172

131. Internal Ply Drop, Tapered Ply Drop Study, Carbon, Tension,
Cracks are 1.5 mm. A: Total G vs. Taper Angle;
B: G_I vs. Taper Angle; Applied Stress = 590.0 MPa. 173

132. Internal Ply Drop, Tapered Ply Drop Study, Carbon, Tension,
Cracks are 1.5 mm. A: G_{II} vs. Taper Angle; B: Far Field
Strain vs. Taper Angle; Applied Stress = 590.0 MPa. 174

133. Internal Ply Drop, Tapered Ply Drop Study, Glass, Tension,
Cracks are 1.5 mm. A: Total G vs. Taper Angle;
B: G_I vs. Taper Angle; Applied Stress = 156.9 MPa. 175

134. Internal Ply Drop, Tapered Ply Drop Study, Glass,
Tension, Cracks are 1.5 mm. A: G_{II} vs. Taper Angle;
B: Far Field Strain vs. Taper Angle; Applied Stress = 156.9 MPa. 175

135. Tapered Ply Drop, $[\pm45_1/0_5/0^*_3/0_5/0^*_3/0_5\pm45_1]$. 176

136. Tapered Ply Drop, Carbon, Tension. A: Total G vs. Crack Length;
B: G_I vs. Crack Length; Applied Stress = 590.0 MPa. 177

137. Tapered Ply Drop, Carbon, Tension. A: G_{II} vs. Crack Length; B: Far Field
Strain vs. Crack Length; Applied Stress = 590.0 MPa. 177

LIST OF FIGURES - CONTINUED

Figure Page

138. Tapered Ply Drop, Glass, Tension. A: Total G vs. Crack Length;
B: G_I vs. Crack Length; Applied Stress = 157.5 MPa..178

139. Tapered Ply Drop, Glass, Tension. A: G_{II} vs. Crack Length;
B: Far Field Strain vs. Crack Length; Applied Stress = 157.5 MPa. 179

140. Tapered Ply Drop, Carbon, Tension, Cracks are 1.5 mm.
A: Total G vs. Taper Angle; B: G_I vs. Taper Angle;
Applied Stress = 590.0 MPa...180

141. Tapered Ply Drop, Carbon, Tension, Cracks are 1.5 mm.
A: G_{II} vs. Taper Angle; B: Far Field Strain vs. Taper Angle;
Applied Stress = 590.0 MPa...180

142. Tapered Ply Drop, Glass, Tension, Cracks are 1.5 mm.
A: Total G vs. Taper Angle; B: G_I vs. Taper Angle;
Applied Stress = 157.5 MPa...181

143. Tapered Ply Drop, Glass, Tension, Cracks are 1.5 mm.
A: G_{II} vs. Taper Angle; B: Far Field Strain vs. Taper Angle;
Applied Stress = 157.5 MPa...181

144. Crack locations, Carbon, Tapered Ply Drop. 182

145. Crack Location, Carbon, Straight Ply Drop. 182

146. Crack Location, Glass, Tapered Ply Drop..183

147. Tapered Ply Drop Model, Carbon, No Cracks, Transverse Strain.................184

148. Tapered Ply Drop, Carbon, 0.36 mm Crack, Transverse Strain.....................185

149. Central Ply Drop, 1 Ply Dropped, Glass, Compression.
A: G vs. Crack Length; B: Strain vs. Crack Length..186

150. Central Ply Drop, 2 Plies Dropped, Glass, Compression.
A: G vs. Crack Length; B: Strain vs. Crack Length..188

LIST OF FIGURES - CONTINUED

Figure Page

151. Central Ply Drop, 1 Ply Dropped, Glass, Tension.
A: G vs. Crack Length; B: Strain vs. Crack Length. 189

152. Central Ply Drop, 2 Plies Dropped, Glass, Tension.
A: G vs. Crack Length; B: Strain vs. Crack Length. 190

153. Internal Ply Drop, Carbon, Tension, Lower Crack Suppressed.
A: G vs. Crack Length; B: Strain vs. Crack Length. 191

154. Internal Ply Drop, Carbon, Tension, Upper Crack Suppressed.
A: G vs. Crack Length; B: Strain vs. Crack Length. 192

155. Internal Ply Drop, Glass, Compression, Lower Crack Suppressed.
A: G vs. Crack Length; B: Strain vs. Crack Length. 193

156. Internal Ply Drop, Glass, Compression, Upper Crack Suppressed.
A: G vs. Crack Length; B: Strain vs. Crack Length. 194

157. Internal Ply Drop, Glass, Tension, Both Cracks.
A: Total G vs. Crack Length; B: G_I vs. Crack Length. 195

158. Internal Ply Drop, Glass, Tension, Both Cracks. A: G_{II} vs. Crack Length; B: Strain vs. Crack Length. 195

159. Internal Ply Drop, Glass, Tension, Lower Crack Suppressed.
A: G vs. Crack Length; B: Strain vs. Crack Length. 196

160. Internal Ply Drop, Glass, Tension, Upper Crack Suppressed.
A: G vs. Crack Length; B: Strain vs. Crack Length. 197

161. External Ply Drop, Glass, Compression, Lower Crack Suppressed.
A: G vs. Crack Length; B: Strain vs. Crack Length. 198

162. External Ply Drop, Glass, Compression, Upper Crack Suppressed.
A: G vs. Crack Length; B: Strain vs. Crack Length. 199

163. External Ply Drop, Glass, Tension, Lower Crack Suppressed.
A: G vs. Crack Length; B: Strain vs. Crack Length. 200

LIST OF FIGURES - CONTINUED

Figure Page

164. External Ply Drop, Glass, Tension, Upper Crack Suppressed.
A: G vs. Crack Length; B: Strain vs. Crack Length. 201

ABSTRACT

This thesis presents the results of a modeling study of the fatigue behavior of fiberglass and carbon fiber reinforced epoxy composite materials intended primarily for wind turbine blades. The modeling effort is based on recent experimental results for infused glass fiber laminates typical of current blades, and hybrid carbon prepreg laminates of potential interest for future blades. There are two focus areas: in-plane performance represented by stress-life (S-N) curves, and out-of-plane ply delamination at details including ply drops and joints, based on fracture mechanics.

In-plane fatigue models for both the mean performance and a statistically fit model with a 95/95 confidence limit were developed for three laminates, each representative of lower cost materials with applications in the wind turbine industry. These include polyester and epoxy resin infused glass fabrics and a hybrid carbon prepreg; two of the materials were tested in the axial and transverse directions. Models were adapted for the S-N results at several uniaxial loading conditions, including special treatment of the time dependence at high loads. Materials are compared in terms of their fatigue exponents, constant life diagrams and in the context of a wind loads spectrum.

The second part of this work contains a modeling study of delamination crack development in various composite structure detail regions using finite element analysis. Geometries include various ply joints, ply drops, and material transition areas, all using relatively thick glass and carbon fiber prepregs typical of lower cost applications. Two dimensional finite element models were used to determine the strain energy release rates, G_I and G_{II}, of delamination cracks by virtual crack closure with contact elements. Results are correlated with experimental data and approximate models where available. The model results, while static in nature, offer insight into trends observed for delamination under fatigue loading for various geometries and material variations, including a more detailed study of tapered ply drops. The results support and help explain experimentally observed trends of fatigue delamination resistance with material (glass and carbon), ply thickness, and crack locations. The influence of ply mis-orientation and ply drop location on the G_I (opening mode) component is also explored.

INTRODUCTION

The performance characteristics of composite materials have proven to be an enabler in many industries due to their light weight, high strength and stiffness, and capability to be formed into complex shapes. Wind turbines have used composite blades for a number of years. For wind energy to be more competitive with other forms of energy, efficiency must be improved. Material costs are a major lifecycle cost in wind turbines; low cost composites have been an area of interest for turbine manufacturers. The end cost per pound of a material used in a wind turbine blade includes manufacturing costs, so ease of manufacturing is important. The material cost requirements of wind turbines mean that manufacturers generally base material selections on cost in terms of resin and fiber systems. This has traditionally meant that lower cost glass fiber materials have been used with lower performance versions of thermoset resins.

In highly loaded structural areas of wind turbine blades, there is growing interest in using carbon composites. The higher strength and stiffness of carbon means that less material can be used, possibly offsetting its higher cost. Beyond lower amounts of materials, the use of carbon can cut costs in other areas. Lowering the weight of the blade means lower cost throughout the turbine, as the hubs, support structures, and other components can be built to handle lighter loads.

Blade design drivers for fiberglass tend to be stiffness, to clear the tower, and tensile fatigue resistance for adequate lifetime. Wind turbines are generally designed to last on the order of 20 to 30 years and 10^8 to 10^9 significant fatigue cycles with minimal maintenance [1]. Designing for fatigue is important.

This thesis quantifies the performance of lower cost materials under fatigue loading. There are two distinct areas of focus. One area is the compiling of several years worth of in-plane fatigue test data into a number of models that will help designers to better predict blade lifetime. The other focus area is modeling the delamination of plies at sites of ply drops used for thickness tapering, and ply joints used for material transitions.

Modeling of In-Plane Fatigue Behavior

Fatigue in composites differs from that in metals in numerous ways. Unlike metals, where fatigue failure is usually due to the development and growth of a crack or cracks to a critical length, composites fail in fatigue under in-plane loads due to a 'wearing out' of materials. Damage accumulates in a wider area, rather than just one crack, and is in a wider range of forms. Damage in composites can consist of matrix cracking, fiber breakage, debonding, transverse ply cracking, and ply delamination. Some or all of these forms of damage may be present.

Another fundamental difference is that in metals, cracks will not tend to grow in compression loading; compression dominated fatigue can be an important failure mode in composites, particularly in delamination. A full fatigue analysis including compression is needed to assign damage to particular cycles in the prediction of failure under spectrum loads.

The wide variety of composite systems adds a level of complexity to the study of fatigue. Different combinations of resins and fibers and different lay-ups all have different fatigue performances. General observations can be made about the influence of these various factors, though to truly qualify a unique material system, it must be tested independently. This thesis addresses materials of interest to recent and, potentially, future blade constructions; earlier studies addressed materials which are now mostly of historical interest in this application. This is the first detailed analysis of the experimental results on which this modeling effort is based. The models are also refined relative to earlier efforts in terms of the static, low cycle, and low amplitude representation. This allows for two parameter fatigue models which are simplified and allow interpretation through a single fatigue parameter, relative to three parameter models [2].

Finite Element Analysis of Ply Drop Delamination

Composite materials are not formed using methods such as machining as are traditional engineering materials. The structure and the material are designed simultaneously, then manufactured to near net shape.

Thickness is added or subtracted to a structure by adding or subtracting plies. Where plies end at ply drops (shown in Figure 1), a three dimensional stress state is created that can be detrimental to the performance of the structure if it leads to separation, or delamination, of plies in the thickness direction.

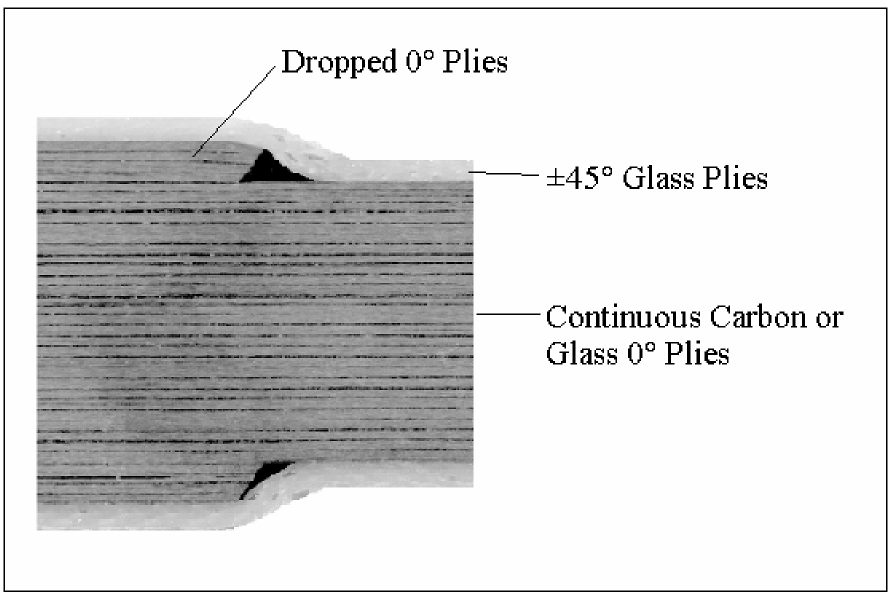

Figure 1: Ply Drop Photograph.

A composite's strength lies in its fibers, and there are generally no fibers connecting plies of material. This means that delamination of plies occurs at stresses much lower than would cause the fibers to fail. Delamination is potentially a major failure mode in structures containing ply drops, particularly for thicker plies typical of low cost composites. Figure 2 is a scanning electron microscope image of a crack at a ply drop which contains a void, as is often observed. (Note: the crack in Figure 2 has been highlighted for clarity.)

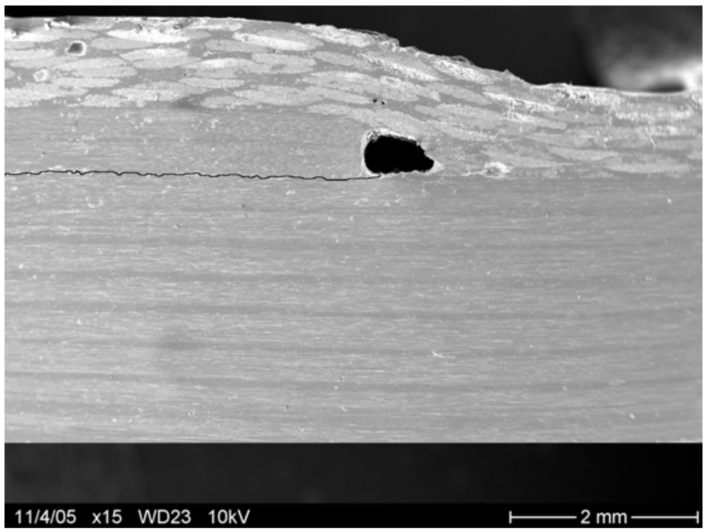

Figure 2: Delamination Crack in External Ply Drop.

Delamination at ply drops has been a tolerable problem with aerospace structures composed of relatively thin (0.15 mm) aerospace prepregs, although fatigue prone applications like helicopter blades have required careful design [3]. Using thin prepregs, however, introduces unwanted manufacturing costs, as many plies of material must be layered to build up the necessary thickness. Therefore, manufacturers use thicker ply composites to save time and cost in manufacturing wind turbine blades. However, the problem with delamination of ply drops has been identified as a failure mode in wind turbine blades [4] and has prompted this study of ply drop delamination behavior. The work described here is intended to improve understanding of results in a related experimental study by characterizing the strain energy release rates for various materials and geometries using finite element analysis (FEA).

MODELING OF IN-PLANE FATIGUE BEHAVIOR

This section of the thesis analyzes data from many years worth of fatigue tests. Test procedures are outlined. Data are fit with models and 95/95 confidence limits, and constant life diagrams are created to organize the data. Finally, the models are applied in a novel comparison between different materials using the WISPERX spectrum (a wind loads spectrum).

Introduction to Materials

All materials studied here are continuous fiber reinforced polymer composites. Materials tested and discussed in this thesis are listed as the following in the DOE/MSU fatigue database [5]: DD16, QQ1, QQ1T, P2B, and P2BT. As noted earlier, experimental results for this section was reported by Samborsky [5]. This thesis is concerned with fitting the data. These materials are described below:

Fiberglass Laminate DD16, Axial Direction

Material DD16 is one of the most extensively characterized composite materials in terms of fatigue performance. This material uses relatively out of date constituents for wind turbine blades, but is valuable for research, as so many tests have been run using it. The fibers are fiberglass, stitched into bundles referred to as D155, with a lay-up of $[90/0/\pm45/0]_S$, where the axial (load) direction is 0° The resin is a polyester resin, Corezyn 63-AX-031; mixed with 1% MEKP (a catalyst). This material is made by injecting the dry fiberglass fabric with resin by RTM, as described below. The material is post-cured at 65°C for at least 2 hours. The resulting volume fiber fraction is 0.33 [5]. DD16 is described in detail in Samborsky's thesis [6] and by Wahl and Nijssen [7, 8].

Fiberglass Laminate QQ1, Axial Direction

Material QQ1 is a more current, higher fiber content, fiberglass composite than DD16 for wind turbine blades, and is more representative of materials being used today. This material is manufactured by injecting a resin into dry fabrics, essentially the same as the process used to make material DD16, and is described below. The material lay-up is $[\pm 45/0_2]_S$. Vantico TDT 177-155 epoxy resin is used to form the matrix. The fabrics are made by Saertex; the 0's are identified as U14EU920-00940-T1300-100000 (0°-864g/m^2, 90°-79 g/m^2, stitching 12 g/m^2) and the ±45's are VU-90079-00830-01270-000000 (800 g/m^2). The material is post cured for eight hours at 70°C. The resulting volume fiber fraction is 0.53. The fiber fractions in this material are 29.8% ±45°, 64.3% 0°, and 5.9% 90° (from transverse strands in the 0° fabric).

Fiberglass Laminate QQ1T, Transverse Direction

Material QQ1T is material QQ1 tested in the transverse (90°) direction. The lay-up is $[\pm 45/90_2]_S$.

Carbon/Glass Hybrid Laminate P2B, Axial Direction

Material P2B is made of mostly carbon prepreg. The lay-up is $[\pm 45/0_4]_S$, where the 0° plies are carbon and the ±45° face sheets are made of a woven glass prepreg. Both materials are made by Newport Adhesives and Composites, Inc. The carbon 0°'s are designated NCT307-D1-34-600 Carbon and the glass ±45°'s are designated NB307-D1

7781 497A (sold as a woven 0/90 prepreg). The manufacturing process used to make the coupons is described below. The fiber volume fraction is 0.55 [5] and the laminate is 85% 0° material by volume (85% of the thickness is 0° ply).

Carbon/Glass Hybrid Laminate P2BT, Transverse Direction

Material P2BT is material P2B tested in the transverse direction. Thus, the lay-up is $[\pm 45/90_4]_S$.

Coupon Manufacture

Vacuum Assisted Resin Transfer Molding

Materials DD16 and QQ1 were manufactured using Vacuum Assisted Resin Transfer Molding (VARTM), see reference [9] for details. In this process, dry sheets of fiberglass fabric were placed in a closed mold. Resin was injected into injection ports while simultaneously a vacuum was pulled at exit ports. This vacuum was approximately 500 – 550 mmHg. Resin flowed through the mold, wetting out the fabric. The pressure difference between the positive gauge pressure at the input port from the pump and the negative gauge pressure at the exit ports creates a pressure gradient, enhancing the resin flow through the fabric.

Prepreg Layup

Material P2B is made from carbon prepreg material using net resin curing (no bleed-off of resin). The prepreg was stored in a freezer at -18° C. Before the lay-up process could begin, the roll of material would be taken out of the freezer and allowed to warm to room temperature. The roll was then cut into sheets approximately 30 x 45 cm (12 x 18 inches). The sheets were then stacked together and rolled with a laminate roller to ensure a good bond between plies. The rolling process involved two people. One person held an edge of the upper ply above the lower ply while the other person rolled the plies together, moving toward the held edge. This method ensures that no air is trapped between the plies.

Once the plies of prepreg were laid up, the resulting laminate was wrapped in Teflon release paper. This was placed on a flat aluminum sheet in a convection oven and covered with vacuum bagging film. The vacuum film was sealed with heat resistant vacuum bag sealant tape. A vacuum was pulled (550 mmHg) and the lay-up was heated to 121° C. The oven ramp rate was approximately 1° C per minute. The oven was held at temperature for three hours and then turned off and allowed to cool overnight. The materials used with the prepreg for the vacuum bagging process are listed in Table 1.

Item	Manufacturer	Product	Notes
Teflon Release Film	Airtech	Release Ease 234TFNP	Non-porous 1080 style glass, 0/90 glass fiber, Teflon coated, Thickness 0.075 mm
Vacuum Bagging Film	Richmond Aircraft Products	VAC-PAK HS 8171-6/66	Co-Extruded High Temperature Nylon 6/66 Film, Thickness 0.051 mm
Vacuum Bag Sealant Tape	Airtech	AT-200Y	Multi-purpose sealant tape Maximum Temperature: 200° C

Table 1: Vacuum Bagging Materials.

Coupon Design

After cooling, the cured plate was removed form the oven and cut into coupons. The majority of coupons used were 2.5 cm by 13 cm, shown in Figure 3. The thickness of these coupons is dependent on the material lay-up. When placed in the grips of the testing machines, this produced a gauge section of about 1.3 cm. These coupons were used for the majority of tests with good results, with a few exceptions listed below.

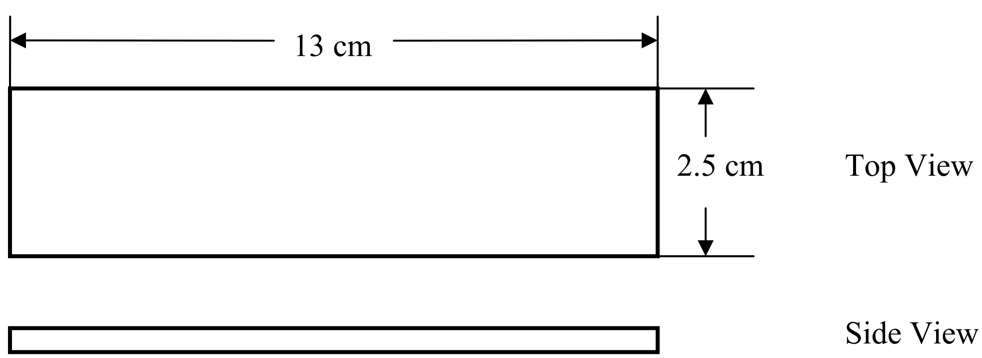

Figure 3: Rectangular Coupon.

Exceptions to this geometry included elongated gauge section coupons, which allowed for the attachment of an extensometer, used in tests to find the elastic modulus of materials. Also, a limited number of dogbone coupons, shown in Figure 4, were used for tension-tension (R = 0.1) fatigue testing of material QQ1. There was, however, no significant difference in fatigue performance between this coupon geometry and the simple rectangular coupon, so the dogbone coupon was discontinued.

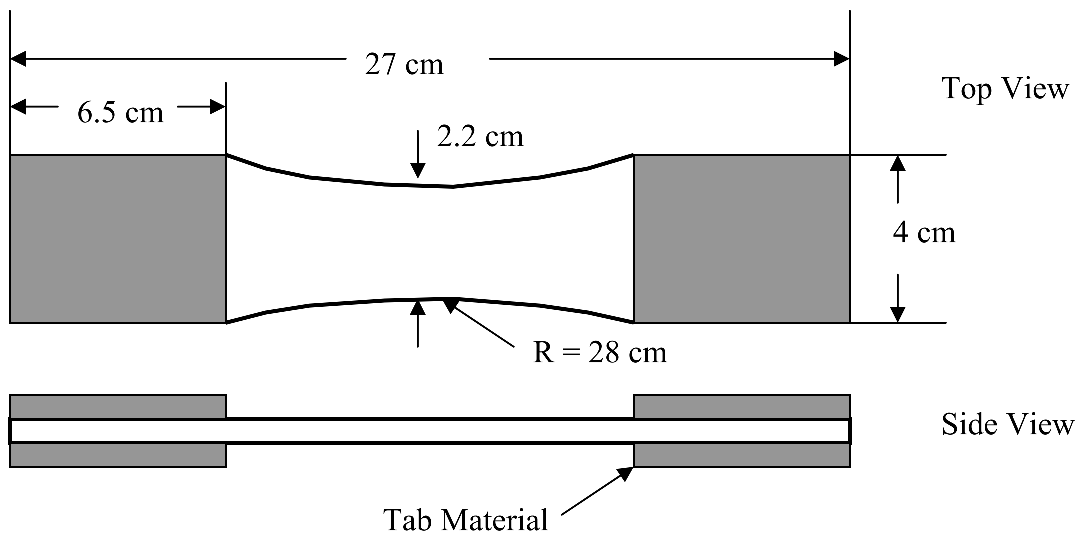

Figure 4: Dogbone Coupon.

Tabs are often used in composite material testing to prevent grip induced damage in the material of interest. In these materials, tabs were only used in the QQ1, R = 0.1 dogbone coupons, which were later discontinued. The tabs were made from Plastifab G10 (1.6 mm, $[0/90]_7$, $V_f = 35\%$) fiberglass and were bonded (using Hysol EA 9309.2NA adhesive) to the dogbone coupons.

Testing

Static Tests

Static strength tests were done under load control at a ramp rate of 13 mm/s. This high ramp rate is similar to the rate used in fatigue testing, and is much faster than for standard tensile tests (which can increase the apparent strength). Failure was considered as the coupon separating into two pieces for tension tests and as ply buckling in the gauge section for compression tests.

Fatigue Tests

All fatigue tests reported here were run under a load control sine waveform constant amplitude. Tests were run at different R values, defined in Figure 5 and Equation 1.

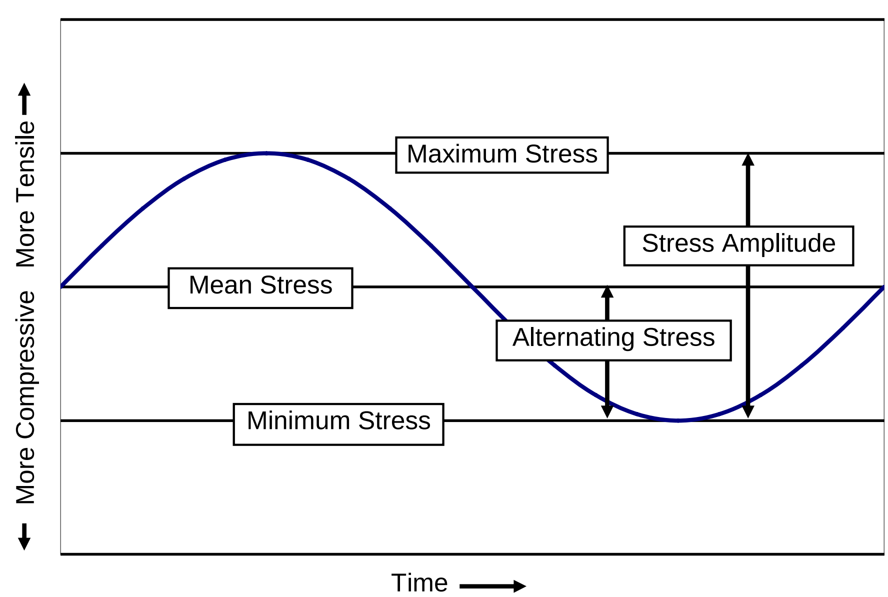

Figure 5: Waveform Definitions.

$$R = \frac{Minimum\ Stress}{Maximum\ Stress} \tag{1}$$

It should be noted that compressive stresses are taken as negative, so the maximum stress in Equation 1 is always the more tensile stress. In a case where the mean stress is compressive, the minimum stress may have a higher absolute value.

The fatigue tests were done under load control to maintain a constant mean and alternating stress over the duration of the test. As the test coupon degrades under fatigue loading, it generally becomes more compliant. Under position control, the stress in the progressively more compliant coupon would decrease over time.

A summary of R values tested is given in Table 2:

	Compression	Mixed	Tension
DD16	1.1, 1.43, 2, 10	-2,-1, -0.5	0.1, 0.5, 0.7, 0.8, 0.9
P2B	10	-2, -1, -0.5	0.1, 0.5
P2BT	10	-2, -1, -0.5	0.1, 0.5, 0.7
QQ1	10	-2, -1, -0.5	0.1, 0.5
QQ1T	10	-2, -1, -0.5	0.1, 0.5, 0.7

Table 2: Fatigue Tests Run for Each Material.

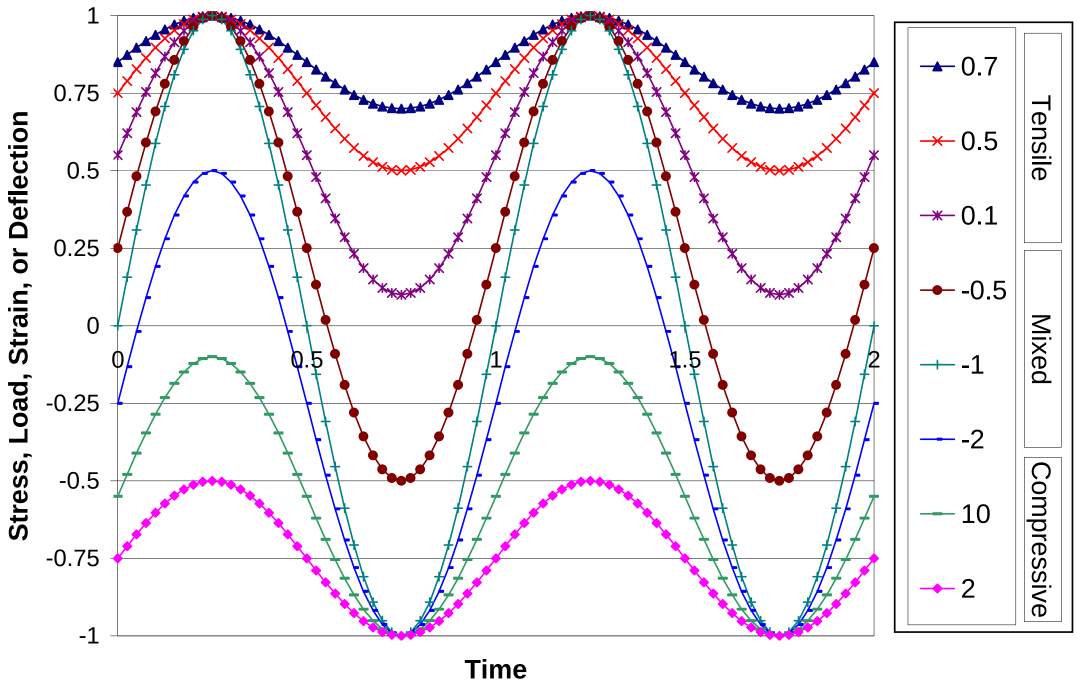

Figure 6: Waveforms for Common R Values.

Figure 6 is a plot of a number of common R Values used for fatigue testing. This figure shows the variation in the waveforms. A number of different testing machines were used to perform the fatigue testing. All of these machines are servo hydraulic machines, made by Instron Corporation. A summary is provided below in Table 3:

Machine	Maximum Load	Maximum Stroke	Used For
Instron 8501	100 kN	100 mm	Longitudinal Materials, Static Tests, Modulus Tests
Instron 8511	10 kN	50 mm	Tension Fatigue Tests for Transverse Materials
Instron 8872	25 kN	100 mm	All Tests for Material DD16, Compression Fatigue Tests for Transverse Materials

Table 3: Summary of Testing Equipment.

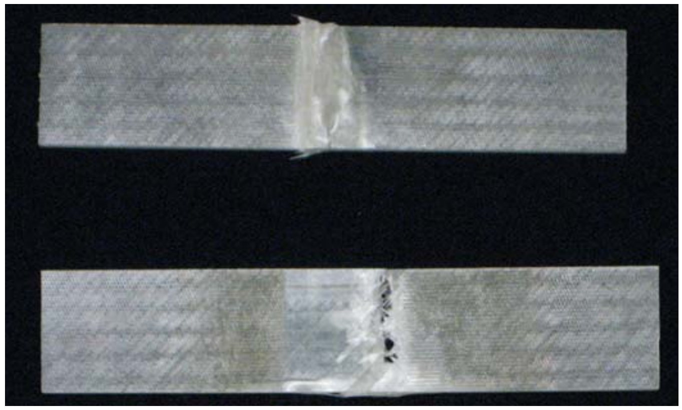

Figure 7: Failed QQ1 Coupons; Upper: Compressive Failure; Lower: Tensile Failure.

All tests were run until the coupon failed completely. In tension dominated tests, this meant the coupon was pulled into two pieces. In compression dominated tests, failure resulted in buckling in the gauge section or associated with the grips until the machine reached a predetermined position limit. Figure 7 shows examples of failed QQ1 coupons. The upper coupon failed in compression; fibers can be seen brooming out on the sides. The lower coupon is a tensile failure and the crack separating the two halves can be easily seen. An important limitation of these experimental data is that most fatigue failures for the axial direction occurred at the grip edge or inside the grips. This is a problem in current blade materials, which are stronger than earlier materials if they have a high 0° ply content. The same difficulty has been reported in recent European studies [8]. Test methodology is currently under study.

Test Results

A total of almost 900 tests were performed by Samborsky to characterize the materials. Table 4 breaks down the number of tests by material. The test results are available in the DOE/MSU Database, Reference 5.

Material	Fatigue Tests	Static Tests	Total Tests
DD16	375	46	421
QQ1	153	19	172
QQ1T	117	8	125
P2B	132	40	92
P2BT	136	18	154
Total	801	96	897

Table 4: Number of Static and Fatigue Tests Performed.

Data Reduction

Static Results

Figure 8 contains typical stress strain curves for materials P2B and QQ1 in both the axial and transverse directions. The loading rate for these tests is a 1 mm/minute, much slower than for static strength tests listed with the fatigue data, in order to beter define the Young's modulus. The strain gauge on the surface of P2BT coupon was damaged by surface cracking; a dotted line extrapolates the existing data to failure.

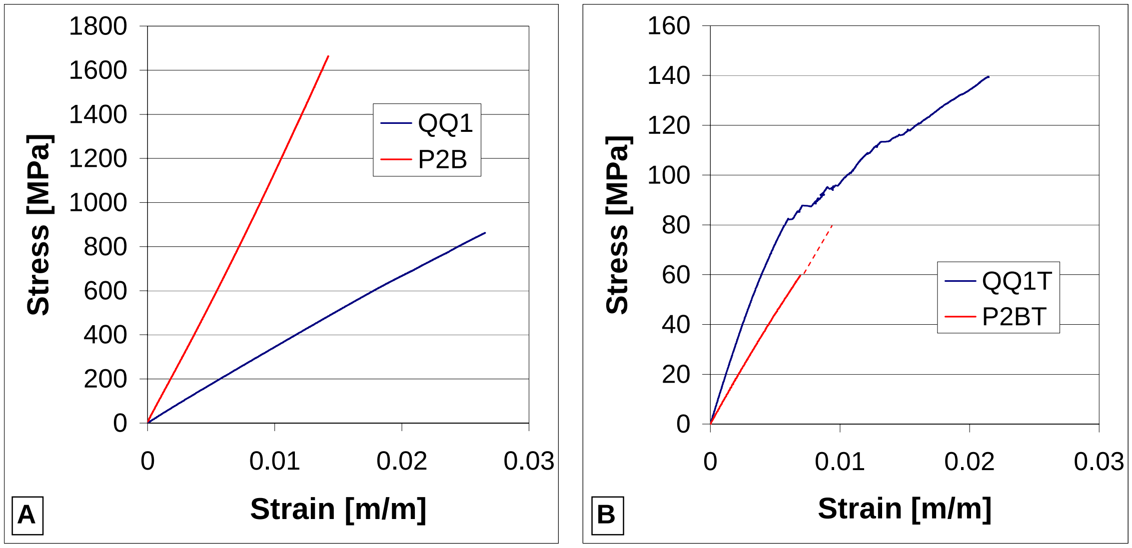

Figure 8: Typical Tensile Stress vs. Strain Diagrams for Materials QQ1 and P2B. A: Axial Direction; B: Transverse Direction.

The mean strengths and Young's modulus were found for the static test data, compiled in Table 5. A notable difference is that the transverse properties of the glass laminate QQ1T are significantly higher than for the carbon hybrid P2BT. The difference derives from the higher transverse ply modulus with glass and the small amount of transverse strands in the 0° glass fabric.

Material	Mean Tensile Strength [MPa]	Mean Compressive Strength [MPa]	Tensile Young's Modulus [GPa]
DD16 (Axial)	631.9	402.1	18.33
QQ1 (Axial)	868.9	689.7	32.97
QQ1T (Transverse)	148.5	274.1	17.05
P2B (Axial)	1535.9	1047.0	100.8
P2BT (Transverse)	79.4	240.1	8.85

Table 5: Mean Static Properties.

Fatigue Models

Two types of equations are generally used to model fatigue data, logarithmic:

$$S(N) = m \cdot \log(N) + b \tag{2}$$

And power law:

$$S(N) = A \cdot N^{B} \tag{3}$$

Where S is the maximum absolute stress and N is the number of cycles to failure and m, b, A, and B are constants. Logarithmic models have been used a great deal in the past, as they generally fit all data, including static data, fairly well. This is partly the case because, until fairly recently, there has been little published high cycle data for composites [10, 11]. Logarithmic equations poorly model fatigue data at high numbers of cycles for some materials and in some load conditions. A logarithmic equation fit to fatigue data is linear on a log-linear scale, with a negative slope. At some high number of cycles to failure, the trend will extrapolate to zero, which is obviously not physically correct.

Power law models tend to provide improved fit at high cycles [10]. Because of this, all data sets for materials here were fit with power law models. However, power law models tend to fit low cycle data poorly. Therefore, many data sets for materials presented here were truncated to exclude some low cycle data, and the static and low amplitude/low cycle data were treated separately.

95/95 Confidence Limits

Establishment of a confidence limit for the fatigue data begins with setting a linear best fit equation to the log test data.

$$\log_{10}\left(S(N)\right) = m \cdot \log_{10}\left(N\right) + b \tag{4}$$

Plotted on a log-log scale, this model is linear. This mean best fit equation serves as a 'mean' value for the stress that varies with the number of cycles. The slope of the equation on a log-log scale, m, corresponds to the exponent B from the power law equations used for the mean fits through the data, providing a convenient check. From the mean fit, the standard deviation (SD) for the data set can be found using Equation 5, where S_i is the actual stress from the data set and N_i is used to calculate the stress from the mean fit equation.

$$SD = \sqrt{\frac{1}{n-1}\sum_{i=1}^{n}\left(\log_{10}\left(S_i\right) - m \cdot \log_{10}\left(N_i\right) + b\right)^2} \tag{5}$$

The standard deviation equation used is for the sample standard deviation, not population, as the test data are only a limited sample of the material and do not represent all possible samples, or the whole population.

The one sided tolerance limit is calculated from the standard deviation by the application of a one-sided tolerance limit multiplier, denoted $c_{1-\alpha,\gamma}$ in Equation 6, following Sutherland and Veers [12]. The confidence level is denoted by $1-\alpha$, and γ signifies the probability that future tests of the material will surpass the S_{CL} strength. A

95% probability with a 95% confidence is commonly used throughout the wind industry [12], and is calculated for this thesis.

$$S_{CL}(N) = 10^{\left(\log_{10}(N) + b - c_{1-\alpha,\gamma} \cdot SD\right)} \tag{6}$$

The one-sided tolerance limit multiplier, $c_{1-\alpha,\gamma}$, is tabulated in many statistics texts and varies with the number of data points used [13]. Application of Equation 6 can be described as “with a 1-α confidence level, we expect that at least γ of all future tests will exceed S_{CL}.” [12] In foregoing results (Tables 6 – 8, 10 and 11), the intercept b and the tolerance limit term $c_{1-\alpha,\gamma} \cdot SD$ are combined into a term labeled “b-tol,” resulting in Equation 7.

$$S_{CL}(N) = 10^{\left(\log_{10}(N) + b - tol\right)} \tag{7}$$

This procedure can be applied to static data as well, though in this case the mean is a single value, not a function. The process is the same, find the mean, $\overline{S}$, the sample standard deviation, and the one-sided tolerance limit, and calculate the confidence limit using Equation 8.

$$\overline{S}_{CL} = \overline{S} - c_{1-\alpha,\gamma} \cdot SD \tag{8}$$

<u>Fits to Test Data</u>

All data were fit using a least squares fit, done in Microsoft Excel. Goodness of fit was measured by the residual squared (R^2) value. In cases where a higher quality of fit could not be seen by visual inspection between different models, the model with the higher R^2 value was chosen.

Fit parameters are given for each R value for each material. Included with the parameters is the static failure mode, listed as either compression or tension. This indicates what failure mode tends to drive failures at low or 1 cycle. Static tensile strength (STS) or static compressive strength (SCS) are given as well. These are the 95/95 tolerance limits of the static values. Mean static values are listed in Table 5. The given mean power law fit parameters correspond to Equation 3. 95/95 model parameters correspond to Equation 7. Figure 9 is an example of a DD16 data set with the model.

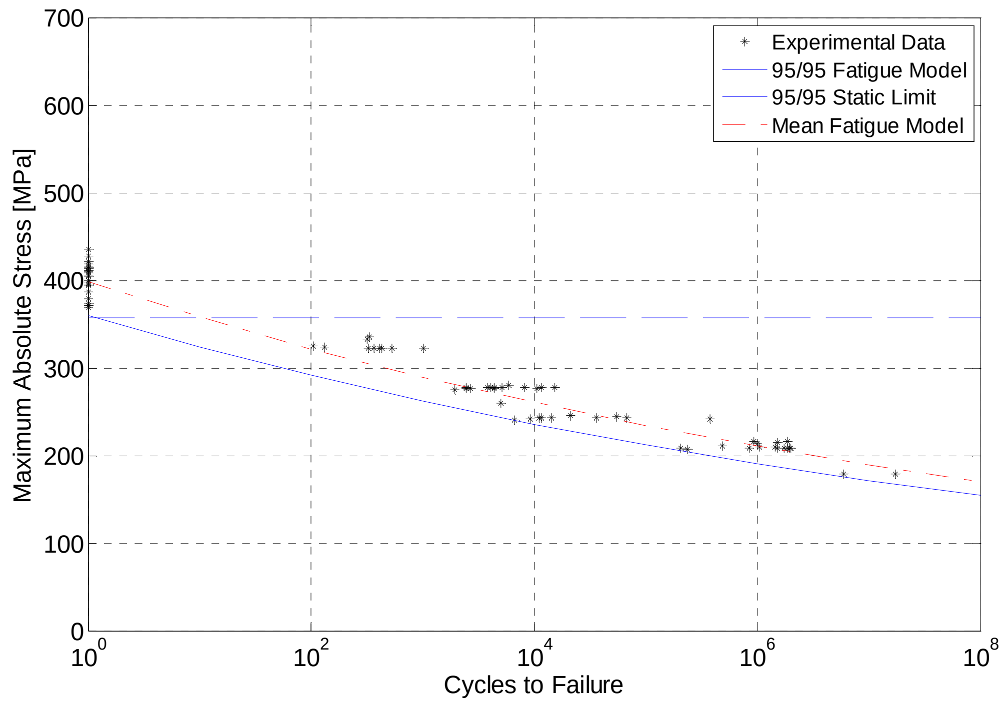

Figure 9: DD16, Axial Direction, Stress vs. Cycles to Failure, 95/95 Fit, R = 10 (Model Fit to Fatigue Data Only, for Stresses which Produce Failure on the Order of 1000 cycles)

In many of the plots below (i.e. Figure 10 - Figure 21), the power law model predicts strengths at low cycles higher than the static strength of the material. This appears to be erroneous from residual strength studies [7, 8]. For mean constant life diagrams, the static strength value is used for cycles below where the model strength exceeds the static strength. The model is usually fit only to the fatigue data, and may not represent the static strength distribution. The static 95/95 limit is shown as a separate dashed line.

Fiberglass Laminate DD16, Axial Direction

DD16 test results show a wide range of material performance, depending on the R value. There is a variance on the order of 350 MPa maximum sustainable stress at 10^8 cycles between a specimen loaded with an R value of -1, fully reversed loading, and an R value of 0.9, tension dominated loading.

Material DD16 fatigue data were first truncated to exclude data points on the order of 1000 cycles or less, so that only data points at stress levels where most of the coupons failed at 1000 or more cycles are included. This was done to better fit the high cycle fatigue data. The low cycle data sometimes follow a shallower trend, and inclusion hurts the quality of the fit at high cycles. An alternative is to use a three parameter fit, which can represent both high and low cycle domains, but at the cost of considerable complexity [2]. The truncated data set is fit with a mean fit (Equation 3) and 95/95 fit (Equation 7). The exponents, B, in Table 6 represent the fatigue sensitivity which is maximum at R = -1, and remains high where tension dominated, R = -2 to 0.8.

R Value	Static Failure Mode	95/95 Static Strength [MPa]	Mean Fit Parameters		95/95 Fit Parameters	
			A	B	m	b-tol
1.1	Compression	357.5	N/A	N/A	N/A	N/A
1.43	Compression	357.5	420.8	-0.0182	-0.0182	2.589
2	Compression	357.5	458.2	-0.0372	-0.0372	2.576
10	Compression	357.5	397.7	-0.0460	-0.0460	2.556
-2	Compression	357.5	648.4	-0.0876	-0.0876	2.772
-1	Compression	357.5	691.1	-0.1280	-0.1280	2.786
-0.5	Tension	539.4	621.8	-0.1134	-0.1134	2.739
0.1	Tension	539.4	637.5	-0.0891	-0.0891	2.743
0.5	Tension	539.4	787.5	-0.0949	-0.0949	2.819
0.7	Tension	539.4	995.6	-0.1059	-0.1059	2.935
0.8	Tension	539.4	985.9	-0.0907	-0.0907	2.937
0.9	Tension	539.4	760.2	-0.0523	-0.0523	2.838

Table 6: Fit Parameters for Material DD16, Axial Direction (Fit to Fatigue Data Only, for Stresses which Produce Failure on the Order of 1000 cycles).

The following figures (Figure 10 through Figure 12) show the mean fit lines through the test data.

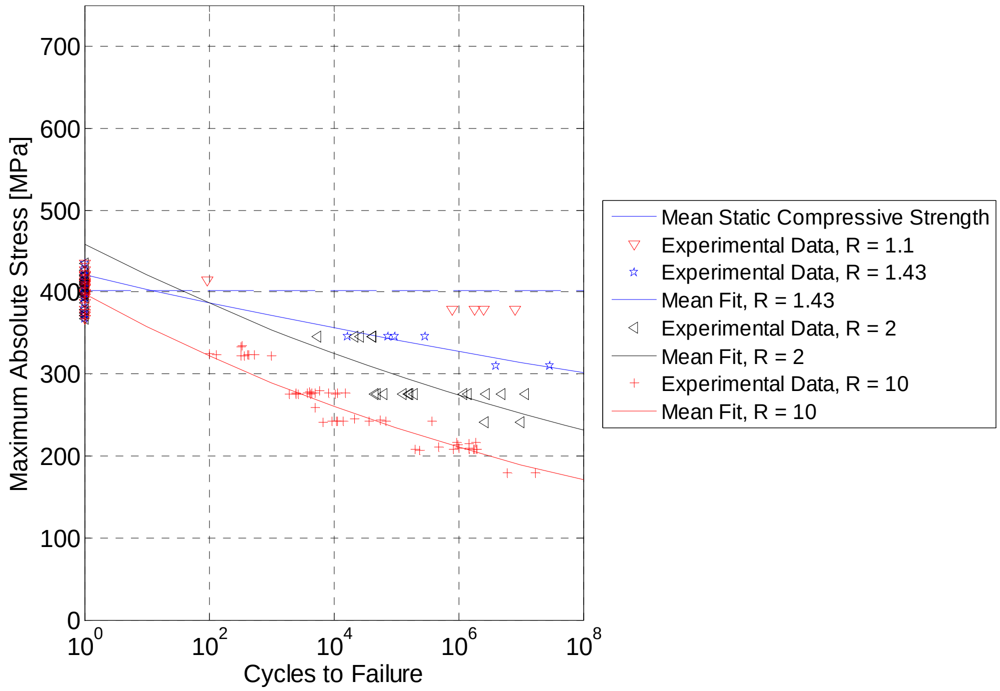

Figure 10: Compression Fatigue, Mean Power Law Fits (Material DD16, Axial Direction).

As seen in Figure 10, a mean fit line was not done for an R value of 1.1 because, after truncating the data to only include data higher than 1000 cycles there is only one stress level represented, making a meaningful fit impossible. Furthermore, these data points are within the range of the static compressive strength.

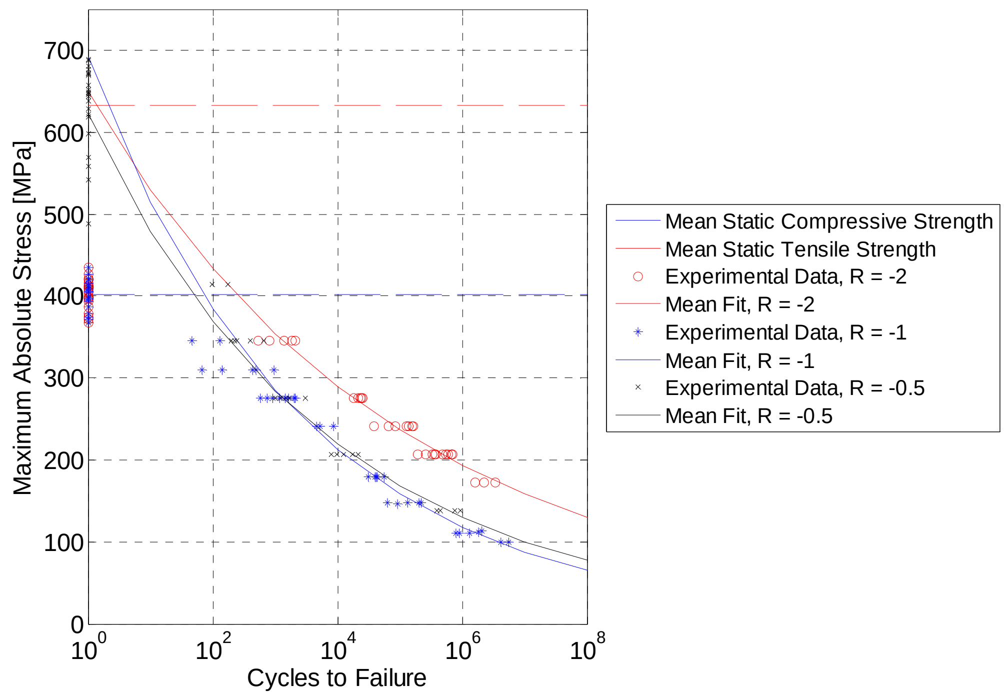

Figure 11: Mixed Fatigue, Mean Power Law Fits (Material DD16, Axial Direction).

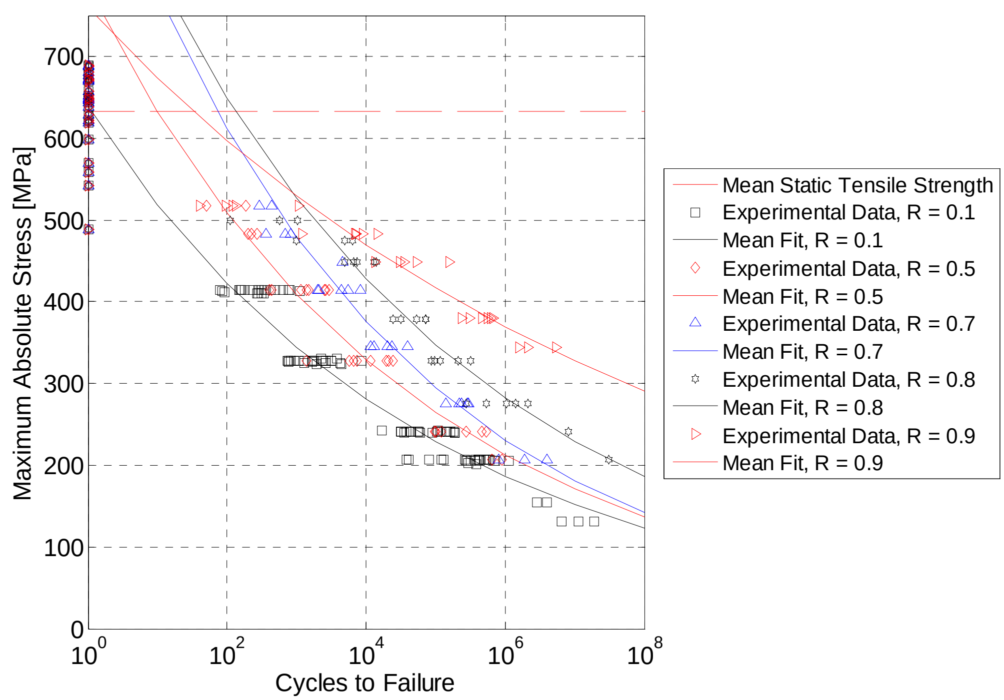

Figure 12: Tensile Fatigue, Mean Power Law Fits (Material DD16, Axial Direction).

Material DD16 was also tested to determine its stress rupture behavior [10]. Stress rupture, also referred to as "static fatigue" is a material characteristic of glass, and glass fiber composites. For many materials, being held under a constant stress at room temperature does little to reduce the strength of the material. Many glasses including E-glass, however, do not share this trait. Held under a constant stress, these glasses will develop and grow cracks in the fibers that will reach the critical length and cause the material to fail. This controls the tensile strength, even at short times [14].

DD16 coupons were quickly loaded and then held at a constant stress until failure. Time to failure varied with the magnitude of the applied tensile stress, as shown in Figure 13.

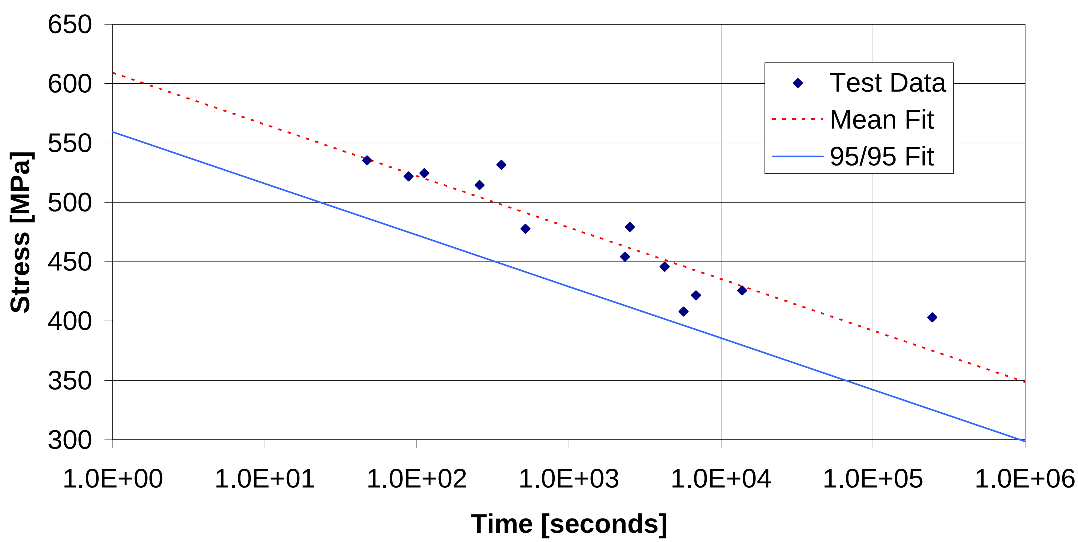

Figure 13: Stress Rupture Data with Models (Material DD16, Axial Direction).

The tolerance limit was calculated in a similar manner as with fatigue data. The logarithmic equation was fit as a best fit, labeled as "Mean Fit" in Figure 13, thus functioning as a mean value. Differences in stress (not log stress in this case) from the predicted values were used to calculate a standard deviation. With the standard deviation and the factor for one sided tolerance limit, based on the number of points, a level of confidence was fitted, as indicated as “95/95 Fit” in Figure 13. The procedure used to develop 95/95 fits is discussed in greater detail in a later section. The mean logarithmic fit is given as Equation 9:

$$S(t) = 609.06 - 43.418 \cdot Log(t) \tag{9}$$

The 95/95 tolerance fit is given as Equation 10:

$$S_{95/95}(t) = 559.23 - 43.418 \cdot Log(t) \tag{10}$$

The time dependence of strength can also be applied to cyclic loading patterns by quantifying the damage (strength loss) that occurs due to the stress rupture effect for each cycle. Time to failure must be adjusted to account for the variation in loading over a loading cycle. To do this, a sinusoidal wave form was assumed for the loading. As stress rupture damage can only occur under tension, no stress rupture damage occurs in compression-compression loading cases. Finding the roots (zero crossings) for this sinusoidal wave form was necessary for loading cases that were reversed loading (negative R values). Damage occurs at all points during a tension-tension (R values between zero and one) loading case.

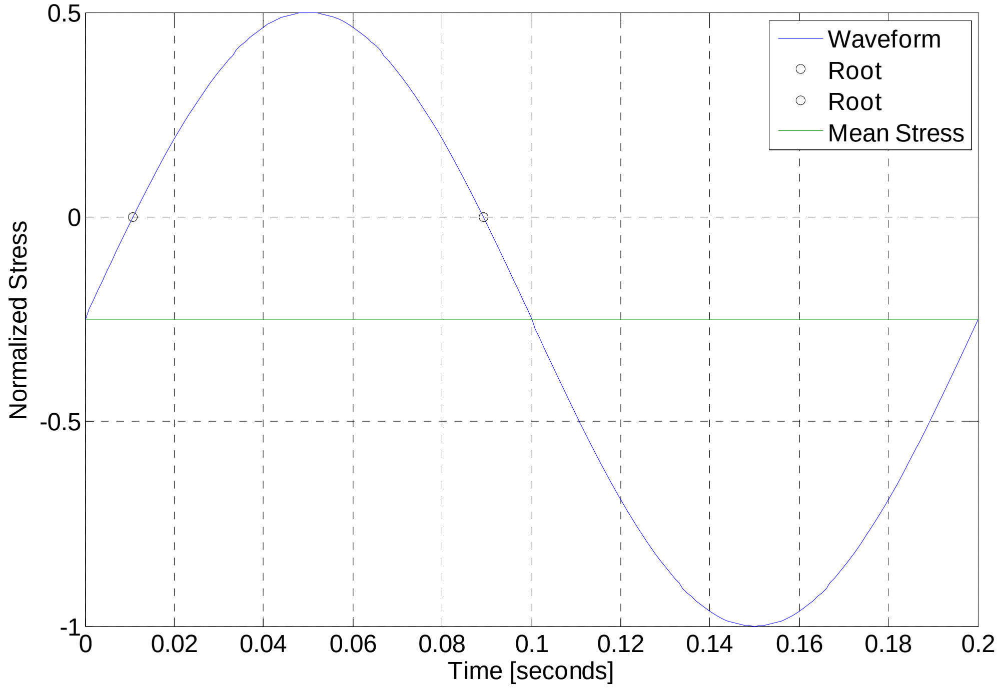

Figure 14: Load Waveform, Stress Rupture Model; f = 5Hz, R = -2.

Damage is quantified by a function of time (t), shown in Equation 11, the inverse of the number of cycles to failure at a given load mixture (S_a = alternating stress and S_m = mean stress) and frequency (f).

$$D(t) = \frac{1}{10^{\left(\frac{559.23 - S_a \cdot \sin(2\pi \cdot f \cdot t) - S_m}{43.418}\right)}} \tag{11}$$

The damage versus time quantified by Equation 11 for a frequency of 5 Hz and an R value of -2 is shown in Figure 15.

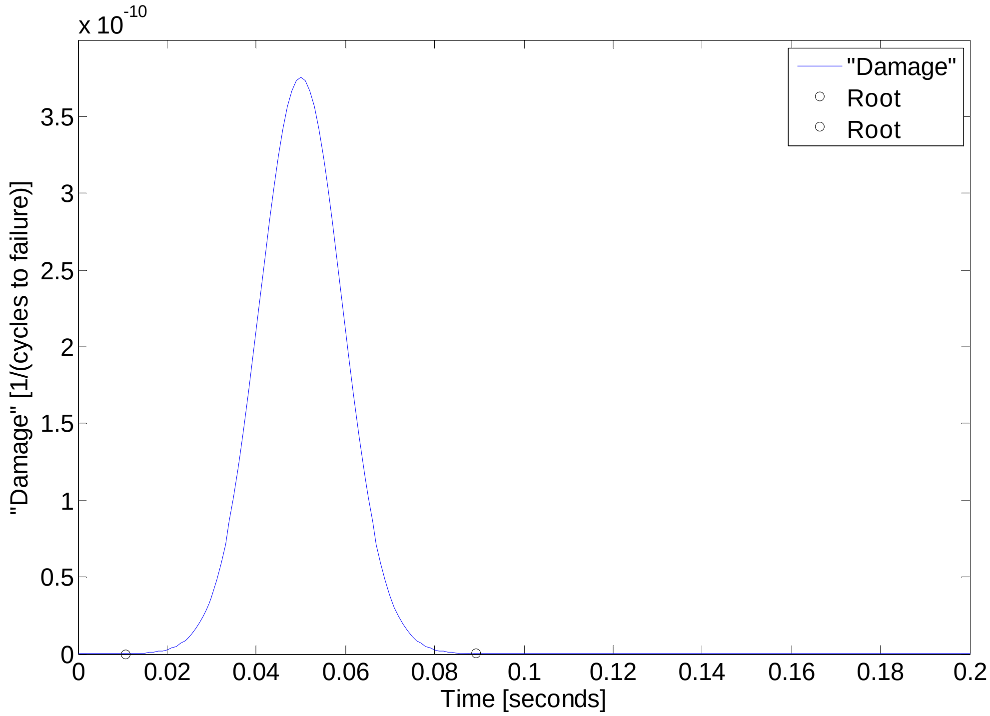

Figure 15: "Damage" per cycle, Stress Rupture Model; f = 5Hz, R = -2 (Material DD16, Axial Direction).

By integrating this damage over the tension portion of the loading waveform, shown by the two roots in Figure 15, a total quantity of damage per cycle is found. This was done numerically using an adaptive lobatto quadrature routine internal to MatLab [15]. The inverse of this term is the number of cycles to failure. Thus, cycles to failure can be found as a function of the stress level, loading waveform (R value), and loading frequency, based on time effects alone.

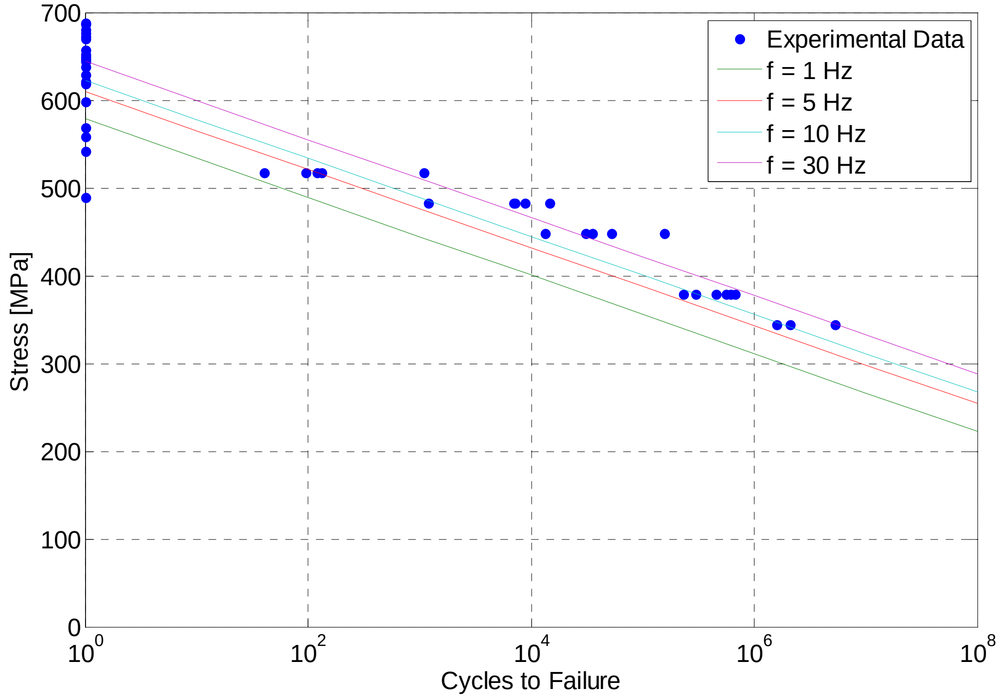

Figure 16: Stress vs. Cycles to Failure, Stress Rupture Model; R = 0.9 (Material DD16, Axial Direction).

Figure 16 shows the DD16 stress rupture model for different loading frequencies plotted with fatigue data from an R value of 0.9. The stress rupture model shows good agreement with the overall trend of the fatigue data, indicating that this mode of failure may drive material behavior at this extreme R-value tension-tension fatigue case.

This model can be integrated with a fatigue life data to get a more accurate estimate of lifetime. Only at the tension-tension end of the spectrum, where there is a low alternating stress and a high mean stress, does the stress rupture model begin to influence the lifetime predictions.

This stress rupture model improves the fit of the DD16 model for low alternating, high mean stress tensile fatigue (R values approaching 1) by calculating the damage accrued by time under load, though it does not affect the model for tensile fatigue with lower mean stresses. Work by Mandell and Meier has shown that a combined effect of cyclic and stress rupture damage may exist at tensile fatigue with lower mean stress [14]. They propose that the stress rupture curve of a glass fiber composite is shifted downward by cyclic loading. Figure 17 presents a schematic of this model. An initial stress rupture (referred to in the figure as static fatigue) curve is shown. Curves with various percentages of reduced short-time static strength are shown below. Cyclic loading reduces the residual strength of a material; it is assumed that this is reflected in the reduced short-time strength, and can be predicted using various residual strength models [2, 7, 8].

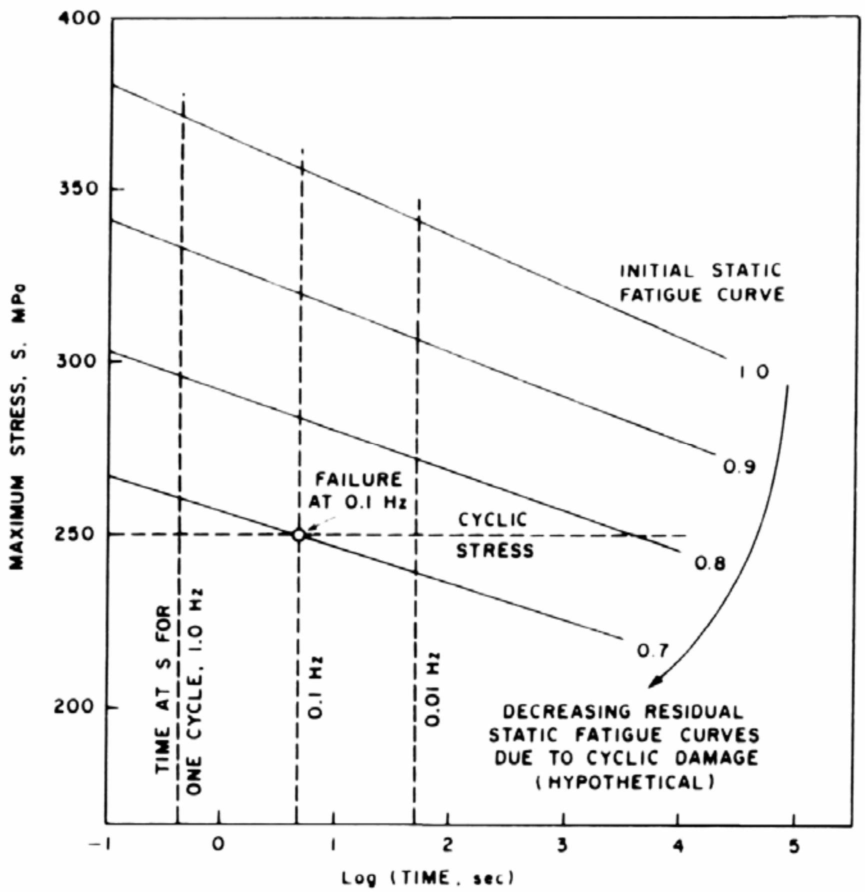

Figure 17: Schematic of Anticipated Square Wave Frequency Effects for Glass Reinforced Epoxy [14].

Application of this model may improve model fits for glass fiber composites under tension fatigue loading with a lower mean stress (R values approaching zero). In low cycle fatigue, the reduced residual strength of the material may combine with a stress rupture phenomenon to drive failure. Further work is needed to verify and apply this model.

Fiberglass Laminate QQ1, Axial Direction

The majority of the data sets for the different R Values of QQ1 were fit with power law equations through all of the fatigue data. For two R values, however, better fits to the higher cycle data were obtained by fitting equations to truncated fatigue data sets. For R = -1, the data fit were at a stress level that produced failures over 10 cycles. For R = 0.5, the data were truncated at a stress level that produced failures on the order of 500 cycles or greater. Table 7 gives the fit parameters. Figure 18 through Figure 20 show these fits. Static tensile, R = 1.0, data were not available for materials QQ1 (or P2B) so stress rupture predictions were not made. As with DD16, the fatigue model trend is shown in the static range, but only the static mean or 95/95 limit line represents the static data.

R Value	Static Failure Mode	95/95 Static Strength [MPa]	Mean Fit Parameters		95/95 Fit Parameters	
			A	B	m	b-tol
10	Compression	595.5	690.4	-0.0445	-0.0445	2.796
-2	Compression	595.5	697.6	-0.0600	-0.0600	2.795
-1	Compression	595.5	931.2	-0.1378	-0.1378	2.902
-0.5	Tension	758.4	1172.6	-0.1407	-0.1407	3.012
0.1	Tension	758.4	1327.6	-0.1556	-0.1556	3.056
0.5	Tension	758.4	1358.9	-0.1313	-0.1313	3.092

Table 7: Fit Parameters for Material QQ1, Axial Direction (Fit to All Fatigue Data, Except Fit to Data for Stresses which Produce Failure above 10 Cycles (R = -1) and 500 Cycles (R = 0.5).

The exponent, B, for material QQ1 has a higher absolute value in the range R = -1 to 0.5 than for DD16, showing increased tensile fatigue sensitivity. The compression dominated exponents are similar to DD16.

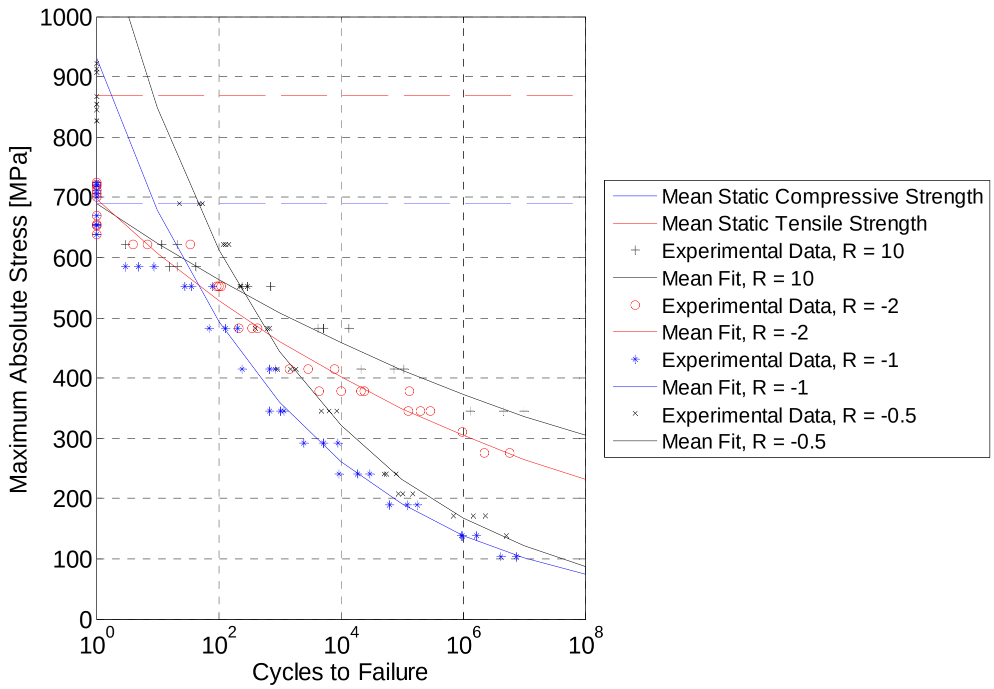

Figure 18: Compression and Mixed Fatigue, Mean Power Law Fits (Material QQ1, Axial Direction).

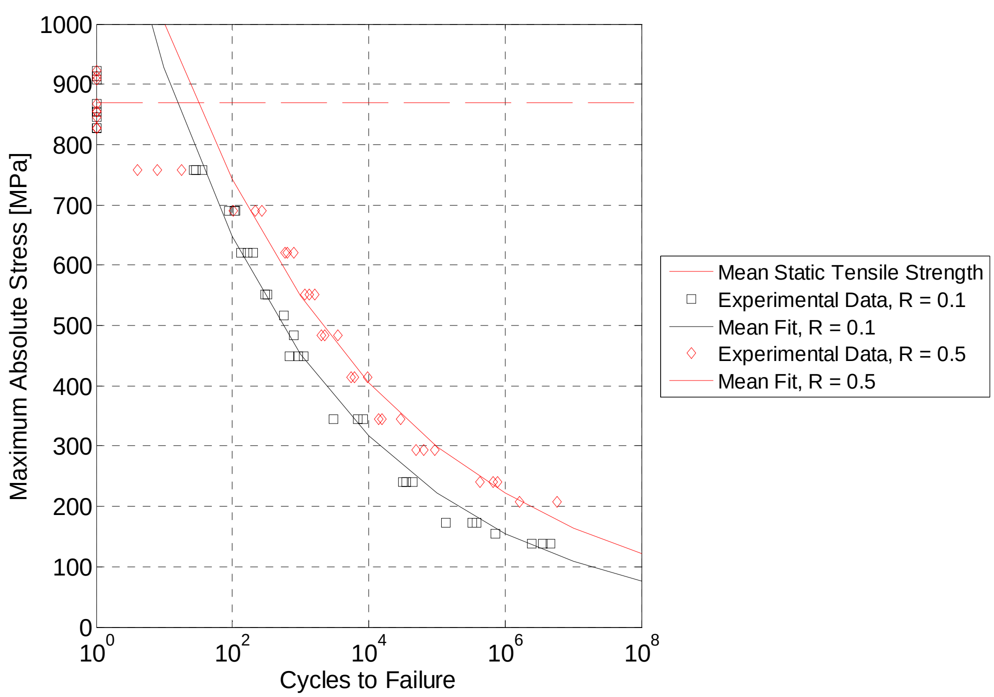

Figure 19: Tensile Fatigue, Mean Power Law Fits (Material QQ1, Axial Direction).

Fiberglass Laminate QQ1T, Transverse Direction

Material QQ1T is modeled with power laws fit though all of the data. Parameters are given in Table 8 and mean fits are shown in Figure 20 and Figure 21. The lower absolute value of B than for the axial direction shows slightly reduced fatigue sensitivity, compared with the axial direction (Table 7).

R Value	Static Failure Mode	95/95 Static Strength [MPa]	Mean Fit Parameters		95/95 Fit Parameters	
			A	B	m	b-tol
10	Compression	232.7	238.6	-0.0434	-0.0434	2.331
-2	Compression	232.7	280.9	-0.1042	-0.1042	2.399
-1	Compression	232.7	174.7	-0.1170	-0.1170	2.169
-0.5	Tension	127.7	165.7	-0.1087	-0.1087	2.138
0.1	Tension	127.7	145.4	-0.0806	-0.0806	2.105
0.5	Tension	127.7	154.9	-0.0709	-0.0709	2.138
0.7	Tension	127.7	140.7	-0.0480	-0.0480	2.091

Table 8: Fit Parameters for Material QQ1T, Transverse Direction (Fit to All Static and Fatigue Data).

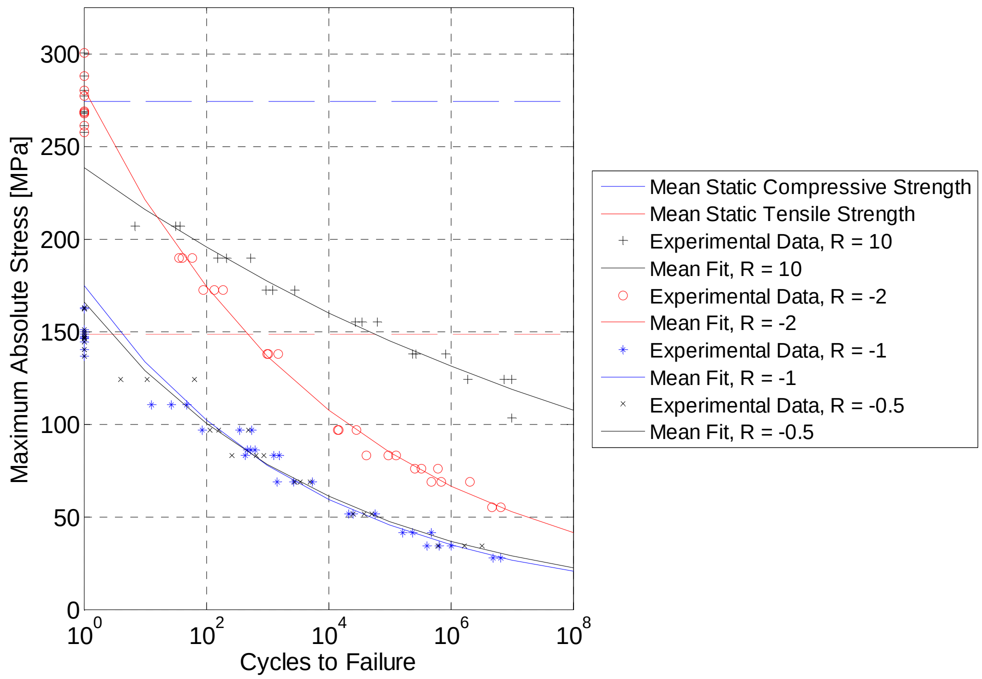

Figure 20: Compression and Mixed Fatigue, Mean Power Law Fits (Material QQ1T, Transverse Direction).

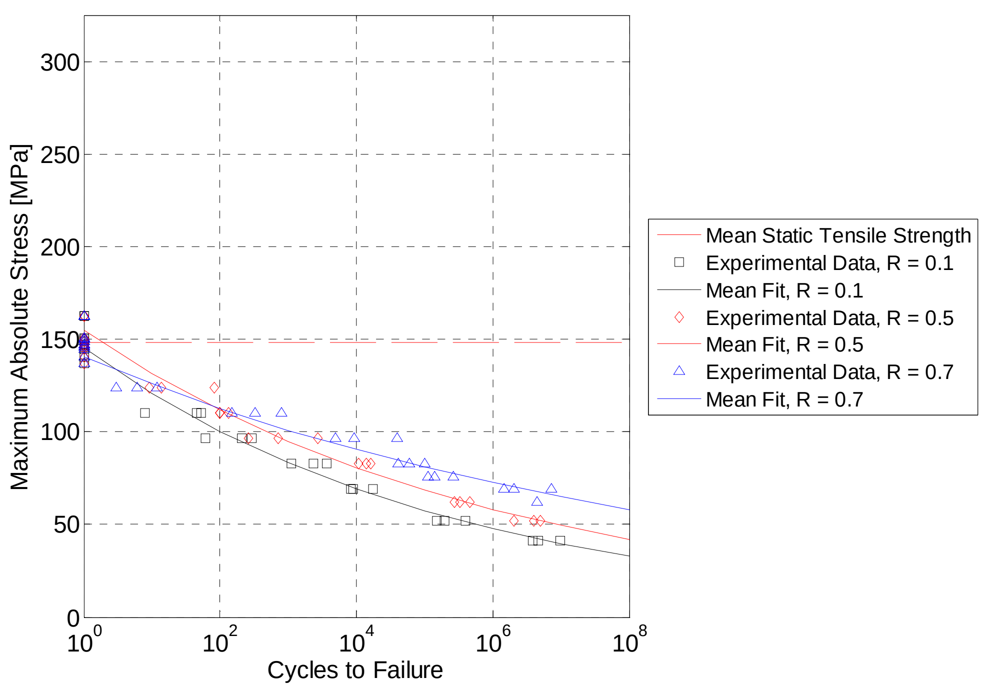

Figure 21: Tensile Fatigue, Mean Power Law Fits (Material QQ1T, Transverse Direction).

<u>Carbon/Glass Hybrid Laminate P2B, Axial Direction</u>

Material P2B test data are all relatively flat compared to the fiberglass laminates and tend to fall into two distinct bands. Fully tensile tests perform better than compressive or mixed loading. P2B data show a fairly flat, linear slope when plotted on a log-linear plot. To determine what type of equation better fits the data, both a logarithmic and power law equation was fitted to each data set. Residual squared values were compared to indicate which form of equation better fit the data. These are shown in Table 9.

R Value	Logarithmic Fit	Power Law Fit
10	0.8407	0.8729
-2	0.9140	0.9161
-1	0.9301	0.9361
-0.5	0.8102	0.8422
0.1	0.8633	0.8740
0.5	0.7516	0.7766
Mean	0.8517	0.8697

Table 9: Comparison of Residual Squared Values for Equation fits for Material P2B (Fit to All Static and Fatigue Data).

The residual squared values in Table 9 show that the P2B data are better fit with a power law equation. Unlike the fiberglass materials, the fits were done for all of the data, both fatigue and static tests. Fit parameters are given in Table 10. Mean fits are shown in Figure 22 and Figure 23. The fatigue sensitivity, B, is significantly lower for all R-values compared with the corresponding axial fiberglass data (Table 7).

R Value	Static Failure Mode	95/95 Static Strength [MPa]	Mean Fit Parameters		95/95 Fit Parameters	
			A	B	m	b-tol
10	Compression	914.2	1038.7	-0.0217	-0.0217	2.973
-2	Compression	914.2	1052.4	-0.0394	-0.0394	2.970
-1	Compression	914.2	1045.0	-0.0385	-0.0385	2.967
-0.5	Compression	914.2	1043.0	-0.0239	-0.0239	2.973
0.1	Tension	1301.1	1531.3	-0.0202	-0.0202	3.145
0.5	Tension	1301.1	1515.6	-0.0148	-0.0148	3.147

Table 10: Fit Parameters for Material P2B, Axial Direction (Fit to All Static and Fatigue Data).

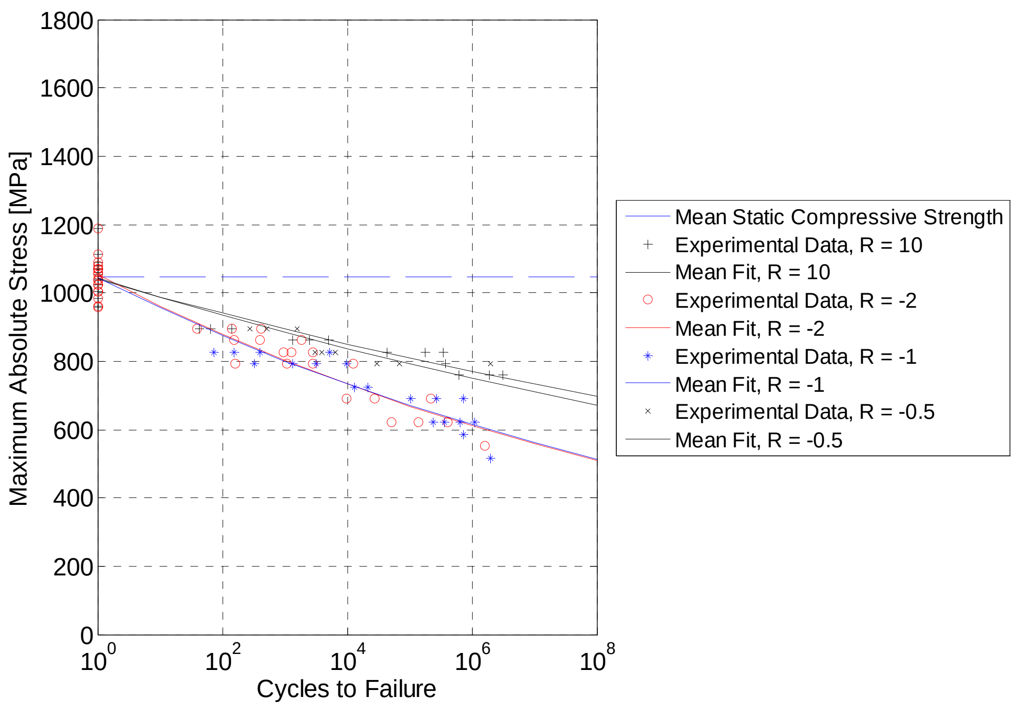

Figure 22: Compression and Mixed Fatigue, Mean Power Law Fits (Material P2B, Axial Direction).

Of note in Figure 22 is the fact that tension dominated mixed fatigue (R = -0.5) data extrapolates to the compressive static strength, not the tensile static strength. Carbon fiber composites tend to show relative weakness to compression.

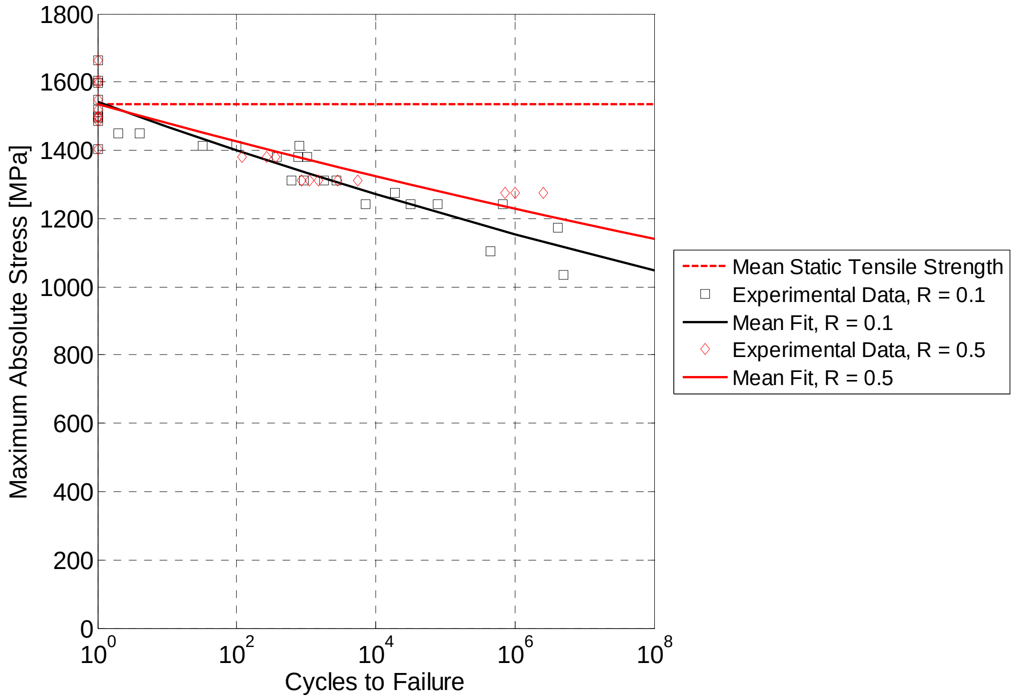

Figure 23: Tensile Fatigue, Mean Power Law Fits (Material P2B, Axial Direction).

Carbon/Glass Hybrid Laminate P2BT, Transverse Direction

Material P2BT test data show a distinct lower band of tension dominated failures and significantly higher compression performance. P2BT is modeled with a power law fit through the fatigue data only, with parameters given in Table 11 and fits shown in Figure 24 and Figure 25. Again, the fatigue sensitivity is lower than for the glass laminate, Table 8, although the strengths and modulus of the glass are higher, as discussed earlier.

R Value	Static Failure Mode	95/95 Static Strength [MPa]	Mean Fit Parameters		95/95 Fit Parameters	
			A	B	m	b-tol
10	Compression	218.6	217.2	-0.0408	-0.0408	2.308
-2	Compression	218.6	170.5	-0.0856	-0.0856	2.189
-1	Tension	71.9	86.6	-0.0717	-0.0717	1.872
-0.5	Tension	71.9	82.5	-0.0689	-0.0689	1.838
0.1	Tension	71.9	81.8	-0.0518	-0.0518	1.846
0.5	Tension	71.9	87.9	-0.0423	-0.0423	1.869
0.7	Tension	71.9	80.1	-0.0214	-0.0214	1.856

Table 11: Fit Parameters for Material P2BT (Fit to All Fatigue Data).

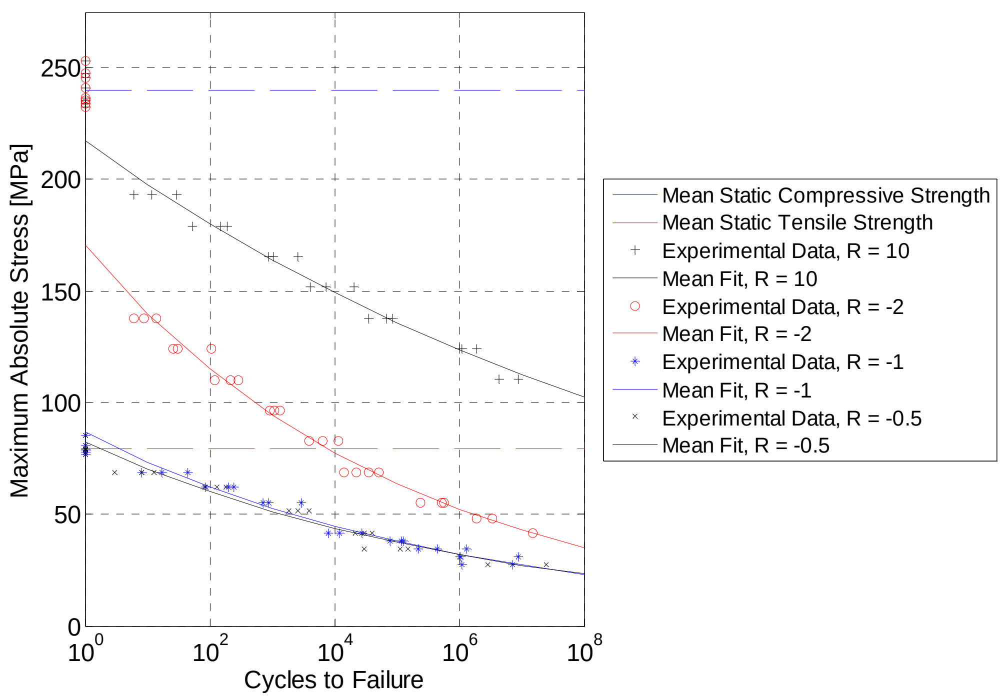

Figure 24: Compression and Mixed Fatigue, Mean Power Law Fits (Material P2BT, Transverse Direction).

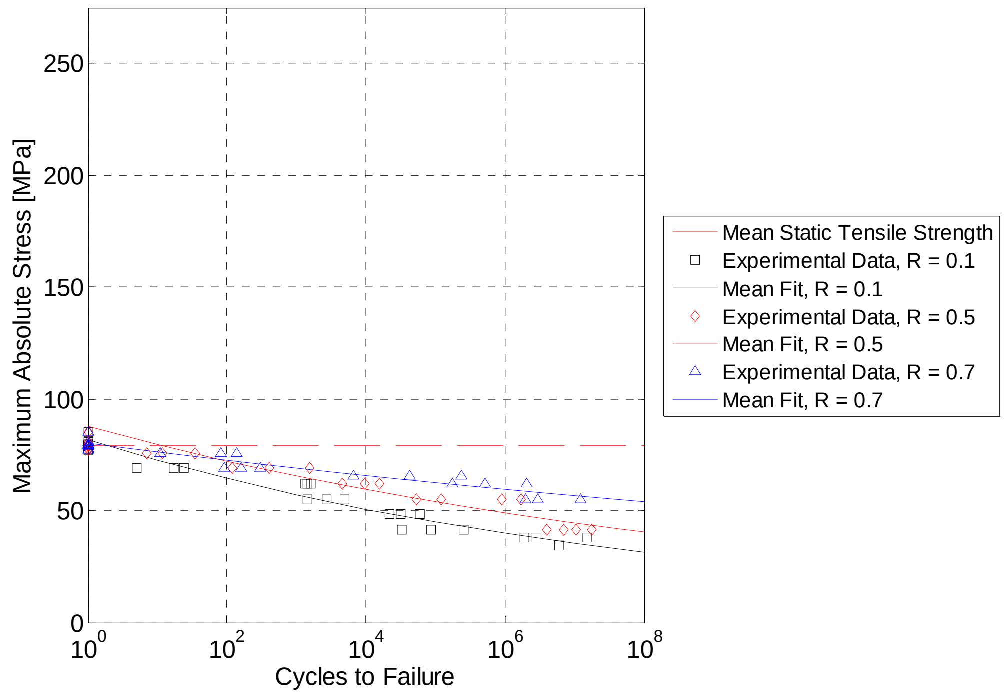

Figure 25: Tensile Fatigue, Mean Power Law Fits (Material P2BT, Transverse Direction).

Constant Life Diagrams

Composite materials generally have differing susceptibility to tension dominated and compression dominated fatigue loading, as is evident in the foregoing. A method of graphically displaying the fatigue life of a material at different ratios of mean and alternating stresses is the constant life diagram, also commonly known as a Goodman diagram [16].

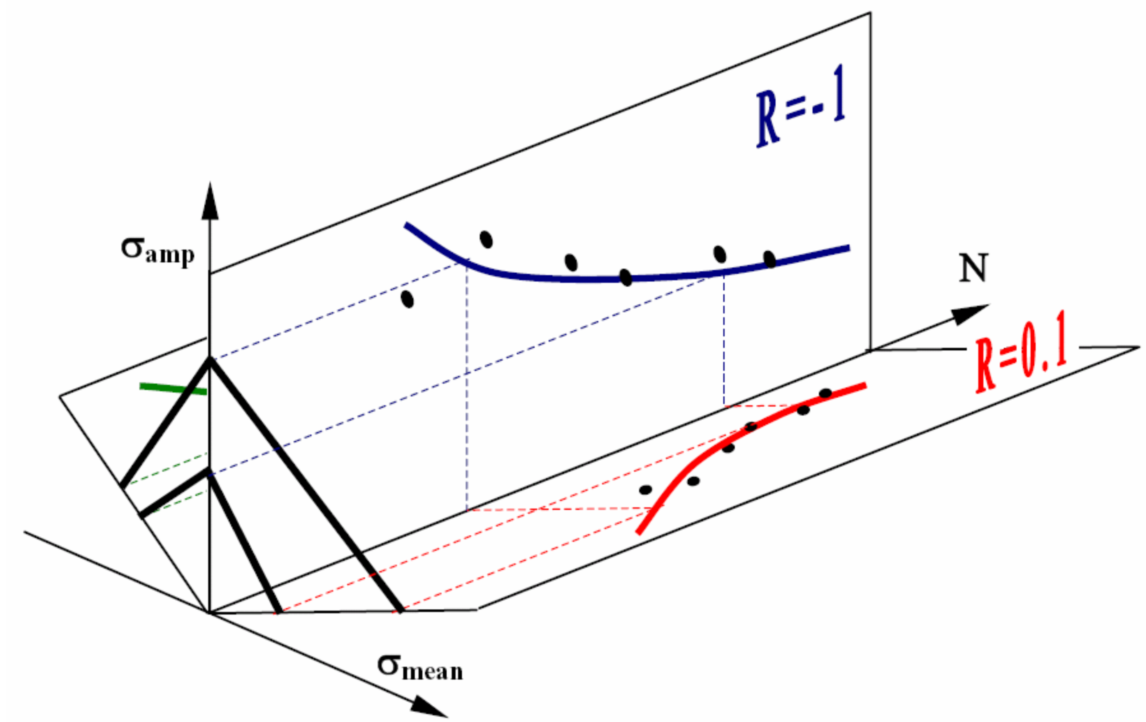

Figure 26: Schematic of the relationship between S-N Curves and Constant Life Diagrams [8]

Constant life diagrams (CLD's) for the materials considered in this study are displayed below. Each of these diagrams is normalized to the mean static tensile strength, noted in Table 5. Normalized mean stress is plotted on the abscissa and normalized alternating stress is on the ordinate. Figure 26 is a schematic showing the relationship of constant life diagrams to stress-life curves [8]. Each plane represents a stress-life curve at one R value; thus, the constant life diagram is a way to display fatigue data from many R values in one diagram. Radial lines mark the different R values. Constant life contours circumscribe the origin; a logarithmic decade of cycles to failure typically separates each one. The CLD can be used in design for assigning damage for each cycle in a load spectrum, from the mean stress and stress amplitude for that cycle.

Constant life diagrams representing both the mean life and 95/95 tolerance life are given for the materials in this thesis. Fatigue tests are generally run to the order of one million (10^6) cycles or less. The following constant life diagrams include extrapolations beyond this region. To differentiate, extrapolated life lines, on the order of 10^7 and 10^8 cycles, are shown as dotted lines in the diagrams. The extrapolation using fatigue models has not been validated for the specific laminates used in this study. Extrapolation of the 95/95 fits is particularly uncertain, but is a practical necessity in predicting the response under spectrum loading.

In general, the one cycle line is determined by the static model. In the case of the mean constant life diagram, the mean UTS or UCS, while in the case of the 95/95 constant life diagram, the 95/95 static tensile or compressive strength. In some cases, the cyclic model would predict one cycle failure at a lower stress than determined by the static properties, the one cycle line is then plotted from the static data rather than the fatigue model. An exception to the use of the static model to determine the one cycle line is the stress rupture model used for material DD16. In this case, the lowest critical condition of the two models is used. The stress rupture model is based on a time under load criterion, and depending on the frequency used to predict failure, may predict failure at a lower stress than the static strength. The high ramp rates used in the static tests reduce the influence of the stress rupture phenomenon.

CLD for Fiberglass Laminate DD16, Axial Direction

Two constant life diagrams are shown for material DD16 because of the influence of loading frequency on the tensile end of the diagram due to the inclusion of the stress rupture model. Diagrams of 1 Hz and 10 Hz loading frequencies are included.

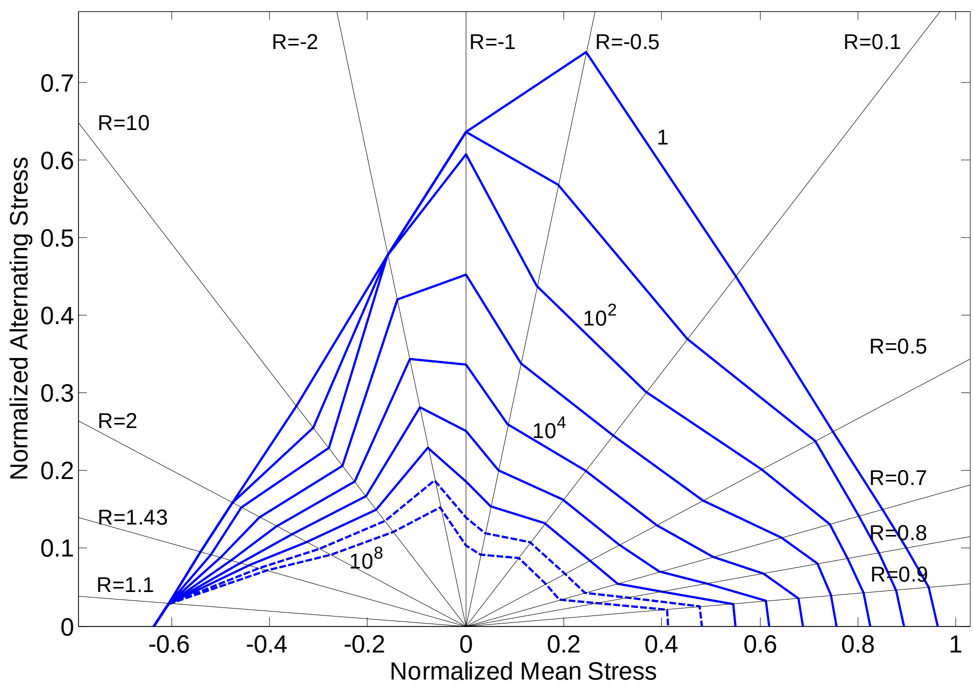

Figure 27: Mean Axial Constant Life Diagram for Material DD16, 1 Hz Frequency.

Figure 27, a constant life diagram for material DD16, shows results for a 1 Hz loading case. Note the difference between the 10 cycle life line in the region of positive normalized mean stress in this case, and the 10 Hz case, shown as Figure 28. The 10 Hz case more closely represents results found in the fatigue testing, as test frequencies tended to be closer to 10 Hz than to 1 Hz [5].

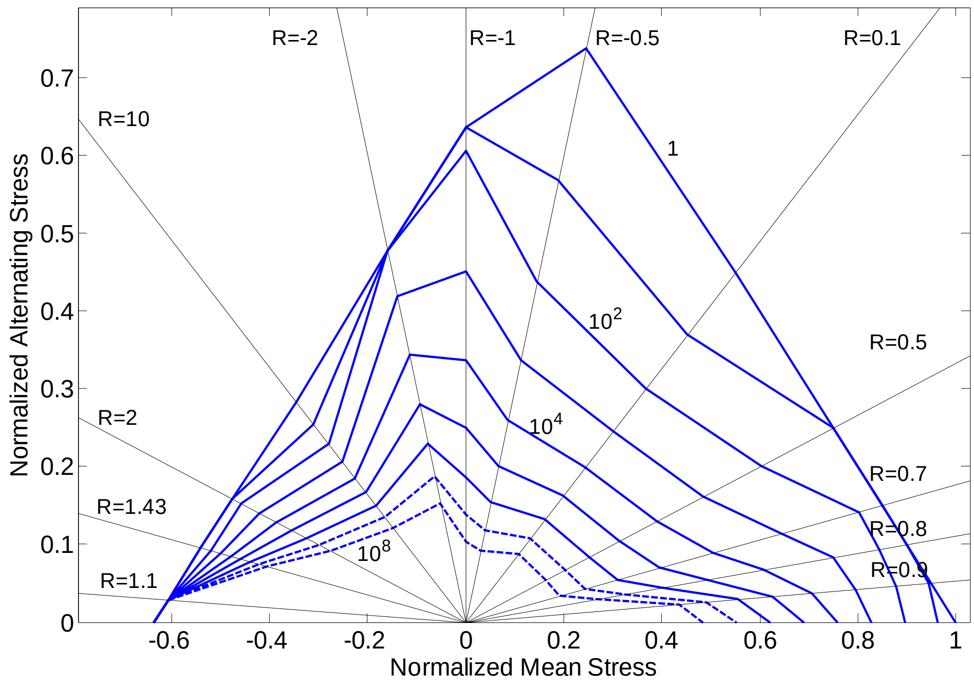

Figure 28: Mean Axial Constant Life Diagram for Material DD16, 10 Hz Frequency.

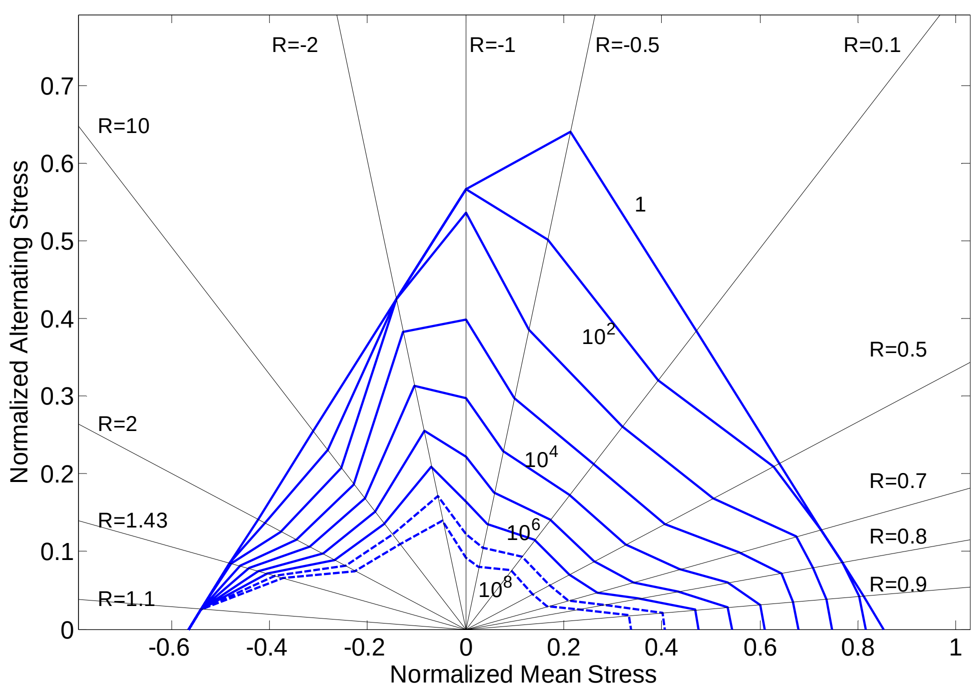

Figure 29: 95/95 Axial Constant Life Diagram for Material DD16, 1 Hz Frequency.

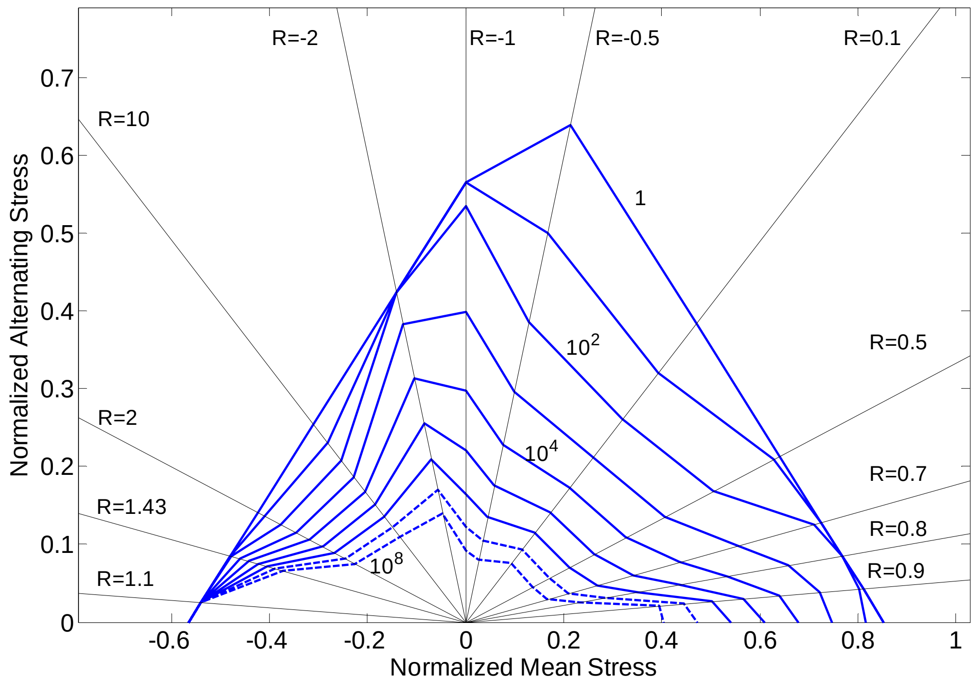

Figure 30: 95/95 Axial Constant Life Diagram for Material DD16, 10 Hz Frequency.

CLD for Fiberglass Laminate QQ1, Axial Direction

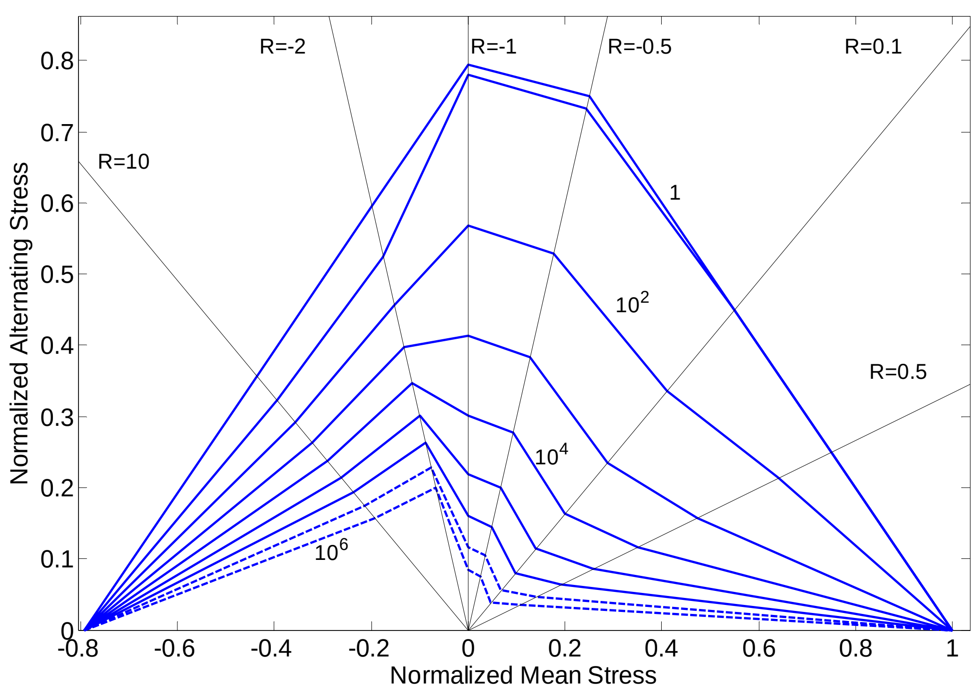

Figure 31: Mean Axial Constant Life Diagram for Material QQ1.

The mean axial constant life diagram for material QQ1, Figure 31, shows that fatigue performance for this more current fiberglass composite is generally similar to the older DD16. The higher fiber content material produces a more severe transition between performance dominated by compression compared with tension at high cycles. Thus, the damage done by a cycle of a given amplitude is very sensitive to the mean stress at reversed loading R-values. Tension is much more damaging than compression at high cycles; much less so at low cycles. The CLD in Figure 31 is the most extreme known for any laminate in the tension-compression transition region [7, 8]. The 95/95 CLD in Figure 32 is also extreme in this respect, with very low mean and alternating stresses at high cycles. A measure of the extreme tensile fatigue sensitivity is the 95/95 maximum stress at 10^8 cycles for R = 0.1 of 64.8 MPa, which is only 7.5% of the mean UTS of 869 MPa.

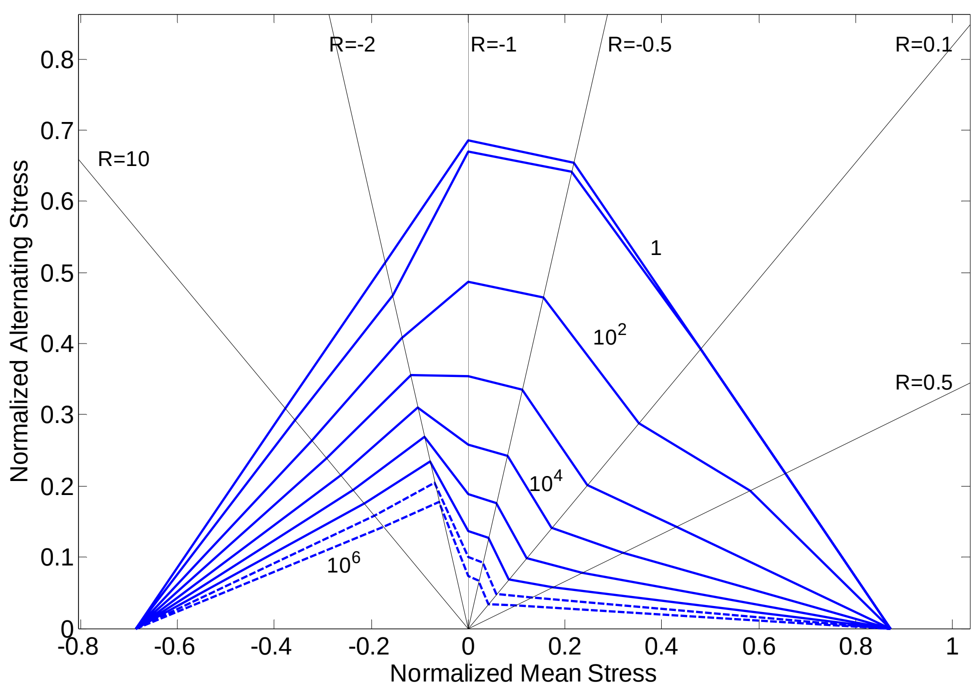

Figure 32: 95/95 Axial Constant Life Diagram for Material QQ1.

Fiberglass Laminate QQ1T, Transverse Direction

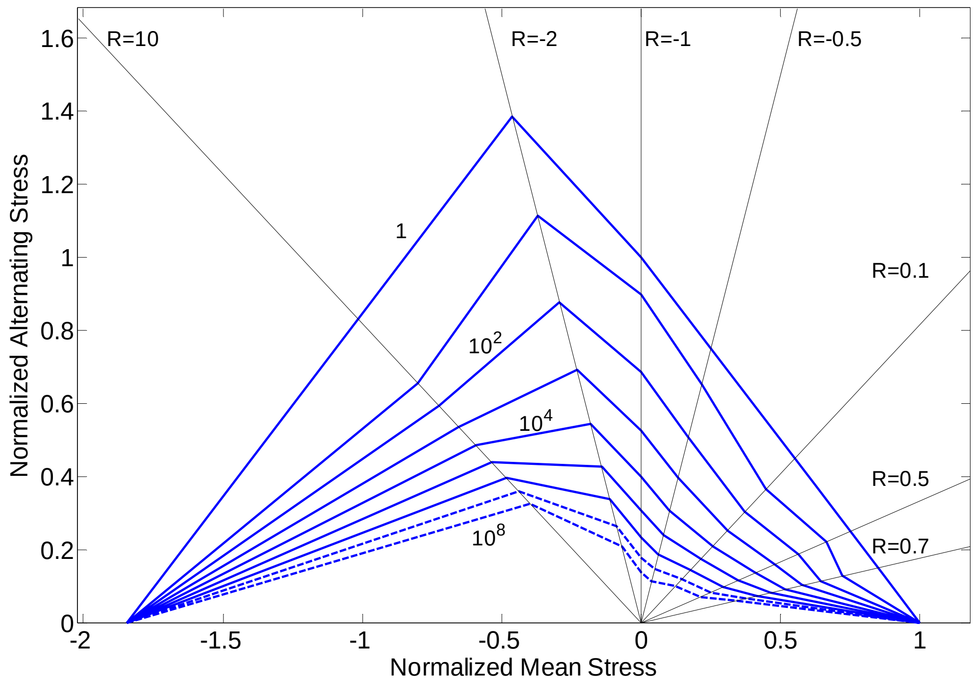

Figure 33: Mean Transverse Constant Life Diagram for Material QQ1T.

The transverse constant life diagrams for fiberglass laminate QQ1T (Figure 33 and Figure 34) are very distorted toward higher strength and fatigue resistance in compression, as is typical for the transverse direction of composites. These results may be used to predict matrix cracking in blades, in combination with shear data which are not currently available.

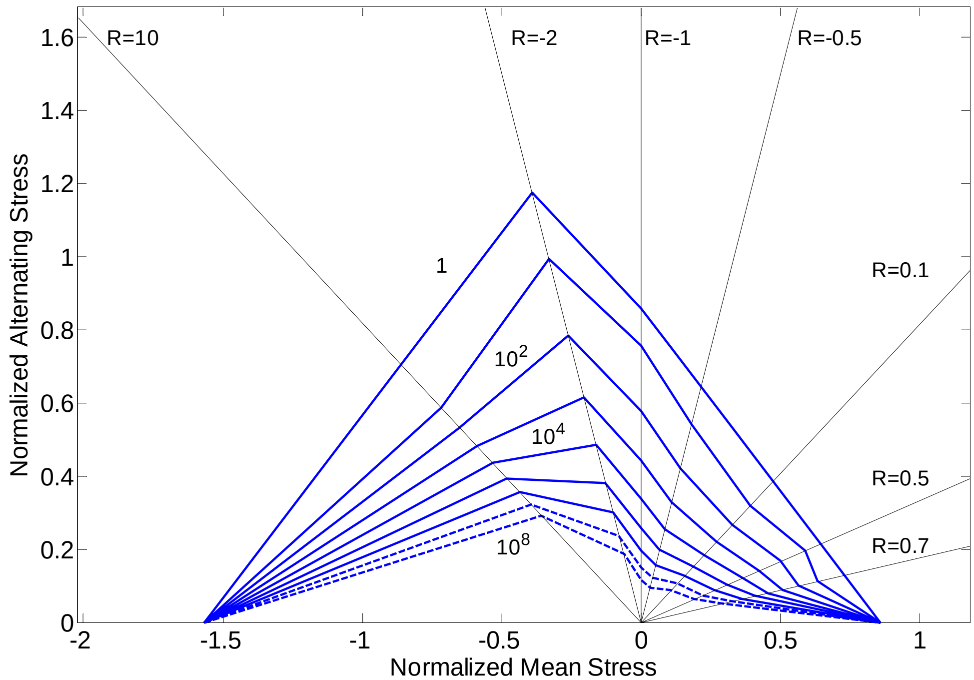

Figure 34: 95/95 Transverse Constant Life Diagram for Material QQ1T.

Axial Carbon/Glass Hybrid Laminate P2B

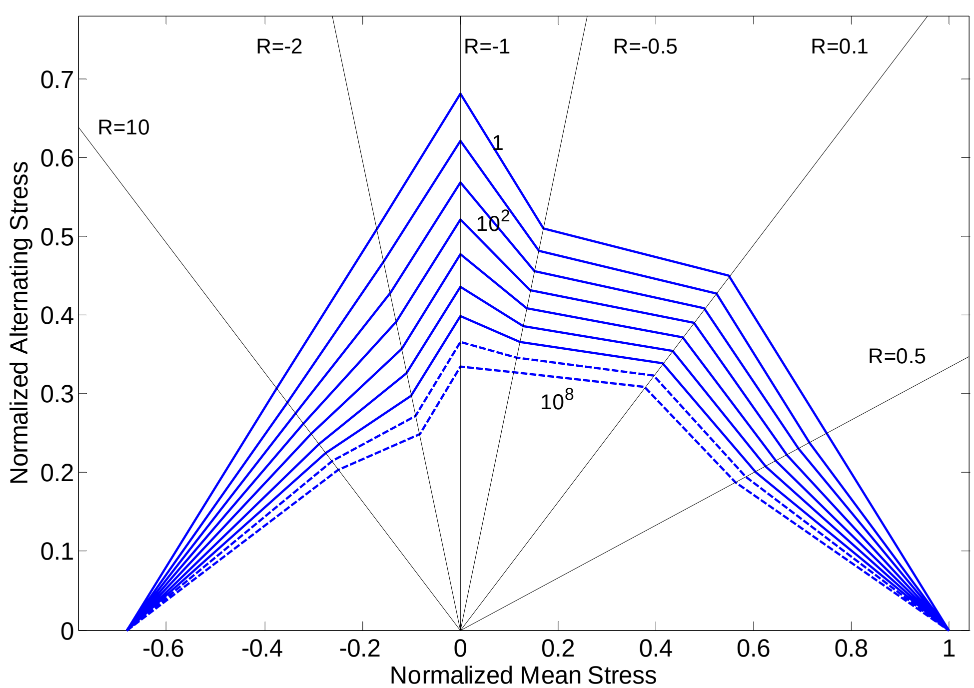

Figure 35: Mean Axial Constant Life Diagram for Material P2B.

The constant life diagram for carbon fiber based material P2B in the axial direction (Figure 35 and Figure 36) reflects a similar ratio of compression to tensile strength compared with fiberglass QQ1, but greatly improved fatigue resistance at all R values. The life lines between R = -0.5 and 0.1 show a mode change, but without the extreme distortion evident for QQ1. Compression drives the failure for R = -0.5 in P2B, which is tension dominated for QQ1. The greatest limitation with carbon in blades may be the much lower static ultimate compressive strains compared with glass, as discussed elsewhere [17].

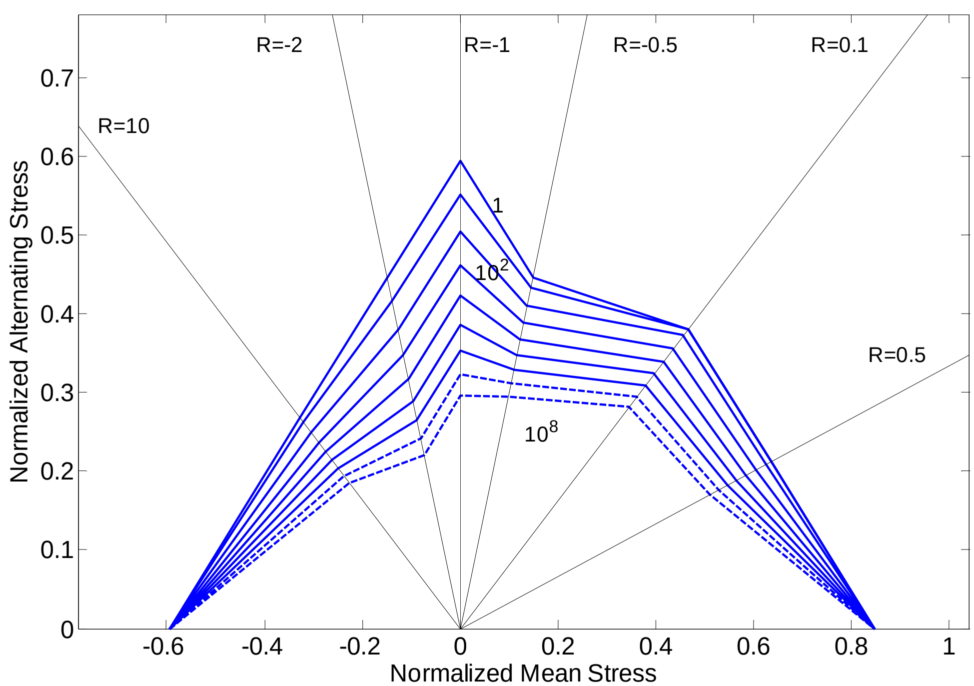

Figure 36: 95/95 Axial Constant Life Diagram for Material P2B.

Carbon/Glass Hybrid Laminate P2BT, Transverse Direction

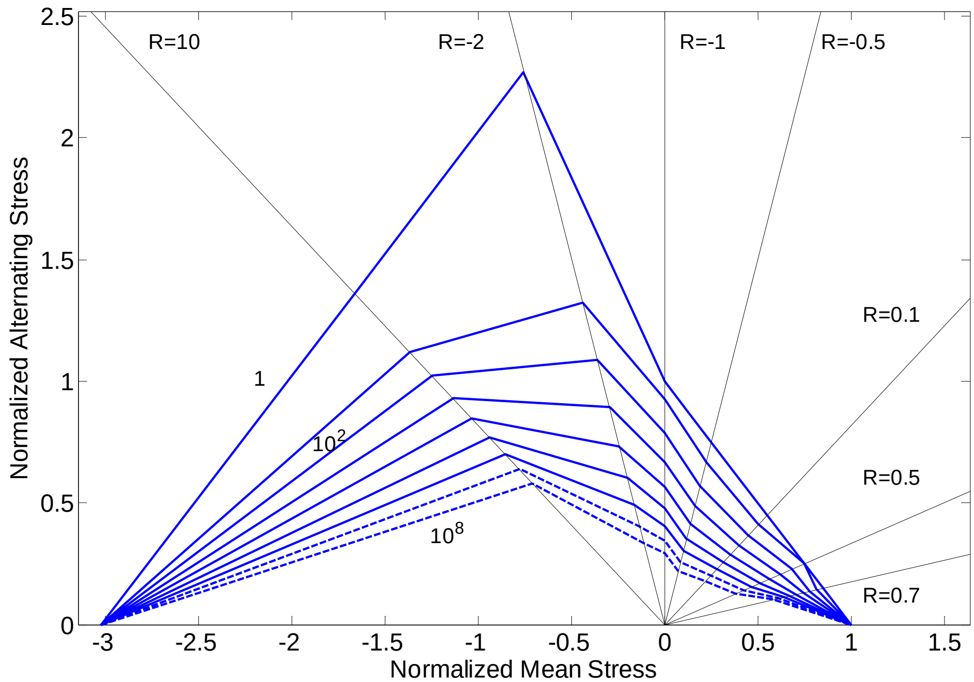

Figure 37: Mean Transverse Constant Life Diagram for Material P2BT.

The mean constant life diagram of carbon based P2BT, shown in Figure 37, is similar in shape to that for fiberglass material QQ1T, also tested in the transverse direction. As noted earlier, QQ1T has higher strength values due to the different contents of plies in various directions and the higher transverse modulus for glass versus carbon.

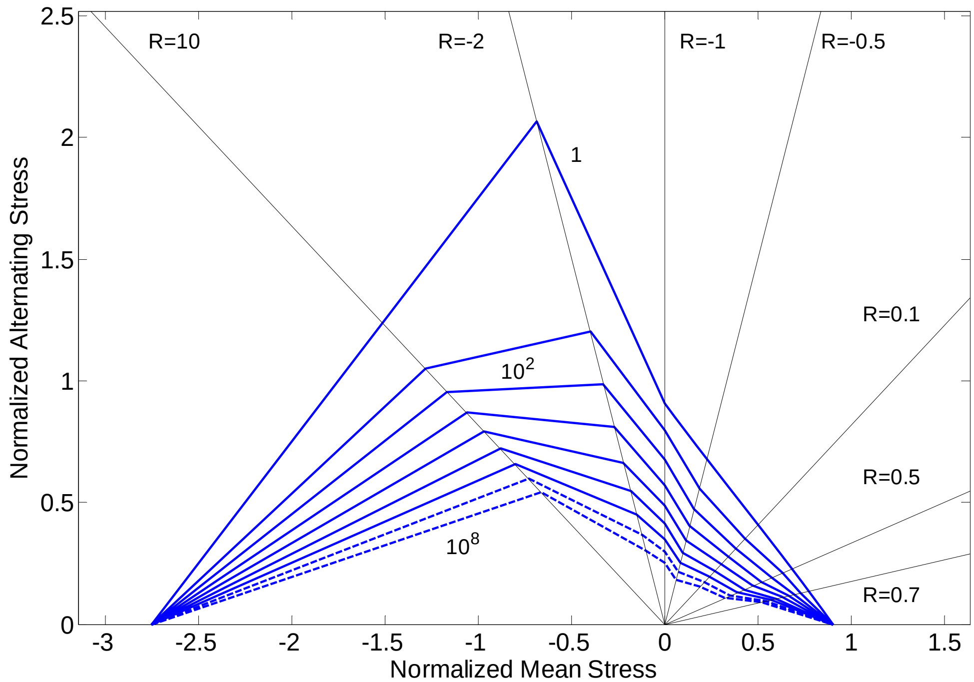

Figure 38: 95/95 Transverse Constant Life Diagram for Material P2BT.

<u>Comparison of P2B and QQ1</u>

Material QQ1 represents an improvement in terms of fiber content and modulus over previous fiberglass composites such as DD16. Both of these materials are fabricated from dry fabrics that are impregnated with resin at the time of manufacture. Both of these materials are also representative of the lower end of the cost range of composite materials. QQ1 is a more current material in terms of wind turbine blades. The greatest difference lies in the fiber volume fraction, 0.53 for QQ1 and 0.36 for DD16.

The stress based mean constant life diagrams of carbon based P2B and glass based QQ1 in the axial direction are plotted together in Figure 39. In terms of stress, carbon composites are far superior to glass composites.

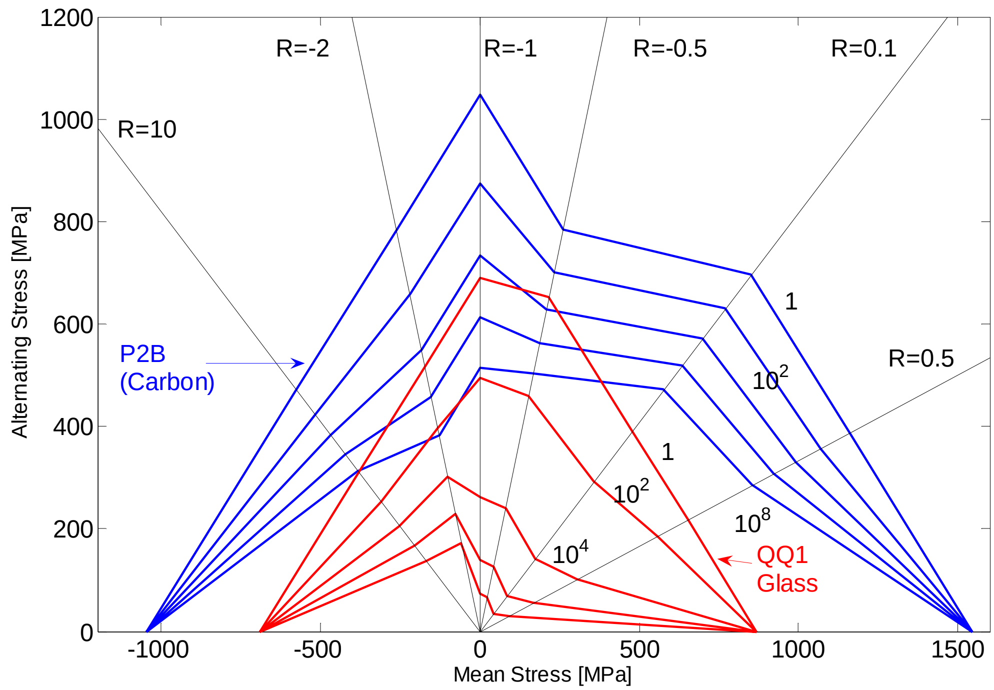

Figure 39: Comparison of Materials QQ1 (Fiberglass) and P2B (Carbon Dominated), Axial Direction, Stress Constant Life Diagram.

Major issues standing in the way of this material change have been carbon's cost and lower performance in compression loading in terms of strain. However, as seen in Figure 40, P2B also outperforms QQ1 in terms of tensile dominated strain at higher cycles. Thus, the strain question for carbon composites in wind turbine applications may only be meaningful at very low cycles, as in extreme wind conditions.

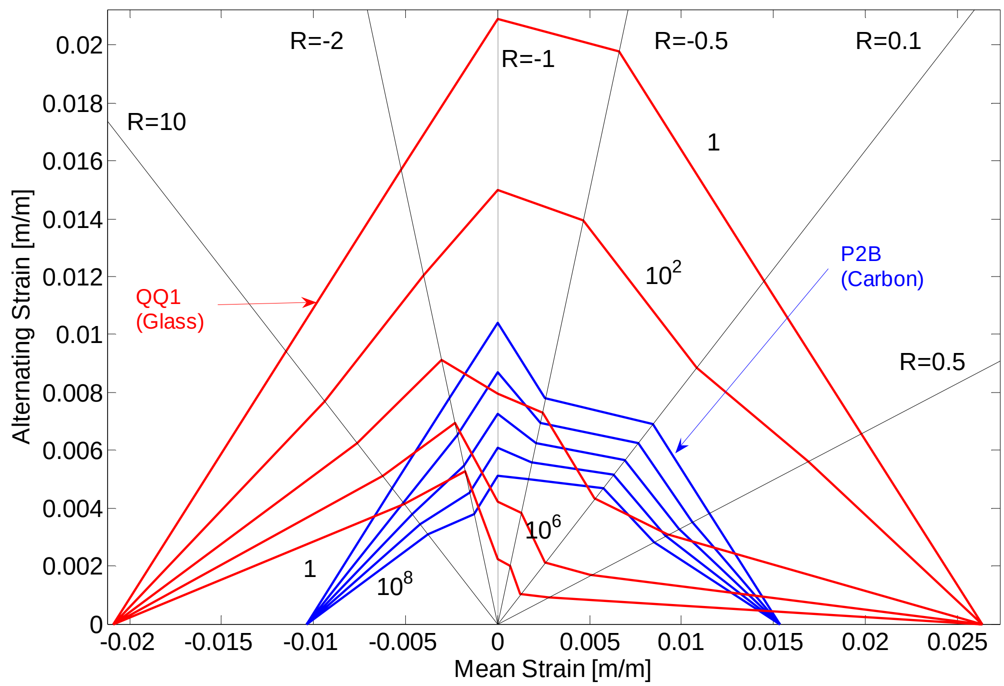

Figure 40: Comparison of Materials QQ1 (Fiberglass) and P2B (Carbon Dominated), Strain Constant Life Diagram.

<u>Spectrum Loading</u>

Constant amplitude loading is not representative of the fatigue loading that most components experience. Outside of some rotating parts, most components undergo a variety of loads over their lifetime. Ideally, it would be possible to test a material under these same loads. However, in many cases, such as wind turbines, the lifetime of the component is many years, and thus it would be prohibitively expensive and time consuming to test materials under the same stresses as the full scale structure. Furthermore, every structure will experience a different set of loads depending on how it is used, where it is located, and other conditions. Therefore, a representative load spectrum is developed that will mimic the loads, and more importantly, the damage caused by those loads, that a structure undergoes [8].

In the wind turbine industry, the WISPER load spectrum was developed in the 1980s to fulfill the need to compare different materials. The WISPER spectrum represents loads in the flap direction of the blade, on the tension side and consists of 265,423 reversal points, or 132,711 cycles. It is a scalable set of integer points, ranging from -24 to 39; a single high load dominates damage calculations. Later, to reduce testing time and expense, the WISPERX spectrum was derived from WISPER. By excluding all cycles with an amplitude level of 8 or less, as shown by the truncation line in Figure 41, the spectrum was reduced in length by an order of magnitude to 12,831 cycles. As Nijssen puts it, “When the WISPERX load sequence was derived from the WISPER Sequence, it was assumed the damage incurred would not change with respect to its ancestor.” [8]

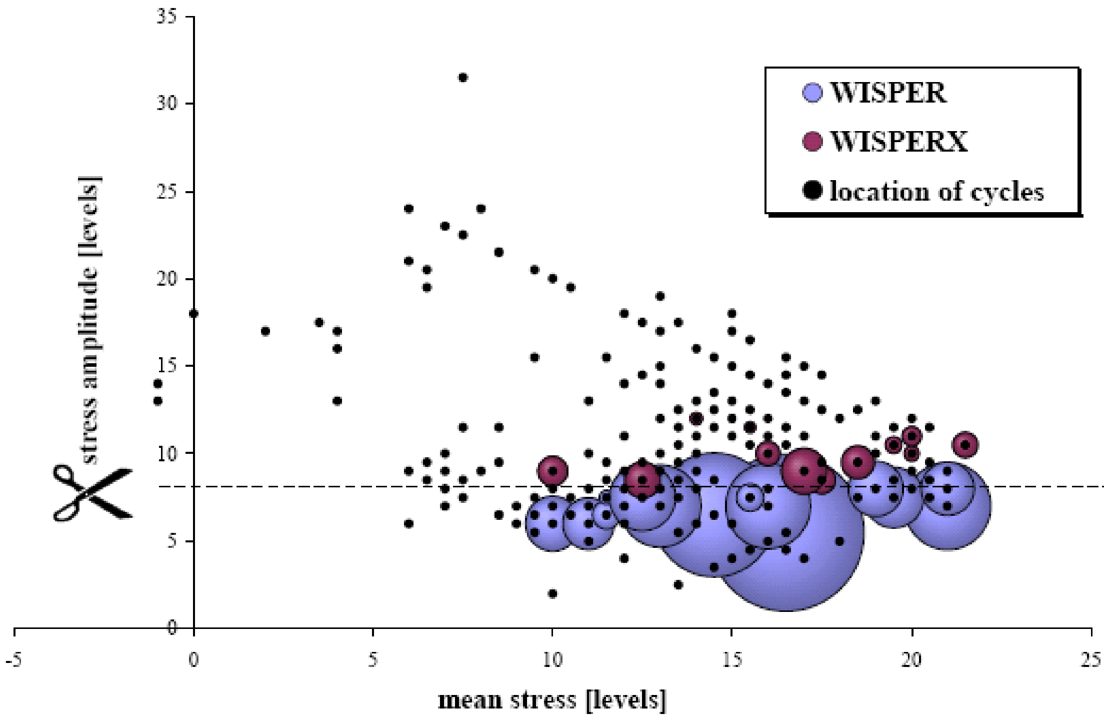

Figure 41: WISPER and WISPERX Spectra Cycles (Size of the Circle Indicates the Number of Cycles), Showing the Truncation Line [8].

There are a few problems with the WISPER and WISPERX spectra. Given that they are on the order of 20 years old, there is concern about its continued validity; wind turbines have evolved a great deal over the years, particularly in size. The WISPER spectrum was developed from data taken from turbines much smaller than those being built today, and may not be representative of larger turbines.

The WISPERX spectrum was used in this thesis to provide a comparison between the different materials. In each case, the WISPERX spectrum was scaled to a stress level where a Palmgren Miner linear damage sum for the spectrum equaled 1 for a given number of passes [16]. This was done to the mean fit. Before the Miner's sum was calculated, the spectrum was modified according to the Rainflow Method of cycle counting, as developed by Endo and Matsuiski, which tends to give better results [18, 19]. Because of this, the spectrum shown in Figure 42 looks slightly different than the one in Figure 41.

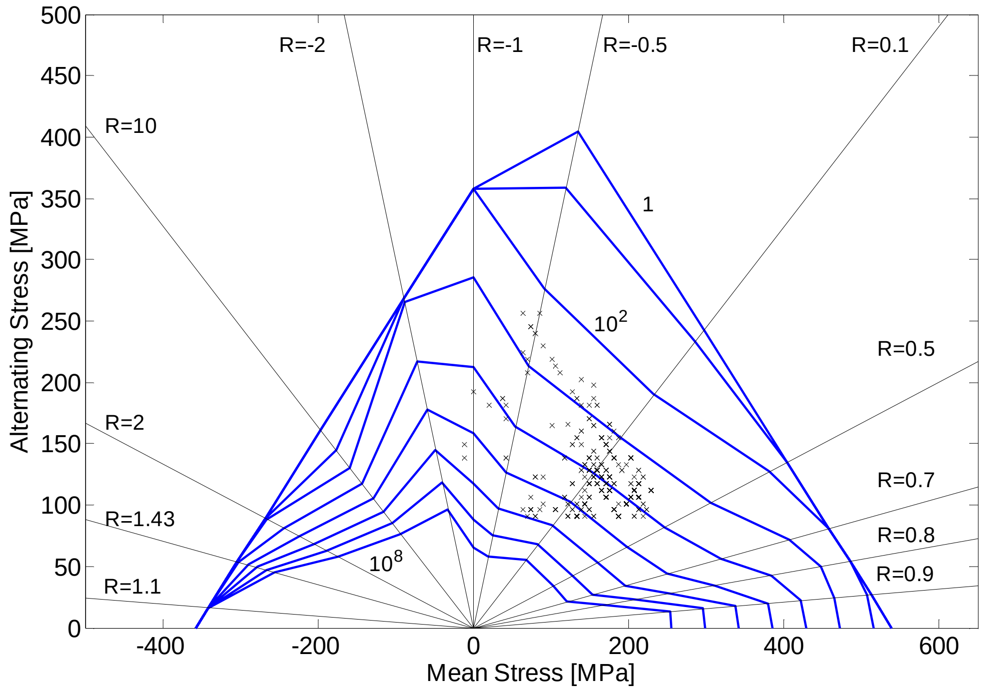

Figure 42: Material DD16, Axial Direction, Mean Constant Life Diagram, Frequency = 10Hz, WISPERX Scale Factor = 416 MPa, Miner's Sum = 1.

Figure 42 is the CLD for material DD16 with the WISPERX spectrum scaled to produce a Miner's sum equal to one in one pass. Figure 43 has the stress scale factors for the axial materials in this thesis required to equal a Miner's sum in 1, 10, 100, and 1000 passes of the WISPERX spectrum. Figure 43 does the same with a strain scale factor. The highest maximum value in the WISPERX spectrum is 1, so the highest stress level after the scale factor is applied is the scale factor. The scaled spectrum is rainflow counted after the scale factor is applied.

The transverse materials, P2BT and QQ1T, were not analyzed extensively in this manner because it makes little sense to do so. These materials will not be loaded in the same way as the longitudinal materials, and thus, a different spectrum would apply. For comparisons sake, however, the scale factor applied to the WISPERX spectrum to achieve a Miner's sum of one in one pass is 59.6 MPa for P2BT and 84.7 MPa for QQ1T.

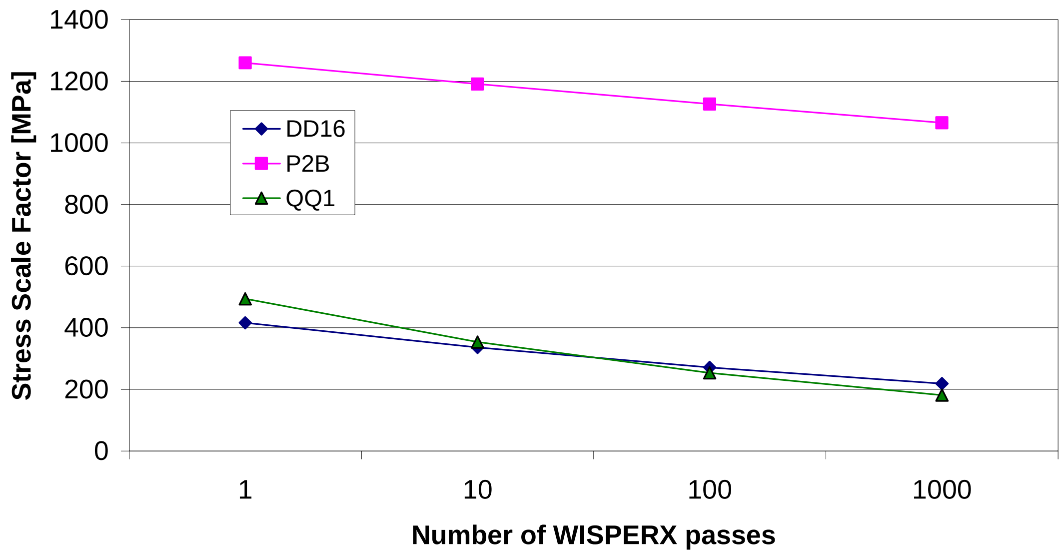

Figure 43: Stress Scale Factors Applied to the WISPERX Spectrum to Achieve a Miner's Sum Equal to 1 (Mean Fit).

An interesting observation from Figure 43 is, comparing the two fiberglass laminates, the poorer fatigue performance of QQ1 as compared to DD16. QQ1 is intended to represent more current fiberglass materials, with higher fiber volume fractions. This helps static strength and modulus, but reduces the fatigue performance at higher cycles under tensile loading, consistent with the expectations from Reference [10]. On a stress basis, the carbon based laminate greatly exceeds the performance of either fiberglass laminate (Figure 43).

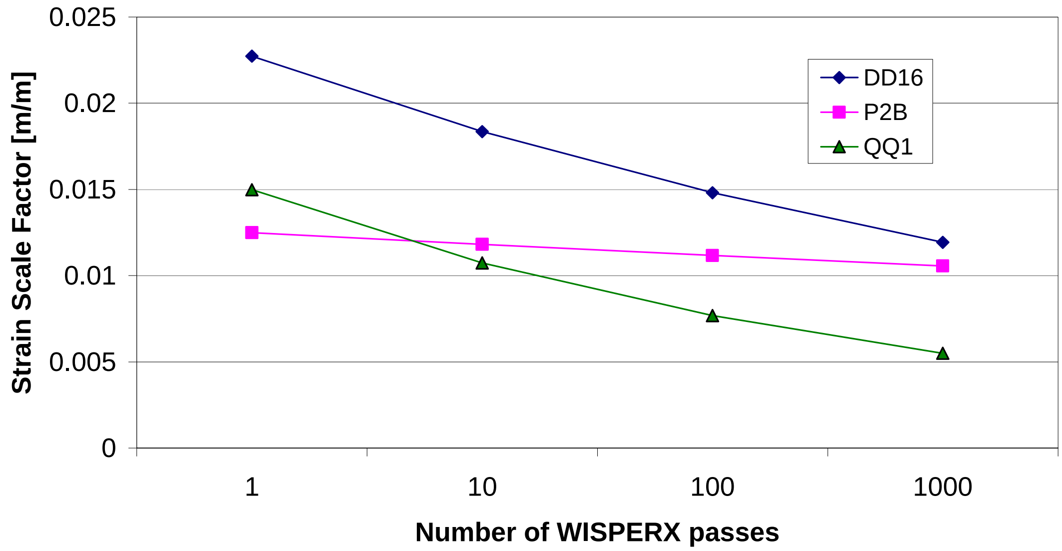

Figure 44: Strain Scale Factors Applied to the WISPERX Spectrum to Achieve a Miner's Sum Equal to 1 (Mean Fit).

Figure 44 shows the scale factors applied to the WISPERX spectrum in terms of strain. Here, the performance of P2B is only superior to QQ1 at higher cycles and then only approaching DD16. DD16, ostensibly the lowest performance composite, performs the best on a strain basis. P2B, however, shows much less fatigue sensitivity, and at WISPERX spectrum passes greater than 1000, will perform well in terms of applied stress or strain.

FINITE ELEMENT ANALYSIS OF PLY DROP DELAMINATION

Motivation for this section is to explore the strain energy release rates, referred to symbolically as G, for various ply drop geometries which have been the subject of experimental fatigue studies. The experimental studies have shown significant delamination for some ply drop cases at applied strains on the order of the high cycle fiberglass fatigue in-plane results in the previous section [17]. Thus, this work is of considerable practical significance, since delamination induced failure could potentially precede in-plane fatigue failure in some cases, particularly with carbon fibers and thick plies. Loads in the models are in the range of those experimentally observed for moderate fatigue lifetimes. However, this study explores only static G values, not fatigue crack growth behavior. Where multiple cracks are modeled, their lengths are assumed to be equal, which is not typically the case for growing static or fatigue cracks. Thus, a complete crack growth simulation has not been carried out. The usefulness of the FEA results lies in improved understanding of the experimental trends with ply drop geometry and materials variations, and the driving forces for delamination growth.

Geometries include external, internal, and central ply drops, ply joints, and the last ply joint elements of a total material transition. The central ply joint model looks at the behavior of the simplest case, two plies butted up against each other at the mid-thickness with no material change, dropped plies, or ply mis-orientation. The external ply drop has the dropped plies on the outside of the 0 ply stack (under the surface ±45's), the internal ply drop is at a typical position between the exterior and centerline, and the central ply drop has the dropped plies at mid-thickness. Appendix A provides results for carbon-glass material transitions, including the last carbon out model representing a material transition area with one ply of carbon in a coupon of mainly glass 0's. The first glass in model represents a transition between mainly carbon and a small portion of glass. Appendix B reports on an experimental and FEA study of tapering of the edges of ply drops, and Appendix C provides additional FEA results not included in the text.

Finite element models were created to compare the strain energy release rates of delamination cracks at various ply drop geometries. The strain energy release rate (SERR) is a measure of how much energy is required to grow a crack by a certain amount. Mode I SERR is denoted G_I, Mode I being the opening mode of crack growth. G_{II} is the mode II SERR, due to in-plane shear. Mode III is out-of-plane shear, but is neglected in this analysis [20].

Previous Work

Extensive previous work has been done on ply drop analysis, including a number of different approaches. Most of these have concentrated on relatively thin ply material for aerospace, where delamination problems are somewhat less severe. Studies have included testing of coupons under static and fatigue loading with various ply drops. Analysis of stress fields around the ply drop region is used to predict crack initiation. Damage analysis has looked at strain energy release rate values of growing delamination cracks using analytical or numerical methods. Baseline delamination data are obtained for pure mode (I or II) or controlled mixed mode (I and II) delamination tests.

Tetheway et al. used both an analytical model, based on shear deformation plate theory and linear-elastic fracture mechanics, and a 2-D FE model to investigate Mode I and II G values of ply drop delamination cracks [21]. Her looked at the singular stress fields in the ply drop region by incorporating a global element capable of capturing the singular behavior into a general finite element analysis [22]. Vidyashankar and Krishna Murty used a 3-D finite element analysis and the Tsai-Wu failure criterion to investigate the initiation of delamination cracks [23]. Mukherjee and Varughese also used FEA and the Tsai-Wu failure criterion to look at how the thickness of the ply drop and the stagger distance between ply drops affects initiation of delamination cracks [24]. Meirinhos et al. performed a parametric study of fatigue tests on varying coupon geometries to better size part thicknesses subject to an out-of-plane stresses [25].

Murri et al. carried out a complete analysis using FEA to study G values at delamination cracks in tapered composite flexbeams, combined with an experimental study of fatigue specimens [3]. This study was able to match the location of delamination cracks well, though attempts to predict the onset of delamination indicate that further refinement of the model and further fatigue testing is necessary. This study bears the closest resemblance to much of the work presented in this thesis, and indicates a direction of possible future work. Simulations with more random delamination geometries have been reported by Krüger and König [26]

Previous studies at Montana State University have included a ply drop parametric experimental study as well as study of other structural details which fail by delamination [10]. Recent work focusing on ply drop research has included an experimental study of the performance of ply drops under static and fatigue loading. Strain levels to produce significant delamination at both glass and carbon fiber ply drops were determined [17].

Background

Geometry of Ply Drop Coupons

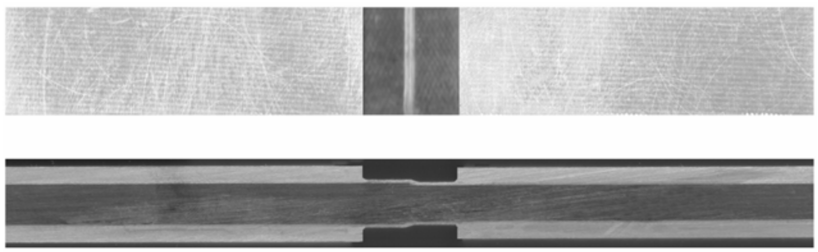

Figure 45: External Ply Drop Test Coupon.

A typical ply drop test coupon from the associated experimental study [17] is shown in Figure 45. This is a photograph of an external ply drop coupon with four plies dropped at each outer surface of the 0 ply stack of a $[\pm45_3/0^*_4/0_{27}/0^*_4/\pm45_3]$ laminate, where the * indicates dropped plies. The upper portion of the figure is a top view of the coupon; the lower portion, a side view. (The black area surrounding the side view is the background of the photo, not part of the coupon.) Fiberglass tabs are bonded to the ends of the coupons to minimize problems with gripping. All ply drop coupons are symmetric about the mid-thickness to eliminate bending that would occur with an asymmetric coupon.

Element Properties

The finite element analysis was carried out with ANSYS. The element type used was PLANE82, an eight-noded parabolic element. This element allows for different properties in the x and y directions, as required for use with two dimensional models of anisotropic materials, such as composites, and is compatible with the quarter point singularity modification outlined below.

<u>FEA Method for calculating G_I and G_{II}</u>

An FEA method based on the virtual crack closure technique to determine G values was originally demonstrated by Kanninen [27] and adapted to composites by Raju [28]. It has been used by various researchers at MSU [10]. This technique obtains a G value in a single run as opposed to other methods that require two finite element analyses using the same model but requiring a slight change in the crack length. The technique for finding G_I involves obtaining three vertical nodal forces (F_{yk}, F_{yj}, F_{yi}) past the crack tip and four vertical nodal displacements (v_l, v_m, v_l', v_m'), as shown in the schematic of the nodal arrangement, Figure 46 [28].

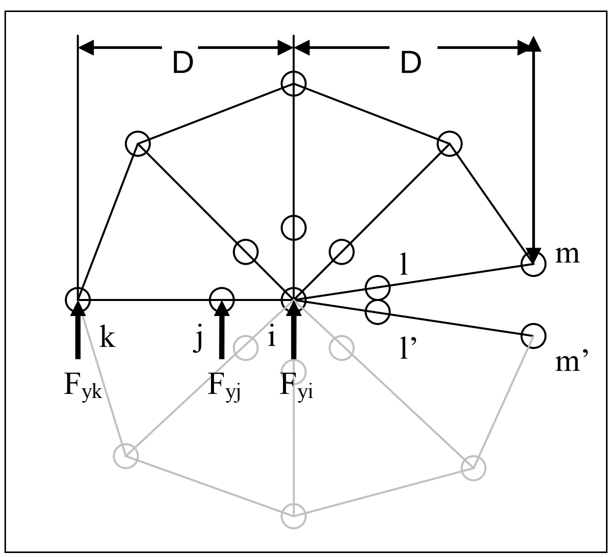

Figure 46: Nodal Arrangement [28].

The method for finding G_{II} is similar, the only difference is the forces and displacements are in the x direction. The mode I values (y direction forces and displacements) are input into Equation 12 to find G_I. Again, finding G_{II} is similar, but with horizontal forces and displacements. The total strain energy release rate is the sum of G_I and G_{II} in the absence of a G_{III} (tearing) component.

$$G_I = \frac{-1}{2 \cdot \Delta} \cdot \left[F_{yi} \cdot \left(t_{11} \cdot v_m + t_{12} \cdot v_l \right) + F_{yj} \cdot \left(t_{21} \cdot v_m + t_{22} \cdot v_l \right) + F_{yk} \cdot \left(t_{31} \cdot v_m + t_{32} \cdot v_l \right) \right] \quad (12)$$

where:

$$t_{11} = 14 - \frac{33 \cdot \pi}{8}$$

$$t_{12} = -52 + \frac{33 \cdot \pi}{2}$$

$$t_{21} = \frac{-7}{2} + \frac{21 \cdot \pi}{16}$$

$$t_{22} = 17 - \frac{21 \cdot \pi}{4}$$

$$t_{31} = 8 - \frac{21 \cdot \pi}{8}$$

$$t_{32} = -32 + \frac{21 \cdot \pi}{2}$$

Equation 12 and Figure 46 involve the use of quarter point singularity elements. The use of this type of element around the crack tip in fracture mechanics analyses allows for better modeling of the stress singularity [29]. Moving the midside node of an eight node element from the midpoint to the quarter point and modifying the element shape function better matches crack tip behavior. Furthermore, the element is collapsed from the quadrilateral shape into a triangular shape. Conveniently, the ‘kscon’ command in ANSYS creates these quarter point elements in a collapsed triangular form at a crack tip [29]. This type of element is shown in Figure 47.

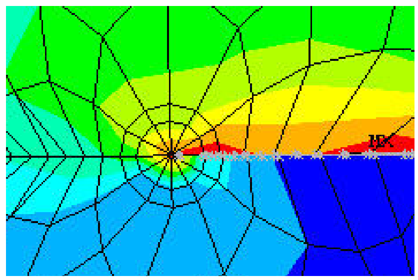

Figure 47: ANSYS ‘kscon’ Crack Tip Elements.

Each FE model calculates G’s for a given loading, material, and crack length and configuration. Therefore, to model G value trends over a range of crack lengths, many FEA runs must be done. The model for each crack length can vary in computation time (on an Intel Pentium 4 computer) from the order of one minute for short cracks to tens of minutes to an hour for longer crack lengths.

Details of FEA Models

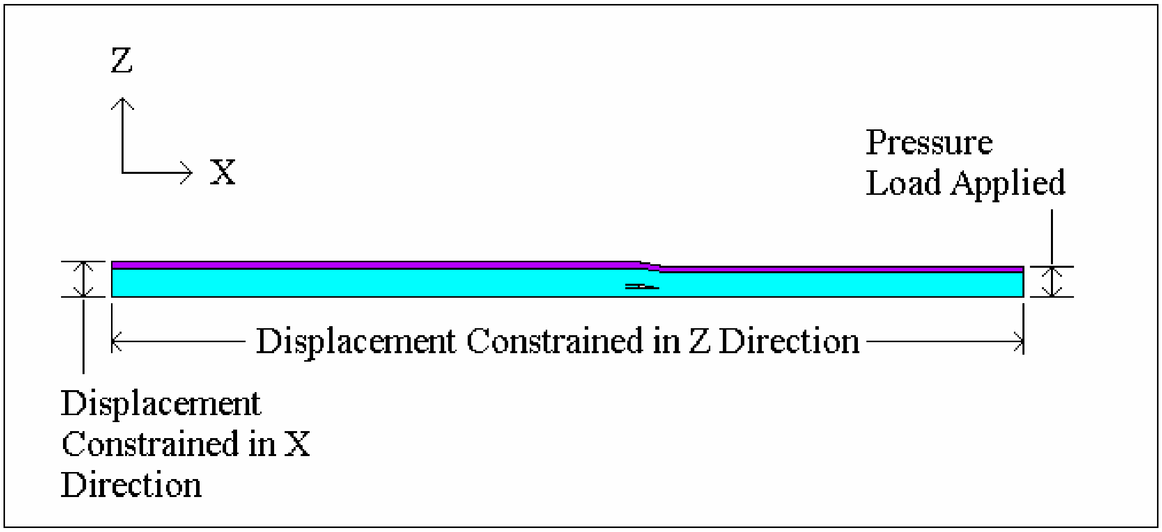

Figure 48: Internal Ply Drop, Showing Loads and Constraints.

Figure 48 shows the loading and constraints of the internal ply drop model, typical of all FEA models. Models used symmetry about mid-thickness. Thus, only half of a test coupon was modeled. One end of the model was held fixed, while the other was loaded with a distributed pressure load. A fixed displacement could also be applied, though a pressure load was closer to what was done with experimental coupons, tested under load control. Furthermore, the results produced by the two loading schemes were close, as can be seen in Figure 49 (Note: The Total G = $G_I + G_{II}$, which assumes that crack growth is collinear; where two cracks are present, the total G is the sum for both cracks unless indicated otherwise. While the Total G indicates the total energy released if the cracks grow, prediction of growth for any individual crack requires consideration of the individual G_I and G_{II} at a particular crack tip, and some mixed-mode criterion.)

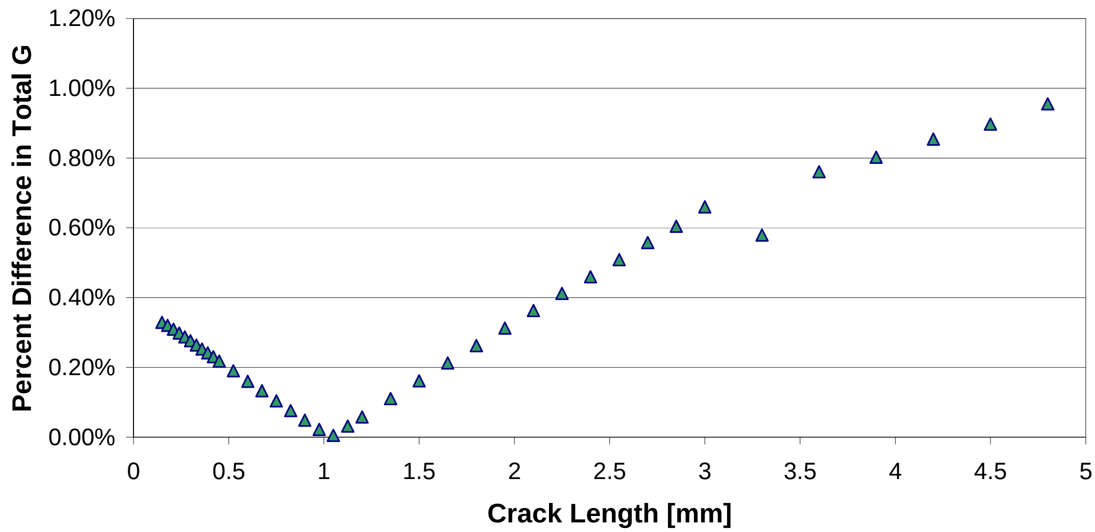

Figure 49: Percent Difference in Total G vs. Crack Length between Displacement and Load Control in Internal Ply Drop Model.

All FEA models feature an extended gauge section, as shown in Figure 50. The total length of the model is approximately 30 times the thickness of the thin section. The extended end regions are intended to ensure that any stress irregularities due to the loading at the ends are evened out, and a uniform strain condition is reached across the model before the area of interest. There will be different stresses present in the 0° plies and the ±45° plies, as these two materials have different longitudinal stiffnesses.

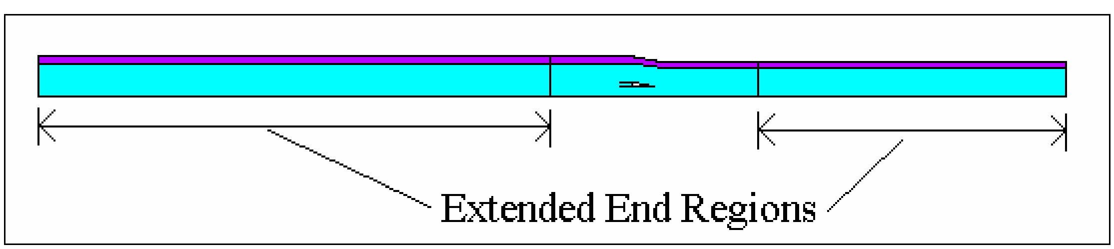

Figure 50: Internal Ply Drop Model, Full Model, Showing Extended Gauge Section.

These extended end regions are meshed with relatively large elements. The area near the ply drop and the cracks has a mesh with intermediately sized elements; while the areas immediately surrounding the cracks have a fine mesh to improve accuracy. Figure 51 shows the location of these areas. The use of different mesh sizing is a result of balancing the need to have a fine mesh to achieve accurate results with the need to minimize computation time.

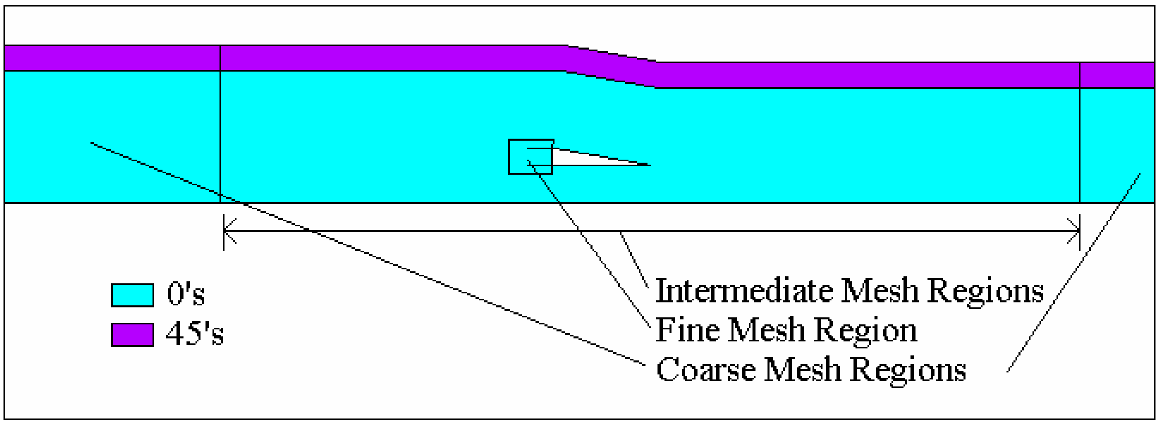

Figure 51: Internal Ply Drop Model, Areas near Ply Drop.

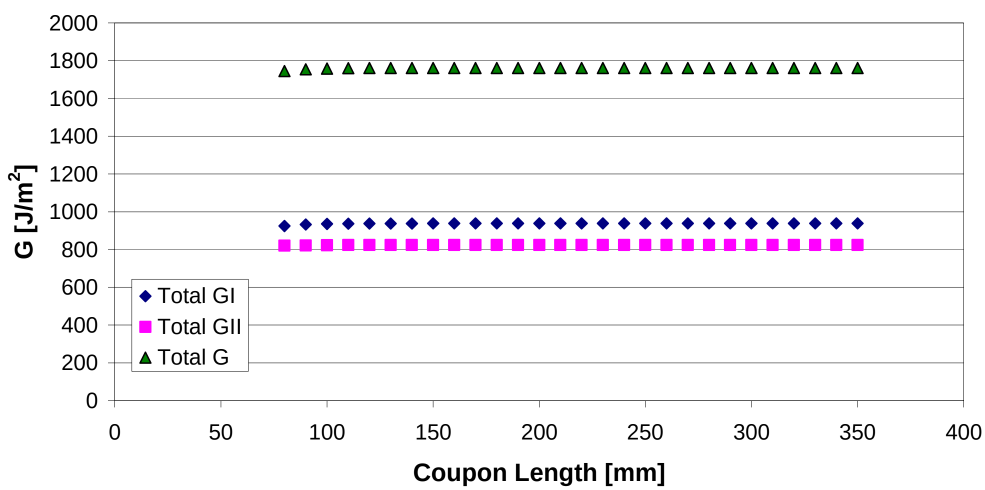

Figure 52: Internal Ply Drop, Carbon, Compression, Two 1 mm long Cracks, G vs. Coupon Length.

A study of the effects of model length on the results was undertaken, and the results indicate that the extended model length is not necessary. The results in Figure 52 show very little change in calculated G values over a wide range of overall model lengths. This also implies that the experimental test coupon length was adequate for end loaded specimens.

Element Sizing

Convergence studies were done on the models to determine element sizing to produce the best balance between accurate results, which is contingent on using enough elements, while not using so many elements that the model takes an inordinate time to solve. Figure 53 is an example of the results of a convergence study. The element sizing for models used in the following sections was chosen in the region of the curve where change was minimal with increasing number of elements.

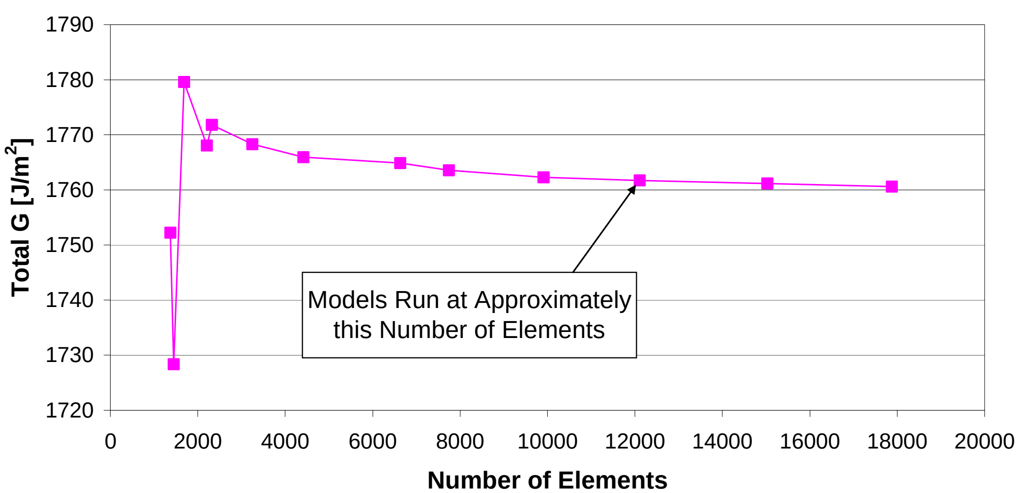

Figure 53: Internal Ply Drop Convergence Study, Total G vs. Number of Elements.

Element sizing for the intermediate regions was half the ply thickness, or 0.15 mm, with 1/8 of a ply thickness for the fine mesh areas, or 0.0375 mm. The coarse mesh elements were 2.5 times the ply thickness, or 0.75 mm. Figure 54 shows the mesh around the cracks for the internal ply drop model, which is similar to the other models. These areas are meshed with the fine and intermediate mesh sizing.

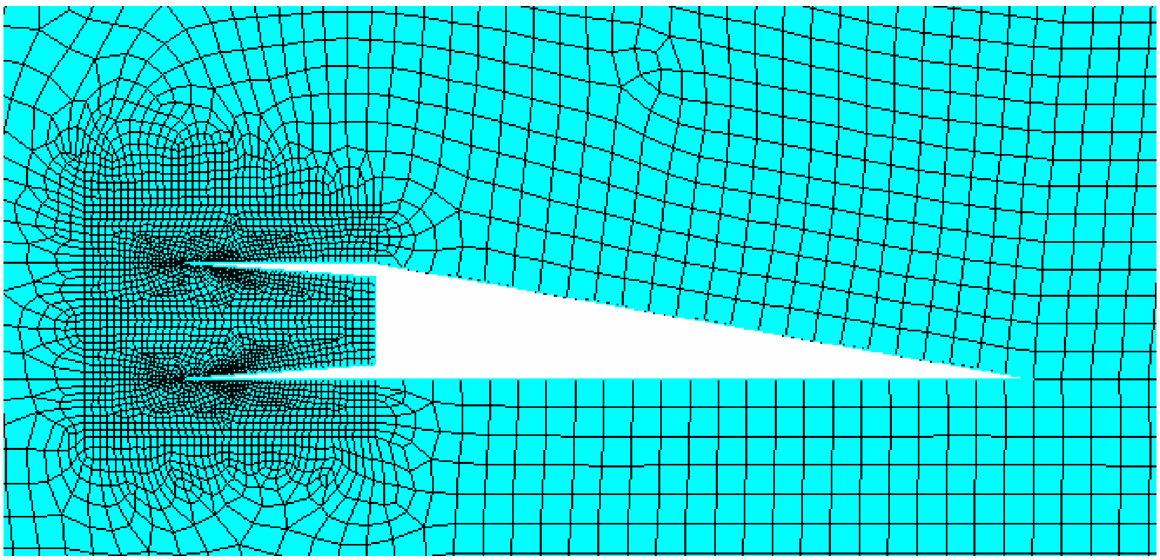

Figure 54: Internal Ply Drop Model, Exaggerated Crack Width.

Figure 54 also shows the near ply drop geometry, with the width of the crack exaggerated for clarity. The model has not been displaced at this point. The initial cracks are triangular, tapering toward the crack tip. A triangular void is assumed ahead of the ply drop as discussed later.

Contact Elements

Contact Elements are a method of preventing elements of the model from overlapping as it deforms under load. Properly functioning contact elements are important for obtaining valid G values. G_I and G_{II} values vary significantly from those presented if contact elements are not used. The coefficient of friction between the faces of the cracks was assumed to be equal to zero in all FEA models. Thus, cracks which close under load can slide freely to produce a G_{II} result which reflects zero friction.

Composite materials are anisotropic, having direction specific properties. Most ply drop geometries involve some mis-oriented continuous 0's ahead of the plydrop where the section thickness of the coupon is reduced. The mis-orientation of this section of the plies must be represented in the model in order to obtain accurate results. To do this, areas of the model that represent the mis-oriented fibers are created, shown in Figure 55, and the coordinate system of the elements in these areas are modified from the global coordinate system to match the their orientation in the coupons. The angle of the mis-oriented plies is fairly consistent from the surface to the ply drop, as seen in Figure 56.

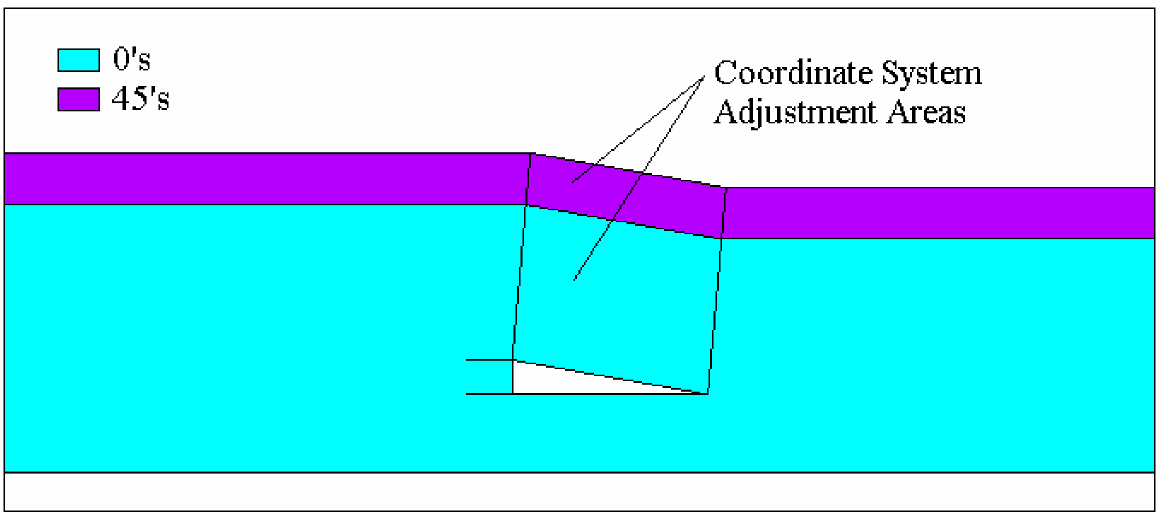

Figure 55: Coordinate System Adjustment Areas.

<u>Angle of Taper</u>

The region ahead of the ply drop may be filled, or partially filled, with resin, or may be mostly void. This study makes the conservative assumption of a void in all models. Establishing a representative angle of the taper between continuous plies on either side of void is important. As shown later with finite elements (Appendix C, Figure 131 through Figure 134), the taper angle has a significant effect on delamination behavior. Therefore, it is important to establish a value that reflects actual observations from experiments. A taper angle of 10° was chosen for all models, after examination of a number of samples; Figure 56 is representative.

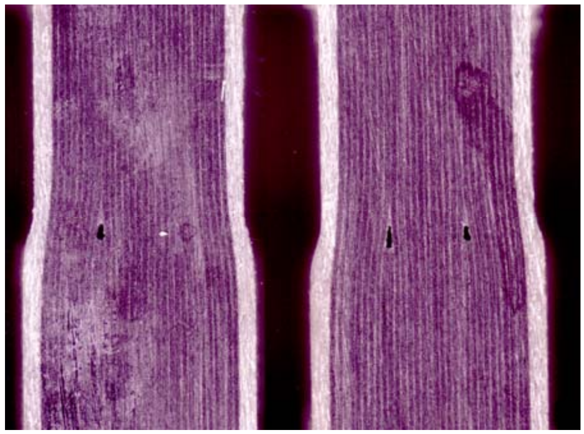

Figure 56: Internal Ply Drops, Two Plies dropped at each Location.

Figure 56 is an image of two internal ply drop coupons, focusing on the region where the plies are dropped, each with two plies dropped. These images have had their color scheme modified to better show ply boundaries. Closer views of the actual ply drops are shown in Figure 57 and Figure 58.

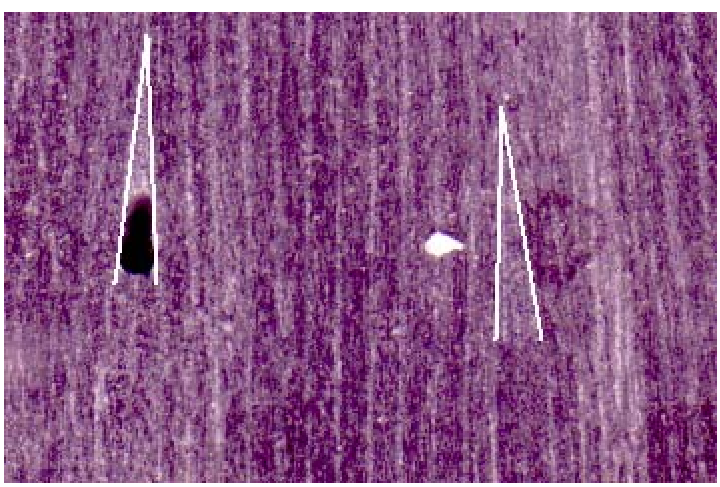

Figure 57: Detail of Double Internal Ply Drops, Taper Angles Highlighted.

Figure 57 a magnified view of the left hand coupon from Figure 56. The taper angles of the ply drops are highlighted to improve clarity. The taper angle on the left is approximately 9° and the angle on the right, with no clear void, 11°. Figure 58 is the right coupon from Figure 56. The angles of the ply drop taper measured here are 11° and 10° for the left and right voids, respectively.

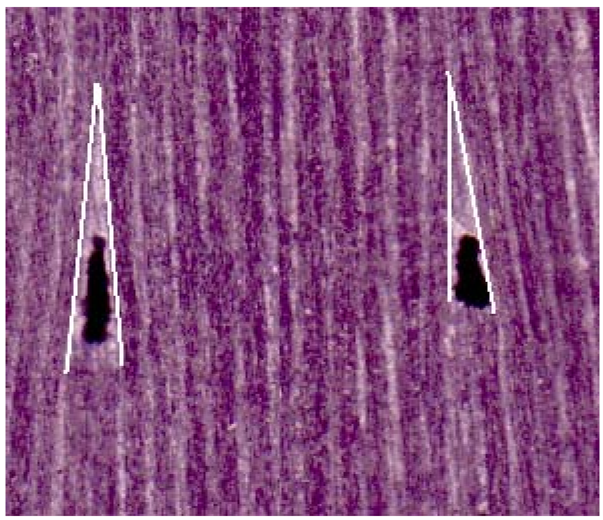

Figure 58: Detail of Double Internal Ply Drops, Taper Angles Highlighted.

Composite Properties

Properties used in the FEA model were obtained from the DOE/MSU database [5]. Materials used are designated NB307-D1 7781 497A (Glass 45's), NCT307-D1-34-600 unidirectional Carbon, and NCT307-D1-E300 unidirectional Glass in the database, all supplied by Newport Adhesives and Composites, and using the same epoxy resin. The glass and carbon fiber zero plies are unidirectional and listed with transversely isotropic properties, but the glass ±45's are listed with properties as a 0/90 laminate and required a coordinate system rotation to find properties for a ±45 laminate [30]. The properties used are listed in Table 12. The materials were in the form of epoxy matrix prepreg, molded without resin bleed off as noted earlier, with fiber volume fractions close to 0.50. The ply thickness of about 0.3 mm is about twice that of most aerospace prepreg.

	Carbon 0's	Glass 0's	Glass ±45's
E_x [GPa]	132	35.5	12.79
E_z [GPa]	8.20	8.33	8.33
ν_{xz}	0.31	0.33	0.421
G_{xz} [GPa]	5.08	8.55	8.50
Ply Thickness [mm]	0.3	0.3	0.3
Fiber Volume Fraction	0.53	0.47	0.39

Table 12: Material Properties.

The transverse modulus listed for the glass 45's is assumed to be the same as those for the glass 0's. The elastic properties for glass 0's in the transverse direction and normal to the plane of the ply are ostensibly the same, and listed as such in the DOE/MSU database. The woven fabric ±45's, however, have different properties along and out of the plane; however, none are listed for the out of plane direction. Given that the properties in that direction are matrix dominated in both the glass 0's and 45's, it is assumed that the properties of the ±45's are close to those of the 0's out of plane [5].

Far-Field Strains

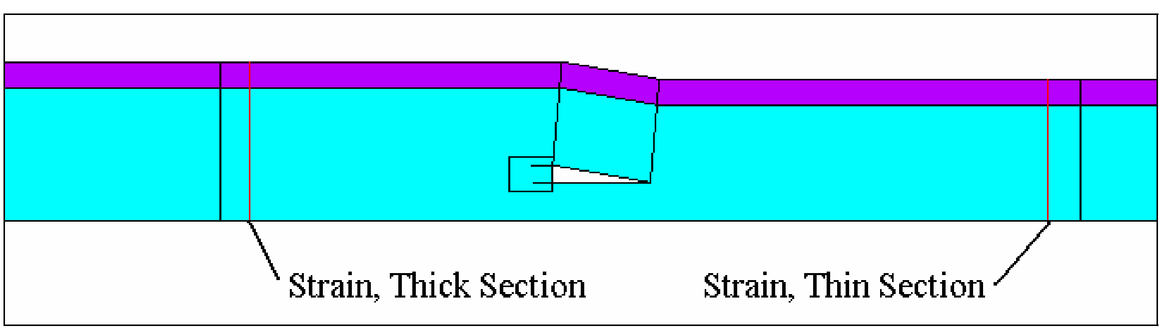

Figure 59: Locations Where Strain Values are obtained in Models.

Far-field strain values are defined from two areas in each model, thin section and thick section. The locations where these strains are taken are shown in Figure 59. These locations were chosen to minimize the effects of the ply drop on the strain fields, while still defining the strains in a region of intermediate element size.

The applied stresses in the models are calculated based on the average strain in the thin section, since the experimental results are reported in terms of stresses and strains on this side of the coupon. For comparison purposes, loads are adjusted to produce a strain of 0.005 m/m, or 0.5% strain, on the thin side unless otherwise stated. The average strain is found by taking a line integral across the marked cross section. The form of the equation used is below:

$$\varepsilon_{avg} = \frac{1}{S}\int \varepsilon \cdot dS \tag{13}$$

G vs. Load

Basic fracture mechanics theory establishes that the magnitude of the G values are proportional to the load, strain, or stress squared [20]. This was verified with the finite element model, as shown in Figure 60. G values are plotted against applied stress squared and show a very linear fit, with a residual squared value of 1. Thus, G values can be scaled to other applied stresses through the applied stress (or strain) squared.

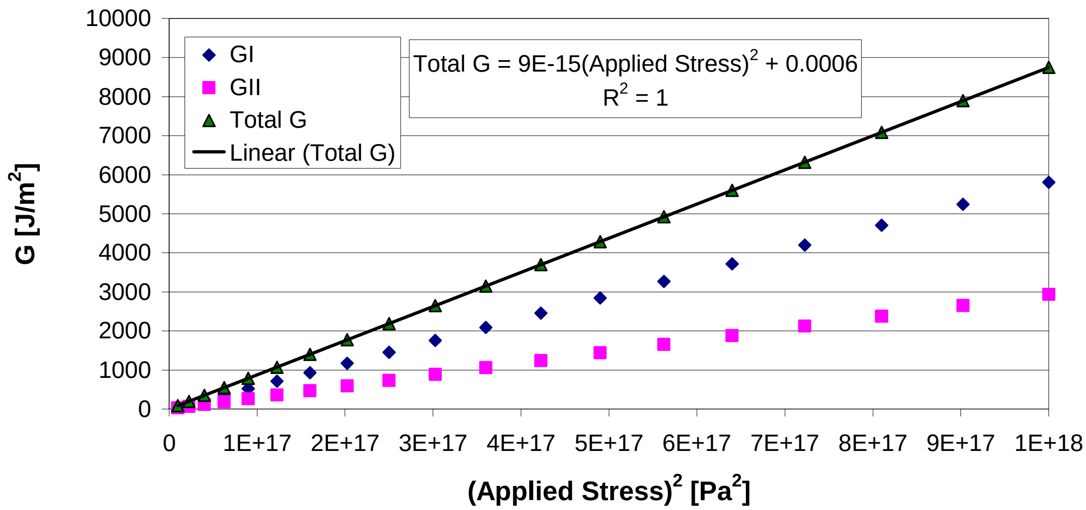

Figure 60: Center Ply Drop, Carbon, Compression, 1 mm Crack, G vs. Applied Stress Squared.

Delamination Resistance of Composite Materials

Many studies of delamination resistance have been carried out. Among these, Reeder presented results of mixed mode fracture toughness of a number of carbon composite systems [31], and Agastra presented similar results for glass fiber composites [32]. Both these studies indicate an interaction effect between mode I and II fracture, seen in Figure 61 from Agastra and Figure 62 from Reeder [32, 31].

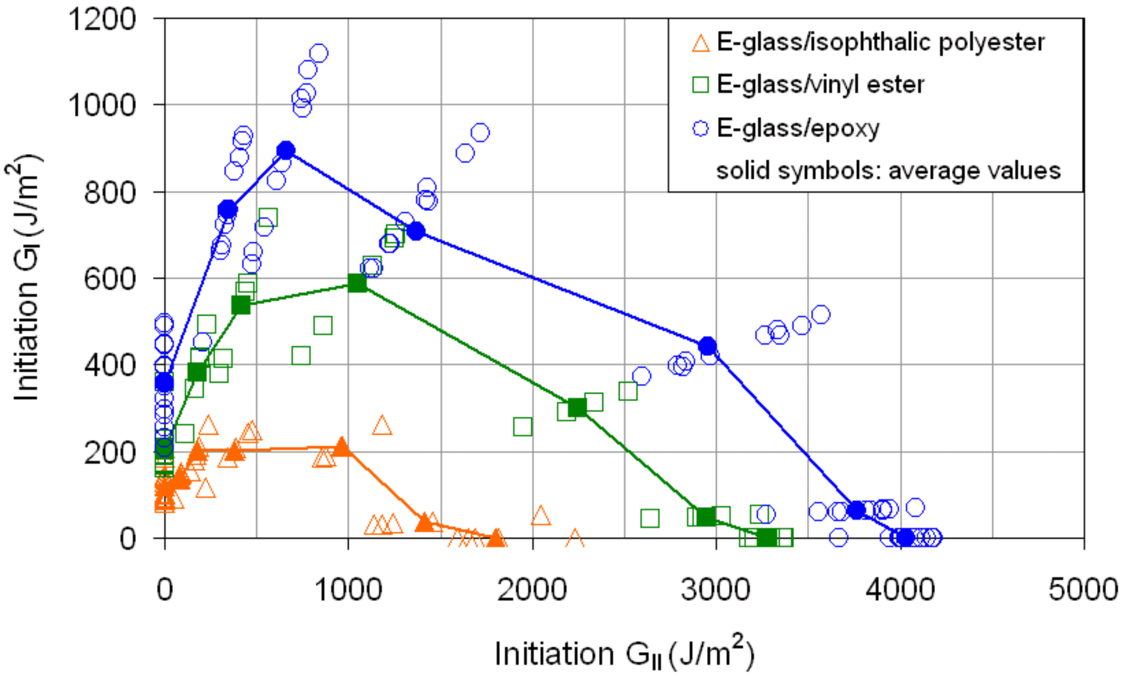

Figure 61: Mixed-Mode Fracture of $[0]_{10}$ E-glass/Isophthalic Polyester, Vinyl Ester and Epoxy, from Agastra (RTM molded, Fiber Volume Fraction about 0.35) [32].

The composite systems presented by Agastra are for lower fiber content systems than the prepreg materials in this study. Agastra found "hackle" formation during crack growth with a mode II component in the matrix rich inter-ply regions; this is theorized to increase delamination resistance [32]. This interaction between modes, mode I with relatively straight cracks at short crack extensions, and mode II with sinusoidal cracks forming hackles, results in a complex response when both modes are present, as at many ply drops. At the lower fiber volume percentages of the materials tested in mixed mode bending, the inter-ply regions will be larger, promoting larger hackles. This produces G_I values at fracture which are far above the pure mode I G_{IC} (Figure 61).

Material	Volume Fiber Fraction (V_F)	G_{IC} [J/m^2]	G_{IIC} [J/m^2]
E-Glass / Epoxy	0.324	356 (94)	4054 (151)
E-Glass / Vinyl Ester	0.342	204 (59)	3283 (86)
E-Glass / Isophthalic Polyester	0.367	116 (27)	1797 (256)
Glass Prepreg	0.47	365 (37)	2306 (188)
Carbon Prepreg	0.53	364 (62)	1829 (87)

Table 13: Results for Pure Mode I and II Delamination Tests. (The Prepreg is that Used for 0° Plies in the Current Study.)

Table 13 lists the volume fiber percentages and delamination resistance, quantified by the critical mode I and II strain energy release rates (G_{IC} and G_{IIC}, respectively), for the materials examined by Agastra and the prepreg materials used for 0° plies in this study. Double cantilever beam (DCB) tests were done to determine G_{IC} and End-Notched Flexure (ENF) tests were used to find G_{IIC} [32, 17].

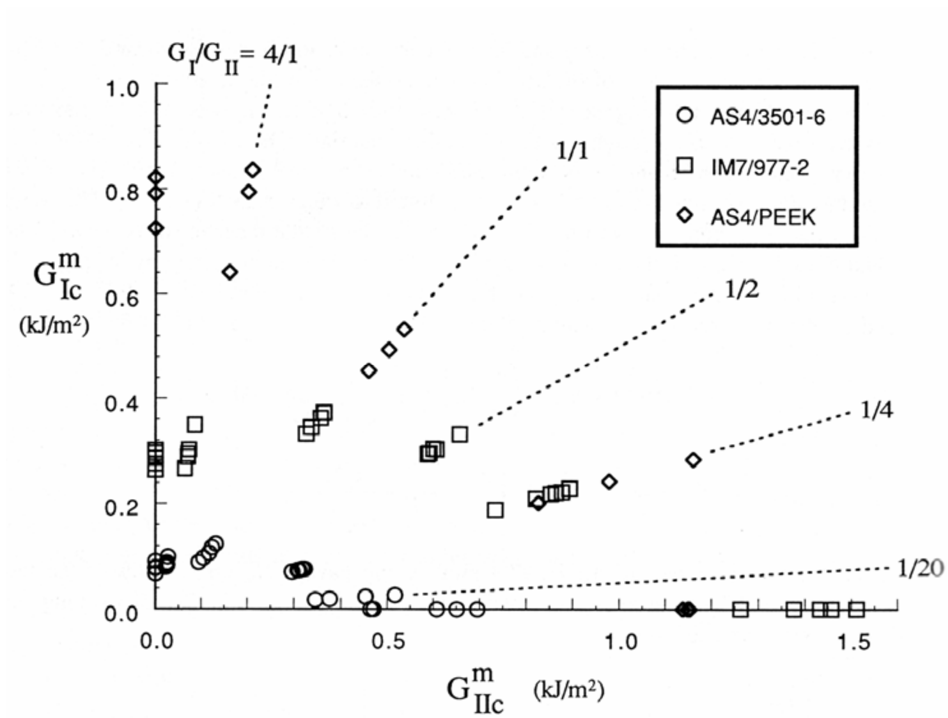

Figure 62: Mixed-Mode Fracture of Graphite Composite Materials [31].

Figure 62 shows the results presented by Reeder. The interaction effect of the mixed mode fracture is less pronounced in these results. The materials examined by Reeder are thinner ply carbon prepreg materials, with a ply thickness of about 0.125 mm, less than half that of the prepregs examined here and have a fiber volume fraction around 0.60 - 0.65. Furthermore, the G_{IIC} of these materials are lower than those of the materials examined here [31], apparently due to the reduced amount of material between plies. Thus, it is likely that the effect of mixed mode fracture on the prepreg materials examined in this study will be somewhere between the results presented by Agastra and Reeder, in terms of the maximum G_I/G_{IC} ratios in mixed mode, due to differences in the ply thickness and resin content. Further testing is required to confirm this. An important observation from these studies is that a moderate G_{II} component at a crack tip can raise the G_I value for delamination well above the pure mode G_{IC} value, apparently by hackle formation [31]. This is evident in some results in this study.

Associated Experimental Study

Earlier work by Samborsky et al. at Montana State University includes an experimental study of test coupons with ply drops [17]. This study included static and fatigue testing of a number of ply drop configurations, including the external and internal ply drops modeled here with FEA. The FE models are based on these experimental coupons, a schematic of which is given as Figure 63 and photographs in Figure 45 and Figure 56. The FE models differ from the experimental coupons in that the FE models have no fiberglass tabs, used to minimize gripping affects from the test fixtures, and the FE models assume that all introduced loads are from end loading. There are no loads introduced along the sides, as are present from lateral clamping in the experimental coupons. The experimental coupons are milled flat on the ends to accommodate end loading in compression testing, though the grips on the sides of the coupons transfer loads as well.

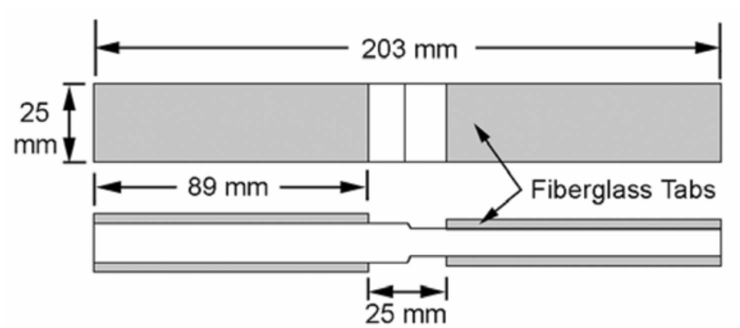

Figure 63: Schematic of Typical Ply Drop Coupon from Experimental Study.

All of the experimental results compared to the FE models here are compression fatigue results. Though there were some tests of a thinner external ply drop configurations run in full reversed and tension fatigue, these used lateral loading exclusively.

Results from the experimental study are introduced in the pertinent sections of the foregoing. These include FEA results for external ply drops with carbon 0's loaded in compression, external ply drops with glass 0's loaded in compression and results for internal ply drops with carbon and glass 0's, loaded in compression.

Finite Element Results for Various Geometries and Materials

Ply Joint

The ply joint model is the simplest delamination model examined. This model examines the case where a total of four central plies contain butt joints with a small gap between ends (Figure 64). There is no ply drop, as the cross section does not change. The ply joint model was developed to investigate the behavior of ply joints, which are present in many composite structures. It is also an opportunity to examine the influence of mis-oriented plies on G; in this model there are none. There are two crack cases, one crack (shown in Figure 64) and two cracks (Figure 65).

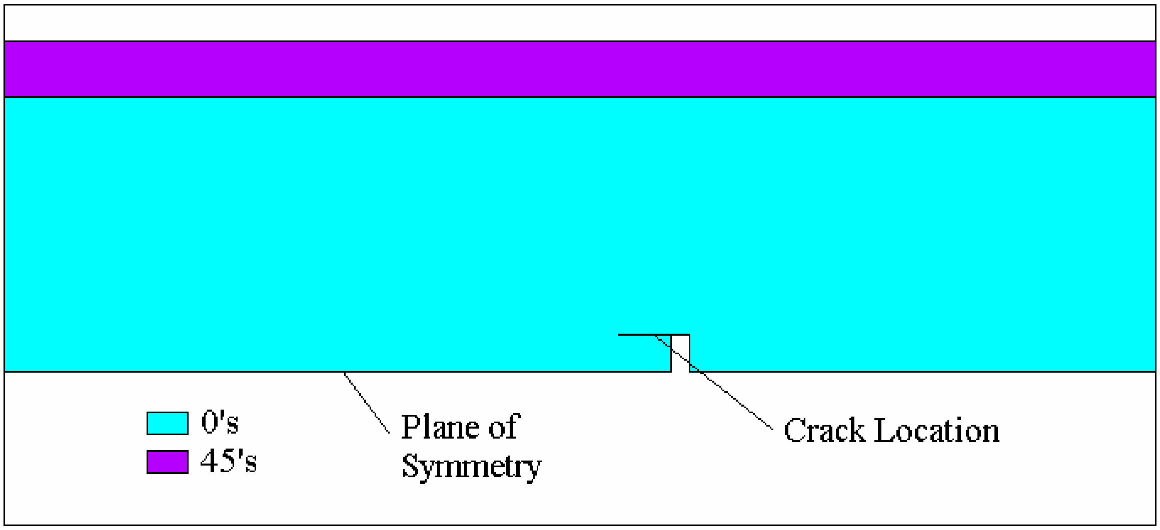

Figure 64: Ply Joint, One Crack, $[\pm45_3/0_{13}/0^*{}_2]_S$.

The two-crack model examines the behavior of two cracks growing, in opposite directions. This is to determine if it is more probable whether one or two cracks develop, and if there are any important interaction effects between the two cracks. This model is symmetric on the transverse axis at the gap, and it would have been possible to further simplify the model by using that axis of symmetry, but the full length was modeled to provide a check for the G values calculated. The values for both the right and left cracks match very closely.

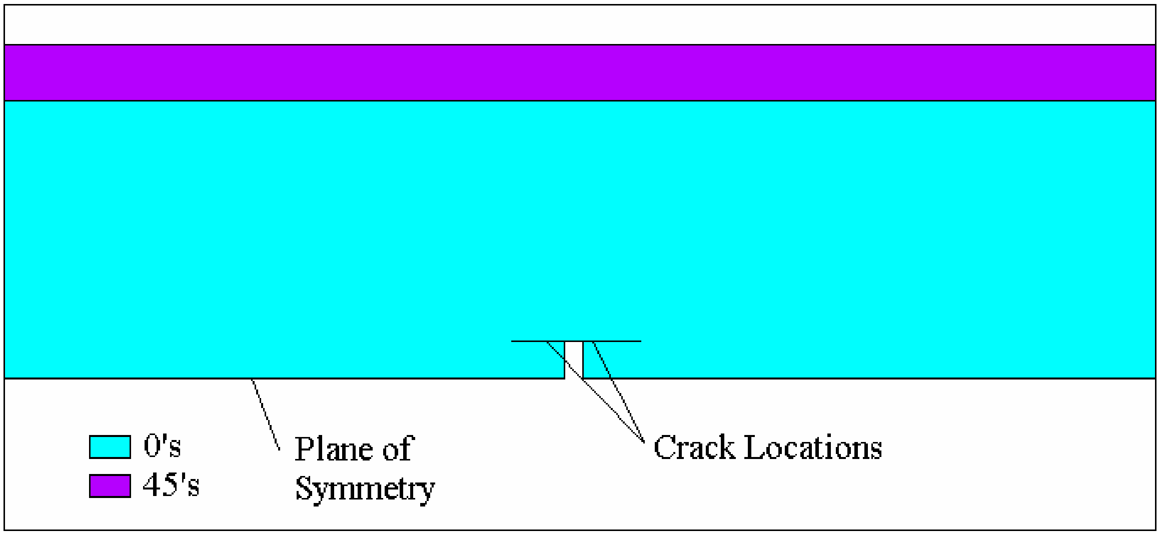

Figure 65: Ply Joint, Two Cracks, $[\pm45_3/0_{13}/0^*_2]_S$.

Ply Joint, Carbon, Compression. Figure 66 and Table 14 give results from the ply joint model with one crack, carbon 0's, and loaded in compression for the ply configuration $[\pm45_3/0_{13}/0^*_2]_S$. G_{II} dominates for this model, as discussed later. There is a small G_I component, 4.8% of the total average G, which is much smaller than most other carbon dominated models loaded in compression. This supports the later conclusion that G_I levels are driven, to a great extent, by the mis-oriented plies present in the ply drop models. The strains in Figure 66B and in later figures provide data for the two sides of the coupon in terms of maximum and minimum strains through the section, relative to the average right side strain of 0.005. (For later ply drop geometries, the thick side is compared relative to the controlled 0.005 strain on the thin side.)

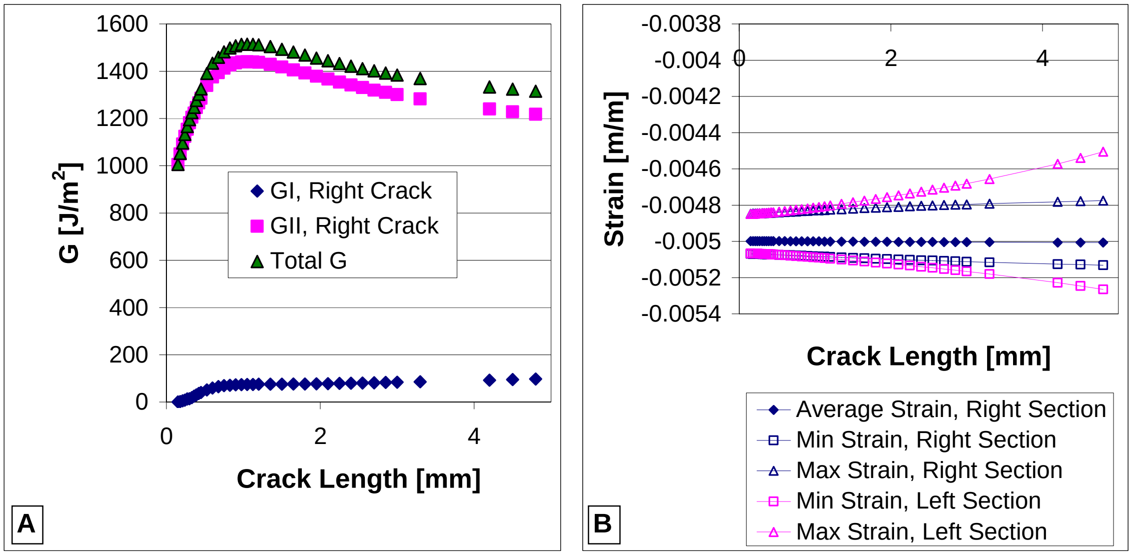

Figure 66: Ply Joint, One Crack, Carbon, Compression. A: G vs. Crack Length; B: Far-Field Strain vs. Crack Length; Load = 559.2 MPa.

	Maximum [J/m^2]	Crack Length at Maximum G [mm]	Average [J/m^2] (0.15 – 3.0 mm)
Total G	1514.7	1.05	1426.0
G_I	97.3	4.8	68.8
G_{II}	1440.4	1.05	1357.2

Table 14: Ply Joint, One Crack, Carbon, Compression, Maximum and Average G.

Figure 67 and Table 15 give results from the ply joint model with two cracks, carbon 0’s, and loaded in compression, same laminate. The results shown are for just one side, to make the comparison between the one and two crack models simpler. The two crack model shows slightly lower G_{II} values than the one crack model, but not so substantial as to allow any conclusions to be drawn about the likelihood of one of the configurations developing over the other. The G_I values with two cracks are slightly higher, but the maximum G_I is still only about 35% of G_{IC}. The second crack tip showed the same results as Figure 67. Thus, with the ply joint at the mid-thickness, release of the interface over twice the length used for Figure 66 has only minor effects. This might not be the case if the joint were near the surface, where bending of the delaminated plies off of the surface could be important [33].

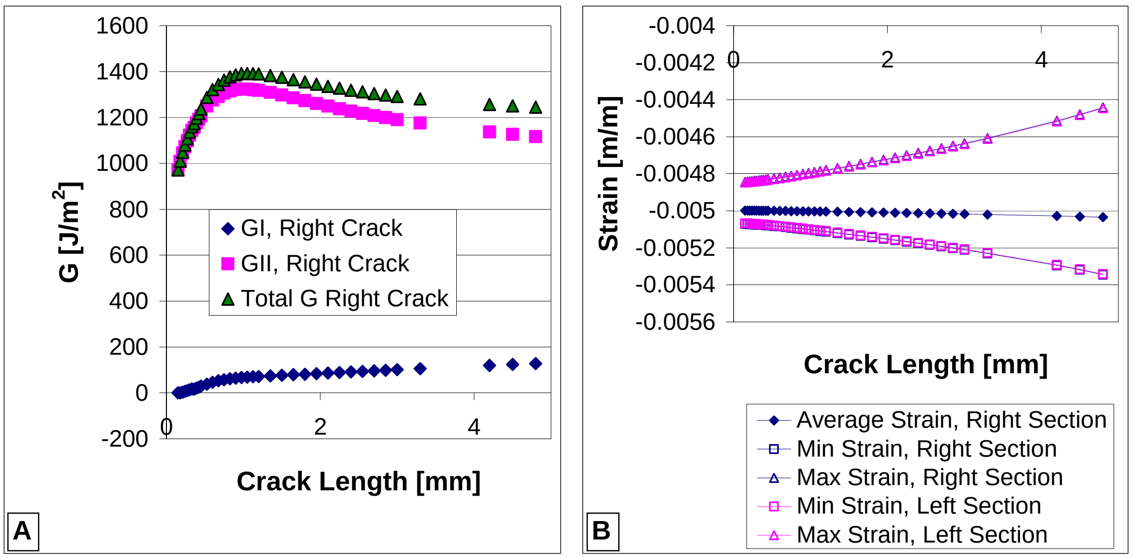

Figure 67: Ply Joint, 2 Cracks, Carbon, Compression. A: G vs. Crack Length; B: Far Field Strain vs. Crack Length; Applied Stress = 559.2 MPa.

	Maximum [J/m^2]	Crack Length at Maximum G [mm]	Average [J/m^2] (0.15 – 3.0 mm)
Total G	1391.8	1.05	1320.5
G_I	128.0	4.8	71.1
G_{II}	1323.8	0.975	1249.4

Table 15: Ply Joint, 2 Cracks, Carbon, Compression, Maximum and Average G.

Ply Joint, Carbon, Tension. Results from the ply joint model with one crack, two plies dropped each side, carbon 0's, loaded in tension, for the same laminate, are shown in Figure 68 and Table 16. There is negligible G_I influence in this loading configuration, typical of tension loading for later cases, as most cracks close. Compression loads produce much higher (more positive) G_I levels than tension loads, an effect that is more pronounced in models with mis-oriented plies, as with ply drops. The average G_{II} component in tension is very close to the average G_{II} in the same model loaded in compression. The direction of the load only changes the direction of the shear displacement, not the magnitude of G_{II}. The absence of a sign on G obscures the direction change of the shear effect along the interface. For reversed loading in fatigue, there is now twice the range of shear stress and displacement, from (+) shear to (-) shear.

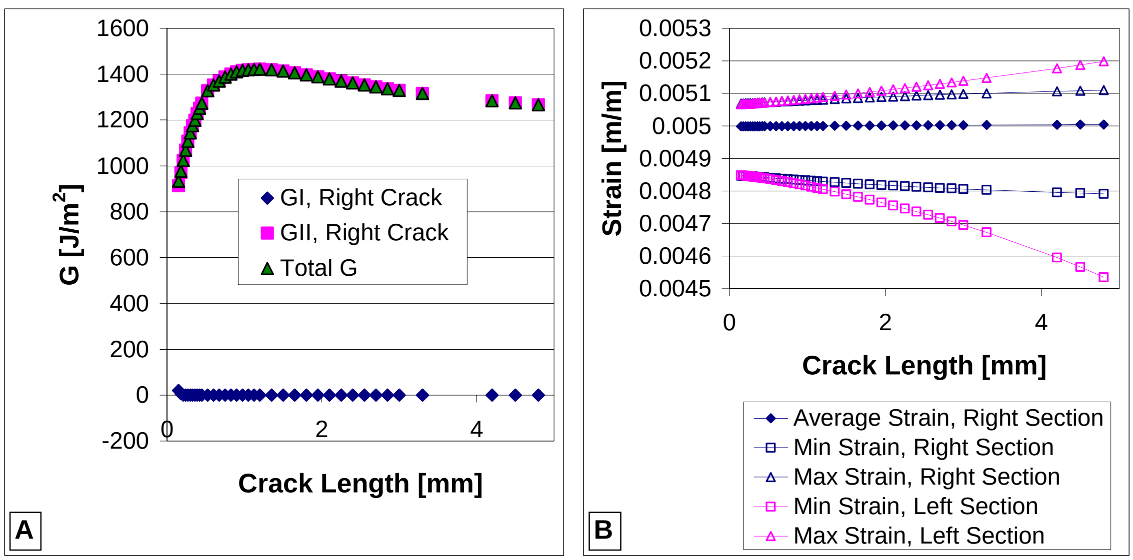

Figure 68: Ply Joint, 1 Crack, Carbon, Tension. A: G vs. Crack Length; B: Far Field Strain vs. Crack Length; Applied Stress = 559.2 MPa.

	Maximum [J/m^2]	Crack Length at Maximum G [mm]	Average [J/m^2] (0.15 – 3.0 mm)
Total G	1421.9	1.2	1354.1
G_I	20.4	0.15	0.2
G_{II}	1421.9	1.2	1353.9

Table 16: Ply Joint, 1 Crack, Carbon, Tension, Maximum and Average G.

<u>Closed Form Approximation to Ply Joint</u>. Ramkumar and Whitcomb derived an approximate strength of materials solution that is appropriate for approximating the total

G in a ply drop [34], which is also applicable to the ply joint geometry. The model is based on the compliance change during crack growth, and the same relationship can be derived from the equality of the change in elastic strain energy during delamination growth with the total G per unit crack extension. The application of this model to the current case neglects the influence of the external ±45 face sheets which contain little strain energy at these strains, and assumes a constant stress across the plies, neglecting the stress gradients, and neglecting bending. The model is rearranged from [34] as Equation 14, with σ as far field stress, t_T is the total thickness of the 0 plies, t_p is the thickness of the jointed or dropped plies, and E_L is the longitudinal elastic modulus. The thicknesses are shown on the schematic in Figure 69.

$$G = \frac{\sigma^2 t_p}{2E_L}\left(\frac{t_T}{t_T - t_p}\right) = \frac{E_L \varepsilon^2 t_p}{2}\left(\frac{t_T}{t_T - t_p}\right) \tag{14}$$

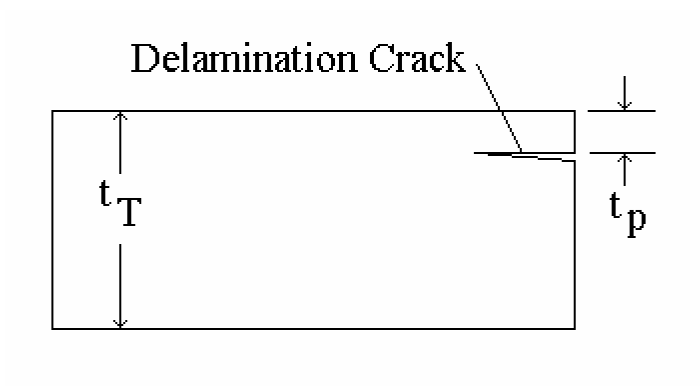

Figure 69: Schematic for Ramkumar and Whitcomb's Strength of Materials Solution, where the Jointed or Dropped Ply has a Thickness t_p.

Samborsky et al. [17] and Im et al. [35] have used a similar approach to obtain strength of materials models. For a very thick laminate, where the second term in Equation 14 is small, Equation 14 becomes:

$$G = \frac{E_L \varepsilon^2 t_p}{2} = \frac{\sigma^2 t_p}{2E_L} = \frac{\sigma \cdot \varepsilon \cdot t_p}{2} \tag{15}$$

For the parameters of the ply joint model in this section (ignoring the ±45 layer), Equation 14 yields a solution of 1142 J/m^2 for a far-field strain of 0.005 m/m (giving a stress of 660 MPa), E_L = 132 GPa, t_p = 0.6 mm, and t_T = 4.5 mm. Equation 15 yields a slightly lower value of 990 J/m^2. These models do not include the delamination length, but are approximate for long delaminations. The total G results in Figure 67 and Figure 68 are slightly higher than the 1142 J/m^2 from Equation 14 for crack lengths of a few mm, but are dropping with increasing crack length. Thus, the FEA results are consistent with the results of Equation 14, but provide individual G_I and G_{II} values which can be used with pure and mixed mode delamination criteria to predict failure. Equations 14 and 15 predict clear trends of G with E_L and ply thickness which are explored in the following FEA results, but with additional identification of G_I and G_{II} components.

Ply Joint, Glass, Compression. Figure 70 and Table 17 are results from the FEA ply joint model with one crack, glass 0's, loaded in compression. Average G_I is 7.5% of the average total G, a slightly higher percentage than present in the carbon model.

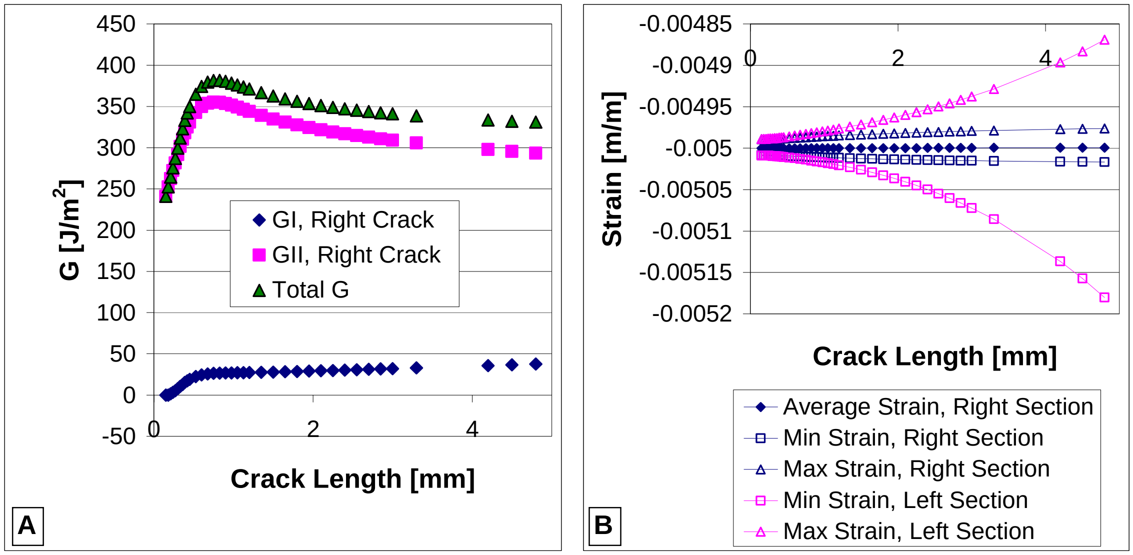

Figure 70: Ply Joint, 1 Crack, Glass, Compression. A: G vs. Crack Length; B: Far Field Strain vs. Crack Length; Applied Stress = 158.6 MPa.

	Maximum [J/m^2]	Crack Length at Maximum G [mm]	Average [J/m^2] (0.15 – 3.0 mm)
Total G	381.6	0.825	352.9
G_I	37.6	4.8	26.3
G_{II}	355.2	0.75	326.7

Table 17: Ply Joint, 1 Crack, Glass, Compression, Maximum and Average G.

Ply Joint, Glass, Tension. Figure 71 and Table 18 are results from the ply joint model with one crack, glass 0's, loaded in tension for the same laminate configuration. This model shows almost exactly the same G_{II}, and thus total G, as the compression model, similar to carbon.

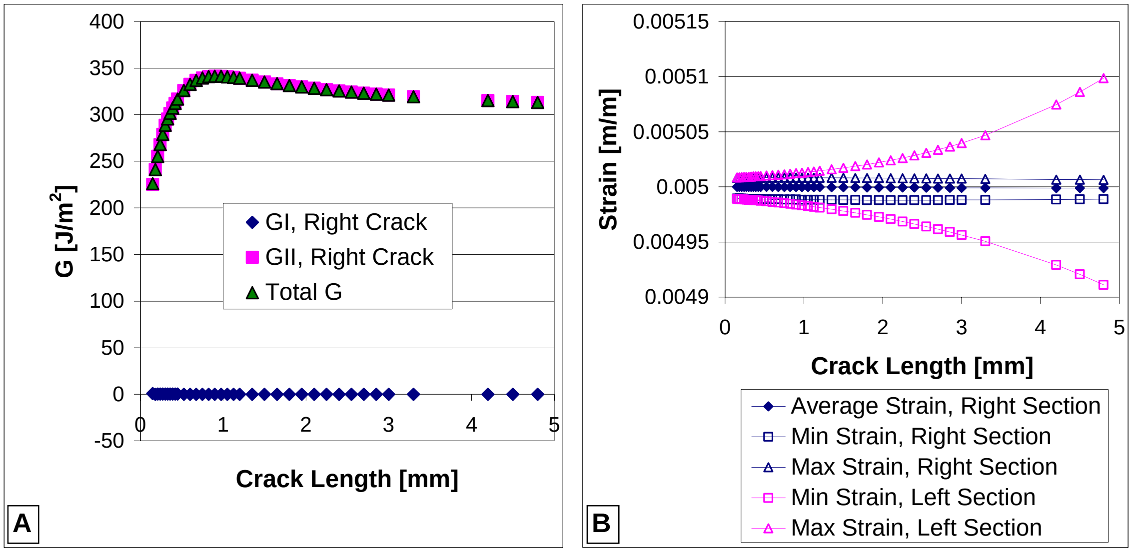

Figure 71: Ply Joint, 1 Crack, Glass, Tension. A: G vs. Crack Length; B: Far Field Strain vs. Crack Length; Applied Stress = 158.6 MPa.

	Maximum [J/m^2]	Crack Length at Maximum G [mm]	Average [J/m^2] (0.15 – 3.0 mm)
Total G	341.4	0.9	326.0
G_I	0.8	0.15	0.0
G_{II}	341.4	0.9	326.0

Table 18: Ply Joint, 1 Crack, Glass, Tension, Maximum and Average G.

The equivalent model with carbon 0's (Figure 68) has 4.15 times the total average G compared with the glass case. This corresponds roughly to the ratio of the longitudinal moduli of carbon to glass, which is 3.72, as predicted by the closed-form approximation, Equation 14. This trend is also in agreement with experimental results described later, for ply drop geometries. It should be noted that these results are for a particular constant far-field strain. (The applied stress is 559 MPa with carbon versus 159 MPa with glass, due to the modulus difference.) This trend with materials would reversed if a constant force were considered, as described later.

Central Ply Drop

The central ply drop model includes drops at the mid-thickness. Given that the FE models use symmetry about the mid-thickness, only half of the ply drop is included in each model. Thus, the drops are described here by the number of dropped plies on each side of the plane of symmetry. A model with one ply dropped represents a ply drop coupon with a total of two plies dropped.

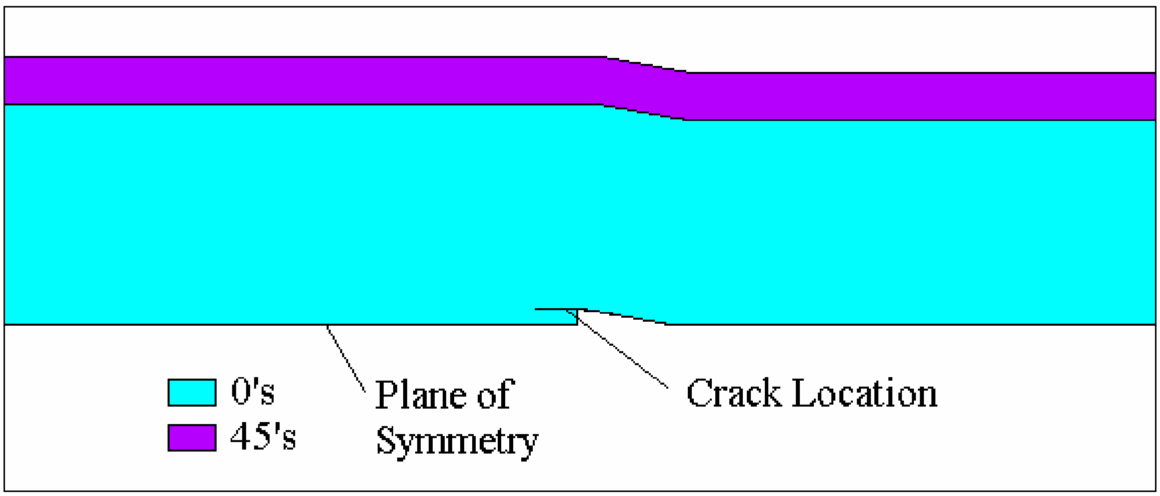

Figure 72: Central Ply Drop, Crack Location, Lay-Up: $[\pm 45_3/0_{13}/0^*_1]_S$.

Given that the drops are at the mid-thickness, the model has the maximum possible number of mis-oriented plies, as all of the plies from the center to the surface have a mis-oriented zone (Figure 72). This model is used for a more detailed investigation of how lay-up affects G values. Results from several different variations of number of continuous 0 plies and dropped plies are presented.

Central Ply Drop, Carbon, Compression. Figure 73 and Table 19 give results from the central ply drop model, with one ply dropped on each half-thickness, for a total of two plies dropped at the single position, with carbon 0's, loaded in compression. As in following ply drop cases, the strain plot (Figure 73B) compares the thick side into which the cracks grow, with the controlled thin side strain. The lay-up is given as $[\pm45_3/0_{13}/0^*_1]_S$. These results, along with the results below, offer an insight into how lay-up affects G values. This model has 13 continuous 0 plies and one dropped ply on each side. G_I makes up 61.5% of the average total G. The ratio of G_I/G_{II} drops from over two at the maximum values, to about one for cracks 4 mm long. G_I values tend to decrease rapidly as the crack grows away from the ply drop site. The maximum G values relative to the static critical values in Table 13 are $G_I/G_{IC} = 2.68$ and $G_{II}/G_{IIC} = 0.244$. Thus, at the far-field strain of 0.5% on the thin side, G_I is far above the pure mode I G_{IC} value, and, if a crack initiated, it could be expected to grow rapidly, at least for a short distance. The mode II component might be adequate to suppress crack growth for longer cases, as discussed earlier for mixed-mode behavior.

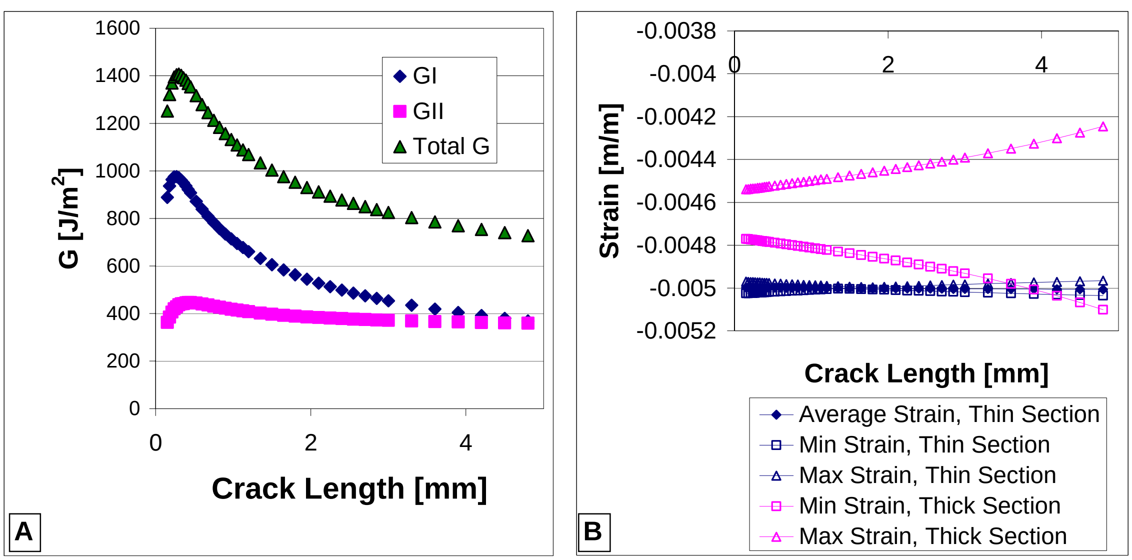

Figure 73: Central Ply Drop, 1 Ply Dropped Each Side, Carbon, Compression. A: G vs. Crack Length; B: Far Field Strain vs. Crack Length; Applied Stress = 548.5 MPa.

	Maximum [J/m^2]	Crack Length at Maximum G [mm]	Average [J/m^2] (0.15 – 3.0 mm)
Total G	1406.9	0.3	1041.4
G_I	975.8	0.27	640.9
G_{II}	445.9	0.45	400.5

Table 19: Central Ply Drop, 1 Ply Dropped Each Side, Carbon, Compression, Maximum and Average G.

Figure 74 and Table 20 give results from the central ply drop model, with two plies dropped on each half-thickness, for a total of four plies dropped, carbon 0's, loaded in compression. The lay-up is $[\pm45_3/0_{13}/0^*_2]_S$. G_I makes up 66.3% of the average total G. The average total G is 2.12 times that for the one ply dropped model, and the crack length at the maximum total G is twice as long. Figure 74 is comparable to Figure 67 for the ply joint. Under compression, the ply drop geometry compared with the ply joint produces much higher G_I values, much lower G_{II}, and a total G which is much higher for short cracks, but the difference diminishes as the crack lengthens. The mode I component diminishes significantly as the crack extends away from the ply drop location. (The applied stress for the ply joint is slightly higher, raising the G's by about 4% from Figure 60.)

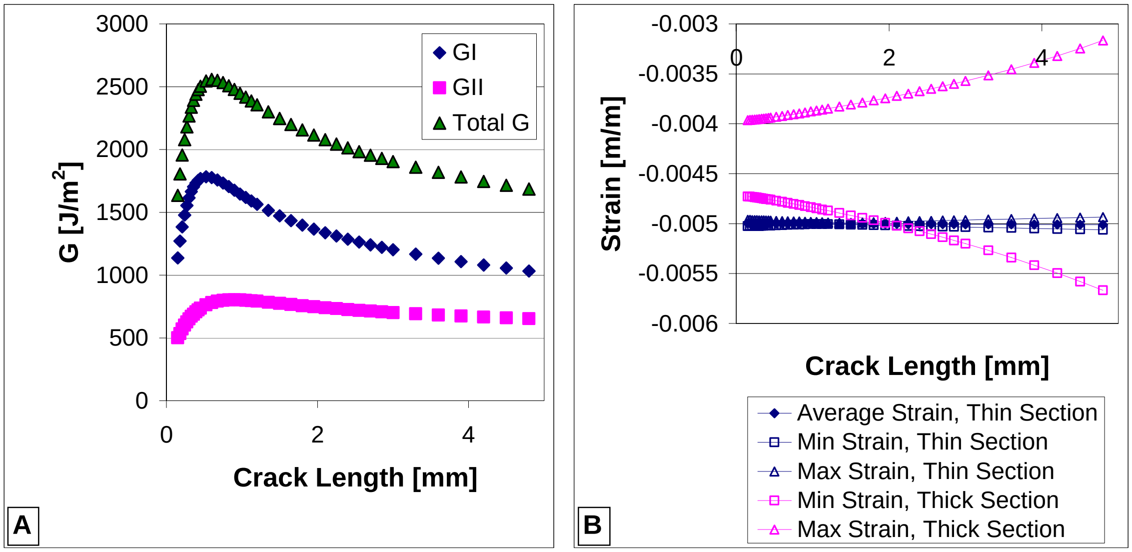

Figure 74: Central Ply Drop, 2 Plies Dropped Each Side, Carbon, Compression. A: G vs. Crack Length; B: Far Field Strain vs. Crack Length; Applied Stress = 548.5 MPa.

	Maximum [J/m^2]	Crack Length at Maximum G [mm]	Average [J/m^2] (0.15 – 3.0 mm)
Total G	2557.0	0.6	2209.2
G_I	1783.0	0.525	1464.5
G_{II}	803.1	0.9	744.7

Table 20: Central Ply Drop, 2 Plies Dropped Each Side, Carbon, Compression, Maximum and Average G.

Figure 75 and Table 21 show results from the doubled laminate thickness central ply drop model, which has two plies dropped on each side, carbon 0’s, and is loaded in compression. The lay-up is $[\pm45_6/0_{26}/0*_2]_S$. G_I makes up 65.0% of total G. The average total G is 2.28 times the one ply dropped model and 1.07 times the two plies dropped model.

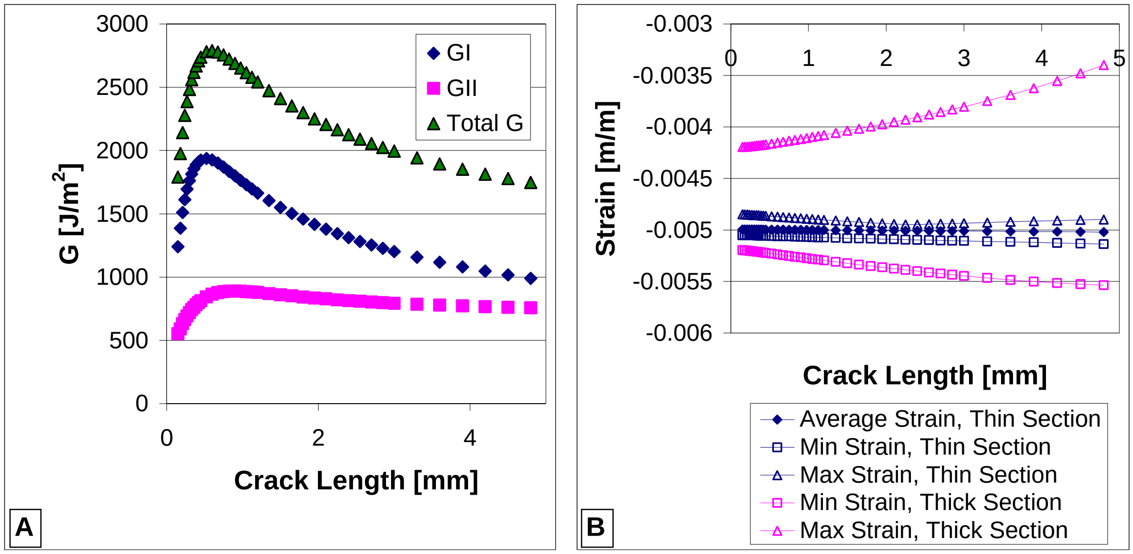

Figure 75: Central Ply Drop, Doubled Laminate Thickness Model, 2 Plies Dropped Each Side, Carbon, Compression. A: G vs. Crack Length; B: Far Field Strain vs. Crack Length; Applied Stress = 549.3 MPa.

	Maximum [J/m^2]	Crack Length at Maximum G [mm]	Average [J/m^2] (0.15 – 3.0 mm)
Total G	2789.4	0.6	2370.3
G_I	1936.5	0.525	1541.5
G_{II}	888.6	0.9	828.8

Table 21: Central Ply Drop, Doubled Laminate Thickness Model, 2 Plies Dropped Each Side, Carbon, Compression, Maximum and Average G.

From Figure 75 and Figure 76, it can be seen that both G_I and G_{II} are approximately proportional to the thickness of the plies dropped, following expectations (Equation 14). Changes in the number of continuous plies has a small effect, as predicted by Equation 14. Also, the ratio of G_I and G_{II} remains fairly consistent for all of the models.

Lay-Up Study, Central Ply Drop, Carbon, Compression. The purpose of the models in this section was to further examine the influence of model thickness on G values. Two central ply drop models with reduced total thickness were run and compared to the central ply drop model with a total of four dropped plies used in the preceding.

Lay up 1, $[\pm45_3/0_{13}/0^*_2]_S$, corresponds in overall thickness to the preceding results. This lay-up is the thickest with 26 continuous 0's and 3 ±45 top sheets on each surface. Lay up 2, $[\pm45_2/0_8/0^*_2]_S$, is a medium thickness model, with 16 continuous 0's and 2 ±45 top sheets on each surface. Lay up 3, $[\pm45_1/0_4/0^*_2]_S$, is the thinnest model, with 8 continuous 0's, and 1 ±45 top sheet on each surface.

All models were loaded by the same applied stress, 548.5 MPa, with very similar strains in the thin section of the model. However, given that all models dropped a total of four plies, the thick sections of the models varied in stiffness and thus produced different strains, as seen in Figure 77B below.

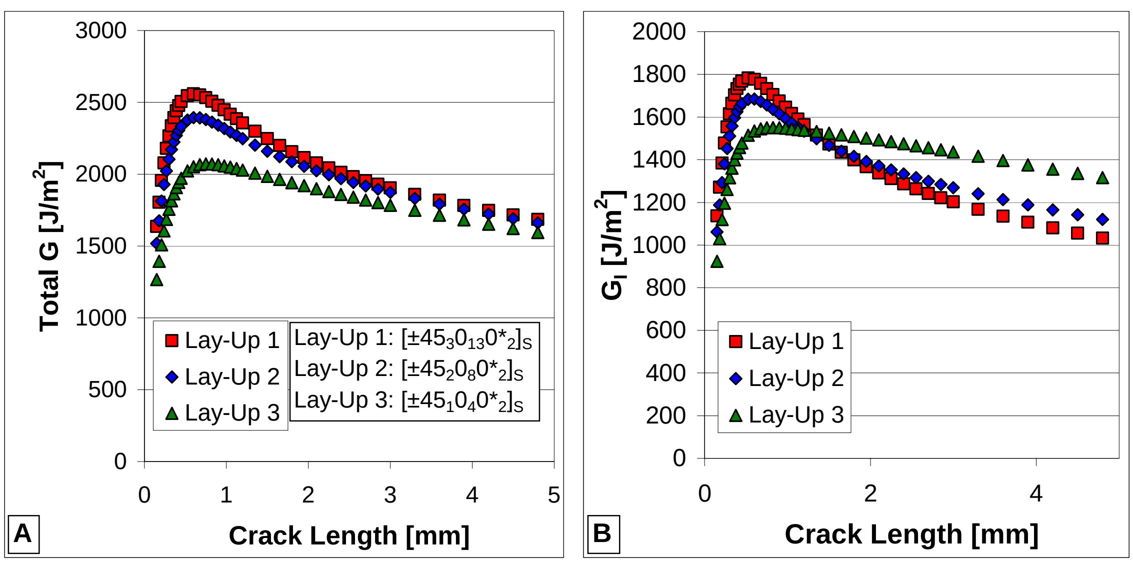

Figure 76: Central Ply Drop, Carbon, Compression, Lay-Up Comparison. A: Total G vs. Crack Length; B: G_I vs. Crack Length; Applied Stress = 548.5 MPa.

Figure 76B shows reasonable similarity between the G_I values, again illustrating the fact that G_I values tend to correlate at the same applied stress, as shown later in the internal ply drop section, specifically Figure 92A.

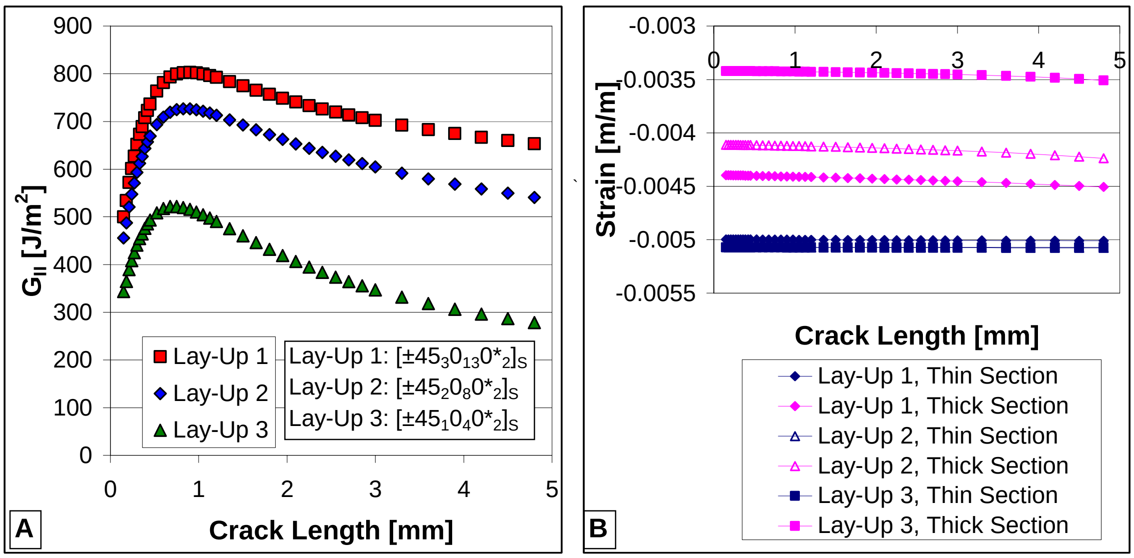

Figure 77: Central Ply Drop, Carbon, Compression, Lay-Up Comparison. A: G_{II} vs. Crack Length; B: Far Field Strain vs. Crack Length; Applied Stress = 548.5 MPa.

Figure 77A shows a wide variation between the different lay-ups when G_{II} is considered, at the same applied stress. This could be due to the different strain levels in the thick sections of the models, which can again be seen in Figure 77B.

To examine the hypothesis that the G_{II} values were driven by the strain or stress squared (Equation 15), all G values were modified by the ratio of the strain squared, given as Equation 16, where the average strain in the thick section of lay-up 1 was used as $\varepsilon_{ThickRef}$. G_2 is the adjusted value.

$$G_2 = G_1 \left(\frac{\varepsilon_{Thick}}{\varepsilon_{Thick\,Ref}} \right)^2 = G_1 \frac{(\sigma \cdot \varepsilon)_{Thick}}{(\sigma \cdot \varepsilon)_{Thick\,Ref}} \qquad (16)$$

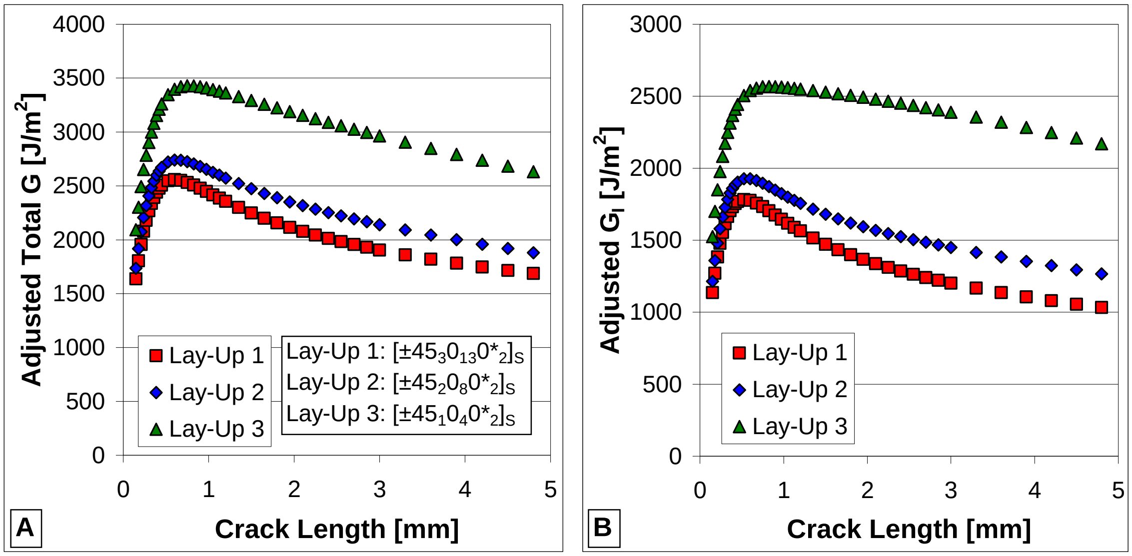

Figure 78: Central Ply Drop, Carbon, Compression, Adjusted Lay-Up Comparison. A: Adjusted Total G vs. Crack Length; B: Adjusted G_I vs. Crack Length.

Figure 78, both A and B, show a greater variation of total G and G_I among the three lay-ups, indicating that they are not driven by the thick side strain squared.

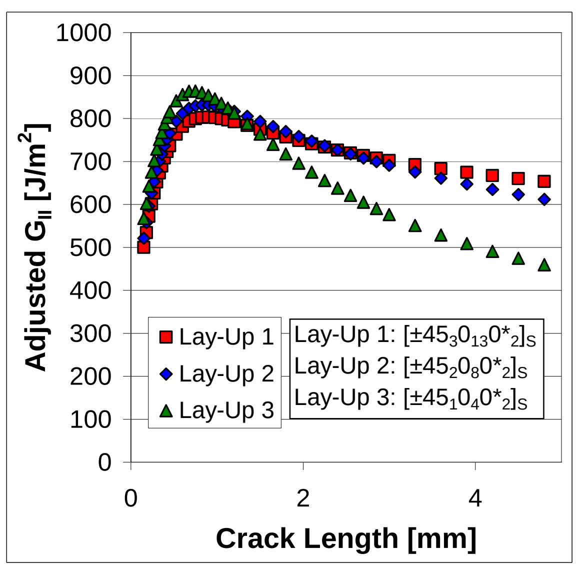

Figure 79: Central Ply Drop, Carbon, Compression, Adjusted Lay-Up Comparison, Adjusted G_{II} vs. Crack Length.

Figure 79 shows a much narrower distribution of the maximum G_{II} values, indicating that strain energy levels in the thick section, where the delamination is growing, correlate the maximum G_{II} values. G_{II} drops off more rapidly with crack growth in the thinner lay-up, consistent with Figure 73 and Figure 74.

Central Ply Drop, Carbon, Tension. Figure 80 and Table 22 are results from the central ply drop model with 1 ply dropped on each side, carbon 0's, loaded in tension. The lay-up is $[\pm45_3/0_{13}/0^*_1]_S$.

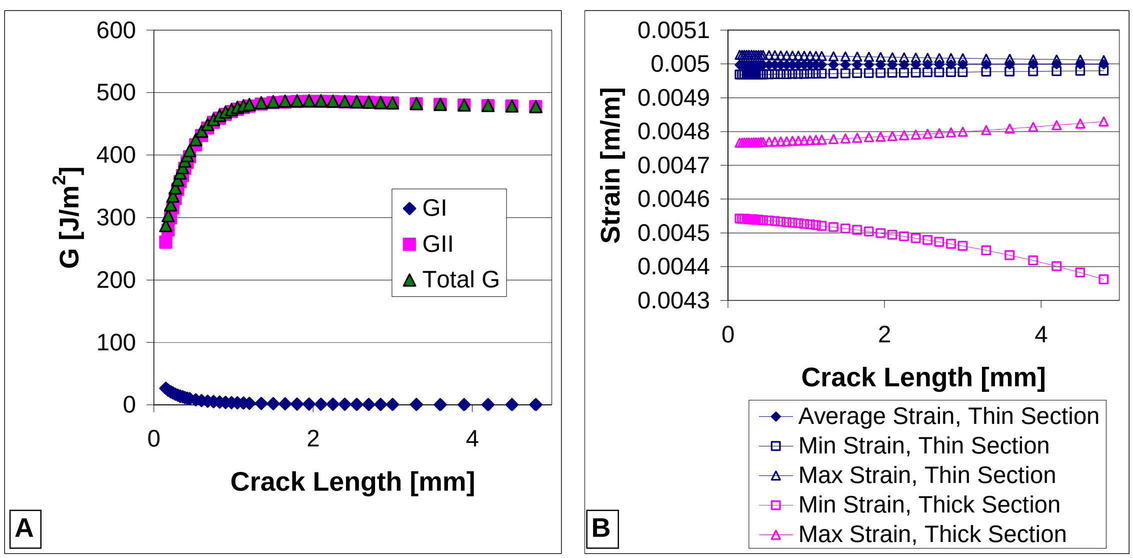

Figure 80: Central Ply Drop, 1 Ply Dropped Each Side, Carbon, Tension. A: G vs. Crack Length; B: Far Field Strain vs. Crack Length; Applied Stress = 548.5 MPa.

	Maximum [J/m²]	Crack Length at Maximum G [mm]	Average [J/m²] (0.15 – 3.0 mm)
Total G	487.0	1.95	464.4
G_I	26.6	0.15	3.8
G_{II}	485.8	2.1	460.6

Table 22: Central Ply Drop, 1 Ply Dropped Each Side, Carbon, Tension, Maximum and Average G.

Strength of materials modeling for this case, calculated using the estimated thick section strain of 0.00465 from Figure 80B, properties from Table 12 and Equation 14 give a result of 461 J/m^2. This value is in close agreement with the Table 22 value of 464 J/m^2 (for a crack between 0.15 and 3.0 mm long). Thus, the model in Equation 14 provides a good approximation for the total G at a ply drop, or to G_{II} if G_I is insignificant, as is the case here due to the tensile load.

Figure 81 and Table 23 are results from the central ply drop, with two plies dropped on each side, carbon 0’s, loaded in tension. The lay-up is $[\pm45_3/0_{13}/0^*_2]_S$. The average total G in this model is 1.66 times the one ply dropped on each side model. Equation 14 gives a result of 877 J/m^2 for an estimated thick side strain of 0.00438 (from Figure 81B). This is in close agreement with G values for longer cracks.

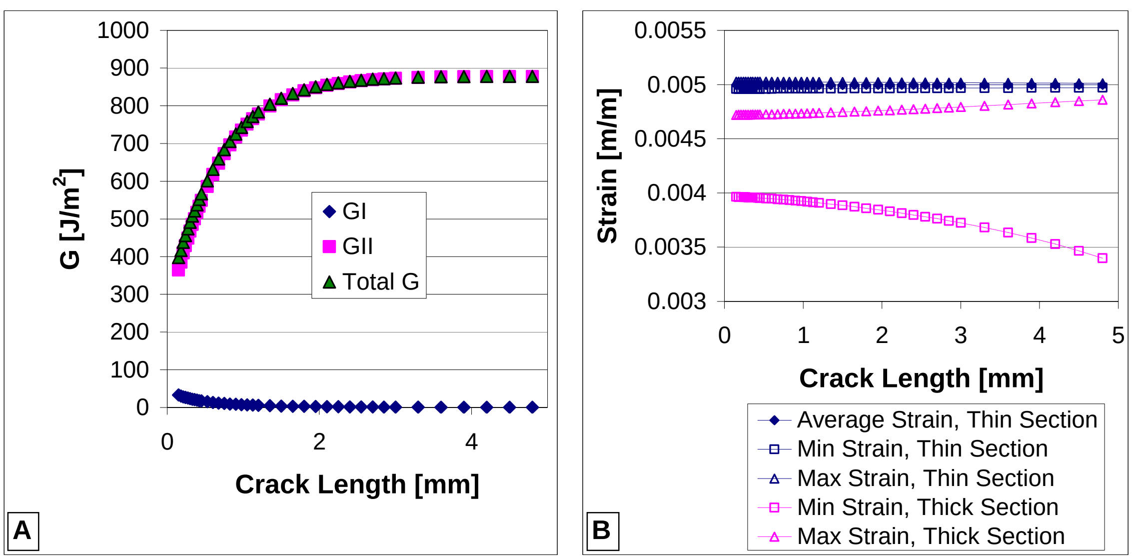

Figure 81: Central Ply Drop, 2 Plies Dropped Each Side, Carbon, Tension. A: G vs. Crack Length; B: Far Field Strain vs. Crack Length; Applied Stress = 548.5 MPa.

	Maximum [J/m^2]	Crack Length at Maximum G [mm]	Average [J/m^2] (0.15 – 3.0 mm)
Total G	878.0	4.5	769.5
G_I	33.2	0.15	6.8
G_{II}	877.5	4.5	762.7

Table 23: Central Ply Drop, 2 Plies Dropped Each Side, Carbon, Tension, Maximum and Average G.

Figure 82 and Table 24 are results from the doubled total thickness central ply drop model, with two plies dropped on each side, carbon 0's, loaded in tension. The lay-up is given as $[\pm45_3/0_{26}/0^*_2]_S$. The average total G in this model is 1.84 times the single ply drop model and 1.11 times two plies dropped model.

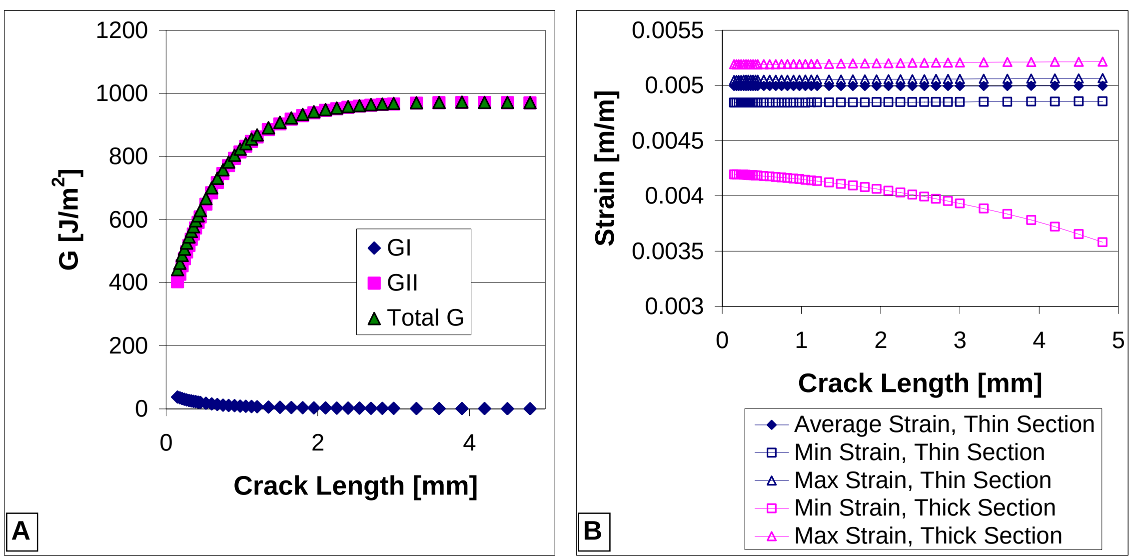

Figure 82: Central Ply Drop, Doubled Model, 2 Plies Dropped Each Side, Carbon, Tension. A: G vs. Crack Length; B: Far Field Strain vs. Crack Length; Applied Stress = 549.3 MPa.

	Maximum [J/m^2]	Crack Length at Maximum G [mm]	Average [J/m^2] (0.15 – 3.0 mm)
Total G	971.6	3.9	852.5
G_I	38.0	0.15	8.3
G_{II}	970.4	3.9	844.2

Table 24: Central Ply Drop, Doubled Model, 2 Plies Dropped Each Side, Carbon, Tension, Maximum and Average G.

With the tension models, the difference in the G levels are still driven more by the number of plies dropped than the number of continuous 0's, but the effect is less pronounced when compared to the compression models due to the absence of substantial G_I levels. G_{II} values of each of the tension models are slightly higher than the compression models, though comparable.

Internal Ply Drop

The internal ply drop model is based on a test coupon used in experiments. The ply drops are at the 1/3 points through the 0° stack, shown in Figure 83; the lay-up is $[\pm45_3/0_9/0^*_2/0_9/0^*_2/0_9/\pm45_3]$. There are three crack cases examined here: both cracks present, lower crack absent (suppressed), and upper crack absent (suppressed). In the case with both cracks present, the cracks are assumed to be the same length, although the results (different G values) suggest that this would not be the case. The models with one crack suppressed are intended to examine interaction effects. In the experiments, either both cracks were present or just the upper crack.

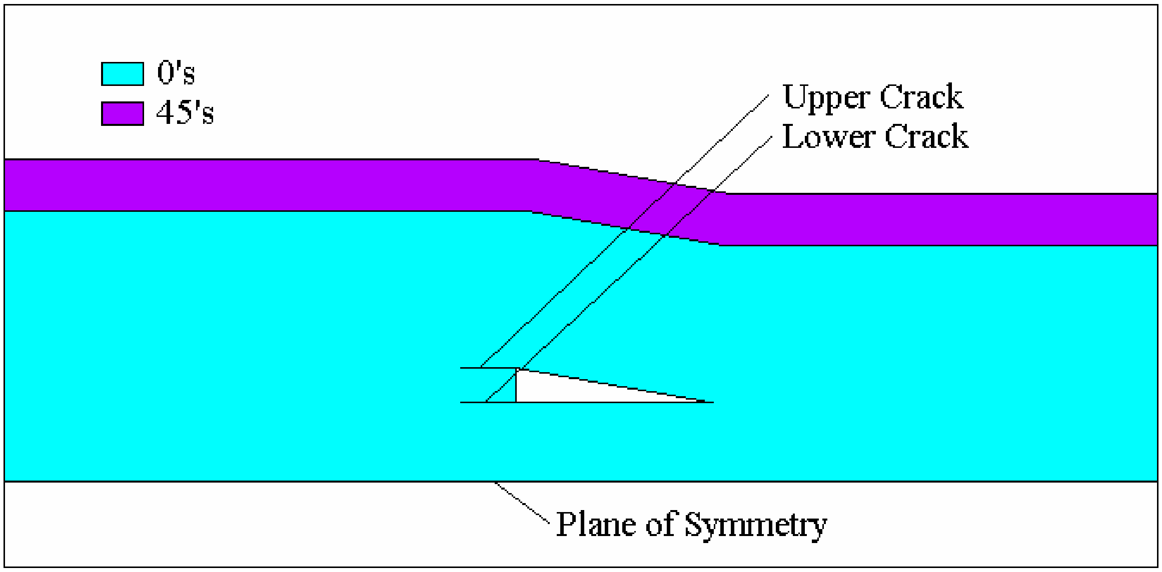

Figure 83: Internal Ply Drop, Crack Locations, [$\pm45_3/0_9/0^*_2/0_9/0^*_2/0_9/\pm45_3$].

Internal Ply Drop, Carbon, Compression. Figure 84 and Figure 85 and Table 25 are the results from the internal ply drop model, run with carbon 0's, loaded in compression, with both cracks present. The total average G_{II}, summed over the two cracks, is similar to twice the G_{II} for the central ply drop with a total of two plies dropped, Figure 73; the factor of two is used to total the G for both cracks in the central ply model. The average G_I for the upper crack is similar to G_I for the central drop. G_I is 52.9% of the total average G, while total G_{II} for both cracks exceeds G_I for long cracks. Like the central ply drop case, the G_I values here are very high; for the upper crack they are above the critical G_I (G_{IC}, from Table 13), indicating that a delamination developing in this type of ply drop under compression loading is driven by G_I. The high G_I values also indicate that critical G levels will be reached at loading levels lower than those used here to produce a strain in the thin section of the model of 0.5%, if cracks are present. The overall total G is 1687 J/m^2, while the doubled value for the central ply drop (Figure

73) is 2083 J/m^2, slightly higher. The differences in G values for the upper and lower cracks led to the consideration of similar ply drops with only one crack present, as was also observed in many experiments. The total G in Figure 84A drops at longer crack lengths, but is still well above the Equation 14 calculation of 880 J/m^2 for this case, with an estimated thick section strain of 0.0044 (Figure 84B).

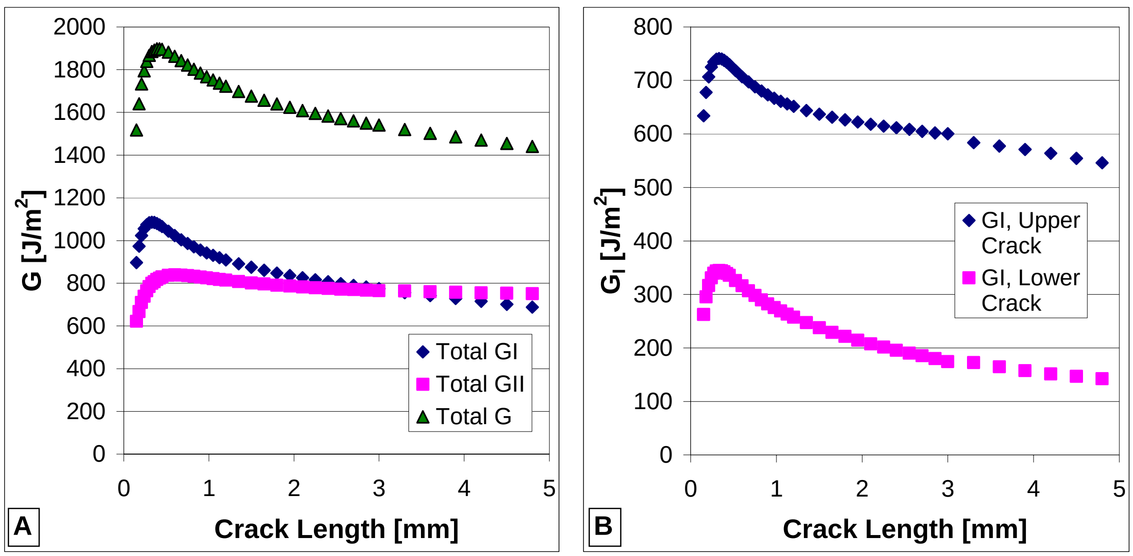

Figure 84: Internal Double Ply Drop, Carbon, Compression, Both Cracks. A: Total G vs. Crack Length; B: G_I vs. Crack Length; Applied Stress = 552.6 MPa.

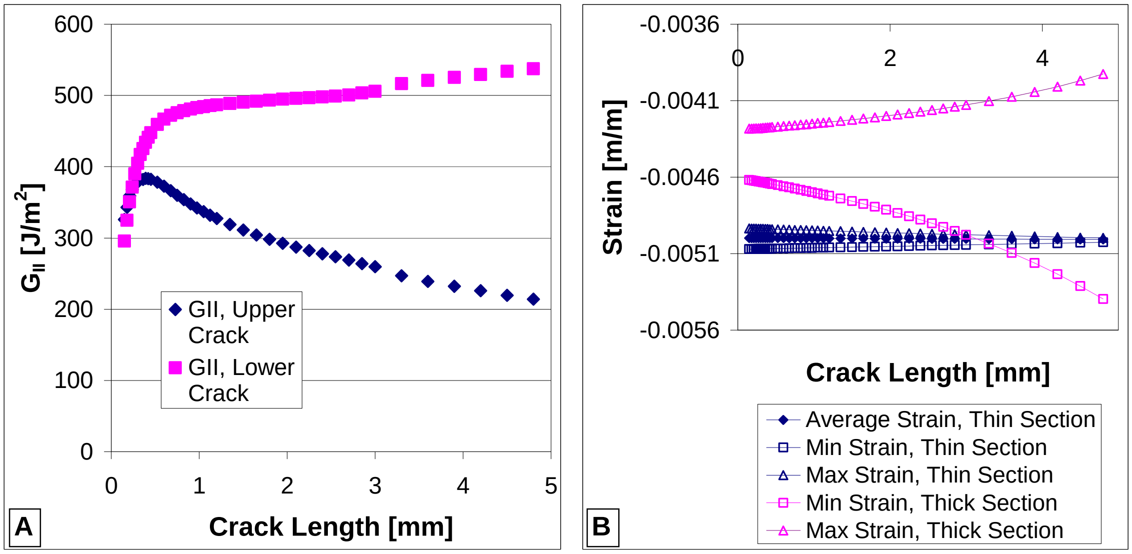

Figure 85: Internal Double Ply Drop, Carbon, Compression, Both Cracks. A: G_{II} vs. Crack Length; B: Far Field Strain vs. Crack Length; Applied Stress = 552.6 MPa.

	Maximum [J/m^2]	Crack Length at Maximum G [mm]	Average [J/m^2] (0.15 – 3.0 mm)
Total G	1897.2	0.39	1686.9
G_I, Upper Crack	740.8	0.33	647.8
G_I, Lower Crack	344.9	0.33	244.6
G_{II}, Upper Crack	383.6	0.39	315.0
G_{II}, Lower Crack	537.6	4.8	479.5

Table 25: Internal Double Ply Drop, Carbon, Compression, Both Cracks, Maximum and Average G.

Figure 86 and Table 26 are from the internal ply drop model, with carbon, loaded in compression, with the lower crack suppressed. This mode of failure is dominated by G_I, as are all internal ply drop models with carbon 0's, loaded in compression. The G_{II} drops to very low levels as the crack extends, as the single crack is unable to unload the strain energy from the dropped plies, as is assumed for the approximate model (Equation

14). The total G drops far below the Equation 14 calculation of 921 J/m^2 (using a thick side strain of 0.0044 from Figure 86B) at longer cracks.

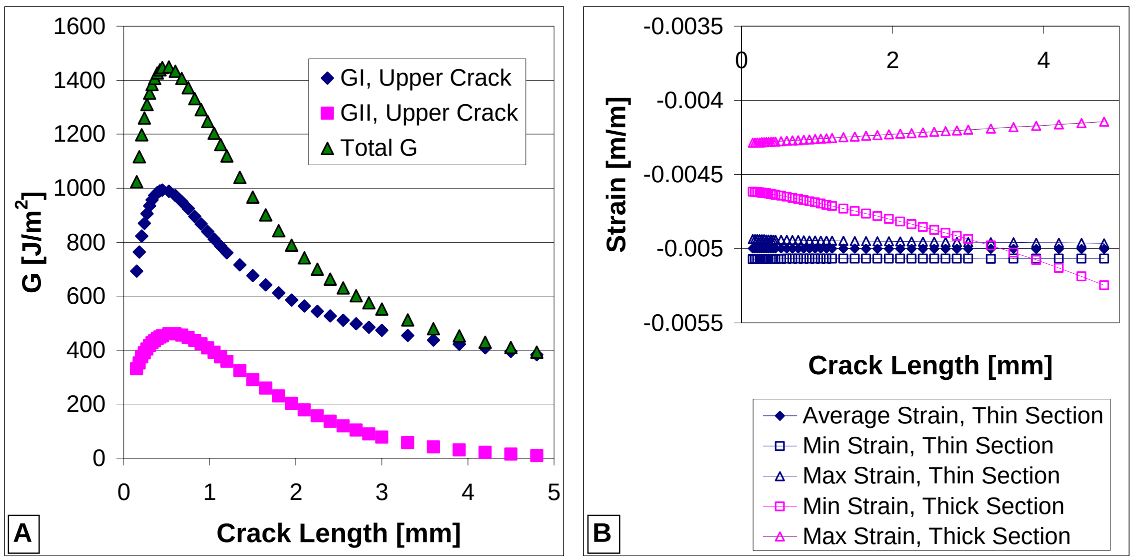

Figure 86: Internal Ply Drop, Carbon, Compression, Lower Crack Suppressed. A: G vs. Crack Length; B: Far Field Strain vs. Crack Length; Applied Stress = 552.6 MPa.

	Maximum [J/m^2]	Crack Length at Maximum G [mm]	Average [J/m^2] (0.15 – 3.0 mm)
Total G	1449.1	0.525	973.9
G_I, Upper Crack	993.3	0.45	697.0
G_{II}, Upper Crack	460.6	0.6	276.9

Table 26: Internal Ply Drop, Carbon, Compression, Lower Crack Suppressed, Maximum and Average G.

Figure 87 and Table 27 are results from the internal ply drop model, with carbon, in compression, with the upper crack suppressed. When G_I and G_{II} are compared to the critical values, G_I is above the G_{IC}, but less than for the lower crack suppressed; G_I still should dominate the failure, but crack growth should be favored in the upper crack position considering G_I values.

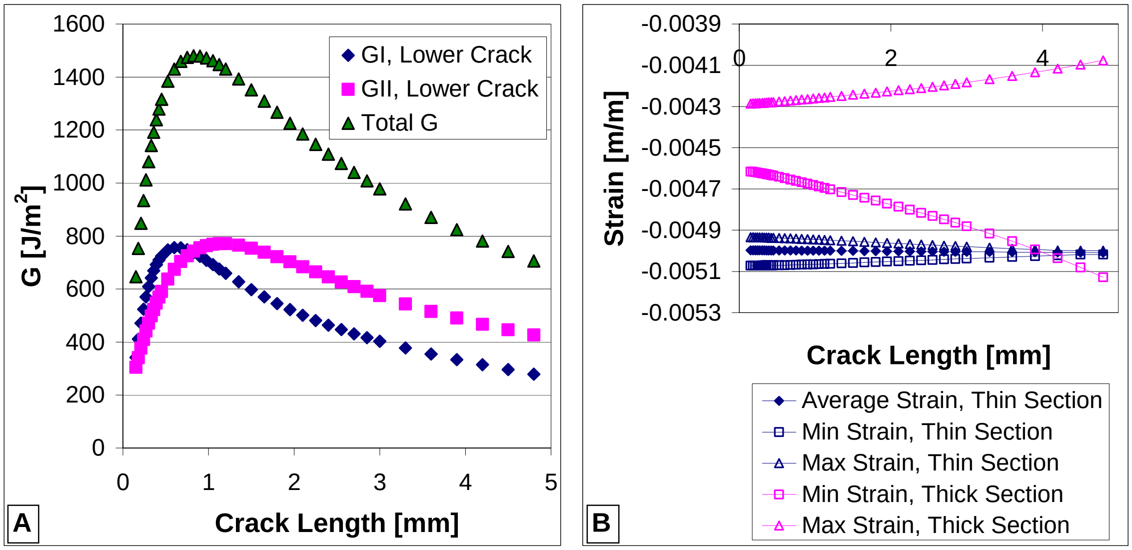

Figure 87: Internal Ply Drop, Carbon, Compression, Upper Crack Suppressed. A: G vs. Crack Length; B: Far Field Strain vs. Crack Length; Applied Stress = 552.6 MPa.

	Maximum [J/m^2]	Crack Length at Maximum G [mm]	Average [J/m^2] (0.15 – 3.0 mm)
Total G	1480.3	0.825	1244.0
G_I, Lower Crack	756.3	0.6	574.7
G_{II}, Lower Crack	771.4	1.125	669.3

Table 27: Internal Ply Drop, Carbon, Compression, Upper Crack Suppressed, Maximum and Average G.

The G levels for both cases with one of the cracks suppressed drop off as the cracks get longer; again supporting the conclusion that delamination of the plies is driven by the group of plies unloading. G values for the model with both cracks tend to level out at a higher value for longer cracks.

Internal Ply Drop, Carbon, Tension. Figure 88 and Figure 89, and Table 28, give results from the internal ply drop model, carbon, in tension, with both cracks present. As is common with tension loading, the G_I influence is minimal. The difference in the G values between the upper and lower crack indicates that the two cracks will not grow at the same rate. The lower crack will grow faster. The tension case was not included in experiments.

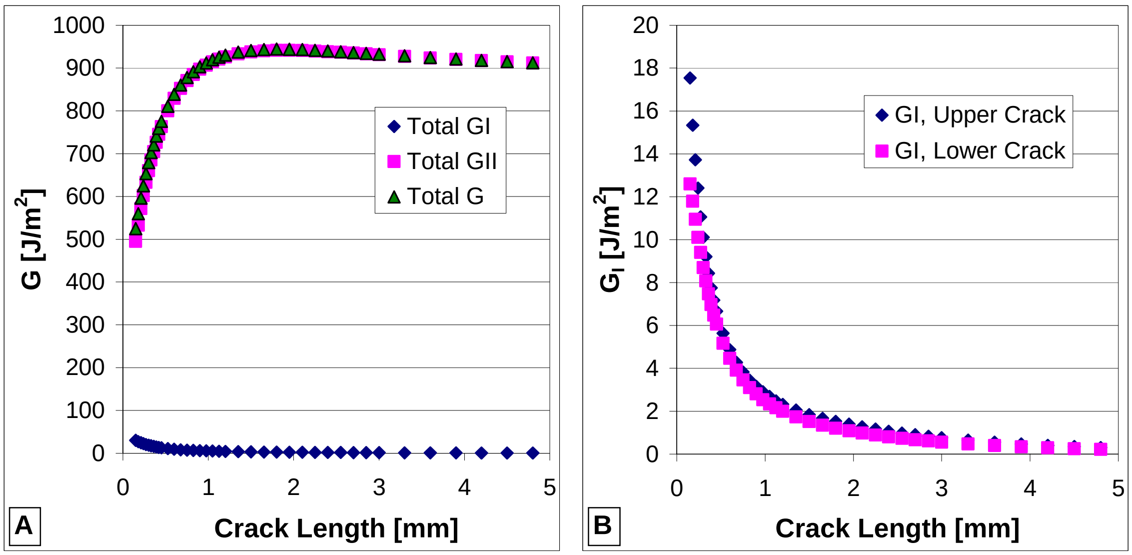

Figure 88: Internal Ply Drop, Carbon, Tension, Both Cracks. A: Total G vs. Crack Length; B: G_I vs. Crack Length; Applied Stress = 552.6 MPa.

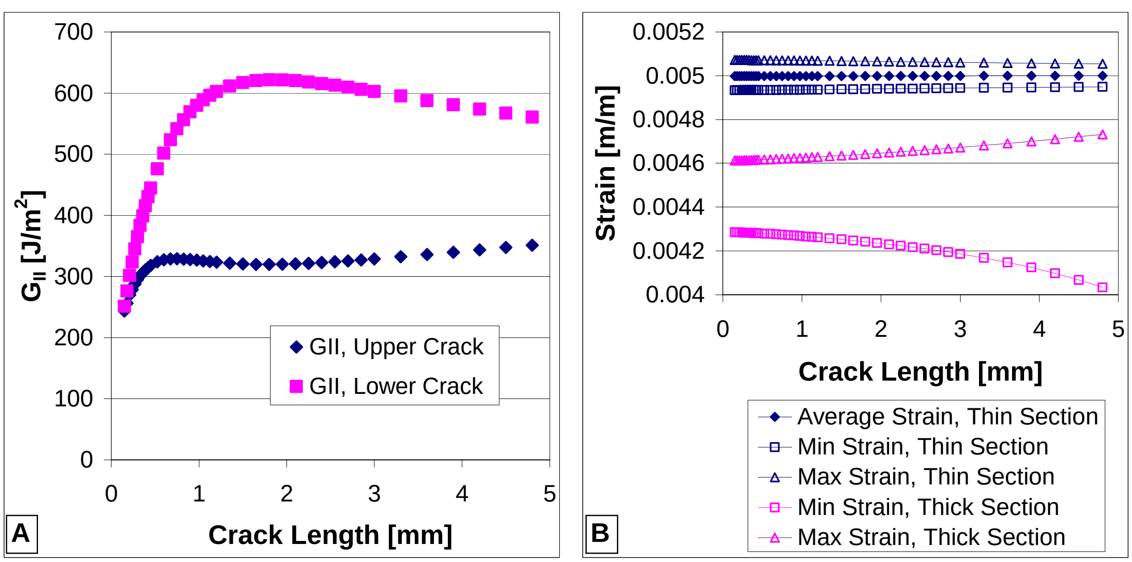

Figure 89: Internal Ply Drop, Carbon, Tension, Both Cracks. A: G_{II} vs. Crack Length; B: Far Field Strain vs. Crack Length; Applied Stress = 552.6 MPa.

	Maximum [J/m^2]	Crack Length at Maximum G [mm]	Average [J/m^2] (0.15 – 3.0 mm)
Total G	944.2	1.8	895.2
G_I, Upper Crack	17.5	0.15	3.0
G_I, Lower Crack	12.6	0.15	2.5
G_{II}, Upper Crack	351.3	4.8	320.1
G_{II}, Lower Crack	621.6	1.8	569.6

Table 28: Internal Ply Drop, Carbon, Tension, Both Cracks, Maximum and Average G.

The total G from Equation 14 is 1136 J/m^2 for a thin side strain of 0.005, slightly high in this case. The approximate strain at the delamination (thick side), from Figure 89B, is 0.0045, which would reduce the Equation 14 prediction to about 921 J/m^2. This is lower than, but on the order of, the average total G of 895.2 J/m^2 listed in Table 28. The Equation 14 calculation is closer to the FEA results under tensile loading, where G_I is very low. The FEA results for G_{II} are similar in magnitude for tension and compression and similar to the central two ply drop case.

Internal Ply Drop, Glass, Compression. Figure 90 and Figure 91, and Table 29, give results from the internal ply drop model, run with glass 0's, loaded in compression, with both cracks present. The overall G levels are much lower for glass than carbon as predicted by Equation 16 at the same strain levels. As with previous models loaded in compression compared to tension, there is a higher level of G_I influence compared to G_{II}. However, the percentage of G_I in the total G is lower in this model, with glass 0's, than with the model with carbon 0's (Figure 84 and Figure 85 and Table 25).

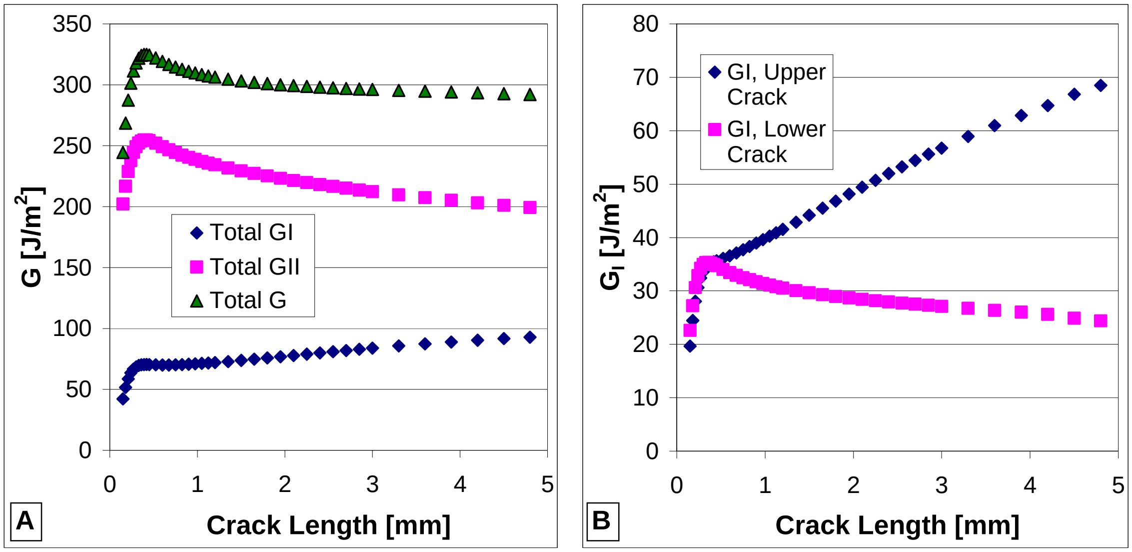

Figure 90: Internal Ply Drop, Glass, Compression, Both Cracks. A: Total G vs. Crack Length; B: G_I vs. Crack Length; Applied Stress = 156.9 MPa.

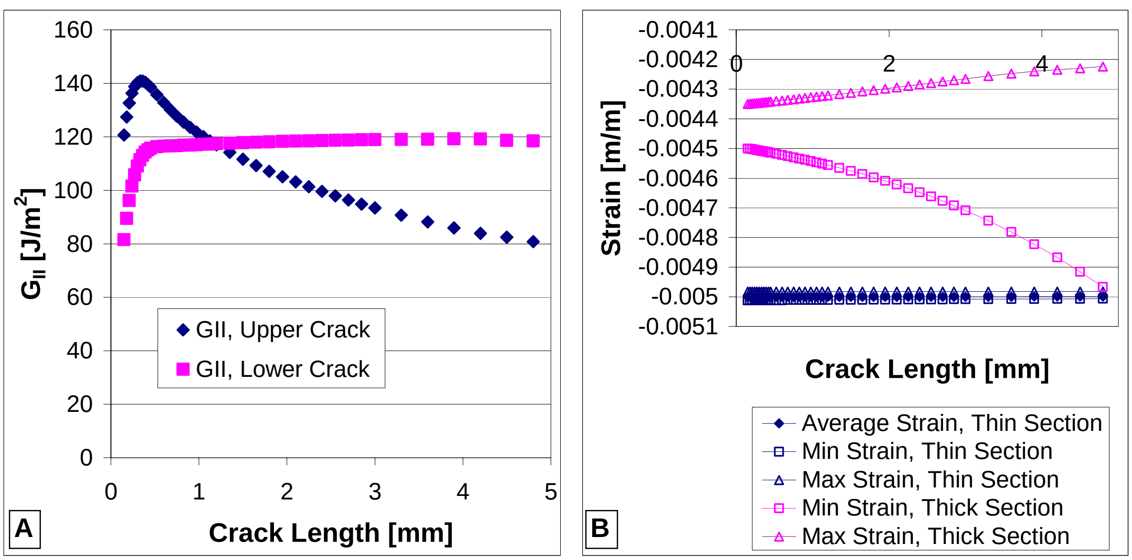

Figure 91: Internal Ply Drop, Glass, Compression, Both Cracks. A: G_{II} vs. Crack Length; B: Far Field Strain vs. Crack Length; Applied Stress = 156.9 MPa.

	Maximum [J/m^2]	Crack Length at Maximum G [mm]	Average [J/m^2] (0.15 – 3.0 mm)
Total G	325.1	0.42	304.3
G_I, Upper Crack	68.5	4.8	44.6
G_I, Lower Crack	35.3	0.36	30.0
G_{II}, Upper Crack	140.9	0.33	113.2
G_{II}, Lower Crack	119.2	3.9	116.5

Table 29: Internal Ply Drop, Glass, Compression, Both Cracks, Maximum and Average G.

Internal Ply Drop Correlations. Figure 92 compares the G value results of two carbon special case runs with the G values obtained for glass internal ply drop runs (at the normal thin-side strain of 0.5%). The glass data are the same as in Figure 90A. Figure 92A compares G_I values where the carbon data for this run were calculated with the model being loaded at the same applied stress as the glass model. The similar range of the G_I values indicates that G_I is driven, for the most part, by load. The total maximum G_I for carbon at the same strain (0.5%) as the glass would be over 1000 J/m^2, an order of magnitude higher than in Figure 92A.

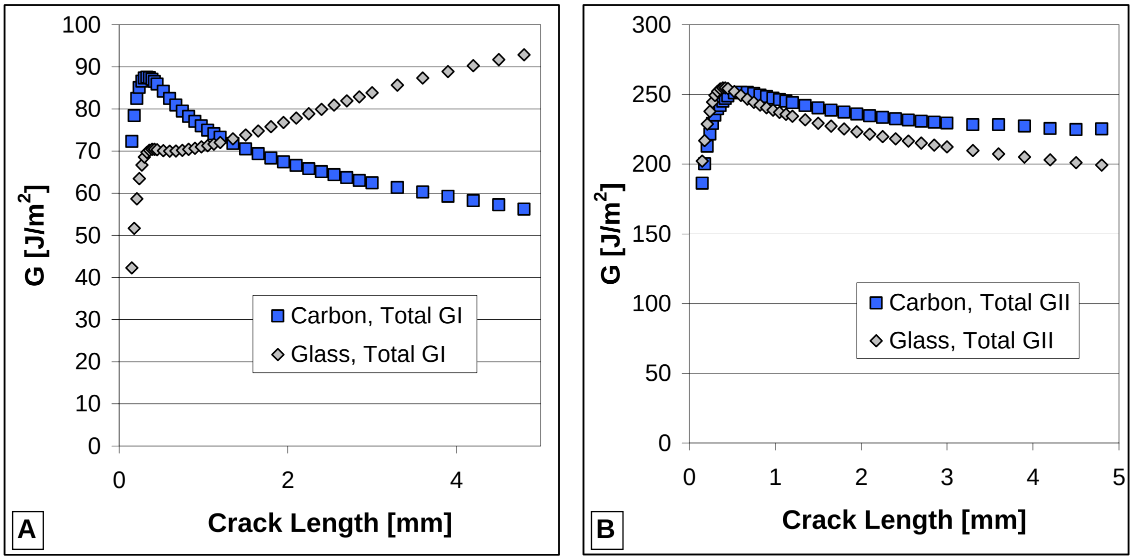

Figure 92: Internal Ply Drop, Compression, Both Cracks. A: Carbon and Glass at the Same Load (156.9 MPa); B: Carbon: Root of the Modulus Ratio Load (Equation 17), Glass: Regular Load, G_{II} vs. Crack Length.

Figure 92B compares G_{II} values. In this case, however, the stress on the thin section of the carbon model (σ_{Car}) is calculated using Equation 17, where σ_{Gla} is the stress in the glass model at 0.5% strain. The same total G will be obtained for materials with different E_L values (at the same dropped ply thickness) if Equation 17 is satisfied.

$$\sigma_{Car} = \sqrt{\frac{E_{LCar}}{E_{LGla}}} \cdot \sigma_{Gla} \tag{17}$$

The close agreement of these two data sets reinforces the conclusion that G_{II} values are driven by the strain energy per unit thickness, $\dfrac{\sigma \cdot \varepsilon \cdot t_p \cdot \Delta\ell}{2}$, in the dropped plies (where $\Delta\ell$ is crack length), given in Equation 14.

Associated Experimental Results. Figure 93 gives results from the associated experimental study and shows results for static and fatigue tests on internal ply drops with carbon and glass 0's [17]. By interpolation, carbon samples will form delamination cracks after on the order of 10 cycles at a maximum compressive strain of 0.5%. This reflects the results of the FEA work, where 0.5% strains resulted in G_I levels above the G_{IC}. Ten cycles may be enough for a crack to initiate and grow to a critical length.

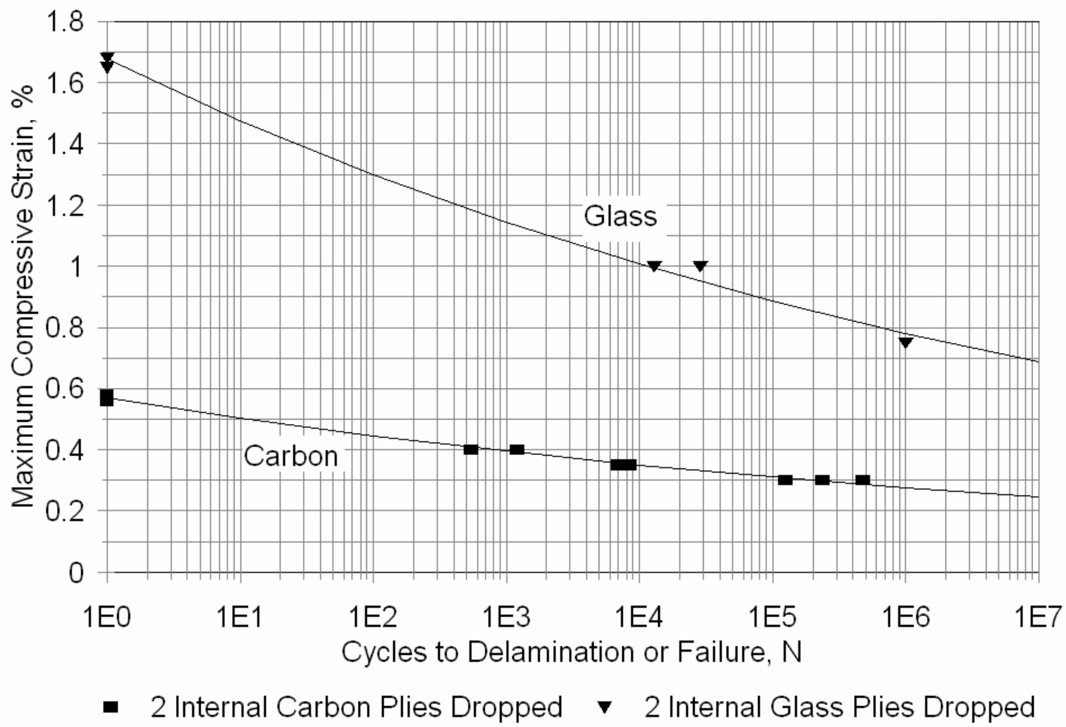

Figure 93: Experimental Results for the Maximum Compressive Strain vs. Cycles to Failure for an Internal Ply Drop with Carbon or Glass 0's $[\pm45_3/0_9/0^*_2/0_9/0^*_2/0_9/\pm45_3]$ R = 10 [17].

For a strain of 0.5%, glass FEA G_I and G_{II} values are both well below critical levels. Experimental results reflect this; at strain levels of 0.75%, a specimen delaminated after approximately 1,000,000 cycles. It is possible that delamination cracks will never develop for glass at strain levels of 0.5%.

External Ply Drop

Like the internal ply drop model, the external ply drop model (Figure 94) also corresponds to a physical test specimen on which a series of fatigue tests were performed. This model has the ply drops on the outermost 0's, as [$\pm 45_3/0^*_2/0_{27}/0^*_2/\pm 45_3$], so that only the ±45 top sheets are mis-oriented. Thus, all of the fibers in the 0 plies are oriented along the longitudinal axis; there is no section of mis-oriented 0 fibers. From a mis-orientation point of view, this is the best geometry. However, if the ±45's fail, there is little to resist delamination, requiring only a single crack to unload the dropped plies.

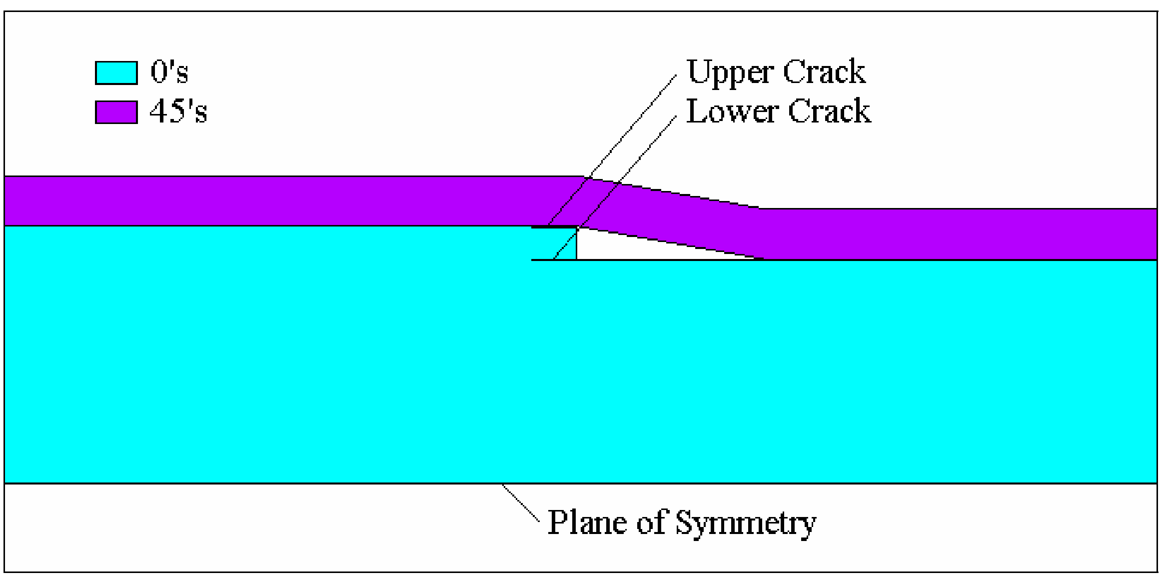

Figure 94: External Ply Drop, Crack Locations, [$\pm 45_3/0^*_2/0_{27}/0^*_2/\pm 45_3$].

This model is run with both carbon and glass 0's, and in both tension and in compression. Cracks are started at the end of the ply drop and grown along the dropped plies. This is from right to left in Figure 94. Three different crack configurations are used: both cracks, upper crack suppressed, and lower crack suppressed. When both cracks are grown together, the cracks are always assumed to be equal length. The two configurations where a crack is suppressed, either upper or lower, are examined to better understand the behavior of a crack without the interaction of the other crack. In experiments, all specimens of various materials and thicknesses failed by a single crack in the lower position, with no upper crack observed [36].

<u>External Ply Drop, Carbon, Compression</u>. Figure 95 and Figure 96, and Table 30, summarize FEA results for the external ply drop model with carbon 0's, loaded in compression, with both the upper and lower cracks in the model. A characteristic of note of these results is the significant G_I values on the upper crack (but much lower than the previous two geometries), and the high G_{II} on the lower crack.

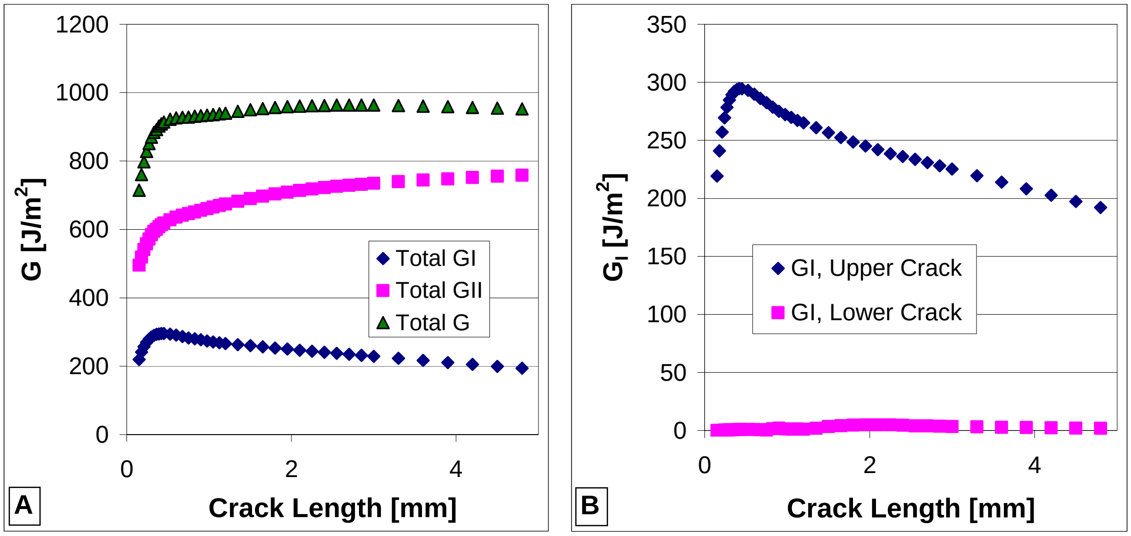

Figure 95: External Ply Drop, Carbon, Compression, Both Cracks. A: Total G vs. Crack Length; B: G_I vs. Crack Length; Applied Stress = 553.9 MPa.

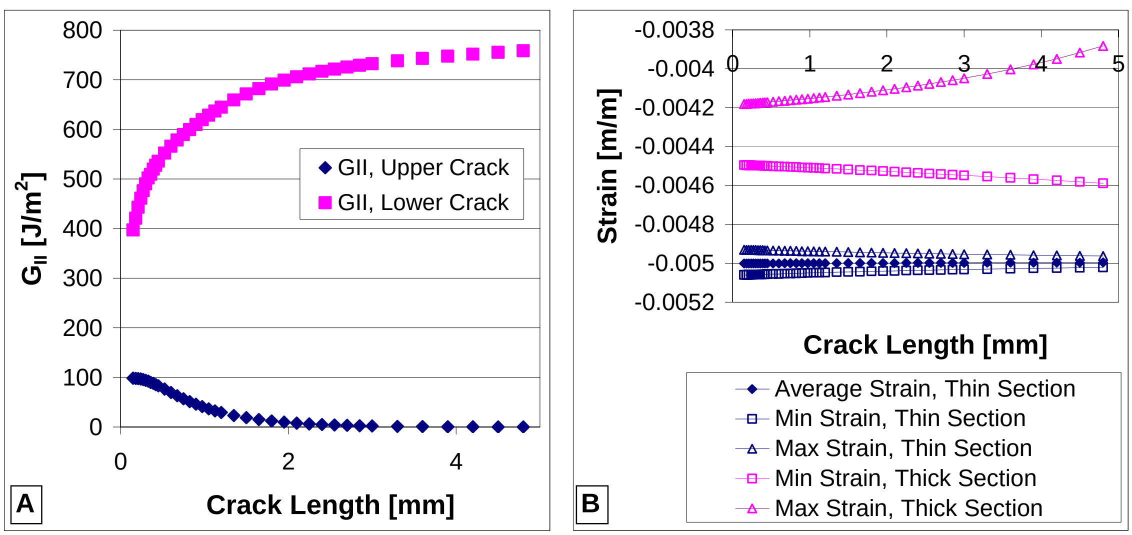

Figure 96: External Ply Drop, Carbon, Compression, Both Cracks. A: G_{II} vs. Crack Length; B: Far Field Strain vs. Crack Length; Applied Stress = 553.9 MPa.

	Maximum [J/m^2]	Crack Length at Maximum G [mm]	Average [J/m^2] (0.15 – 3.0 mm)
Total G	963.7	2.7	939.2
G_I, Upper Crack	294.7	0.42	256.1
G_I, Lower Crack	4.8	1.95	2.8
G_{II}, Upper Crack	98.3	0.15	30.2
G_{II}, Lower Crack	758.4	4.8	650.2

Table 30: External Ply Drop, Carbon, Compression, Both Cracks, Maximum and Average G.

Figure 97 and Table 31 summarize the results for the external ply drop model, with carbon 0's, loaded in compression, and with the lower crack suppressed. Thus, just the upper crack is present in this model. An interesting characteristic of these results is again the moderate G_I values at short crack lengths. This may be due to the ±45 outer plies. This would imply a tendency for upper cracks to initiate, which has not been seen in experimental results shown earlier (Figure 2). It was theorized that the ±45 outer plies may become more compliant under fatigue loading, and this would explain why no upper cracks have been seen in coupons. Therefore, another run was done with modified properties in the ±45 plies.

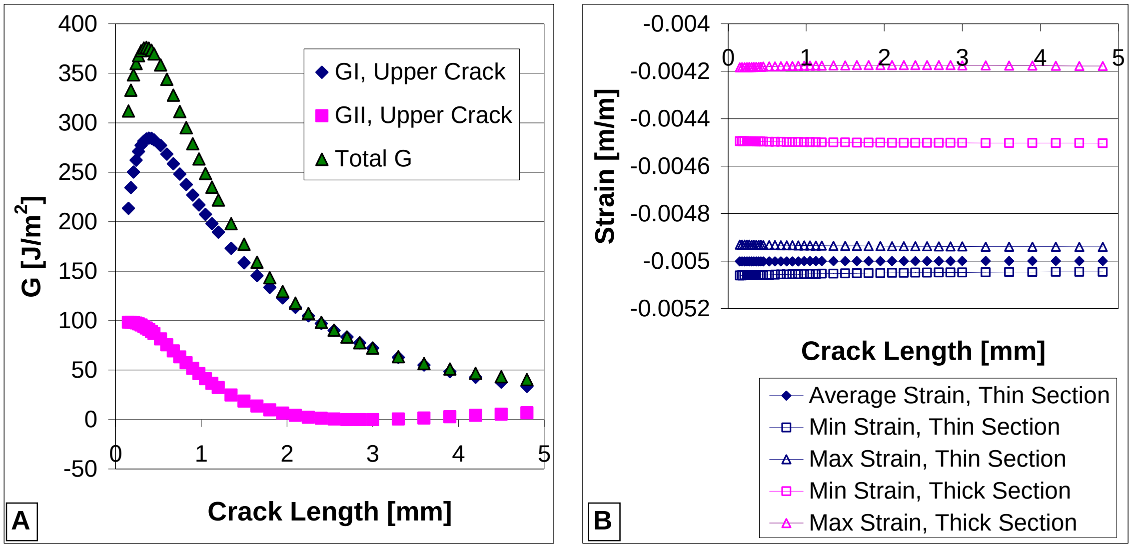

Figure 97: External Ply Drop, Carbon, Compression, Lower Crack Suppressed. A: G vs. Crack Length; B: Far Field Strain vs. Crack Length; Applied Stress = 553.9 MPa.

	Maximum [J/m^2]	Crack Length at Maximum G [mm]	Average [J/m^2] (0.15 – 3.0 mm)
Total G	376.2	0.36	196.5
G_I, Upper Crack	284.4	0.39	166.0
G_{II}, Upper Crack	98.5	0.15	30.4

Table 31: External Ply Drop, Carbon, Compression, Lower Crack Suppressed, Maximum and Average G.

The properties of the 45's were adjusted in such a way to represent damage to the matrix, while maintaining fiber integrity. The stiffness of the matrix dominated elastic constants was reduced to 20% of their original level. That was done by finding 20% of the shear modulus and out of plane modulus for the properties of the 0/90 lay-up, and then performing a coordinate system rotation.

Figure 98 and Table 32 give results of the modified external ply drop run, with softened ±45 plies. The G_I and total G values are significantly lower. With the softened

±45 plies, the maximum G_I is over 3 times lower than the results for un-softened model. This reduces the likelihood of initiation of the upper delamination crack significantly.

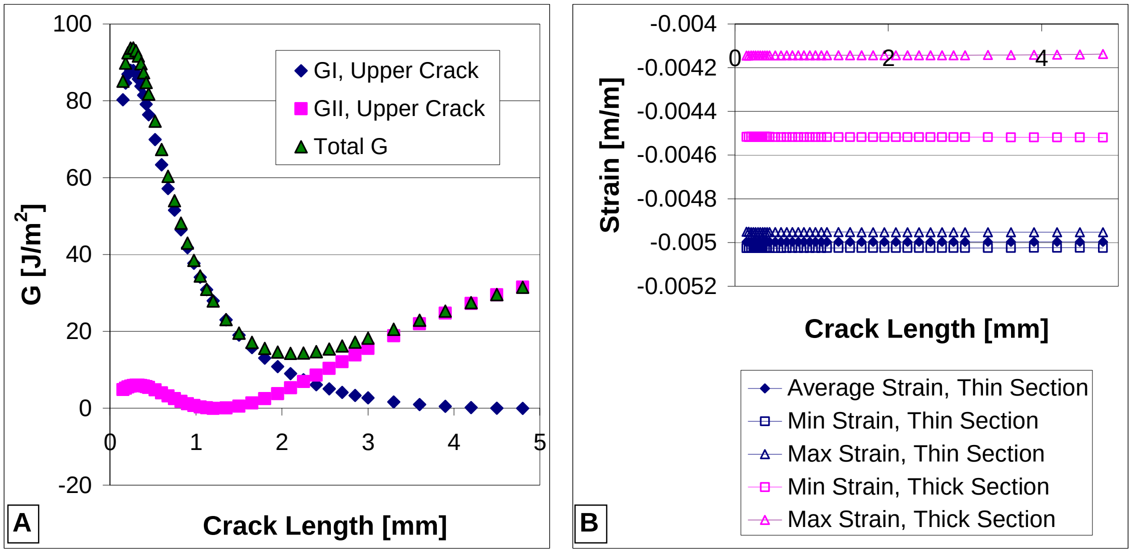

Figure 98: External Ply Drop, Softened 45's, Carbon, Compression, Lower Crack Suppressed. A: G vs. Crack Length; B: Far Field Strain vs. Crack Length; Applied Stress = 553.9 MPa.

	Maximum [J/m²]	Crack Length at Maximum G [mm]	Average [J/m²] (0.15 – 3.0 mm)
Total G	93.8	0.27	33.6
G_I, Upper Crack	87.9	0.24	28.6
G_{II}, Upper Crack	31.5	4.8	5.0

Table 32: External Ply Drop, Softened 45's, Carbon, Compression, Lower Crack Suppressed, Maximum and Average G.

Figure 99 and Table 33 summarize results for the external ply drop model run with carbon, in compression, with the upper crack suppressed. This crack configuration, with only the lower crack growing, is a common result seen experimentally. Crack growth is G_{II} dominated in this case, with only a small amount of G_I influence. The G_{II}

level is about twice the total G_{II} for the central and internal ply drops (Figure 73A and Figure 85A) which have two cracks and also two plies dropped, at a strain of 0.5%.

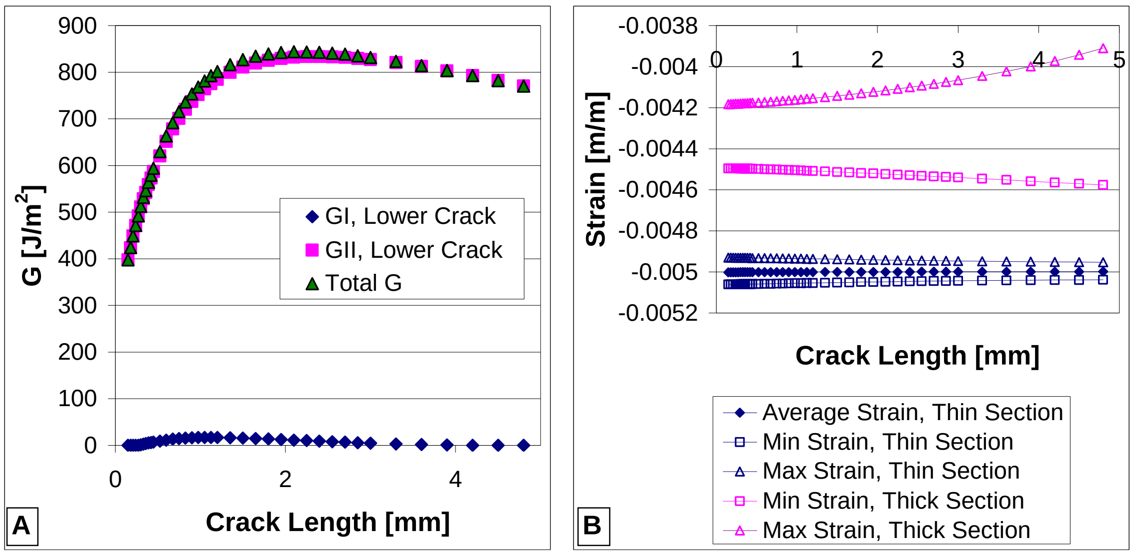

Figure 99: External Ply Drop, Carbon, Compression, Upper Crack Suppressed. A: G vs. Crack Length; B: Far Field Strain vs. Crack Length; Applied Stress = 553.9 MPa.

	Maximum [J/m^2]	Crack Length at Maximum G [mm]	Average [J/m^2] (0.15 – 3.0 mm)
Total G	843.7	2.1	771.0
G_I, Lower Crack	17.1	1.125	11.1
G_{II}, Lower Crack	833.6	2.4	759.9

Table 33: External Ply Drop, Carbon, Compression, Upper Crack Suppressed, Maximum and Average G.

Because the case with softened ±45 plies was examined in the external ply drop model with the lower crack suppressed, this was also done with the upper crack suppressed, with results in Figure 100 and Table 34. Results here further reinforce the results from Figure 98 and Table 32, indicating the likelihood of only the lower crack developing. These results show slightly higher G_{II} values. The ±45's prevent the dropped plies from being completely unloaded due to the lower crack alone.

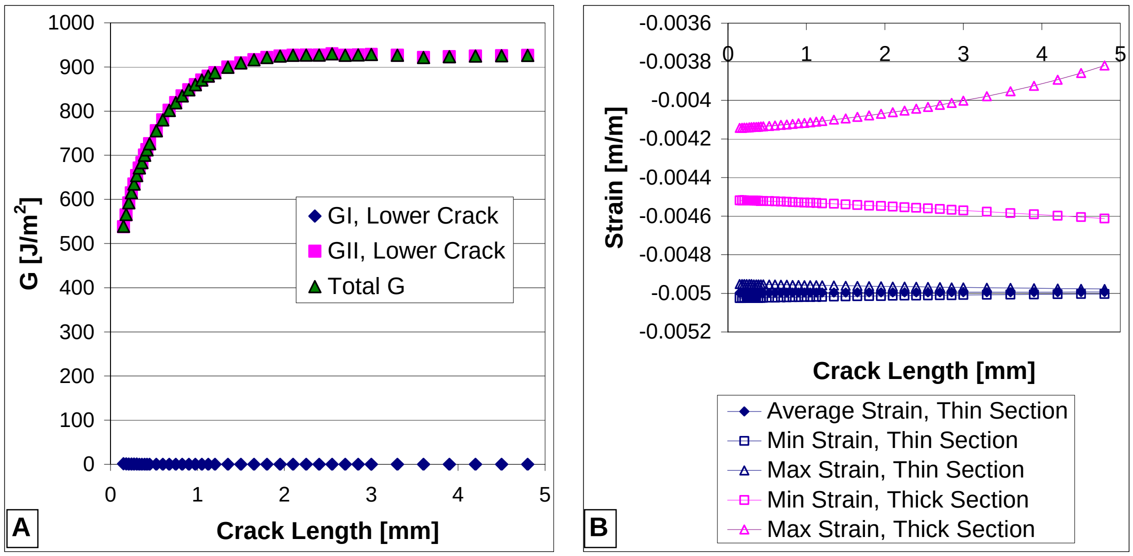

Figure 100: External Ply Drop, Softened 45's, Carbon, Compression, Upper Crack Suppressed. A: G vs. Crack Length; B: Far Field Strain vs. Crack Length; Applied Stress = 553.9 MPa.

	Maximum [J/m^2]	Crack Length at Maximum G [mm]	Average [J/m^2] (0.15 – 3.0 mm)
Total G	929.0	2.55	866.4
G_I, Lower Crack	1.3	0.15	0.1
G_{II}, Lower Crack	929.7	2.55	866.4

Table 34: External Ply Drop, Softened 45's, Carbon, Compression, Upper Crack Suppressed, Maximum and Average G.

Associated Experimental Results. Figure 101 gives results from the associated experimental study for external ply drops with carbon 0's, with two external plies dropped [17]. At 0.5% strain, delamination cracks will grow rather quickly once initiated, on the order of 100 cycles. This agrees with the high G_{II} levels found with the FE model.

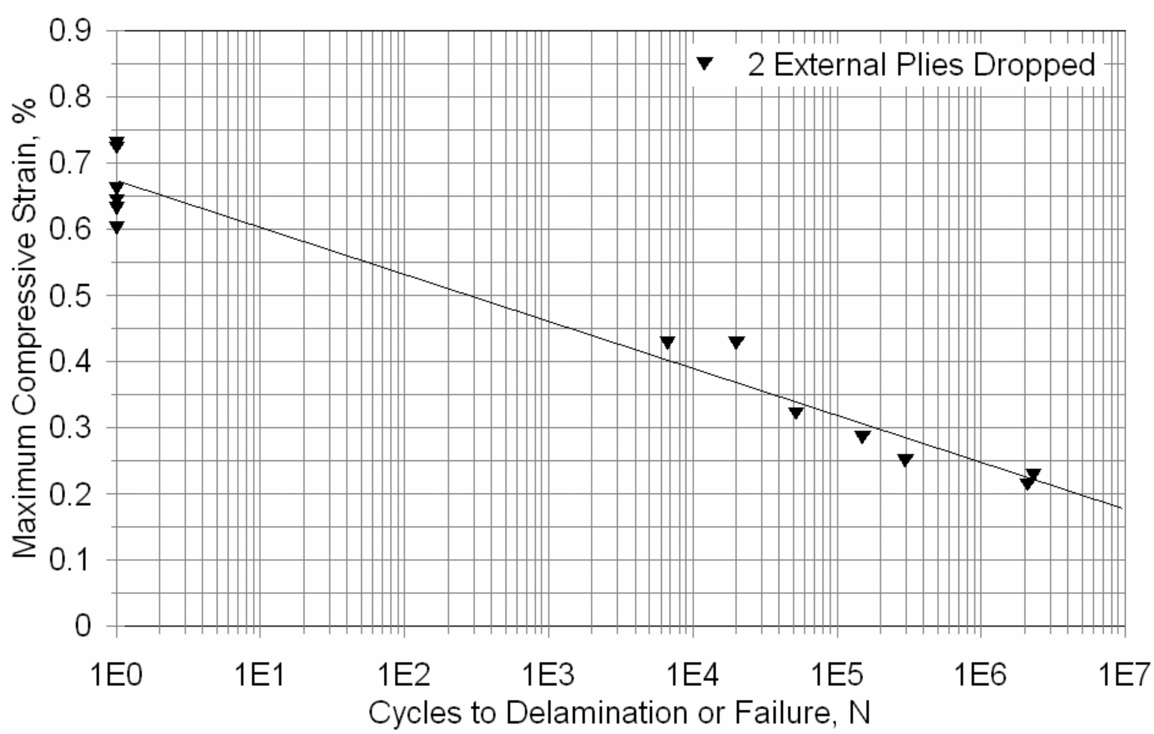

Figure 101: Experimental Results for the Maximum Compressive Strain vs. Cycles to Failure for an External Ply Drop, 2 Plies Dropped, with Carbon 0's $[\pm45_3/0^*_2/0_{27}/0^*_2/\pm45_3]$, R = 10 [17].

External Ply Drop, Carbon, Tension. Figure 102 and Figure 103 and Table 35 are results from the external ply drop model, run with carbon, in tension, with both cracks present. High G_{II} values present in the lower crack indicate a propensity for delamination to develop there. Further results below reinforce this conclusion.

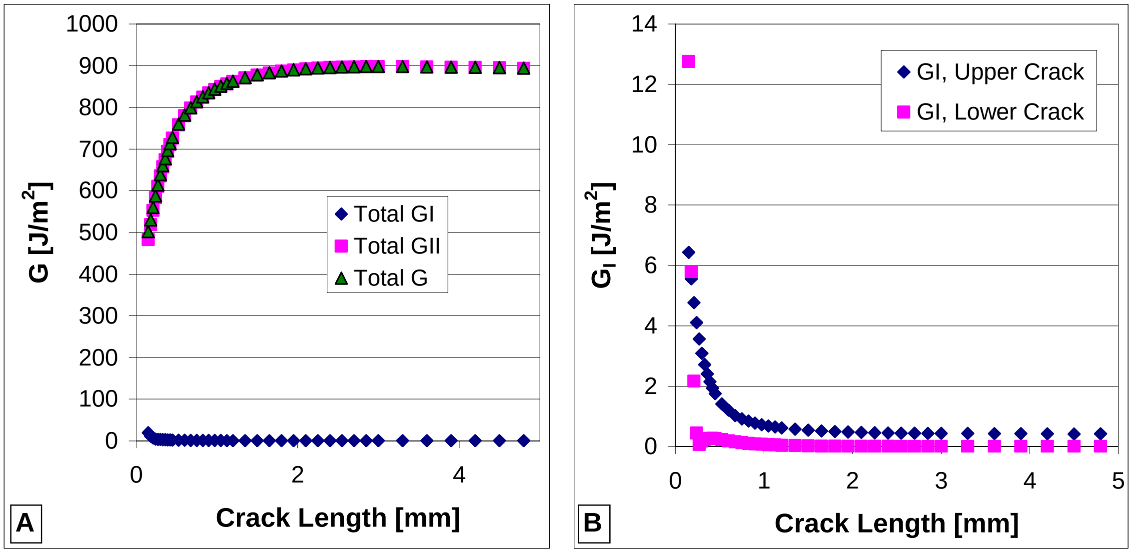

Figure 102: External Ply Drop, Carbon, Tension, Both Cracks. A: Total G vs. Crack Length; B: G_I vs. Crack Length; Applied Stress = 553.9 MPa.

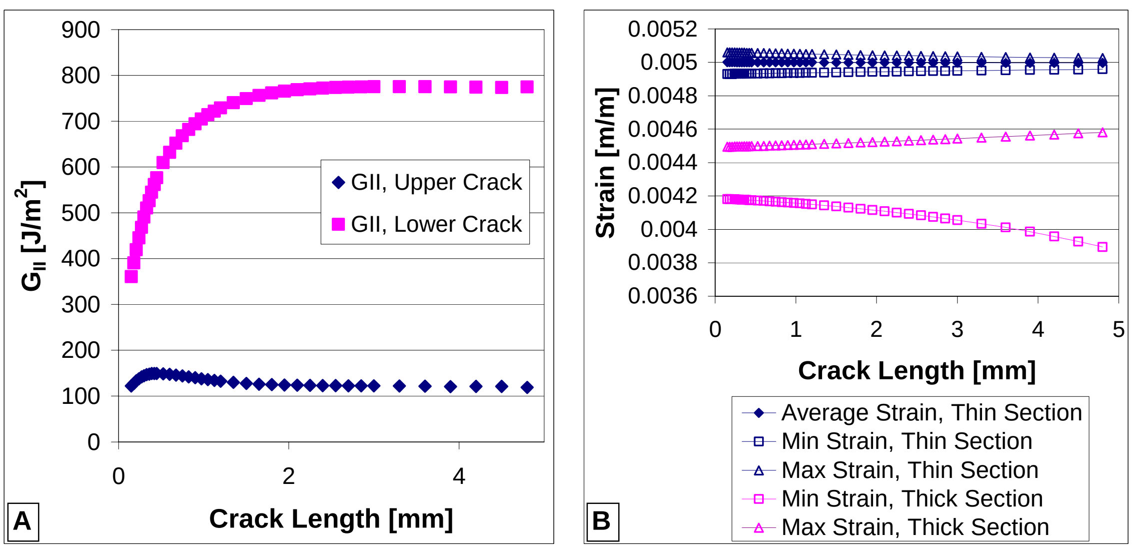

Figure 103: External Ply Drop, Carbon, Tension, Both Cracks. A: G_{II} vs. Crack Length; B: Far Field Strain vs. Crack Length; Applied Stress = 553.9 MPa.

	Maximum [J/m^2]	Crack Length at Maximum G [mm]	Average [J/m^2] (0.15 – 3.0 mm)
Total G	898.0	3.0	842.3
G_I, Upper Crack	6.4	0.15	0.9
G_I, Lower Crack	12.8	0.15	0.2
G_{II}, Upper Crack	149.3	0.45	131.0
G_{II}, Lower Crack	775.4	3.3	710.1

Table 35: External Ply Drop, Carbon, Tension, Both Cracks. Maximum and Average G.

Lower G values in the external ply drop model, with carbon, in tension, with the lower crack suppressed (Figure 104 and Table 36), indicate that this is not a likely way cracks will develop. A more likely manner is the crack growing in the manner modeled below, in Figure 105 and Table 37.

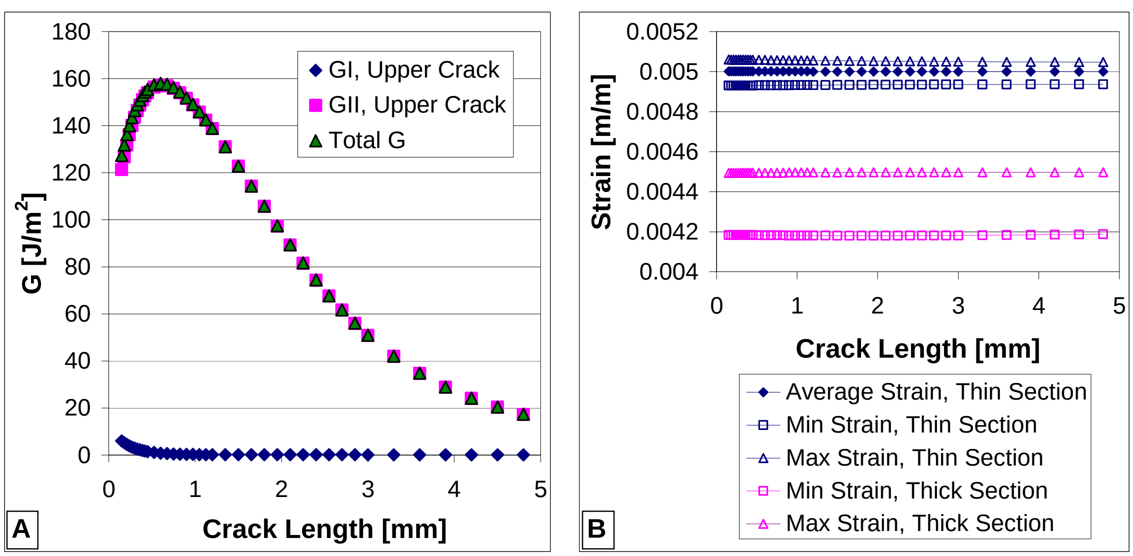

Figure 104: External Ply Drop, Carbon, Tension, Lower Crack Suppressed. A: G vs. Crack Length; B: Far Field Strain vs. Crack Length; Applied Stress = 553.9 MPa.

	Maximum [J/m^2]	Crack Length at Maximum G [mm]	Average [J/m^2] (0.15 – 3.0 mm)
Total G	158.1	0.6	113.0
G_I, Upper Crack	6.0	0.15	0.6
G_{II}, Upper Crack	157.3	0.6	112.5

Table 36: External Ply Drop, Carbon, Tension, Lower Crack Suppressed, Maximum and Average G.

Figure 105 and Table 37 are results from the external ply drop model, run with carbon 0's, in tension, and with the upper crack suppressed. Compared with the results above, with the lower crack suppressed, this model indicates that it is much more likely for a lower crack to grow.

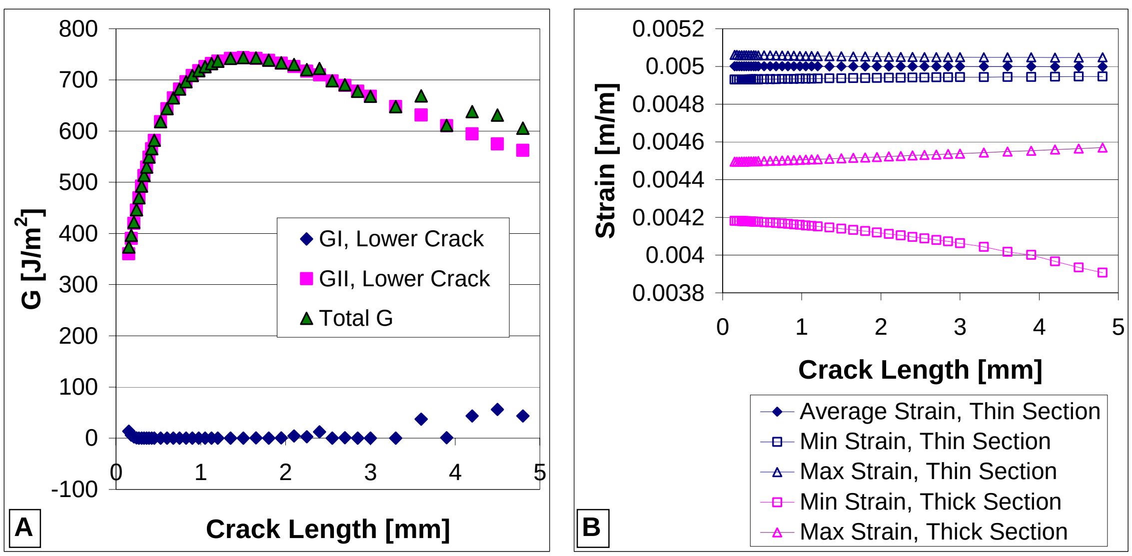

Figure 105: External Ply Drop, Carbon, Tension, Upper Crack Suppressed. A: G vs. Crack Length; B: Far Field Strain vs. Crack Length; Applied Stress = 553.9 MPa.

	Maximum [J/m^2]	Crack Length at Maximum G [mm]	Average [J/m^2] (0.15 – 3.0 mm)
Total G	743.7	1.5	686.2
G_I, Lower Crack	56.3	4.5	1.4
G_{II}, Lower Crack	743.5	1.5	684.8

Table 37: External Ply Drop, Carbon, Tension, Upper Crack Suppressed, Maximum and Average G.

Application of Equation 14 for a thick side strain of 0.00435 yields a prediction for the total G of 860 J/m^2, again ignoring the ±45's. This is higher than the FEA results in Figure 105, probably due to the incomplete unloading of the dropped plies when only one crack is present. The Equation 14 result is a better approximation for Figure 102A with both cracks in tension, and is close to the compression case in Figure 95A, with both cracks present.

External Ply Drop, Glass, Compression. Figure 106 and Figure 107, and Table 38, are results from the external ply drop model, with glass 0's, loaded in compression, and with both cracks present. This model shows similar behavior to the corresponding carbon model, results above in Figure 95 and Figure 96 and Table 30.

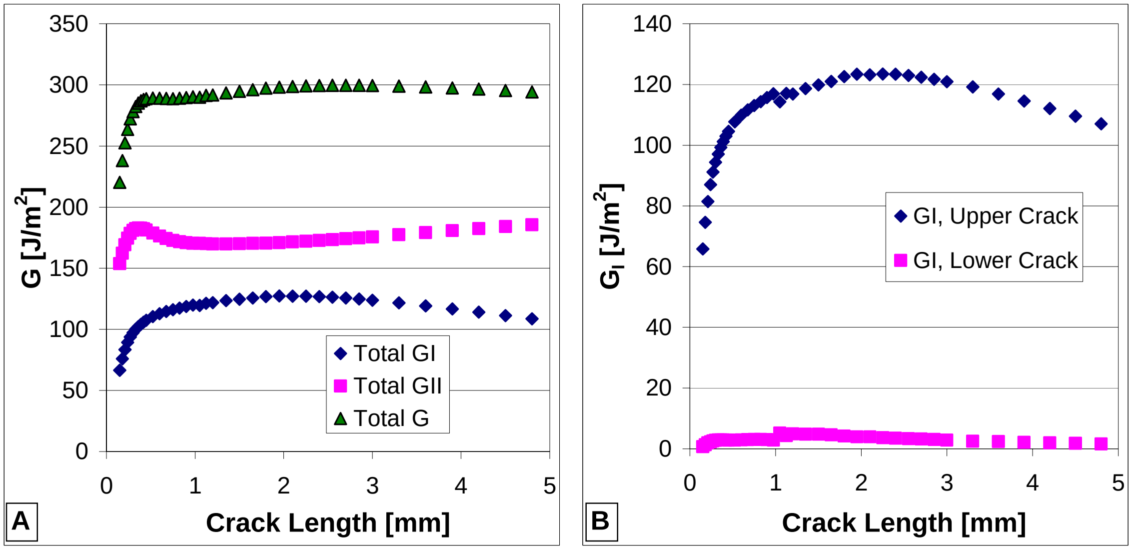

Figure 106: External Ply Drop, Glass, Compression, Both Cracks. A: Total G vs. Crack Length; B: G_I vs. Crack Length; Applied Stress = 160.0 MPa.

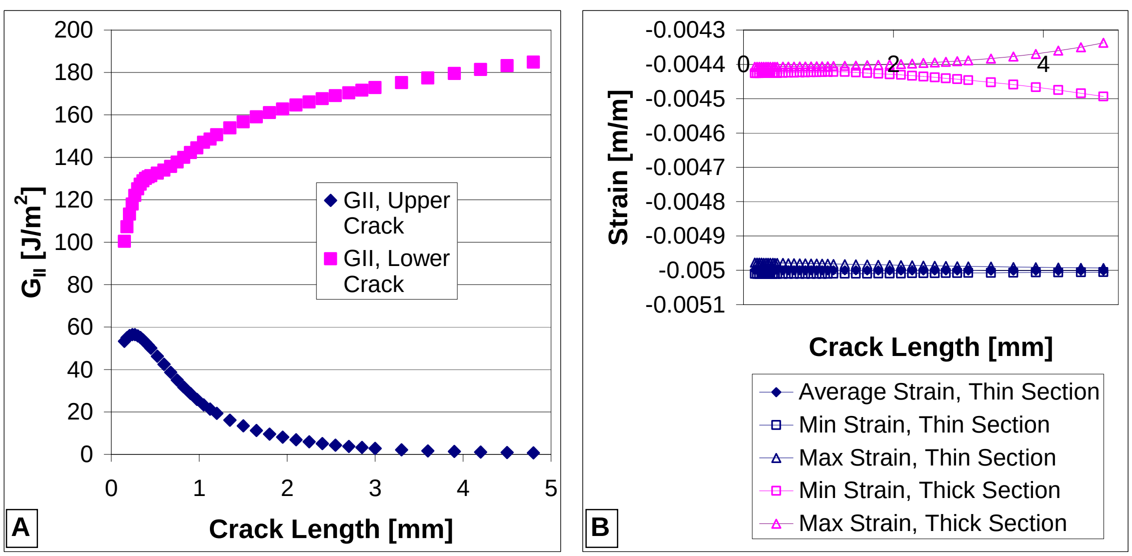

Figure 107: External Ply Drop, Glass, Compression, Both Cracks. A: G_{II} vs. Crack Length; B: Far Field Strain vs. Crack Length; Applied Stress = 160.0 MPa.

	Maximum [J/m^2]	Crack Length at Maximum G [mm]	Average [J/m^2] (0.15 – 3.0 mm)
Total G	299.7	2.7	292.6
G_I, Upper Crack	123.5	2.25	116.3
G_I, Lower Crack	5.2	1.05	3.6
G_{II}, Upper Crack	56.5	0.24	19.5
G_{II}, Lower Crack	184.9	4.8	153.2

Table 38: External Ply Drop, Glass, Compression, Both Cracks, Maximum and Average G.

Glass and carbon have similar critical G_{IC} and G_{IIC} values, but glass develops lower G values for a given strain. These results mirror those for the carbon in compression, though it is doubtful that the softening of the ±45's would have as great an effect, as the difference between the longitudinal and transverse stiffness of glass is much less than in carbon.

Associated Experimental Results. Figure 108 gives results from the associated experimental study for external ply drops with glass 0's, with two external plies dropped. At 0.5% strain, it is unlikely that a delamination will develop within 10^7 cycles. The low G values found numerically reflect this; they are well below critical values.

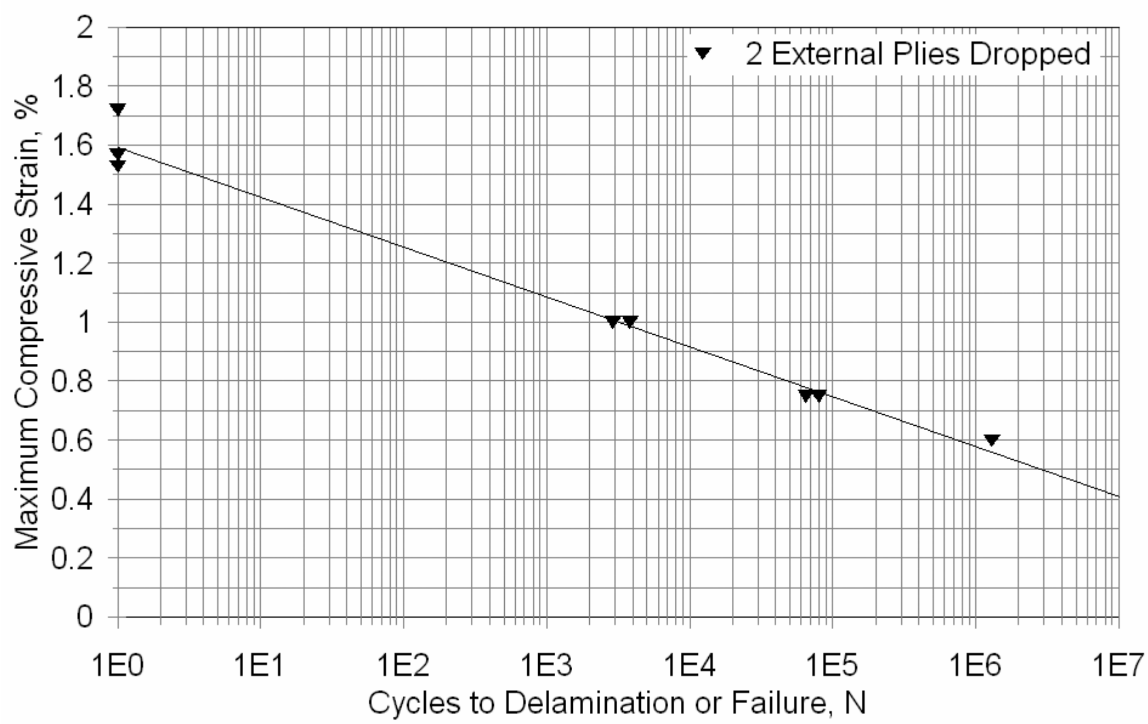

Figure 108: Experimental Results for the Maximum Compressive Strain vs. Cycles to Failure for an External Ply Drop 2 Plies Dropped, Glass 0's [$\pm45_3/0^*_2/0_{27}/0^*_2/\pm45_3$], R = 10 [17].

<u>External Ply Drop, Glass, Tension</u>. Figure 109 and Figure 110 and Table 39 are results from the external ply drop model, with glass, run in tension, with both cracks. As with most tension model results, there is minimal G_I influence.

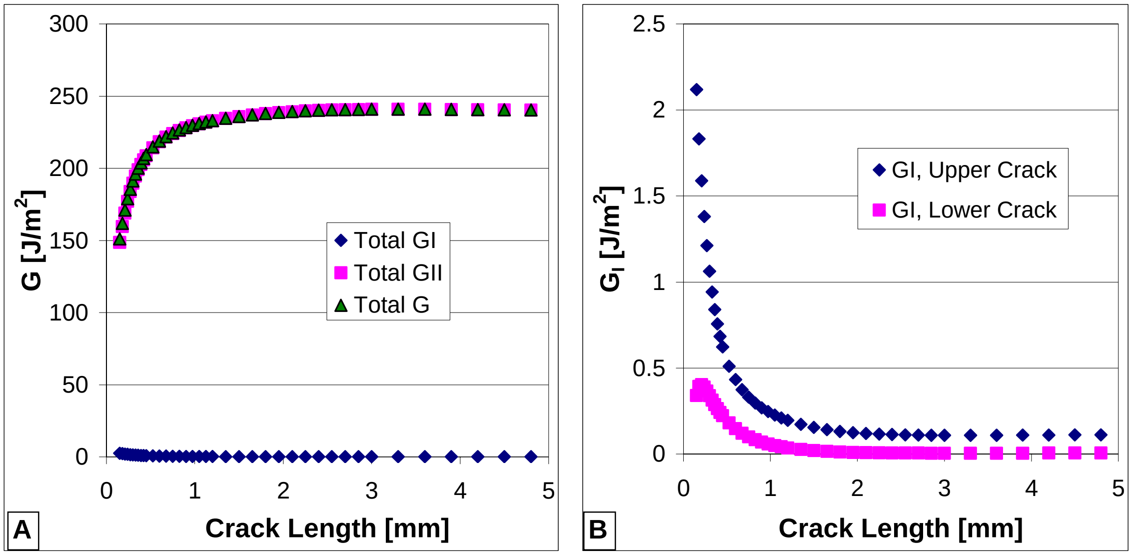

Figure 109: External Ply Drop, Glass, Tension, Both Cracks. A: Total G vs. Crack Length; B: G_I vs. Crack Length; Applied Stress = 160.0 MPa.

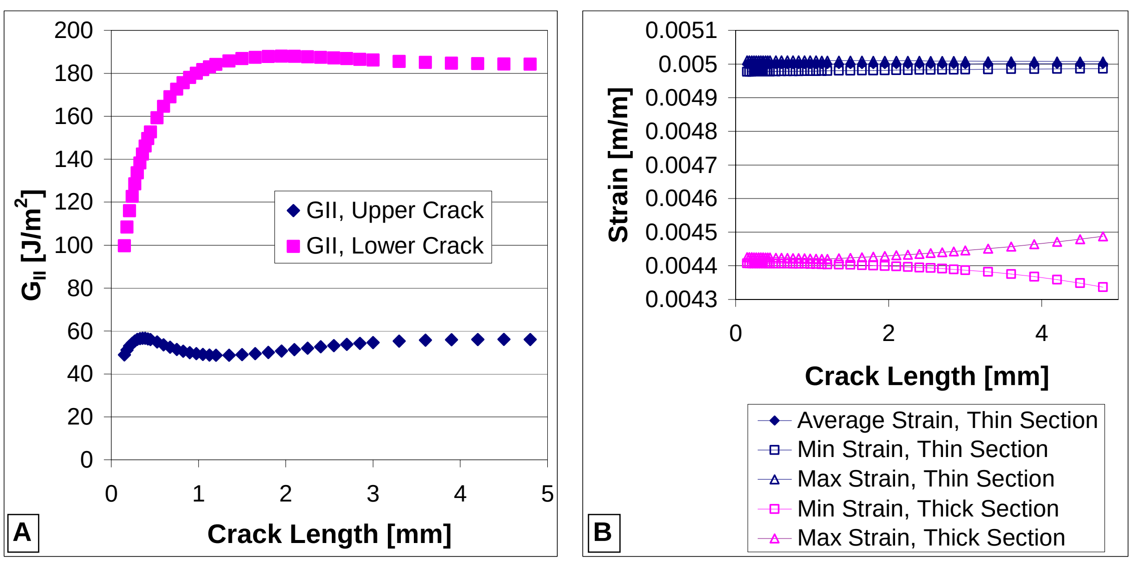

Figure 110: External Ply Drop, Glass, Tension, Both Cracks. A: G_{II} vs. Crack Length; B: Far Field Strain vs. Crack Length; Applied Stress = 160.0 MPa.

	Maximum [J/m^2]	Crack Length at Maximum G [mm]	Average [J/m^2] (0.15 – 3.0 mm)
Total G	241.0	3.3	229.6
G_I, Upper Crack	123.5	2.25	116.3
G_I, Lower Crack	5.2	1.05	3.6
G_{II}, Upper Crack	56.6	0.36	51.7
G_{II}, Lower Crack	187.9	1.95	177.5

Table 39: External Ply Drop, Glass, Tension, Both Cracks, Maximum and Average G.

Comparison of G_{II} for Different Geometries

Figure 111 shows a comparison of G_{II} values for the external, internal, and central ply drop models, each loaded in tension, with carbon 0's. The comparisons were made with the models under tension, as this minimizes the G_I influence, and the values shown are close to the total G for the models. The external and internal models included two plies dropped and both cracks present (Figure 102 and Figure 88, respectively). The central ply drop model, by nature of the ply drop location along a plane of symmetry, has only one dropped ply and one crack on each side. Therefore, for this model, the G_{II} values shown in Figure 80 are doubled in Figure 111. All of these models were loaded with an applied stress close to 550 MPa. From Figure 111, it can be seen that these three models show close agreement in G_{II} levels for the range of crack lengths considered.

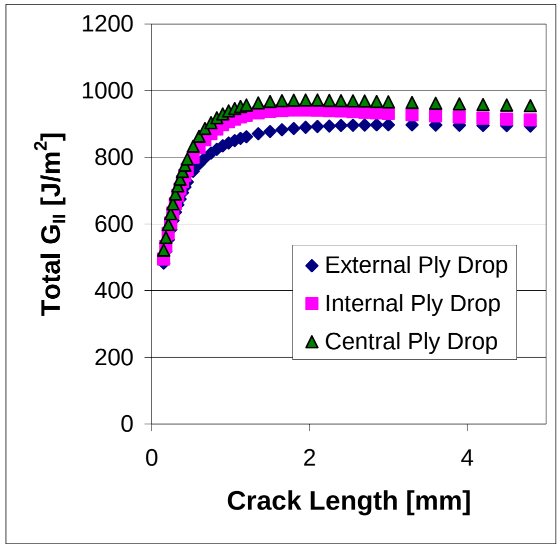

Figure 111: Comparison of Total G_{II} Values (G_{II} for both cracks, added together), External, Internal, and Central Ply Drops, Carbon, Tension, Two Plies Dropped.

Comparable G_{II} values for the central ply joint would show G_{II} to be about 1300 to 1400 J/m^2 after adjustment for geometry and load. Thus the ply drop geometry generally lowers the G_{II} levels significantly compared with ply joints, while also introducing significant G_I levels discussed earlier.

CONCLUSIONS

Modeling of In-Plane Fatigue Behavior

- Power law models generally fit in-plane fatigue S-N data better than logarithmic models at high cycles, and show consistent exponents over a range of R values, unlike three parameter models.

- Glass fiber Material QQ1 in the axial direction is more susceptible to high cycle tensile fatigue than the older, ostensibly lower performance DD16, probably due to the higher fiber volume fraction. A severe change in fatigue resistance is evident on the constant life diagram near the transition from tension to compression domination. Both observations should be a concern of wind turbine designers.

- Carbon dominated hybrid material P2B in the axial direction shows vastly superior fatigue performance compared to fiberglass material QQ1 in terms of stress. In terms of strain, P2B approaches QQ1 at higher cycles and exceeds it for tensile R values.

- In the context of predicted lifetimes under the WISPERX load spectrum, the carbon dominated hybrid material P2B in the axial direction shows much superior performance compared to fiberglass laminates QQ1 and DD16 in terms of applied stress scale factors at spectrum passes ranging from 1 to 1000. On an applied strain scale factor basis, P2B is predicted to match or outperform the fiberglass laminates after the order of 1000 WISPERX spectrum passes. Predictions based on the WISPERX spectrum highlight the greater fatigue sensitivity of QQ1 in comparison to older DD16 on the basis of both applied stress and strain scale factors.

- Time under load effects can be included for stress rupture failures of glass at high R values and lower cycles. The results can be combined with cyclic data as a function of frequency on a constant life diagram.

Finite Element Analysis of Ply Drop Delamination

- FEA model results for total G levels agree with approximate closed form models.

- FEA model results agree with the trends with material (glass vs. carbon), ply thickness, and crack position in experimental results.

- For the same ply drop geometry at the same applied strain, glass is much more resistant to delamination than carbon due to the modulus difference.

- Depending on the severity of the ply drop, loading, and ply drop location, delamination crack growth may be driven by G_I or G_{II}, and the mode driving the crack growth may change as the crack grows.

- G_I (opening mode) values are low for tensile loading and also for the central ply joints and moderate for the surface 0° ply drop. These geometries do not involve mis-orientation of the 0° plies. G_I is very high for the central and interior ply drop geometries, and probably drives the delamination process. G_I is approximately proportional to the thickness of the plies dropped, and correlates for glass and carbon materials at the same applied stress.

- G_{II} levels are driven by the number of dropped plies, and thus, the number of plies being unloaded as delamination cracks grow. G_{II} is driven by the strain energy in the material and therefore correlates with different materials at the same applied load, stress, or strain squared.

- The surface 0° ply drop geometry does not contain mis-oriented 0° plies, and might be preferred. However, the effects of fatigue damage in the outside ±45° layers requires further study, since their failure could enable unloading of the dropped plies along a single interface.

- Ply butt joints with carbon-glass transitions (Appendix A) showed G levels similar to the ply joints with no material change, for respective sides of the joint (carbon plies or glass plies) delaminating, adjusting for differences in ply thickness and load. As expected, the carbon side showed the highest G values and delaminated first in experiments.

- Tapering of ply drop edges can increase lifetimes to delamination for ply drops with carbon 0's (Appendix B). Tapering ply drop edges with glass 0's decreased lifetimes experimentally, but failures occurred away from the ply drop area.

Recommendations for Future Work

Modeling of In-Plane Fatigue Behavior

Grip Failures. In the associated experimental study, most coupons with a high percentage of 0 fibers failed in the grips. Further work on the significance of these grip failures to the accuracy of the fatigue data is needed. This may show that the data gathered is overly conservative. There needs to be an understanding of the accuracy of the current test methodologies, and the effects on S-N modeling and extrapolation to higher cycles.

High Cycle Fatigue Data. Work with very high cycles on strands has shown that power law models provide good fits at high cycles [10]. However, these tests may unnaturally exclude factors present in standard coupon geometries. Therefore, tests with standard coupons run to very high cycles (10^7-10^8 cycles) using current materials should be conducted to confirm extrapolations and the findings of the strand tests. Results available for earlier materials, including DD16, in this cycle range support current assumptions.

Multiaxial Fatigue Data. Fatigue data necessary for a full ply-by-ply multiaxial fatigue analysis should be developed. This would enable fatigue analysis in a structural context, including matrix cracking.

Low Cycle Fatigue Data. Low cycle data tends to be under represented in fatigue data sets, but can be important in extreme loading and in validation tests with spectrum loading. More low cycle data should be collected for materials.

Stress Rupture / Residual Strength. Failure of glass fiber reinforced composites under tension may be driven by a combination of reduced residual strength and stress rupture. Further study of these combined effects may yield a model that better fits experimental data.

Spectrum Loading Lifetime Predictions. Lifetime predictions based on spectrum loading are the most useful for applications with variable loadings, such as wind turbines. Further work should be done to improve the correlation of predictions with experimental data, and to obtain spectra relevant to very large turbines.

Finite Element Analysis of Ply Drop Delamination

Experimental Program. FEA models predict a strong influence of G_I levels depending on the number of mis-oriented plies, and whether the model is loaded in compression or tension. These factors are most strongly present in the central and internal ply drop models. There are major differences in the G_I levels between the tension and compression loading cases. Furthermore, though internal ply drops were tested in the associated experimental study, they were not tested at the same load level in tension; the external ply drop, though tested in both tensile and compressive fatigue, doesn't have nearly the number of mis-oriented plies. There is also a related question of delamination growth into the thin side of the ply drop, which would also likely be G_I dominated.

Thus, it may be interesting to run a ply drop coupon with a high number of mis-oriented 0 plies in both tensile and compressive fatigue to examine the influence of the G_I component. This may require a thinner coupon than used by Samborsky et al. to stay within the capabilities of the available testing machines. Coupons with thicker ply drops, as used in Appendix B, may also result in more delamination on the thin side, at least for local crack extensions, and could be included in further study.

Crack Growth Model Based on G Levels. Results from the thesis work indicate that many ply drop delamination configurations will most likely include two cracks. In this thesis where two cracks were modeled, they were arbitrarily assigned equal lengths. Wide variations in the G levels between the two modeled cracks seen in the results indicate that crack growth for the two cracks will be at different rates, and thus the assumption of equal length is inaccurate.

A crack growth model based on the integration of the Paris equation or numerical simulations would offer a more complete treatment. The Paris equation, given as Equation 18 below, relates crack growth rate, da/dN, with SERR range, ΔG [34].

$$\frac{da}{dN} = A(\Delta G)^n \tag{18}$$

The parameters A and n are found experimentally for a given material. Data for this type of relationship have been reported by many authors, such as Ramkumar and Whitcomb [34]. The crack growth model can be integrated to predict the crack geometry at any point in the lifetime and for various loading conditions [16].

Full Simulation. Ultimately, prediction of delamination in a blade structure may require a full simulation of initiation and growth, based on pure and mixed mode fatigue crack growth data. Initiation is a fatigue phenomenon, though it differs from crack growth. Initiation of ply drop delamination is thought to generally occur at the end of the ply drop, a region that is matrix dominated. Because of the importance of the matrix in initiation, a model that treats this region in closer detail, and better represents the matrix rich regions at the end of the drop and between plies, might be necessary. Prediction of the location of crack initiation and initiation cycles may be possible using a method similar to the Tsai-Wu failure criterion or another method. Murri et al. predicted initiation using material data based solely on mode II tests [3]. Their FE models showed that delamination growth was at least 95% mode II at peak values, reflective of applied tension loading. Models with compression loading, however, will show a much greater influence of mode I, as seen in this thesis. A mixture of mode I and II complicates maters, as there are interaction effects. Successful treatments of initiation and growth have been carried out in studies of structural details at MSU [37], and mixed mode simulation and experiments have been reported by Krüger and König [26]

Further development of the FE models is also required. Models must be able to calculate crack growth based on G levels and loading and update crack lengths. The process is iterative, and in order to run efficiently, must be self contained. This may be possible within the FEA software package script file language, or require integration with another package.

Substructure Testing and Analysis. Delamination may spread to produce structural failure, or arrest. Testing and analysis of larger elements like beams may be required to study this issue, as well as effects such as ply drop spacing and full material transitions (Appendix A).

REFERENCES

1. Mandell, J.F., Reed, R.M. Jr. and Samborsky, D.D., "Fatigue of Fiberglass Wind Turbine Blade Materials." Contractor Report SAND92-7005, Sandia National Laboratories, Albuquerque, NM (1992).

2. Sutherland, H.J. and J.F. Mandel. "The Effect of Mean Stress on Damage Predictions for Spectral Loading of Fibreglass Composite Coupons" Wind Energy. Volume 8, Issue 1, (2005) pp. 93 – 108.

3. Murri, G.B., J.R. Schaff, and A.L. Dobyns. "Fatigue and Damage Tolerance Analysis of a Hybrid Composite Tapered Flexbeam." American Helicopter Society Forum May 9-11, 2001 in Washington DC. (2001).

4. Hartman, D. "Advances in Blade Design and Material Technology." Presentation for WINDPOWER 2005 Session 5C. (2005).

5. DOE/MSU Composite Material Fatigue Database, March 2, 2006. Version 15.0 Available at: http://www.coe.montana.edu/composites/documents/March%202%202006%20Composite%20fatigue%20Database%2015.pdf

6. Samborsky, D.D., "Fatigue of E-glass Fiber Reinforced Composite Materials and Substructures," M.S. Thesis, Department of Civil Engineering, Montana State University, (1999).

7. Wahl, N, Mandell, J.F., and Samborsky, D.D., "Spectrum Fatigue Lifetime and Residual Strength for Fiberglass Laminates," Contractor Report SAND2002-0546, Sandia National Laboratories, Albuquerque, NM (2002).

8. Nijssen, R.P.L., Fatigue Life Prediction and Strength Degradation of Wind Turbine Rotor Blade Composites. Knowledge Centre Wind turbine Materials and Constructions and Design and Production of Composite Structures Group, Faculty of Aerospace Engineering, Delft University. (2006).

9. Cairns, D.S. and J. Skramstad. "Evaluation of Hand Lay-Up and Resin Transfer Molding In Composite Wind Turbine Blade Manufacturing." Contractor Report SAND00-1425, Sandia National Laboratories, Albuquerque, NM (2000).

10. Mandell, J.F., Samborsky, D.D., and Cairns, D.S. "Fatigue of Composite Materials and Substructures for Wind Turbine Blades," Contractor Report SAND2002-0771, Sandia National Laboratories, Albuquerque, NM (2002).

11. Wei, G., "High Cycle Longitudinal and Transverse Fatigue of Unidirectional Glass/Polyester Composites," M.S. Thesis, Department of Chemical Engineering, Montana State University, (1995).

12. Sutherland, H.J. and Veers, P.S., “The Development of Confidence Limits for Fatigue Strength Data,” A collection of 2000 ASME Wind Energy Symposium Technical Papers, AIAA-2000-0063, (January 2000).

13. Natrella, M.G. Experimental Statistics. NBS Handbook 91, National Bureau of Standards, Washington, DC (1963); (reprinted 1966).

14. Mandell, J.F. and Meier, U., “Effects of Stress Ratio, Frequency, and Loading Time on the Tensile Fatigue of Glass-Reinforced Epoxy.” Long-Term Behavior of Composites. ASTM STP 813, T. K. O’Brien, Ed., American Society for Testing and Materials, (1983). pp. 55-77.

15. MatLab Function Reference. “quadl” The MathWorks, Inc. (2005).

16. Stephens, R.I., A. Fatemi, R.R. Stephens, H.O. Fuchs. Metal Fatigue in Engineering. 2nd Edition, Wiley-Interscience New York. (2006).

17. Samborsky, D.D., D.P. Avery, P. Agastra and J.F. Mandell. “Delamination and Failure at Ply Drops in Carbon Fiber Laminates Under Static and Fatigue Loading.” 2006 Wind Energy Symposium, Reno, NV ASME/AIAA. (2006).

18. Matsuiski, M. and Endo, T. Fatigue of metals subjected to varying stress, Japan Society of Mechanical Engineering. (1969).

19. Downing, S.D. and D.F. Socie. ”Simple Rainflow Counting Algorithms” International Journal of Fatigue. Vol. 4, no. 1, (January 1982). pp. 31-40.

20. Broek, D. Elementary Engineering Fracture Maechanics. 4th ed., Dordrecht, The Netherlands, Martinus Nijhoff Publishers. (1986).

21. Tetheway, B.R. Jr., J.W. Gillespie, Jr., and D.J. Wilkins. “Delamination in Thickness Tapered Composite Laminates.” Journal of Engineering Materials and Technology. Volume 115, (April 1993). pp. 193-199.

22. Her, S.C. “Stress Analysis of Ply Drop-Off in Composite Structures.” Composite Structures, Volume 57, Issues 1-4, (July 2002). pp. 235-244.

23. Vidyashankar, B.R. and A.V. Krishna Murty. “Analysis of Laminates with Ply Drops.” Composites Science and Technology, Volume 61, Issue 5, (April 2001). pp. 749-758.

24. Mukherjee, A. and B. Varughese. “Design Guidelines for Ply Drop-Off in Laminated Composite Structures.” Composites Part B: Engineering., Volume 32, Issue 2, (2001). pp. 153-164.

25. Meirinhos, G., J. Rocker, J.-P. Cabanac and J.-J. Barrau. “Tapered Laminates Under Static and Fatigue Tension Loading.” Composites Science and Technology, Volume 62, Issue 4, (March 2002). pp. 597-603.

26. Krüger, R. and König, M., “Prediction of Delamination Growth Under Cyclic Loading,” Composite Materials: Fatigue and Fracture (Sixth Volume), ASTM STP 1285, E. A. Armanios, Ed., American Society for Testing and Materials, (1997). pp. 162-178.

27. Rybicki, E.F., and M.F. Kannmen. "A Finite Element Calculation of Stress Intensity Factors by a Modified Crack Closure Integral. Engineering Fracture Mechanics, Vol. 9. (1977). pp. 931-938.

28. Raju, I.S. “Calculation of Strain Energy Release Rates with Higher Order and Singular Finite Elements.” Engineering Fracture Mechanics. 28:3. (1987). pp. 251-274.

29. ANSYS Structural Guide. Chapter 12.2. Solving Fracture Mechanics Problems. (2005).

30. Barbero, E.J. Introduction to Composite Materials Design. Taylor and Francis, Florence KY. (1998).

31. Reeder, J.R., “A Bilinear Failure Criterion for Mixed Mode Delamination.” Composite Materials: Testing and Design. (Eleventh Volume), ASTM STP 1206, E.T. Camponeschi, Jr., Ed., American Society for Testing and Materials, Philadelphia, (1993). pp. 303-322.

32. Agastra, P., “Mixed Mode Delamination of Glass Fiber/Polymer Matrix Composite Materials,” M.S. Thesis, Department of Chemical Engineering, Montana State University, (2003).

33. Pelegri, A.A., G.A. Kardomateas, and B.U. Malik, "The Fatigue Growth of Internal Delaminations under Compressive Loading in Cross Ply Composite Plates," Composite Materials: Fatigue and Fracture. (Sixth Volume), ASTM STP 1285, E.A. Armanios, Ed., American Society for Testing and Materials, (1997). pp. 146-163.

34. Ramkumar, R.L. and J.D Whitcomb, “Characterization of Mode I and Mixed-Mode Delamination Growth in T300/5208 Graphite/Epoxy,” Delamination and Debonding of Materials, ASTM STP 876, W.S. Johnson, ED., American Society for Testing and Materials, Philadelphia., (1985).

35. Im, J., J.F. Mandel, S.S. Wang, F.J. McGarry. “Surface crack growth in fiber composites. MIT Report, NASA CR-135094, (1976).

36. Personal Communication with J.F. Mandell, (November 2006).

37. Mandell, J.F., D.S. Cairns, D.D. Samborsky, R.B. Morehead, and D.J. Haugen. “Prediction of Delamination in Wind Turbine Blade Structural Details.” Journal of Solar Energy Engineering Volume 125, Issue 4, (November 2003) pp. 522-530.

APPENDICES

APPENDIX A:

MATERIAL TRANSITION DELAMINATION

<u>Material Transition, Last Carbon Out</u>

The last carbon out model (schematic shown in Figure 112) was developed to explore the behavior of a physical test specimen representing the extreme ends of a total carbon to glass 0° material transition, which would be done ply-by-ply in a sequence of steps. This model and test specimen are part of a group of models designed to study the behavior of cracks at material transition areas. In this case, the model is of a transition from a hybrid of glass and carbon 0 plies to only glass 0's. The lay-up is $[\pm45_2/0_1/0^*{}_1/0_8/0^{\#}{}_1]_S$, where the * indicates the dropped ply near the outside and the # indicates the jointed ply at the mid-plane.

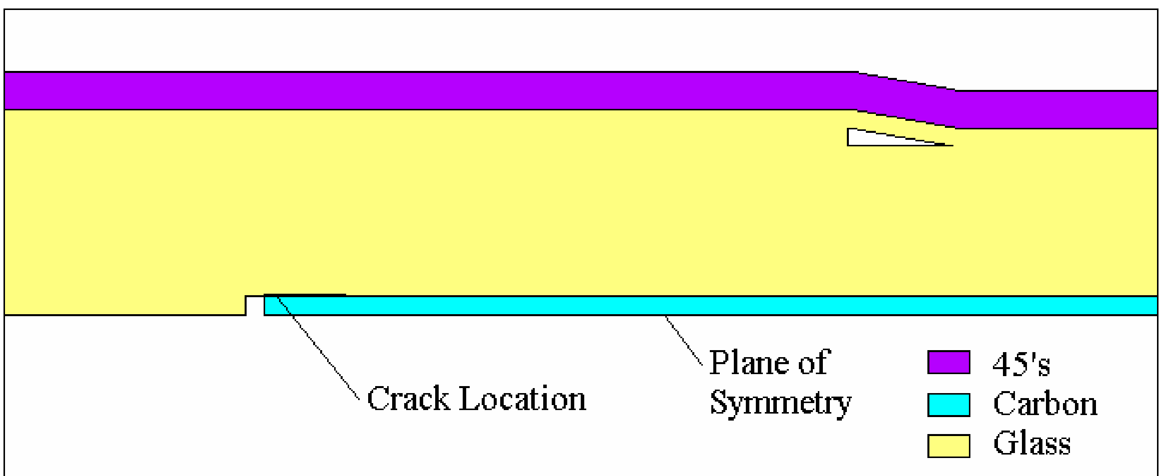

Figure 112: Last Carbon Out, $[\pm45_2/0_1/0^*{}_1/0_8/0^{\#}{}_1]_S$.

The area of the model with only glass 0's has an extra ply to lessen the effects of the stiffness change at the ply transition. The cross sectional area made of only the less stiff glass 0's is increased to better match the area with the stiffer carbon ply. The extra glass ply is dropped at an offset to the material transition joint to lessen the interaction between the two features.

A small gap, one ply thickness (0.3 mm) in length, is included at the material transition joint to better model crack behavior under compression loading. Without the gap, the two plies in the FEA model buttress together perfectly, with no overlap, and result in unnatural G_I values. An actual coupon will have a matrix rich region there, and possibly fiber overlap, which will allow for movement between the abutting plies. Including a gap allows for conservative results, without undo G_I influence.

Two different crack configurations are modeled. One has the crack growing along the carbon ply, as shown in Figure 112. The other crack configuration grows the crack from the material joint into the glass, along the ply interface.

Last Carbon Out, Compression. Figure 113 and Table 40 are results from the last carbon out model, loaded in compression, with the crack along carbon ply. The average G_I is 16% of the average total G.

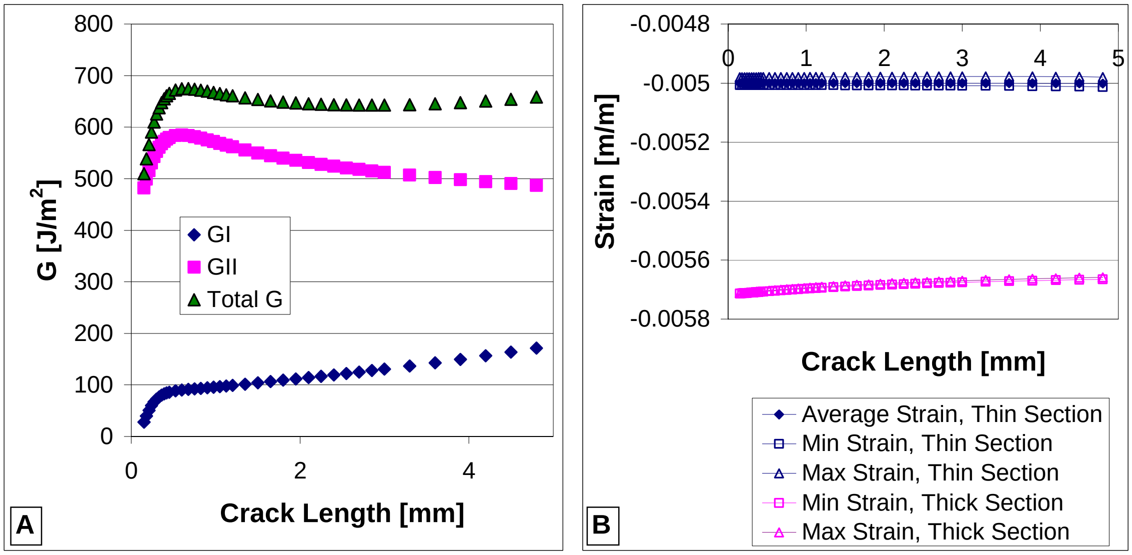

Figure 113: Last Carbon Out, Compression, Crack along Carbon Ply, A: G vs. Crack Length; B: Far Field Strain vs. Crack Length; Applied Stress = 201.7 MPa.

	Maximum [J/m^2]	Crack Length at Maximum G [mm]	Average [J/m^2] (0.15 – 3.0 mm)
Total G	674.7	0.675	649.5
G_I	171.3	4.8	103.8
G_{II}	584.7	0.6	545.8

Table 40: Last Carbon Out, Compression, Crack along Carbon Ply, Maximum and Average G.

Figure 114 and Table 41 are results from the last carbon out model, loaded in compression, with the crack grown into the glass (not along the carbon ply). The G_I is 17% of the total G, a similar percentage to model with the crack along the carbon ply.

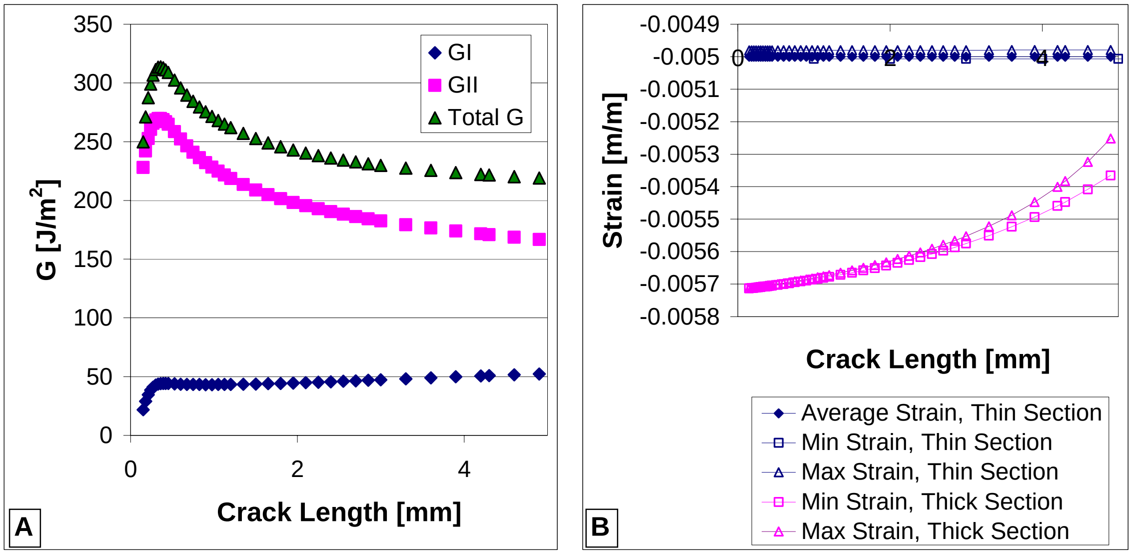

Figure 114: Last Carbon Out, Compression, Into Glass, A: G vs. Crack Length; B: Far Field Strain vs. Crack Length; Applied Stress = 201.7 MPa.

	Maximum [J/m^2]	Crack Length at Maximum G [mm]	Average [J/m^2] (0.15 – 3.0 mm)
Total G	313.8	0.36	258.7
G_I	52.3	4.9	44.0
G_{II}	269.8	0.33	214.7

Table 41: Last Carbon Out, Compression, Into Glass, Maximum and Average G.

A comparison of the results from the two compression models, one with the crack along the carbon ply and one with the crack into the glass, indicates that it is more likely for delamination cracks to develop along the carbon ply. The average total G for the model with the crack grown along the carbon ply is 2.51 times higher than the model with the crack grown into the glass. This is roughly in agreement with Equation 15, for the strain energy being released from the carbon vs. glass ply. The magnitude of G_{II} is consistent with the ply drop FEA results, Figure 111, with the same two plies dropped if the G_{II} magnitude is decreased to account for the total G_{II} of the two cracks. The G values are also consistent with the ply joint results which do not involve a material transition, if the respective carbon or glass case is considered, as well as the ply thickness difference.

<u>Last Carbon Out, Tension</u>. Figure 115 and Table 42 are results from the last carbon out model, loaded in tension, with the crack along the carbon ply. As with most tension models, there is minimal G_I influence, and it is at its maximum at initiation.

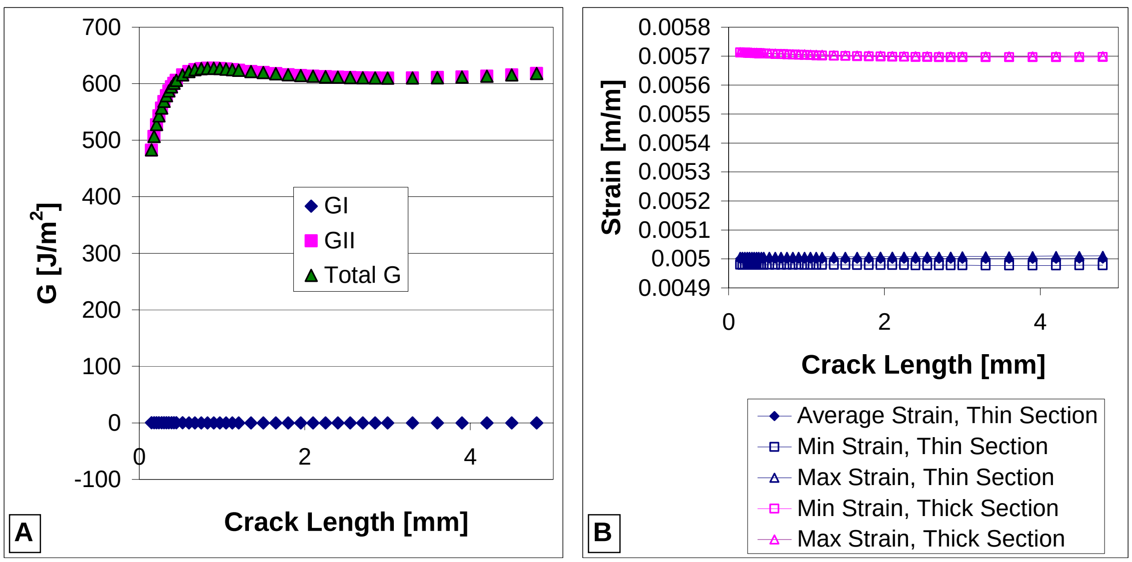

Figure 115: Last Carbon Out, Tension, Crack along Carbon Ply, A: G vs. Crack Length; B: Far Field Strain vs. Crack Length; Applied Stress = 201.7 MPa.

	Maximum [J/m^2]	Crack Length at Maximum G [mm]	Average [J/m^2] (0.15 – 3.0 mm)
Total G	627.3	0.825	611.3
G_I	0.3	0.15	0.0
G_{II}	627.3	0.825	611.3

Table 42: Last Carbon Out, Tension, Crack along Carbon Ply, Maximum and Average G.

Figure 116 and Table 43 are result from the last carbon out model, loaded in tension, with the crack grown into the glass portion of the model.

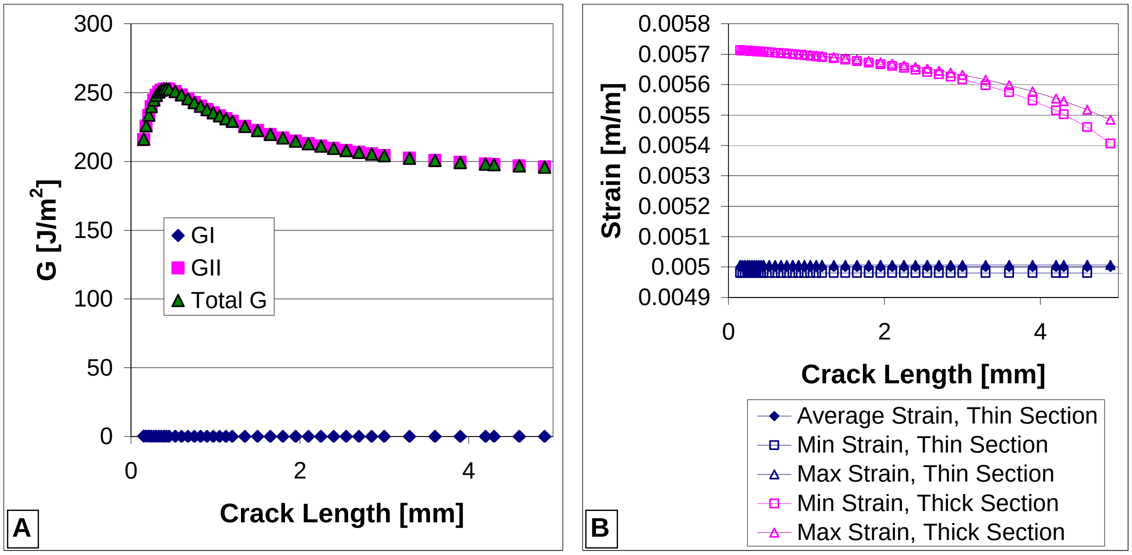

Figure 116: Last Carbon Out, Tension, Into Glass, A: G vs. Crack Length; B: Strain vs. Crack Length.

	Maximum [J/m^2]	Crack Length at Maximum G [mm]	Average [J/m^2] (0.15 – 3.0 mm)
Total G	252.7	0.42	224.2
G_I	0.3	0.15	0.0
G_{II}	252.6	0.42	224.1

Table 43: Last Carbon Out, Tension, Into Glass, Maximum and Average G.

The results from the two tension loaded models reinforce the conclusion that a delamination crack will grow along the carbon ply, as the average total G of that model is 2.73 times the total average G of the model with the crack grown into the glass. This is similar to the proportion from the compression model.

<u>Material Transition, First Glass In</u>

Like the last carbon out model, the first glass in model (schematic shown above in Figure 117) is a model designed to study the behavior of cracks at material transition areas. In this case, the model is of a transition from a hybrid of glass and carbon 0 plies to only carbon 0's.

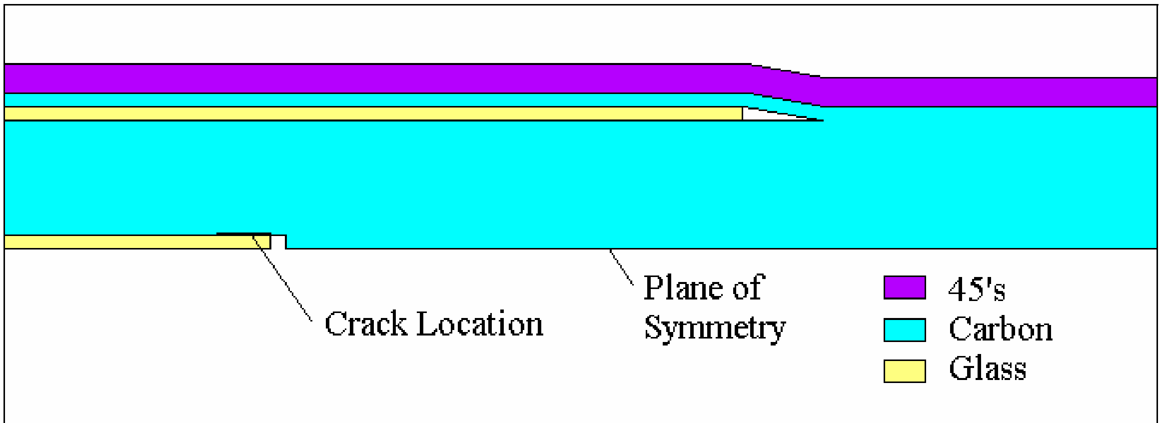

Figure 117: First Glass In, $[\pm45_2/0_1/0^*_1/0_8/0^{\#}_1]_S$.

The area of the model with the ply joint also has an extra glass ply near the outside of the model to lessen the affects of the stiffness change at the ply transition. As before, the ends of the two glass plies, the ply joint at the centerline of the model and the dropped glass ply near the exterior, do not line up, as with the last carbon out model. The lay up is $[\pm45_2/0_1/0^*_1/0_8/0^{\#}_1]_S$, where the * indicates the dropped ply near the outside and the # indicates the jointed ply at the mid-plane.

As before, two different crack configurations are modeled. One has the crack growing along the carbon ply, as shown in Figure 112. The other crack configuration grows the crack from the material joint into the glass, along the ply interface.

<u>First Glass In, Compression</u>. Figure 118 and Table 44 are results from the first glass in model, loaded in compression, with the crack growing along the glass ply. These results show similar G values to the last carbon out model with the crack grown into the

glass (Figure 114), though a lower percentage of G_I, which makes up 3.5% of the average total G.

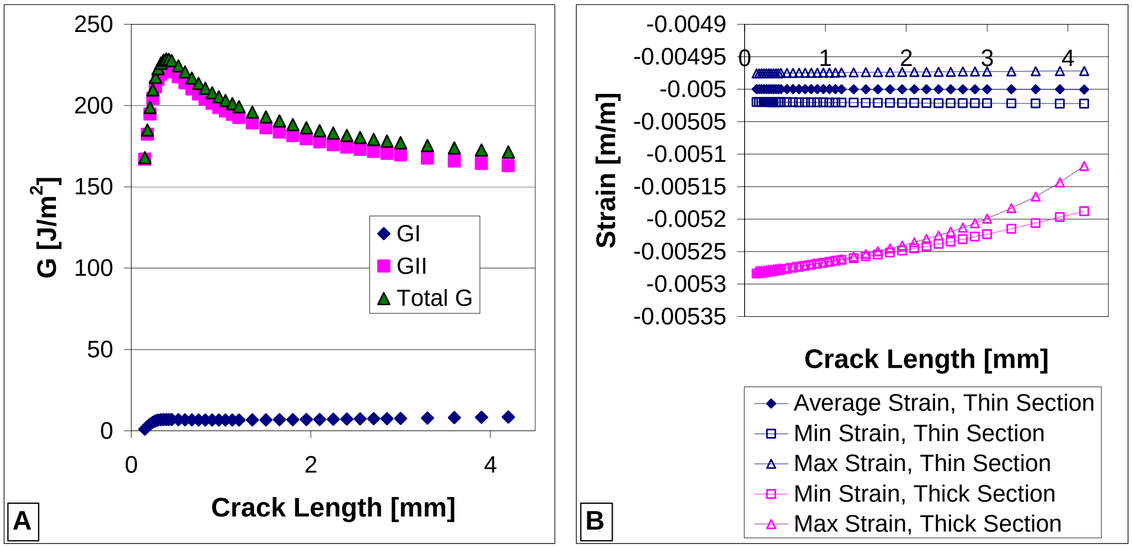

Figure 118: First Glass In, Compression, Crack along Glass Ply, A: G vs. Crack Length; B: Far Field Strain vs. Crack Length; Applied Stress = 563.6 MPa.

	Maximum [J/m^2]	Crack Length at Maximum G [mm]	Average [J/m^2] (0.15 – 3.0 mm)
Total G	228.6	0.39	195.6
G_I	8.5	4.2	6.8
G_{II}	221.6	0.39	188.8

Table 44: First Glass In, Compression, Crack along Glass Ply, Maximum and Average G.

Figure 119 and Table 45 are results from the first glass in model, loaded in compression, with the crack growing into the carbon. Average G_I is 3.7% of the average total G. This model differs from that model that has the crack growing along the glass ply in that it has a much higher average total G; 2.9 times higher. This indicates that it is unlikely that a crack will grow along the glass ply. It is much more likely to grow into the carbon, as observed experimentally.

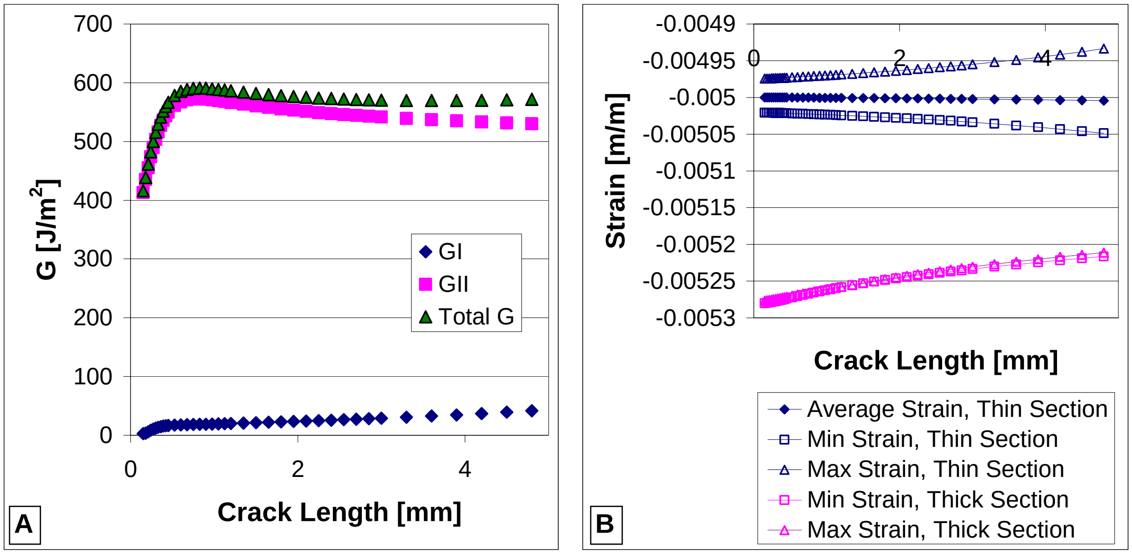

Figure 119: First Glass In, Compression, Crack into Carbon, A: G vs. Crack Length; B: Far Field Strain vs. Crack Length; Applied Stress = 563.6 MPa.

	Maximum [J/m^2]	Crack Length at Maximum G [mm]	Average [J/m^2] (0.15 – 3.0 mm)
Total G	590.9	0.825	571.7
G_I	41.6	4.8	21.3
G_{II}	572.5	0.825	550.4

Table 45: First Glass In, Compression, Crack into Carbon, Maximum and Average G.

First Glass In, Tension. Figure 120 and Table 46 are results from the first glass in model, loaded in tension, with the crack along the glass ply.

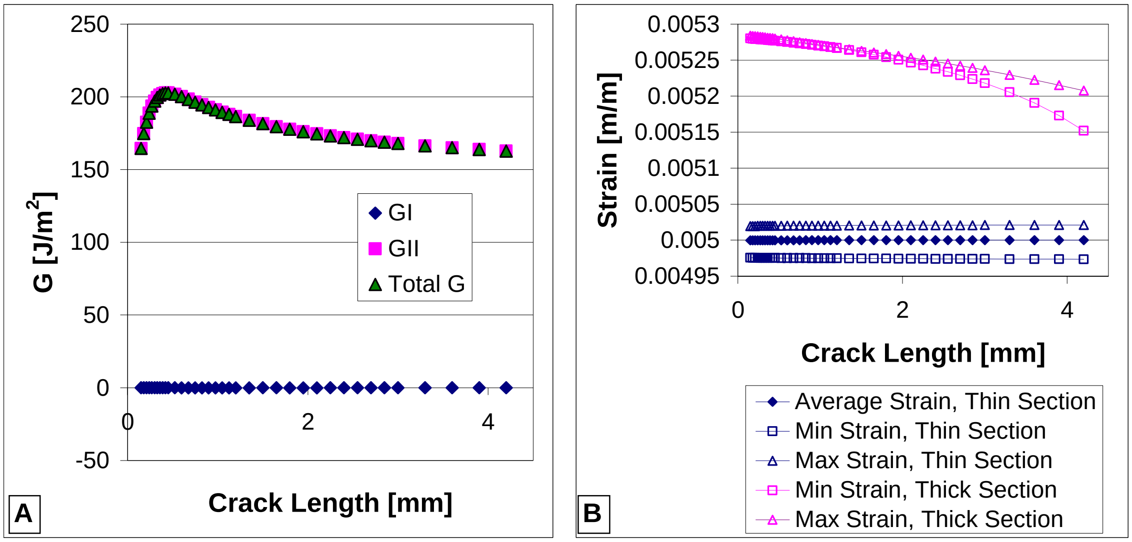

Figure 120: First Glass In, Tension, Crack along Glass Ply, A: G vs. Crack Length; B: Strain vs. Crack Length.

	Maximum [J/m^2]	Crack Length at Maximum G [mm]	Average [J/m^2] (0.15 – 3.0 mm)
Total G	202.7	0.45	182.3
G_I	0.0	4.2	0.0
G_{II}	202.7	0.45	182.3

Table 46: First Glass In, Tension, Crack along Glass Ply, Maximum and Average G.

Results from the first glass in model, in tension, with the crack along ply are given in Figure 121 and Table 47. The conclusions made from the results from the model loaded in tension are reinforced here, as again the delamination crack growing into the carbon material produces higher G values; 3.1 times higher.

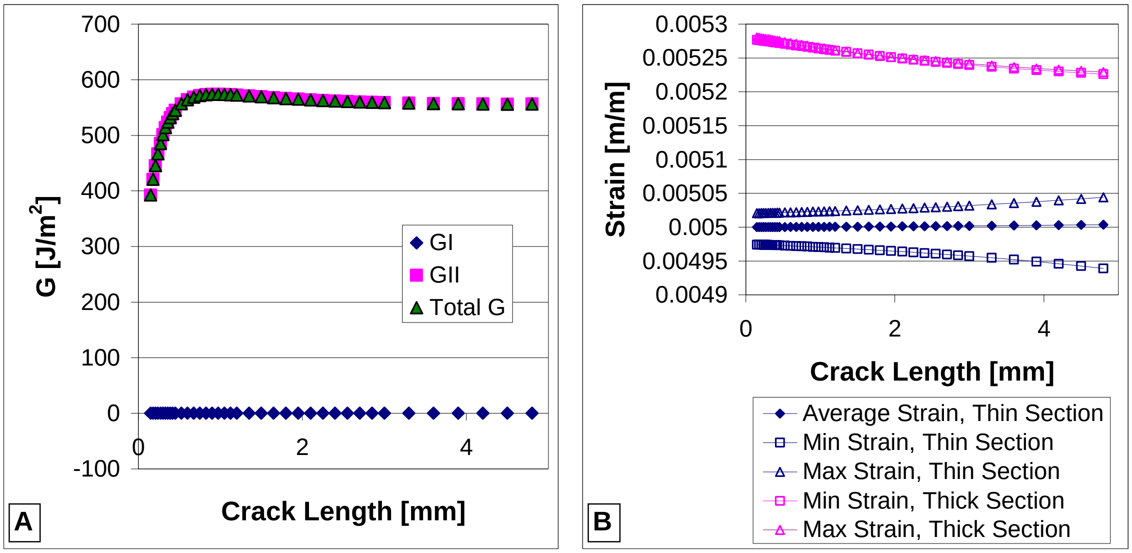

Figure 121: First Glass In, Tension, Crack into Carbon, A: G vs. Crack Length; B: Strain vs. Crack Length.

	Maximum [J/m^2]	Crack Length at Maximum G [mm]	Average [J/m^2] (0.15 – 3.0 mm)
Total G	573.9	0.975	557.7
G_I	0.1	0.15	0.0
G_{II}	573.9	0.975	557.7

Table 47: First Glass In, Tension, Crack along Ply, Maximum and Average G.

Both the last carbon out and first glass in models indicate that for the same applied strain, the delamination cracks are more likely to grow along a carbon ply, regardless as to whether the majority of the 0 plies in the model are glass or carbon. The higher strain energy in a carbon ply versus a glass ply at a given strain drives the development of delamination cracks.

APPENDIX B:

TAPERED PLY DROP STUDY

Project goals

This study was carried out as a project in MSU course ME 551 – Advanced Composite Materials by Tim Wilson, J.C. Blockey and Mitch Frankel. The goal of this project was to determine if the added difficulty and expense of cutting ply drops with a taper was offset by the benefits. The idea is that the resistance to ply drop delamination could be improved by suppressing crack initiation. Tapering a ply drop should reduce the stress concentration at the ply drop, increasing the strength and decreasing the tendency to delaminate. This study included both the use of numerical finite element and experimental methods.

Static and fatigue tests were performed to characterize the strength. Inspection of coupons was done to identify areas where cracks developed. Finite element models were created to compare the G levels of delamination cracks in the tapered and straight configurations of internal ply drops.

Originally, it was intended to use only glass prepreg, but material shortages switched the focus to carbon prepreg. A smaller sampling of glass was included as a comparison. Materials used were the same Newport prepregs as used in the ply drop studies.

Methodology

Coupon Manufacture. The coupon modeled is designated a $[\pm45_1/0_5/0_3{*}/0_5/0_3{*}/0_5/\pm45_1]$. The zeroes in these coupons were either made with glass or carbon fibers. Two different types of ply drop geometries were used in the coupons made for testing. A group of coupons with tapered ply drops and a control group with straight ply drops were made. Both groups had the same layup; just the geometry of the ply drop itself was varied. This allows for a direct comparison of the results.

The straight ply drop coupons were laid up as usual. The three dropped plies were cut with a utility knife held at a 90° angle. The tapered ply drop was more complex. A plate of aluminum was machined to a 10 degree angle to form a long wedge. This wedge was clamped over three plies of prepreg and used to guide a razor blade. By carefully removing small amounts of material from the edge of the prepreg with the blade held in the proper orientation by the wedge, a tapered edge was formed.

The coupons were about 11.5 inches long and 0.75 inch wide. In the carbon coupons, the thickness of the thinner end was 0.22 inch while the thicker end was 0.29 inch. The thicknesses for the glass coupons were 0.18 and 0.25 inch for the thinner and thicker ends, respectively. The ply drop is located at the center of the gage section. A ply drop was put on each side of the coupon as to minimize the creation of a bending moment in the coupon.

Coupon Testing

Coupons were tested in an Instron 8802 and an Instron 8501, both servo-hydraulic material testing machines. Static tests were run in position control until the first delamination was heard. The coupon was inspected to confirm the existence of a delamination crack and the test was resumed until the coupon completely failed.

All fatigue tests were run at R = 0.1, pure tension fatigue. The testing machines were run in load control to maintain the desired stresses in the thin section. Coupons were considered failed when they developed a crack of 6.4 mm (¼ inch) length or more.

A total of 26 carbon coupons were tested. Of these, 14 were tapered ply drop and 12 straight ply drop coupons. Due to the material shortage, only 11 glass coupons were tested; 6 tapered ply drop and 5 straight ply drop. This number of tests did not allow a thorough characterization of the behavior of the material, but did offer a comparison to the carbon coupons.

Scanning Electron Microscope Study. The Scanning Electron Microscope (SEM) was used to examine two coupons that had been fatigue tested for 175,000 and 801,000 cycles. It was hoped that cracks in early stages of development would be seen, and thus validate assumptions on where the cracks initiated and grew. However, no cracks were seen. The SEM pictures, of which an example is given as Figure 122, did allow for the close inspection of the coupon geometry. The angle at the tips of the taper, ideally 10°, was observed to be about 12°, and the offset between the tips, ideally zero, was observed to be approximately 0.8 mm.

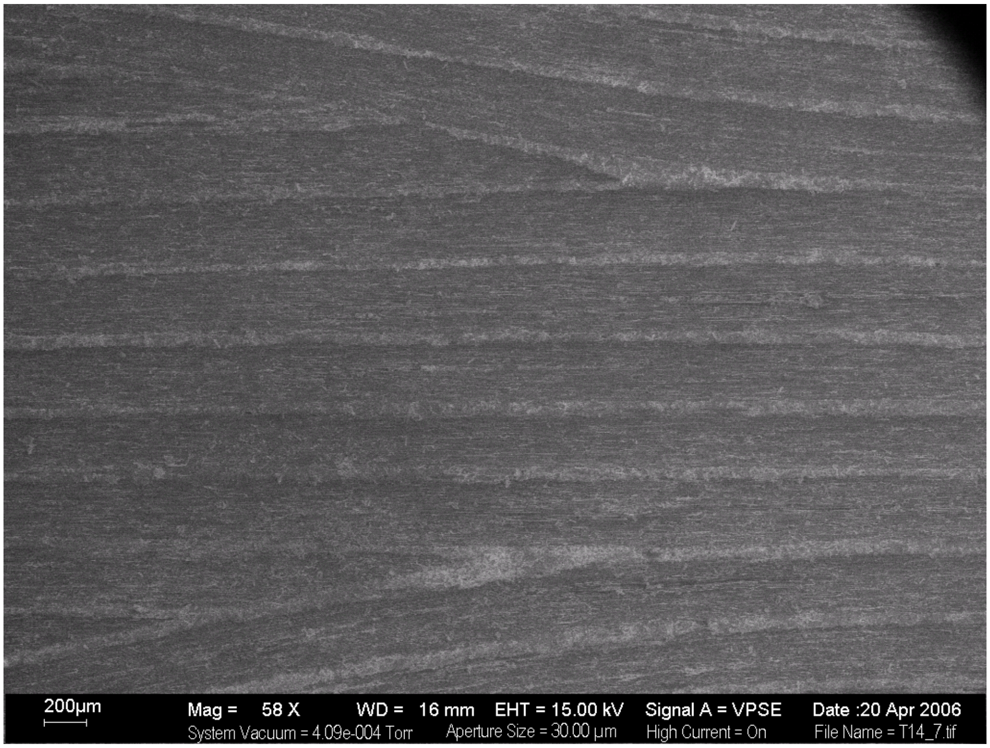

Figure 122: Electron Microscope Image showing both Tips of a Tapered Ply Drop.

Experimental Results

The testing results for the carbon coupons shown in Figure 123 reflect what was expected. All coupons, in both the static and fatigue tests, failed due to the creation of a delamination crack, though the location of these cracks varied, as described later. The tapered ply drop coupons showed a marked improvement over the straight ply drop ones. There is an improvement of over 0.1% strain between the tapered and straight coupons. This translates to over a 17% difference.

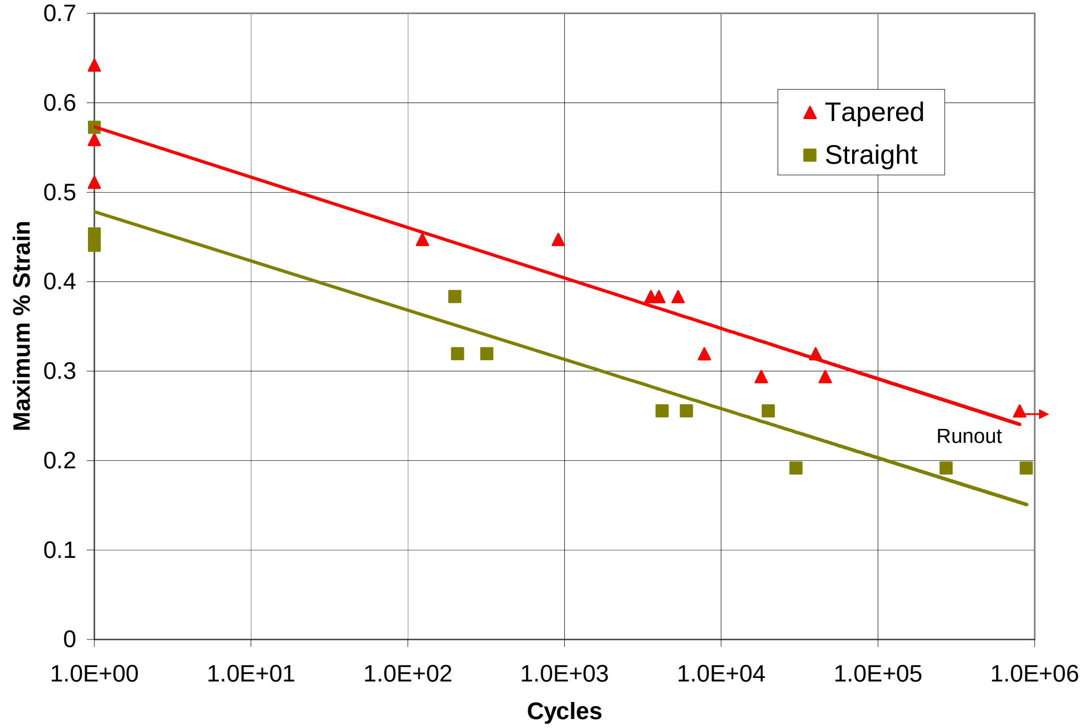

Figure 123: Comparison of 10° Tapered vs. Straight Ply Drops in Carbon Prepreg Samples (Max Strain vs. Cycles to 6.4 mm Delamination).

The data shown in Figure 123 are fit with a logarithmic model, given earlier as Equation 2, with the trend line shown in the figure. Fit parameters for the carbon coupons, in terms of percent strain, are given in Table 48.

Coupon Type	m	b
Tapered Carbon	-0.05987	0.5783
Straight Carbon	-0.05503	0.4784

Table 48: Carbon Coupon Logarithmic Fit Parameters, Percent Strain.

The glass results, Figure 124, were surprising for a number of reasons. With glass, the straight ply drop coupons performed better than the tapered coupons in both the static and fatigue tests, by about 0.3% strain, or a difference of over 12%. In fact, all of the straight ply drop coupons failed catastrophically in the grips, prior to developing delamination cracks. This indicates that performance of the straight ply drop coupons with glass is likely near the performance limits of a glass coupon without a ply drop; a highly unexpected result. However, it is expected that the fatigue resistance of prepreg glass laminates would be much better than materials like QQ1, described earlier [10]. All of the tapered coupons tested in fatigue failed due to the initiation and growth of a delamination crack, though the static tests failures were indistinguishable from grip failures.

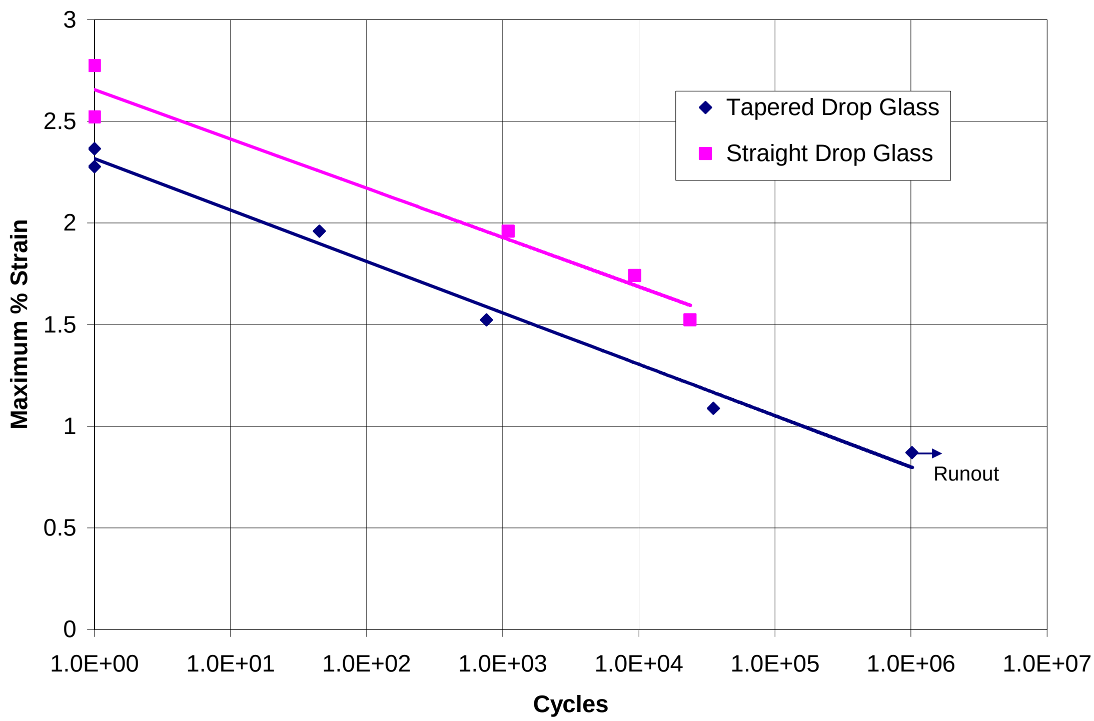

Figure 124: Comparison of Tapered vs. Straight Ply Drops in Glass Prepreg Coupons (Max Stress vs. Cycles to 6.4 mm Delamination).

Table 49 has the fit parameters for Equation 2 for the glass coupons, in terms of percent strain.

Coupon Type	m	b
Tapered Glass	-0.2528	2.316
Straight Glass	-0.2422	2.656

Table 49: Glass Coupon Logarithmic Fit Parameters, Percent Strain.

Another surprising result is that the glass coupons out-performed the carbon coupons. While it was expected that glass would perform better in terms of strain, due to its lower modulus of elasticity, the glass performed better in terms of stress as well, as seen in Figure 125. However, glass showed a greater susceptibility to fatigue, and the best carbon intercepts the worst glass at around a million cycles.

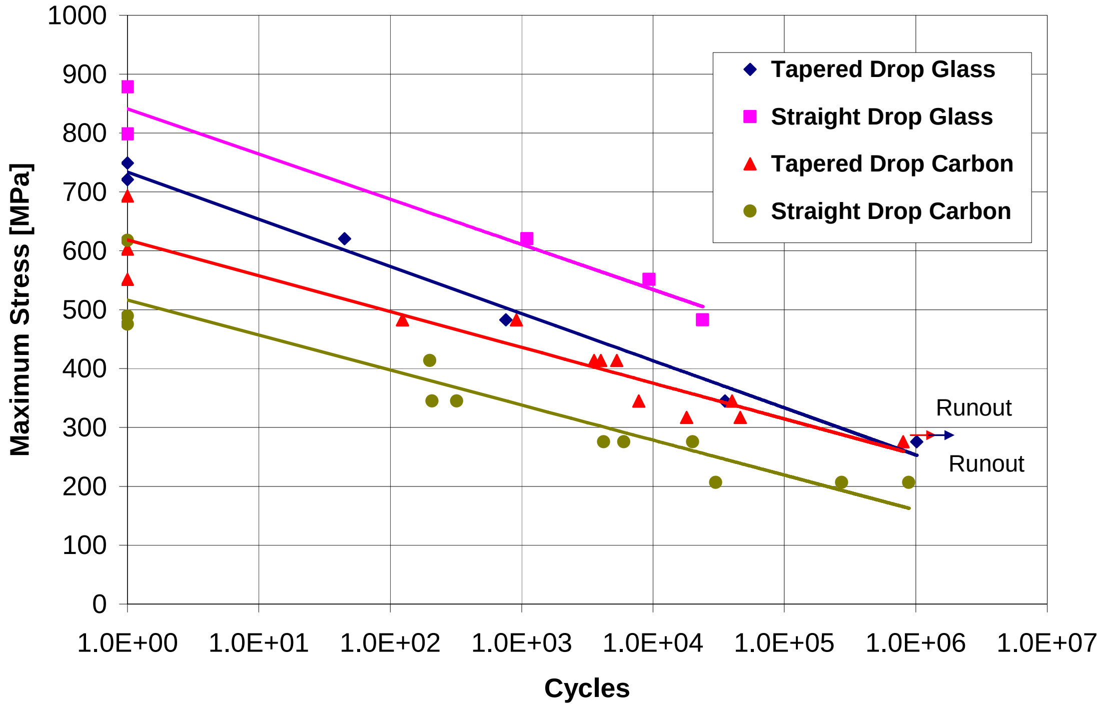

Figure 125: Comparison of Tapered vs. Straight Ply Drops in Glass Prepreg Coupons (Max Stress vs. Cycles to 6.4 mm Delamination).

Fit parameters for the coupons in terms of stress are given in Table 50.

Coupon Type	m	b
Tapered Glass	-80.08	733.7
Straight Glass	-76.73	841.1
Tapered Carbon	-60.79	618.4
Straight Carbon	-59.43	516.2

Table 50: Coupon Logarithmic Fit Parameters, Stress.

Straight Internal Ply Drop, Tapered Ply Drop Study

A model of the straight internal ply drop was created with two cracks on either side of the dropped plies. A schematic of the straight ply drop is shown in Figure 126. The lay-up is $[\pm45_1/0_5/0^*_3/0_5/0^*_3/0_5/\pm45_1]$.

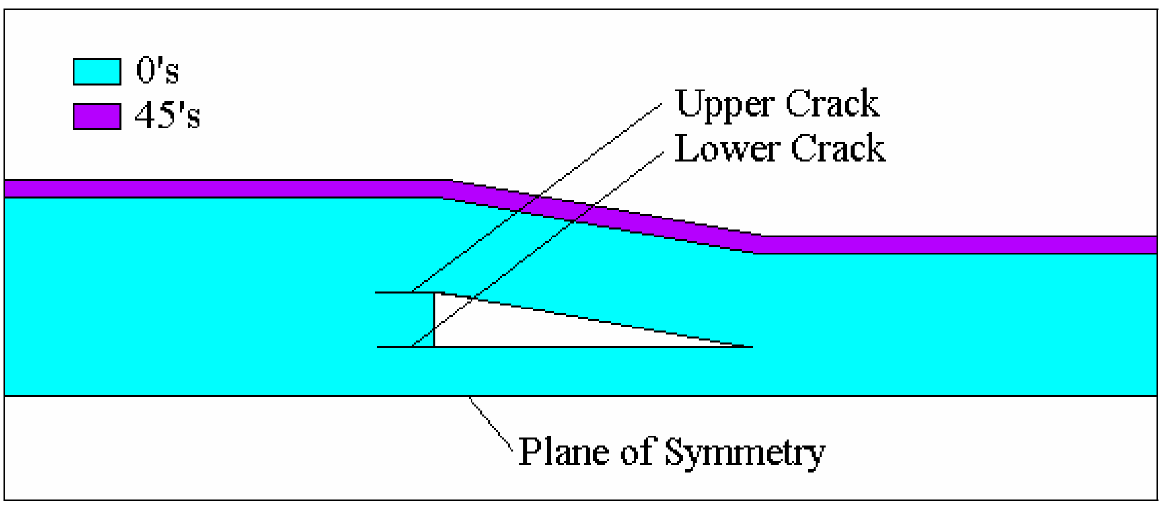

Figure 126: Internal Ply Drop, Tapered Ply Drop Study, $[\pm45_1/0_5/0^*_3/0_5/0^*_3/0_5/\pm45_1]$.

The model included two cracks to simulate the unloading of the dropped plies as the cracks grew. All models were loaded under tension, as this is how the physical test specimens were loaded. Included in this study was an examination of how the taper angle affects G values.

Straight Internal Ply Drop, Tapered Ply Drop Study, Carbon, Tension. Figure 127 and Figure 128 and Table 51 show results from the internal ply drop model of the ply drop project, with carbon 0's, loaded in tension. These results show the typical low G_I values of a model under tensile loading. The differences between the G_{II} values of the upper and lower cracks mean that the cracks will not grow at the same rate, contrary to what was assumed. For longer cracks, the G_{II} values for both cracks were slightly above the values for two internal ply drops in Figure 89.

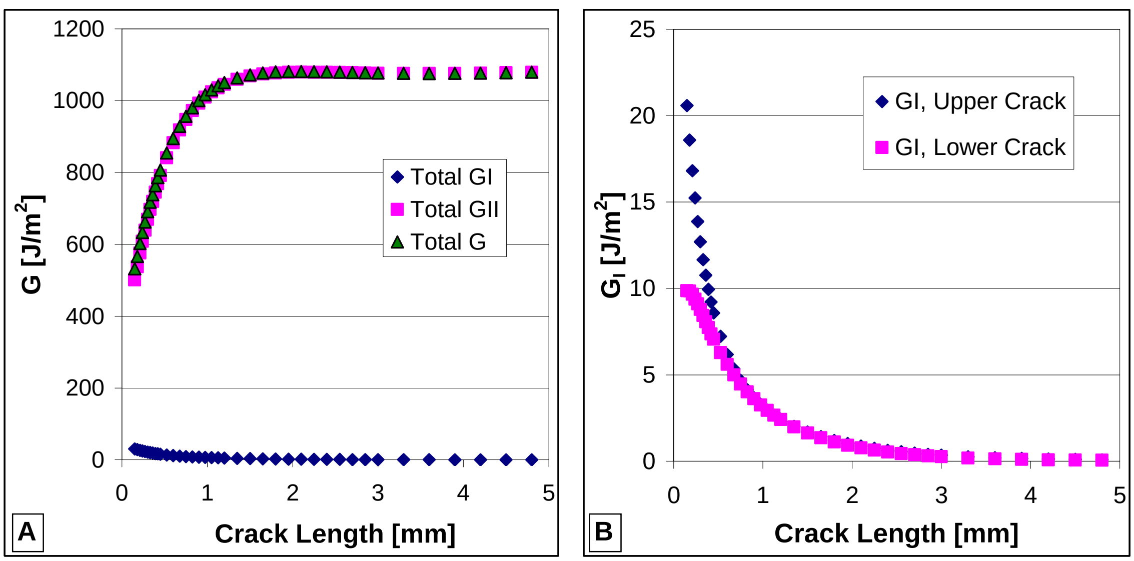

Figure 127: Internal Ply Drop, Tapered Ply Drop Study, Carbon, Tension. A: Total G vs. Crack Length; B: G_I vs. Crack Length; Applied Stress = 590.0 MPa.

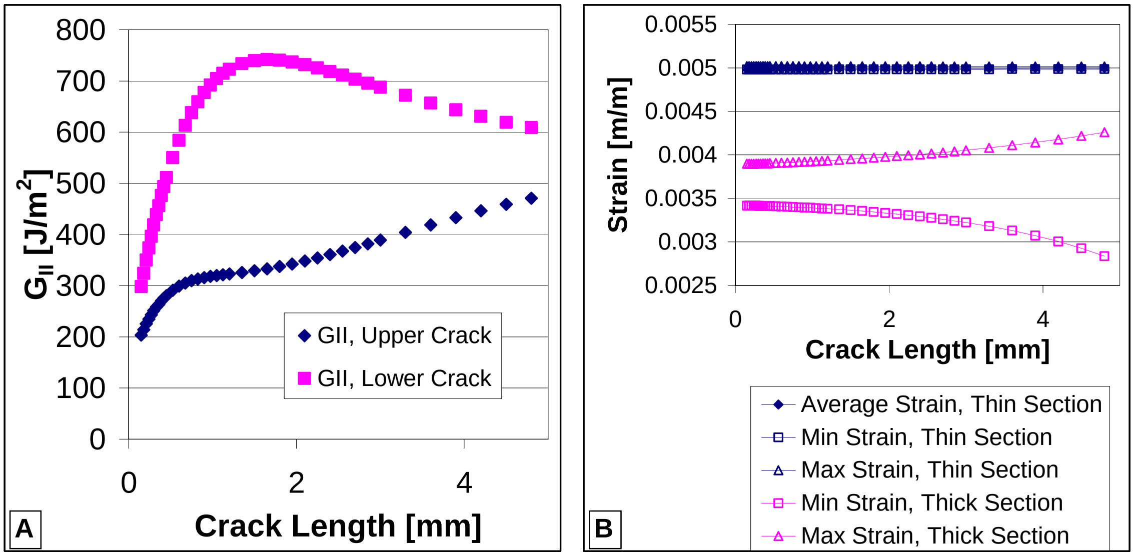

Figure 128: Internal Ply Drop, Tapered Ply Drop Study, Carbon, Tension. A: G_{II} vs. Crack Length; B: Far Field Strain vs. Crack Length; Applied Stress = 590.0 MPa.

	Maximum [J/m^2]	Crack Length at Maximum G [mm]	Average [J/m^2] (0.15 – 3.0 mm)
Total G	1081.7	2.1	1005.3
G_I, Upper Crack	20.6	0.15	3.3
G_I, Lower Crack	9.9	0.15	2.6
G_{II}, Upper Crack	470.7	4.8	329.1
G_{II}, Lower Crack	741.6	1.65	670.3

Table 51: Internal Ply Drop, Tapered Ply Drop Study, Carbon, Tension, Maximum and Average G.

Straight Internal Ply Drop, Tapered Ply Drop Study, Glass, Tension. Figure 129 and Figure 130 and Table 52 are results from the internal ply drop model of the ply drop project, with glass 0's, loaded in tension. The G_{II} values for the glass model are closer together than those of the carbon model. This may indicate that the cracks in glass delaminations will tend to be closer together as the delaminations progress.

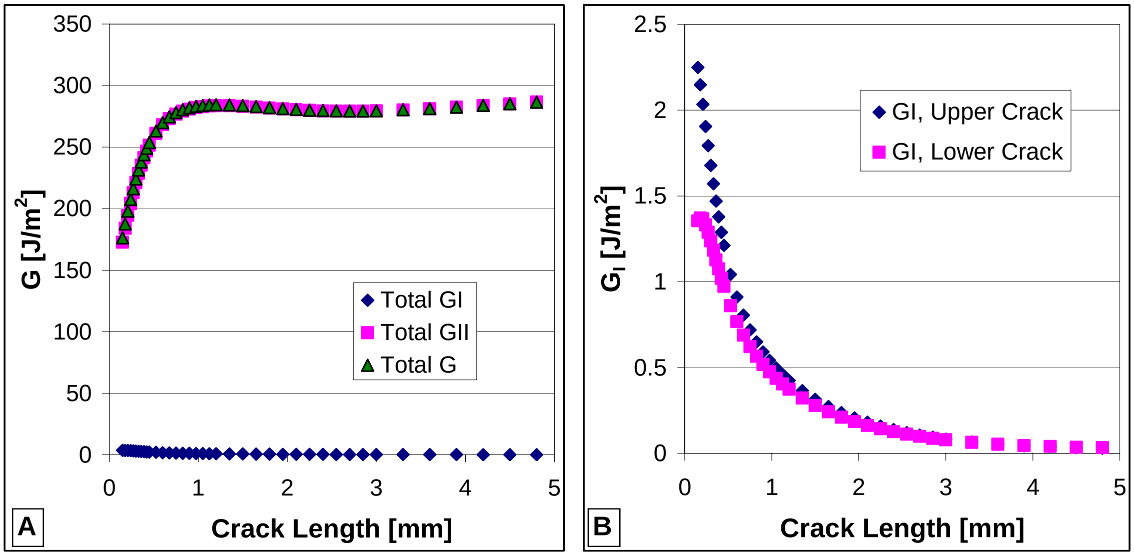

Figure 129: Internal Ply Drop, Tapered Ply Drop Study, Glass, Tension. A: Total G vs. Crack Length; B: G_I vs. Crack Length; Applied Stress = 156.9 MPa.

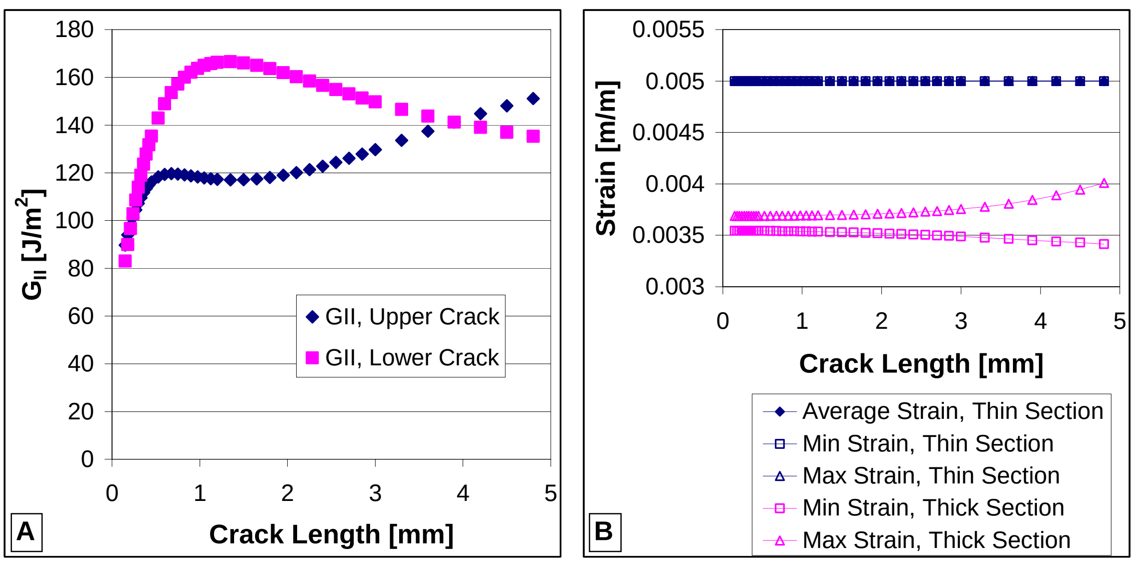

Figure 130: Internal Ply Drop, Tapered Ply Drop Study, Glass, Tension. A: G_{II} vs. Crack Length; B: Far Field Strain vs. Crack Length; Applied Stress = 156.9 MPa.

	Maximum [J/m^2]	Crack Length at Maximum G [mm]	Average [J/m^2] (0.15 – 3.0 mm)
Total G	286.6	4.8	273.8
G_I, Upper Crack	2.2	0.15	0.5
G_I, Lower Crack	1.4	0.18	0.4
G_{II}, Upper Crack	151.2	4.8	118.9
G_{II}, Lower Crack	166.6	1.35	154.0

Table 52: Internal Ply Drop, Tapered Ply Drop Study, Glass, Tension, Maximum and Average G.

Straight Internal Ply Drop, Tapered Ply Drop Study, Carbon, Tension, Influence of Taper Angle. Figure 131 and Figure 132 are results from the internal ply drop model of the ply drop project examining the influence of taper angle on G values. These results are for carbon 0's, loaded in tension, with 1.5 mm cracks present. These values show that reducing the angle of the taper will reduce the total G values present in a delamination crack. G_I values are, as expected for a tensile loaded model, low. There is an interesting trend present in the G_{II} values. The total G_{II} goes down with decreasing taper angle, but the G_{II} values for the upper crack go up. However, even at low taper angles, the G_{II} of the upper crack is still lower than the G_{II} of the upper crack, indicating that the lower crack is more likely.

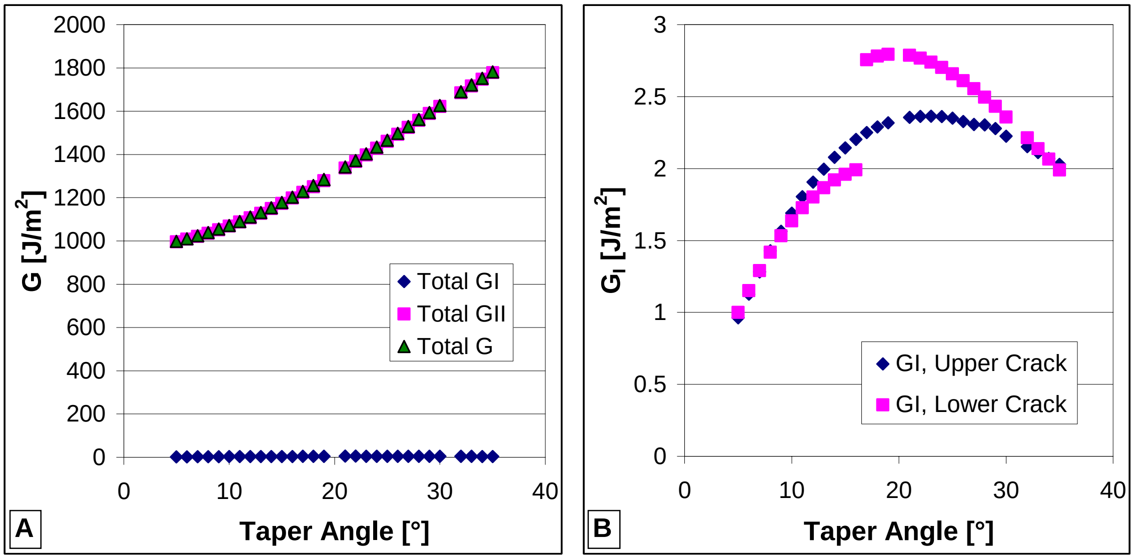

Figure 131: Internal Ply Drop, Tapered Ply Drop Study, Carbon, Tension, Cracks are 1.5 mm. A: Total G vs. Taper Angle; B: G_I vs. Taper Angle; Applied Stress = 590.0 MPa.

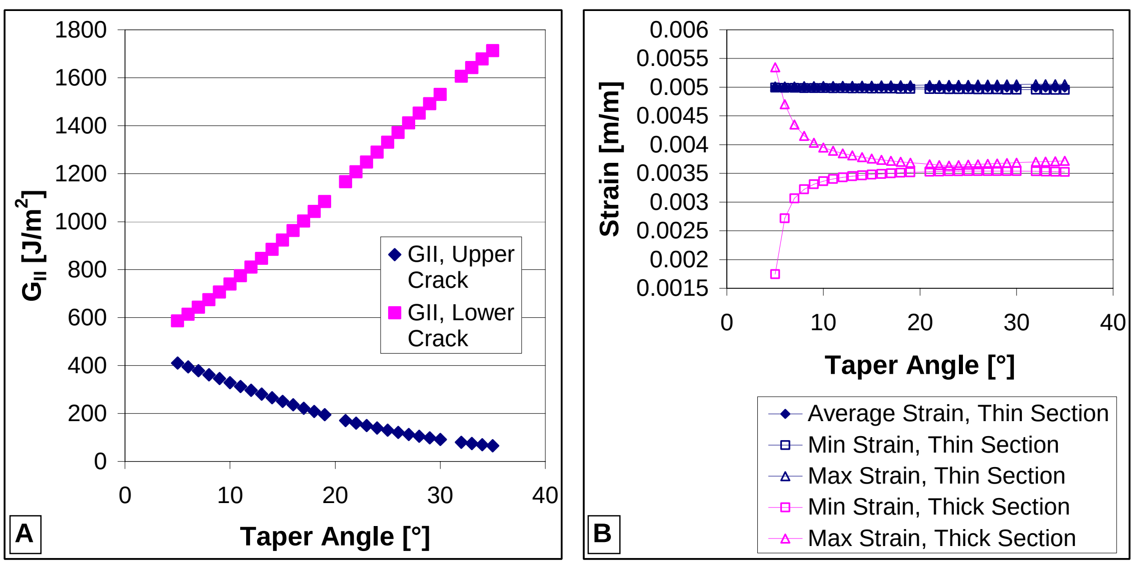

Figure 132: Internal Ply Drop, Tapered Ply Drop Study, Carbon, Tension, Cracks are 1.5 mm. A: G_{II} vs. Taper Angle; B: Far Field Strain vs. Taper Angle; Applied Stress = 590.0 MPa.

Straight Internal Ply Drop, Tapered Ply Drop Study, Glass, Tension, Influence of Taper Angle. Figure 133 and Figure 134 are results examining the influence of taper angle from the internal ply drop model of the ply drop project, with glass 0's, loaded in tension, with 1.5 mm cracks. The trends present in the glass results for G versus taper angle mirror those found in the carbon model.

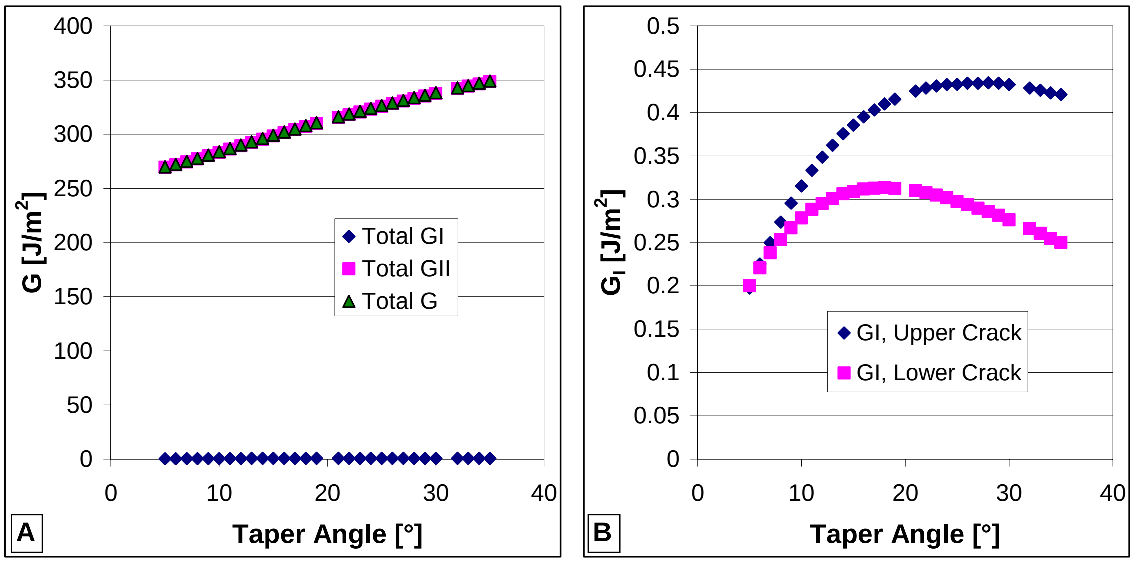

Figure 133: Internal Ply Drop, Tapered Ply Drop Study, Glass, Tension, Cracks are 1.5 mm. A: Total G vs. Taper Angle; B: G_I vs. Taper Angle; Applied Stress = 156.9 MPa.

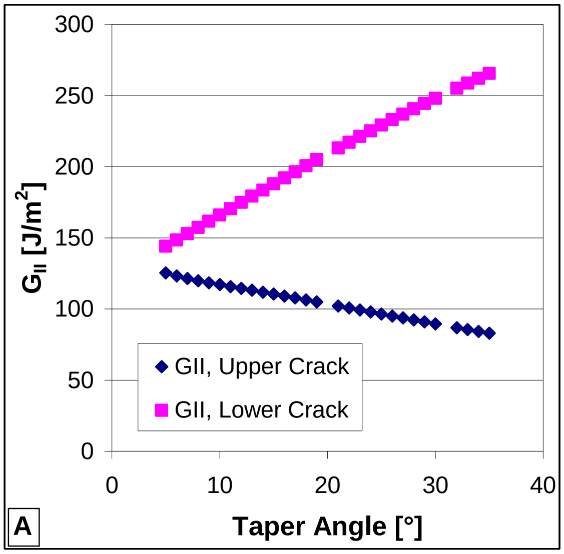

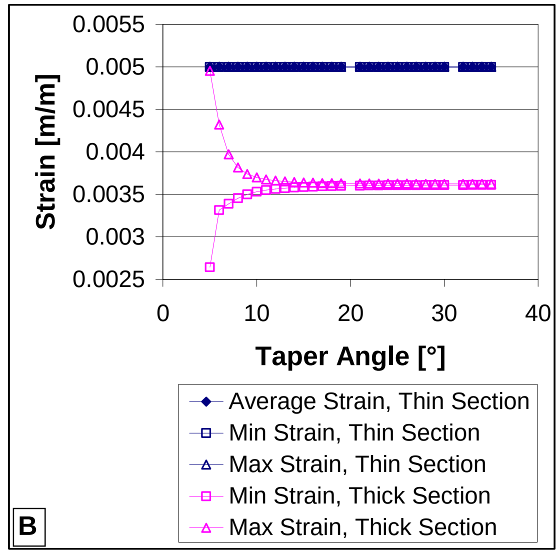

Figure 134: Internal Ply Drop, Tapered Ply Drop Study, Glass, Tension, Cracks are 1.5 mm. A: G_{II} vs. Taper Angle; B: Far Field Strain vs. Taper Angle; Applied Stress = 156.9 MPa.

<u>Tapered Ply Drop</u>

The tapered ply drop model assumes cracks that initiate at the apex of the taper, thus beginning at the same point, as shown in Figure 135. This model grows two cracks simultaneously, to simulate the unloading of the dropped plies as the cracks grow. The lay-up is [$\pm45_1/0_5/0*_3/0_5/0*_3/0_5/\pm45_1$].

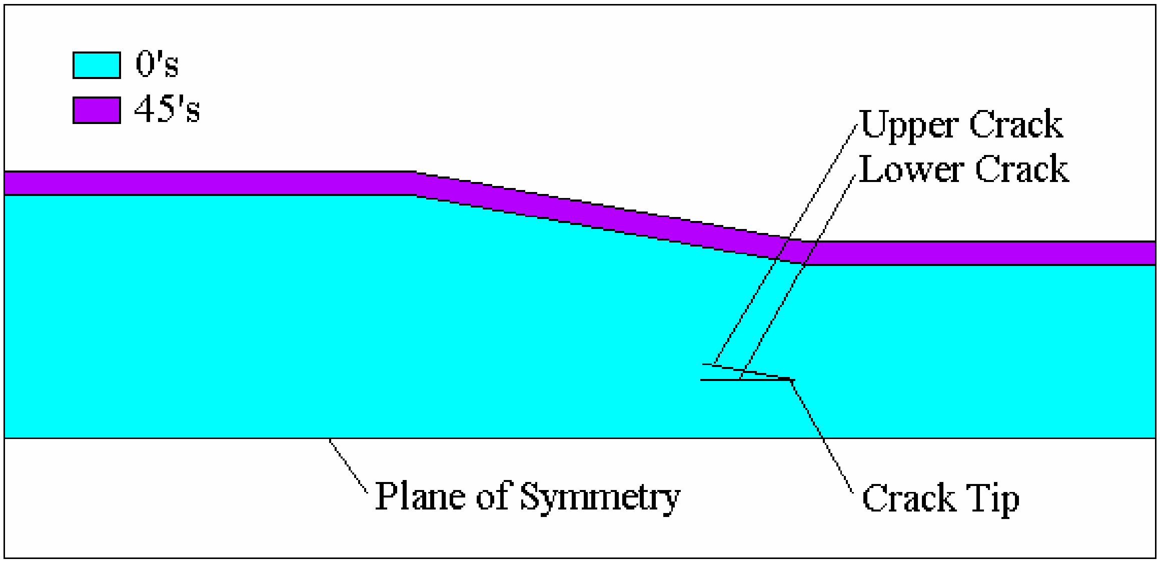

Figure 135: Tapered Ply Drop, [$\pm 45_1/0_5/0^*_3/0_5/0^*_3/0_5 \pm 45_1$].

Crack lengths in these results begin at 0.36 mm, different than the 0.15 mm initial crack length of the other models, because of meshing problems. Because the cracks in the model initiate in the same place, it is difficult to mesh near the tip of the taper with short cracks.

Tapered Ply Drop, Carbon, Tension. Figure 136 and Figure 137 and Table 53 are results from the tapered ply drop model of the ply drop project, with carbon 0's, loaded in tension. Compared to the corresponding internal ply drop model, (Figure 127 and Figure 128, Table 51), the tapered ply drop results show lower G values at short crack lengths, indicating that the taper will reduce initiation of delamination cracks.

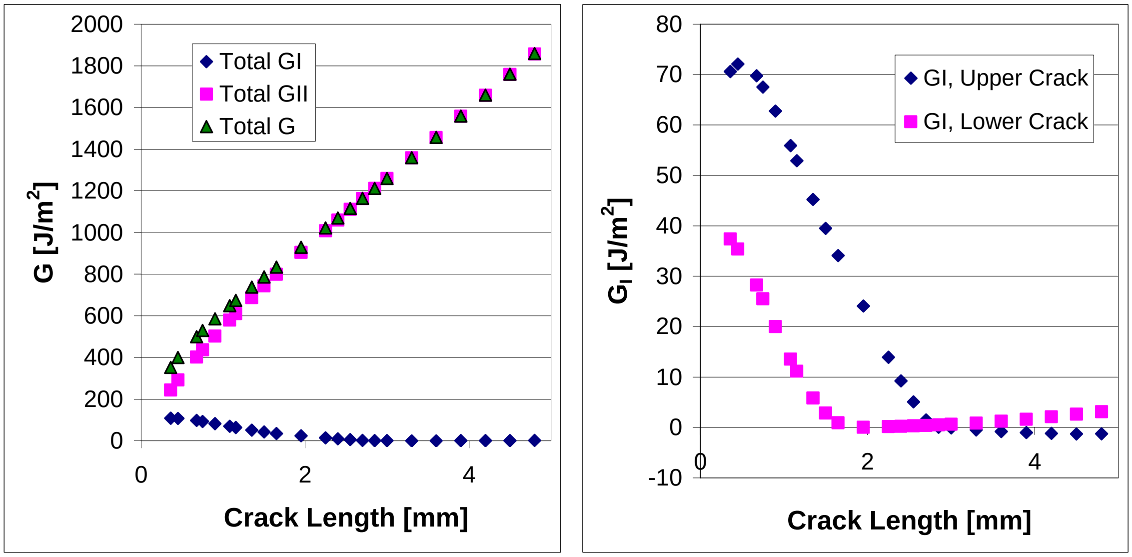

Figure 136: Tapered Ply Drop, Carbon, Tension. A: Total G vs. Crack Length; B: G_I vs. Crack Length; Applied Stress = 590.0 MPa.

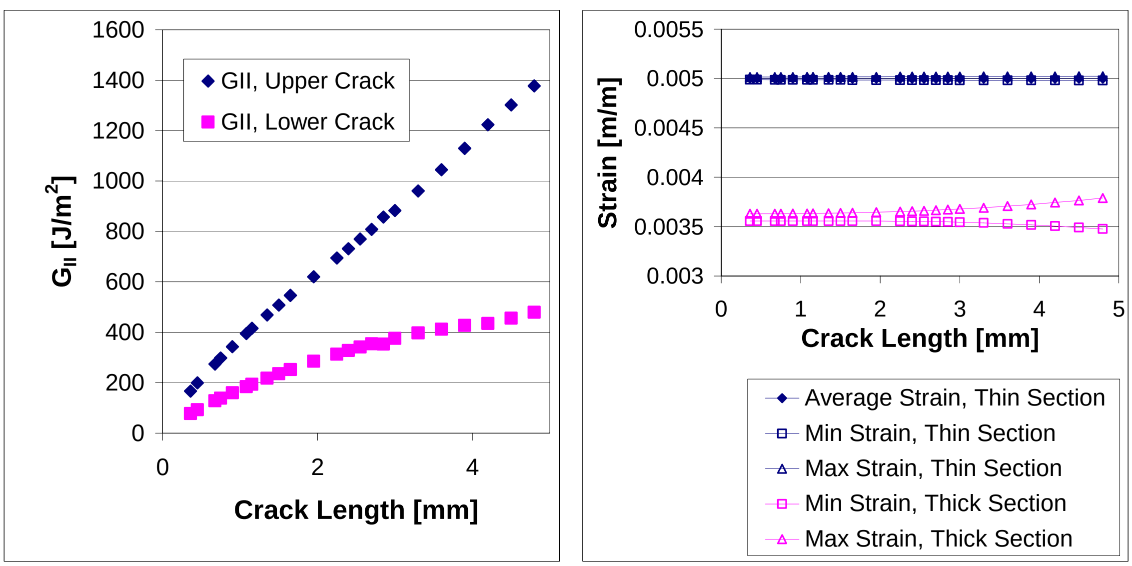

Figure 137: Tapered Ply Drop, Carbon, Tension. A: G_{II} vs. Crack Length; B: Far Field Strain vs. Crack Length; Applied Stress = 590.0 MPa.

	Maximum [J/m^2]	Crack Length at Maximum G [mm]	Average [J/m^2] (0.36 – 3.0 mm)
Total G	1858.3	4.8	834.7
G_I, Upper Crack	72.0	0.45	34.6
G_I, Lower Crack	37.4	0.36	8.7
G_{II}, Upper Crack	1377.1	4.8	545.5
G_{II}, Lower Crack	479.3	4.8	245.9

Table 53: Tapered Ply Drop, Carbon, Tension, Maximum and Average G.

Tapered Ply Drop, Glass, Tension. Figure 138 and Figure 139 and Table 54 are results from the tapered ply drop model with glass 0’s, loaded in tension. Again, these results indicate the taper will reduce initiation of delamination cracks, compared with the corresponding internal ply drop model.

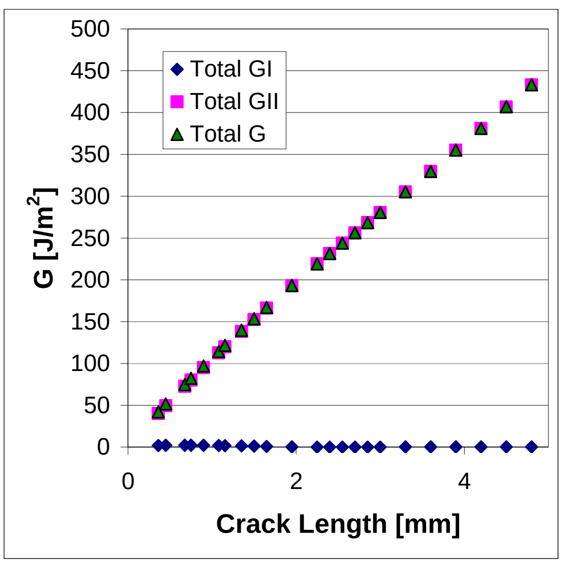

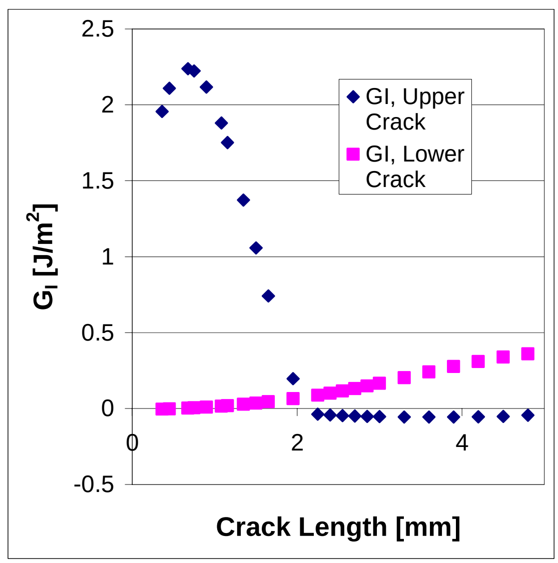

Figure 138: Tapered Ply Drop, Glass, Tension. A: Total G vs. Crack Length; B: G_I vs. Crack Length; Applied Stress = 157.5 MPa.

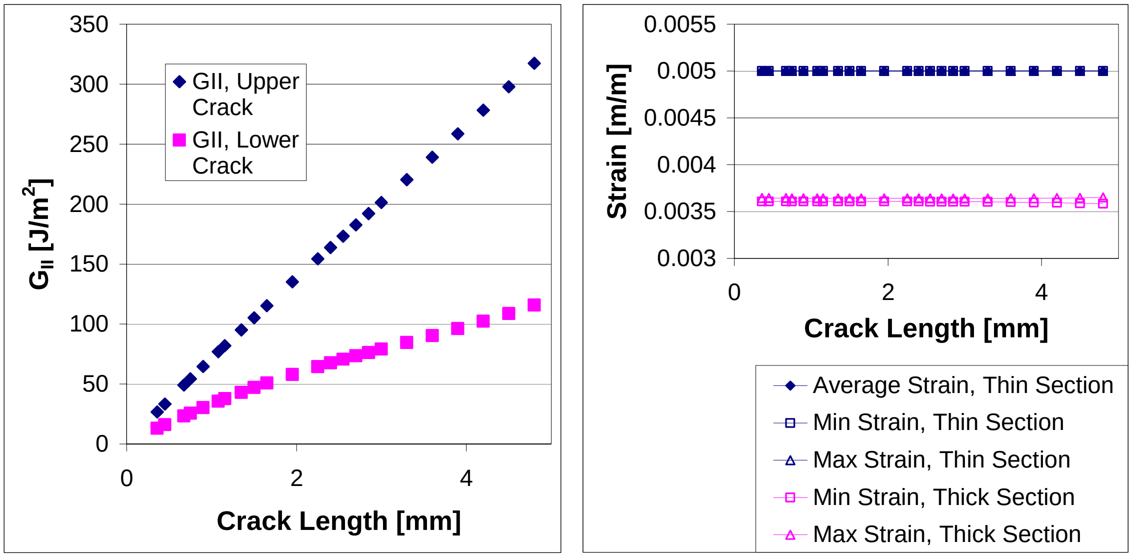

Figure 139: Tapered Ply Drop, Glass, Tension. A: G_{II} vs. Crack Length; B: Far Field Strain vs. Crack Length; Applied Stress = 157.5 MPa.

	Maximum [J/m^2]	Crack Length at Maximum G [mm]	Average [J/m^2] (0.36 – 3.0 mm)
Total G	433.4	4.8	166.9
G_I, Upper Crack	2.2	0.675	0.9
G_I, Lower Crack	0.4	4.8	0.1
G_{II}, Upper Crack	317.3	4.8	116.2
G_{II}, Lower Crack	115.8	4.8	49.7

Table 54: Tapered Ply Drop, Glass, Tension, Maximum and Average G.

<u>Tapered Ply Drop, Carbon, Tension, Influence of Taper Angle</u>. Figure 140 and Figure 141 are results from examining the influence of taper angle on the tapered ply drop model of the ply drop project with carbon 0's, loaded in tension, with 1.5 mm cracks. These results indicate that the taper angle affects G values significantly, just as in the interior ply drop model. There are further benefits to reducing the taper angle beyond 10°, though manufacturing becomes more of an issue past this point

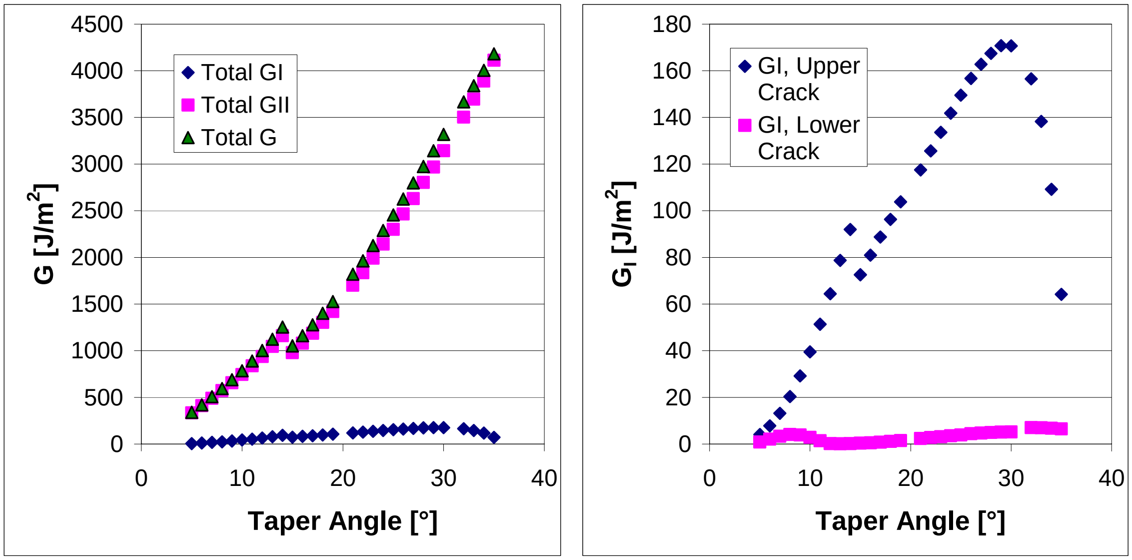

Figure 140: Tapered Ply Drop, Carbon, Tension, Cracks are 1.5 mm. A: Total G vs. Taper Angle; B: G_I vs. Taper Angle; Applied Stress = 590.0 MPa.

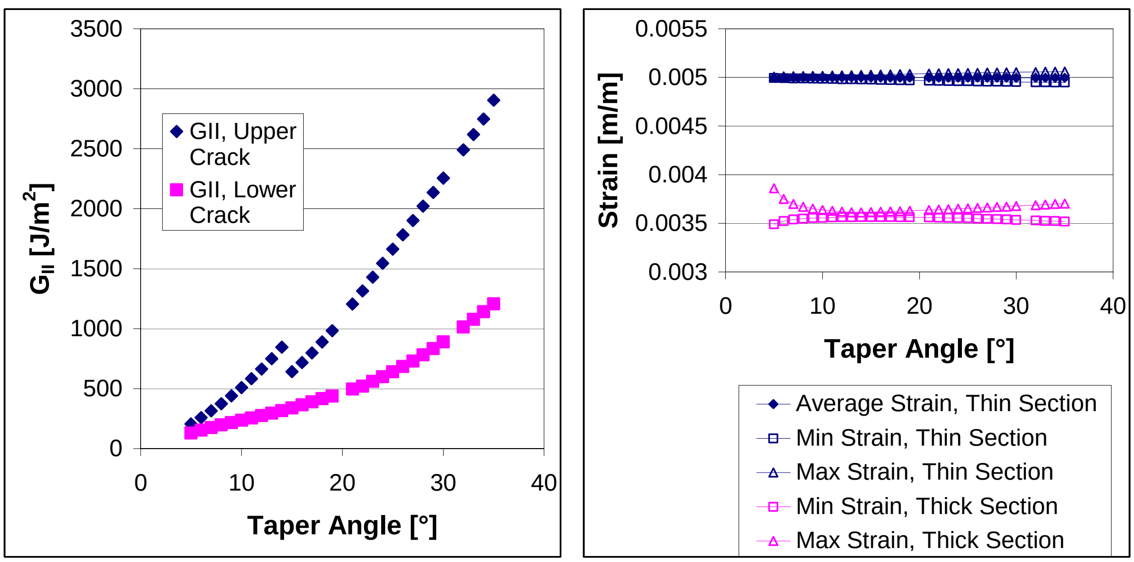

Figure 141: Tapered Ply Drop, Carbon, Tension, Cracks are 1.5 mm. A: G_{II} vs. Taper Angle; B: Far Field Strain vs. Taper Angle; Applied Stress = 590.0 MPa.

Tapered Ply Drop, Glass, Tension, Influence of Taper Angle. Figure 142 and Figure 143 are results from the tapered ply drop with glass 0's, loaded in tension, with

1.5 mm cracks. The conclusions drawn from these results mirror those from the carbon model.

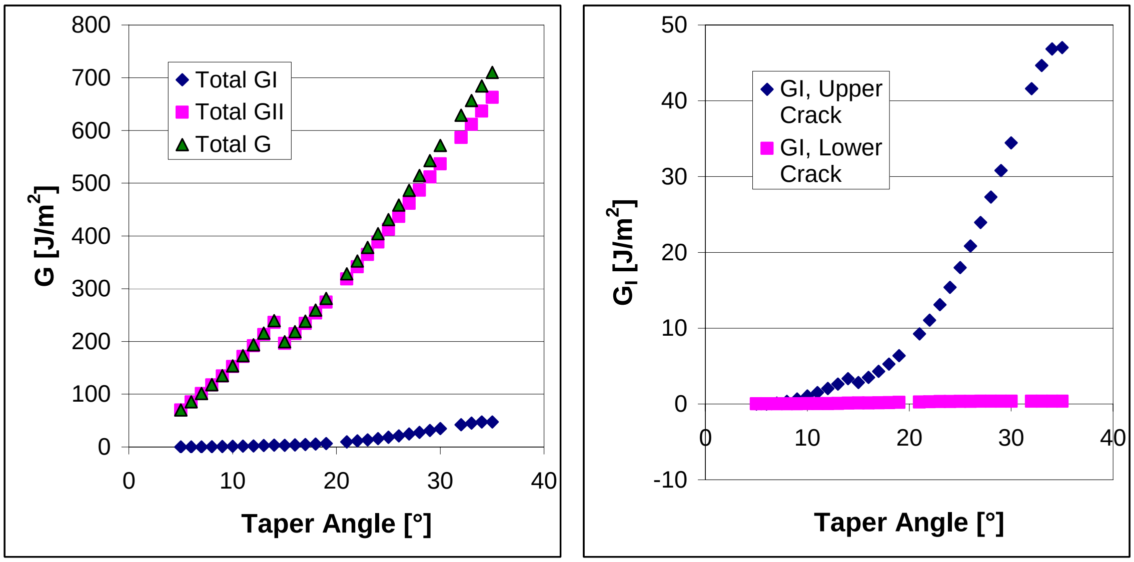

Figure 142: Tapered Ply Drop, Glass, Tension, Cracks are 1.5 mm. A: Total G vs. Taper Angle; B: G_I vs. Taper Angle; Applied Stress = 157.5 MPa.

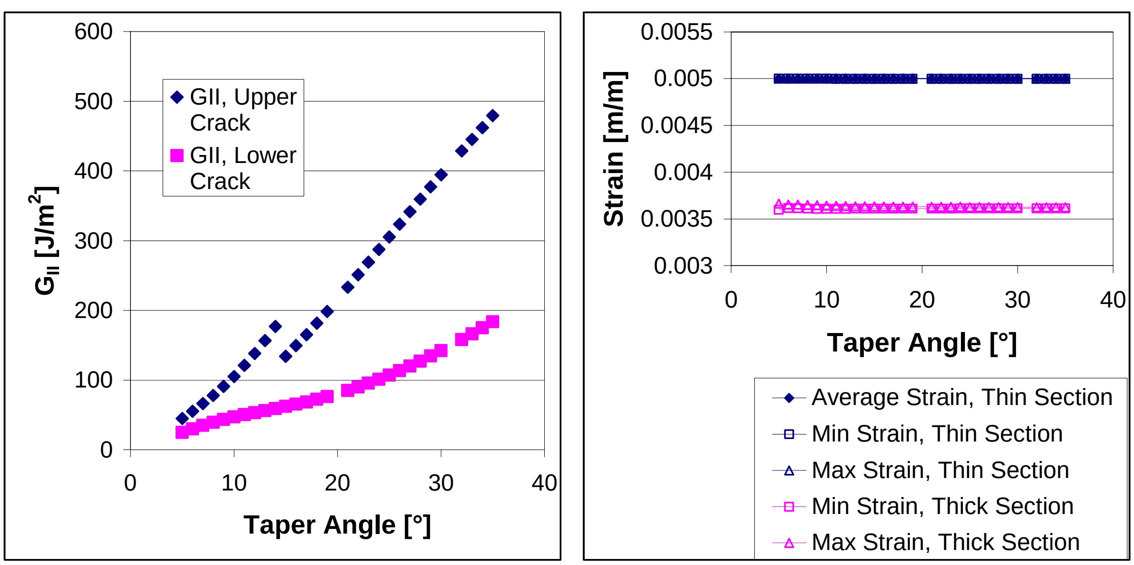

Figure 143: Tapered Ply Drop, Glass, Tension, Cracks are 1.5 mm. A: G_{II} vs. Taper Angle; B: Far Field Strain vs. Taper Angle; Applied Stress = 157.5 MPa.

Experimental Observations

It was assumed in the FEA models that the cracks were going to initiate and grow at the apex of the ply drop in the tapered coupons and at the end of the dropped plies in the straight coupons. This is reflected in the location of the cracks in the ANSYS models. In reality, the cracks did not always grow at these locations, as seen in Figure 144, Figure 145, and Figure 146.

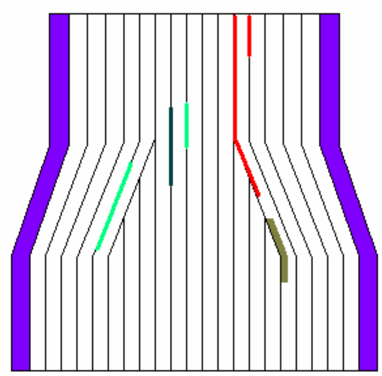

Figure 144: Crack locations, Carbon, Tapered Ply Drop.

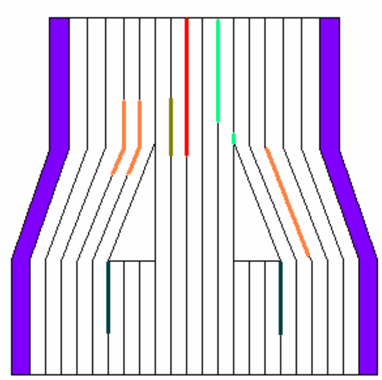

Figure 145: Crack Location, Carbon, Straight Ply Drop.

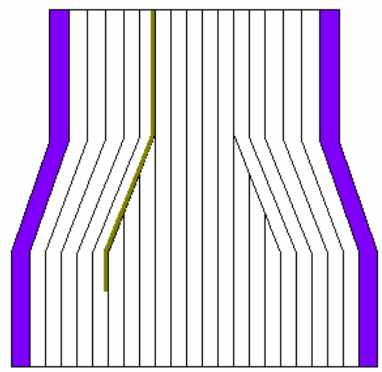

Figure 146: Crack Location, Glass, Tapered Ply Drop.

Furthermore, the cracks that did develop did not behave as expected. It was assumed that two delamination cracks would grow along the dropped plies, unloading these plies as they grew. This would be a mode II dominated growth pattern. Many of the cracks that did develop were single cracks, often in the center plies. This is indicative of a mode I domination. They were often observed on the thin side of the coupon.

Numerical Observations

Crack behavior seen experimentally was different from what was modeled. What was deemed as a stronger mode I influence than predicted was seen as the cause of the cracks opening in many different locations. Therefore, an examination of ply strains was done to examine the validity of the crack behavior assumptions.

Figure 147 shows the tip of the ply drop in the tapered ply drop model with no cracks. Maximum transverse strain is plotted. The circular region where the two predicted cracks intersect indicates that the maximum transverse strain, which will cause a mode I crack to open. This indicates that a crack started due to mode I influence would tend to initiate here, as expected.

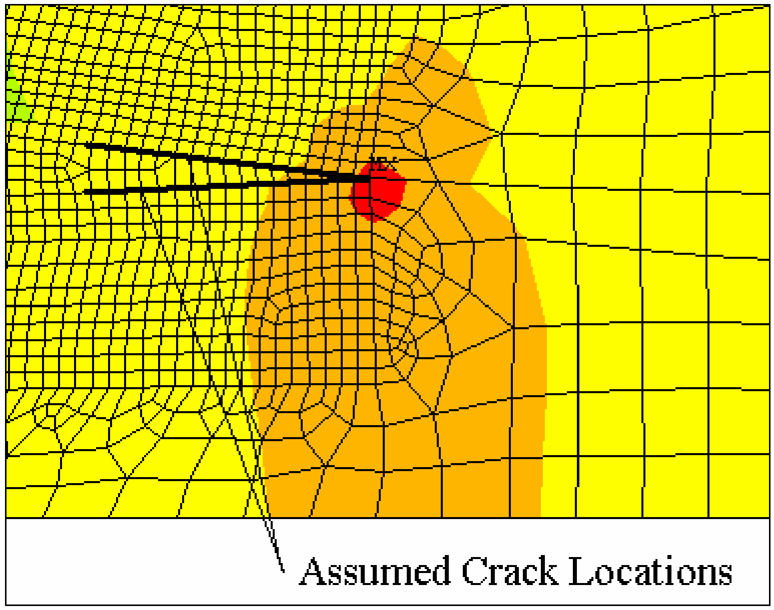

Figure 147: Tapered Ply Drop Model, Carbon, No Cracks, Transverse Strain.

Figure 148 adds the expected crack geometry to the model shown in Figure 147. However, rather than seeing the maximum transverse strain at the tip of the cracks, the maximum occurs at the tip of the taper, indicating that the crack would be more likely to grow in this direction, contrary to what was assumed.

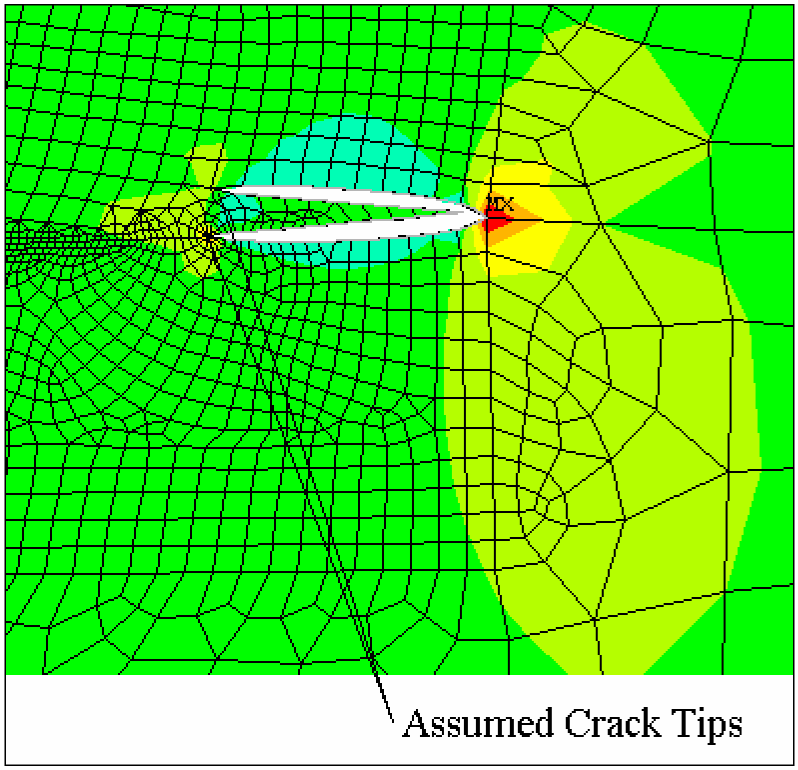

Figure 148: Tapered Ply Drop, Carbon, 0.36 mm Crack, Transverse Strain.

APPENDIX C:

ADDITIONAL FEA RESULTS

This appendix includes FEA runs of interest, which were not described in the body of the thesis.

Central Ply Drop

Glass, Compression. Results from the central ply drop, with one ply dropped, glass 0's, loaded in compression are given as Figure 149 and Table 55. The average G_I makes up 22.7% of the total average G.

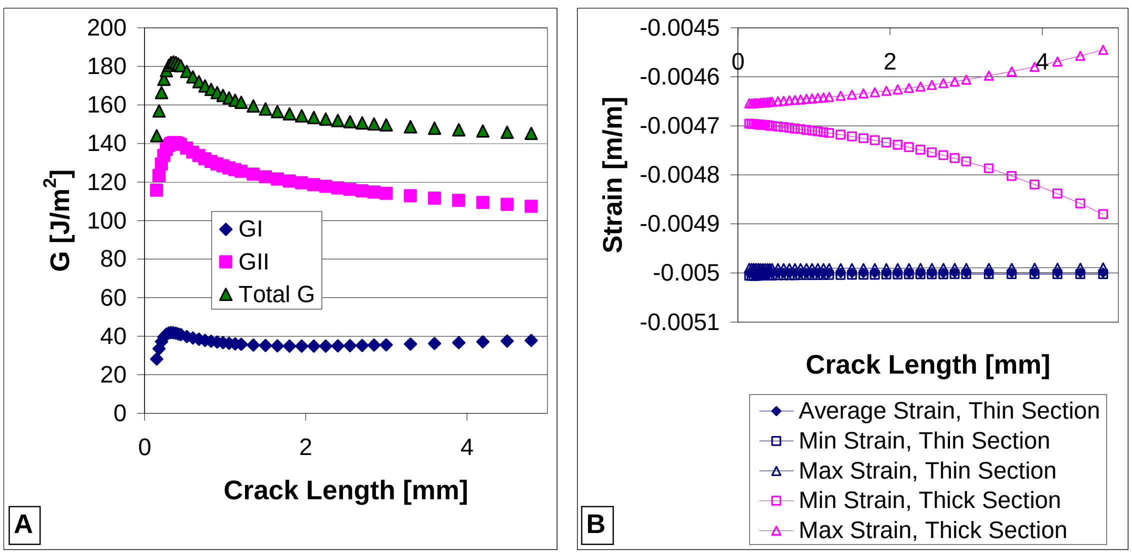

Figure 149: Central Ply Drop, 1 Ply Dropped, Glass, Compression. A: G vs. Crack Length; B: Strain vs. Crack Length.

	Maximum [J/m^2]	Crack Length at Maximum G [mm]	Average [J/m^2] (0.15 – 3.0 mm)
Total G	182.3	0.36	160.2
G_I	41.9	0.33	36.3
G_{II}	140.4	0.36	123.9

Table 55: Central Ply Drop, 1 Ply Dropped, Glass, Compression, Maximum and Average G.

Figure 150 and Table 56 are results from the central ply drop model, with two plies dropped, glass 0's, and loaded in compression. G_I is 27.8% of total G, higher than the one ply dropped model, though not significantly.

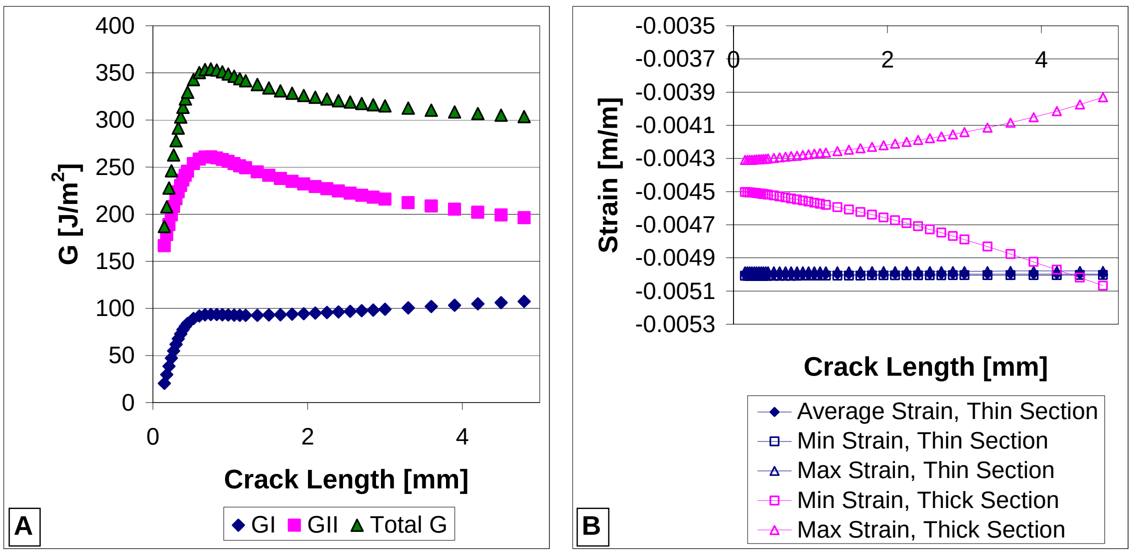

Figure 150: Central Ply Drop, 2 Plies Dropped, Glass, Compression. A: G vs. Crack Length; B: Strain vs. Crack Length.

	Maximum [J/m^2]	Crack Length at Maximum G [mm]	Average [J/m^2] (0.15 – 3.0 mm)
Total G	354.2	0.75	325.7
G_I	107.3	4.8	90.4
G_{II}	260.7	0.75	235.2

Table 56: Central Ply Drop, 2 Plies Dropped, Glass, Compression, Maximum and Average G.

<u>Glass, Tension</u>. Figure 151 and Table 57 are results from the central ply drop model, with one ply dropped, glass 0's, and loaded in tension.

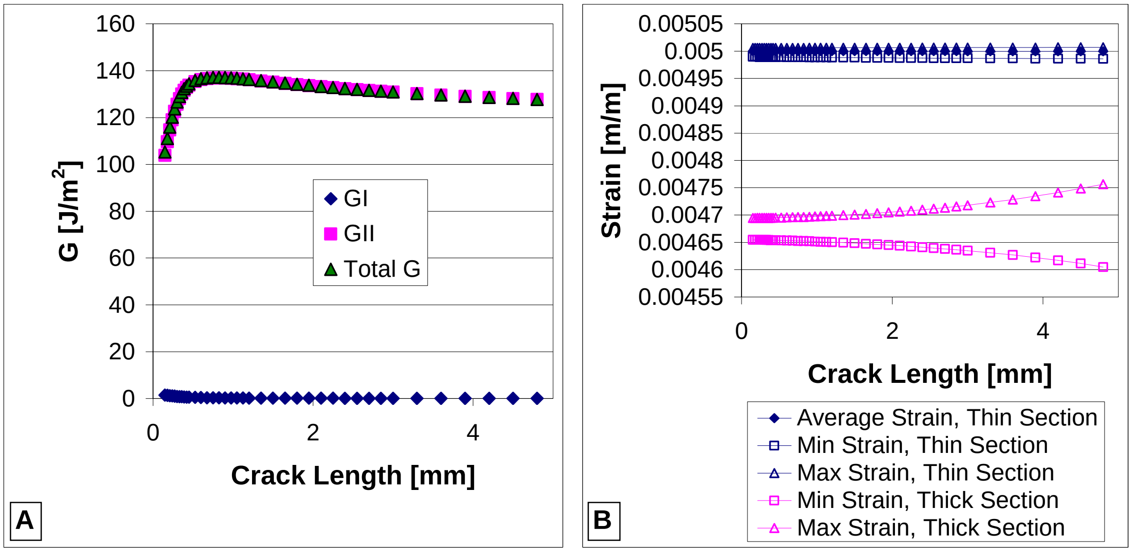

Figure 151: Central Ply Drop, 1 Ply Dropped, Glass, Tension. A: G vs. Crack Length; B: Strain vs. Crack Length.

	Maximum [J/m^2]	Crack Length at Maximum G [mm]	Average [J/m^2] (0.15 – 3.0 mm)
Total G	137.2	0.825	133.3
G_I	1.5	0.15	0.3
G_{II}	136.9	0.825	133.0

Table 57: Central Ply Drop, 1 Ply Dropped, Glass, Tension, Maximum and Average G.

Figure 152 and Table 58 are results from the central ply drop model, with two plies dropped, glass 0’s, tension. The total G for this model is 1.8 times the one ply dropped model.

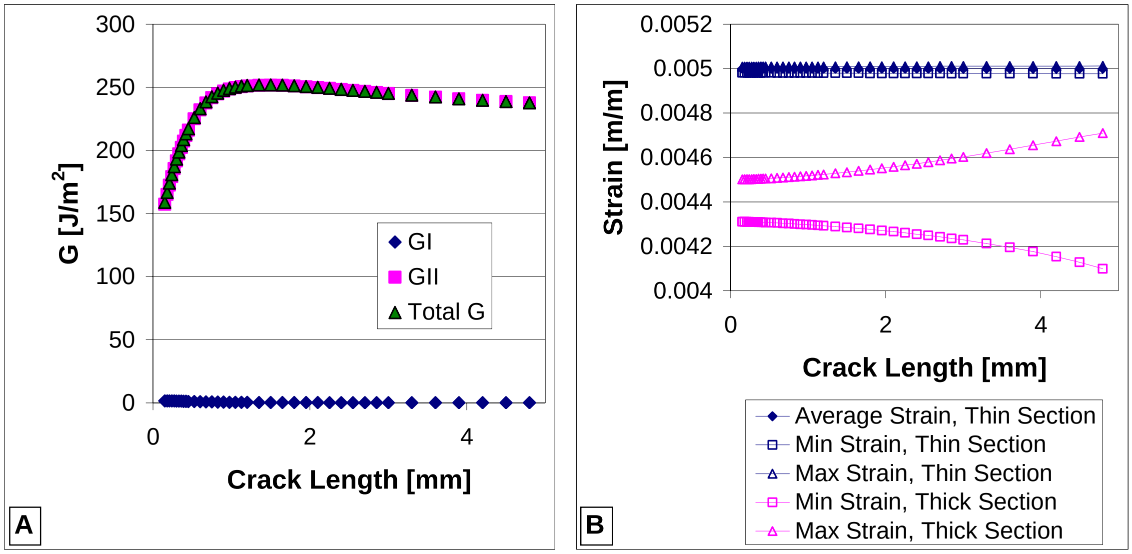

Figure 152: Central Ply Drop, 2 Plies Dropped, Glass, Tension. A: G vs. Crack Length; B: Strain vs. Crack Length.

	Maximum [J/m^2]	Crack Length at Maximum G [mm]	Average [J/m^2] (0.15 – 3.0 mm)
Total G	251.9	1.5	241.3
G_I	1.6	0.18	0.5
G_{II}	251.6	1.5	240.8

Table 58: Central Ply Drop, 2 Plies Dropped, Glass, Tension, Maximum and Average G.

Internal Ply Drop

Carbon, Tension. Figure 153 and Table 59 show results from the internal ply drop model, with carbon, loaded in tension, with the lower crack suppressed. G values for this model are lower than the same model with the upper crack suppressed, indicating that this crack will grow slower than the lower crack.

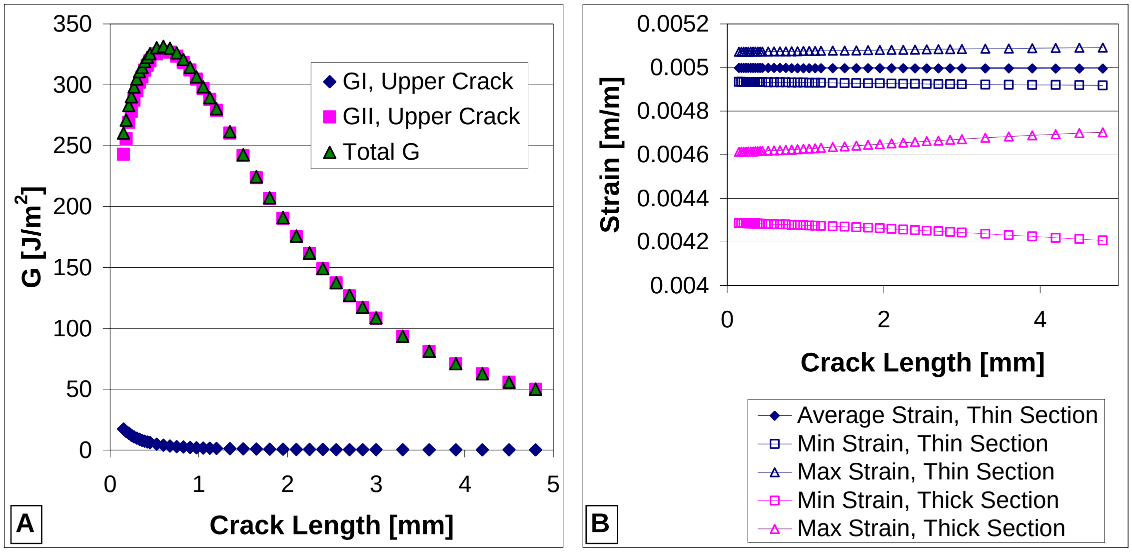

Figure 153: Internal Ply Drop, Carbon, Tension, Lower Crack Suppressed. A: G vs. Crack Length; B: Strain vs. Crack Length.

	Maximum [J/m^2]	Crack Length at Maximum G [mm]	Average [J/m^2] (0.15 – 3.0 mm)
Total G	331.5	0.6	229.8
G_I, Upper Crack	17.3	0.15	2.2
G_{II}, Upper Crack	327.5	0.6	227.6

Table 59: Internal Ply Drop, Carbon, Tension, Lower Crack Suppressed, Maximum and Average G.

Results from the internal ply drop model, with carbon 0's, loaded in tension, with the upper crack suppressed are given in Figure 154 and Table 60. These results, as well as from the lower crack suppressed model, are interesting, because the G values drop off as the crack length increases. This is different than the model with both cracks present, which maintains higher G values at longer crack lengths.

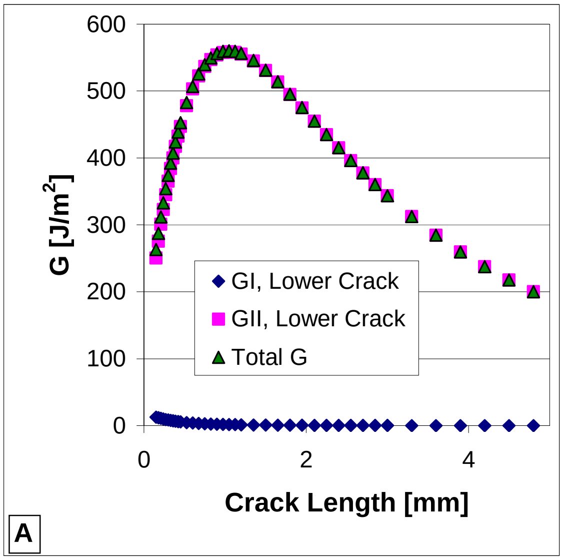

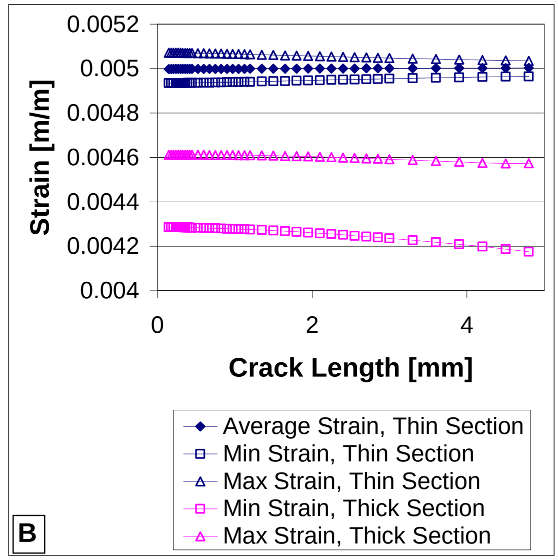

Figure 154: Internal Ply Drop, Carbon, Tension, Upper Crack Suppressed. A: G vs. Crack Length; B: Strain vs. Crack Length.

	Maximum [J/m^2]	Crack Length at Maximum G [mm]	Average [J/m^2] (0.15 – 3.0 mm)
Total G	560.3	1.05	466.2
G_I, Lower Crack	12.6	0.15	1.9
G_{II}, Lower Crack	558.7	1.05	464.3

Table 60: Internal Ply Drop, Carbon, Tension, Upper Crack Suppressed, Maximum and Average G.

Glass, Compression. Figure 155 and Table 61 are results from the internal ply drop model, with glass 0's, loaded in compression, with the lower crack suppressed. The maximum total G for the upper crack is higher for the lower crack suppressed model than the model with both cracks, but the average total G is lower. The G levels drop after an initial spike, indicating that G levels are reduced if the delamination crack does not unload a ply.

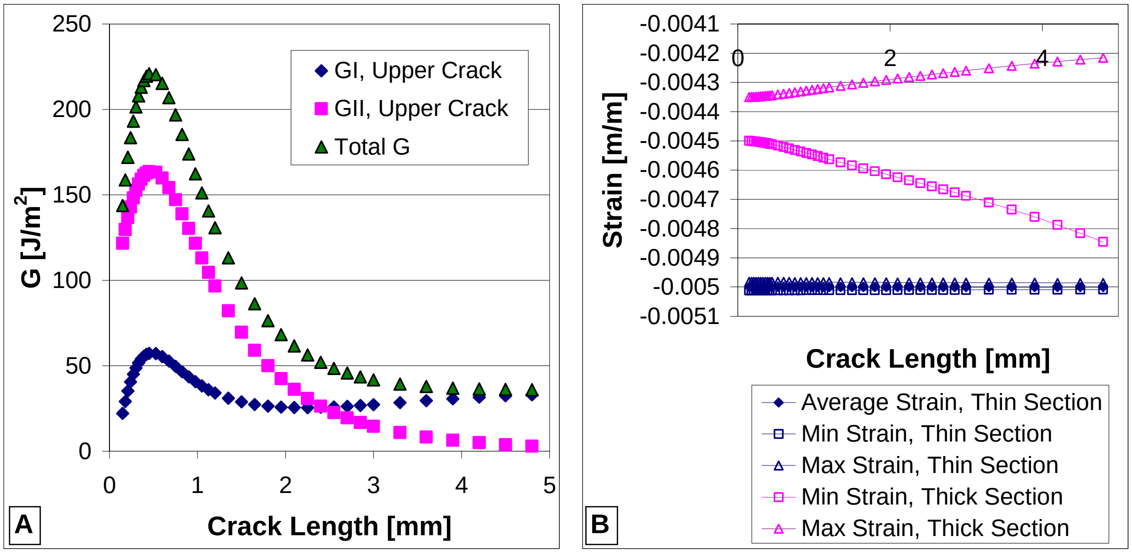

Figure 155: Internal Ply Drop, Glass, Compression, Lower Crack Suppressed. A: G vs. Crack Length; B: Strain vs. Crack Length.

	Maximum [J/m^2]	Crack Length at Maximum G [mm]	Average [J/m^2] (0.15 – 3.0 mm)
Total G	220.9	0.45	112.6
G_I, Upper Crack	57.3	0.45	34.2
G_{II}, Upper Crack	163.6	0.45	78.5

Table 61: Internal Ply Drop, Glass, Compression, Lower Crack Suppressed, Maximum and Average G.

Figure 156 and Table 62 are results from the internal ply drop model, with glass, loaded in compression, with the upper crack suppressed. These results mirror the conclusions made from the lower crack suppressed model above.

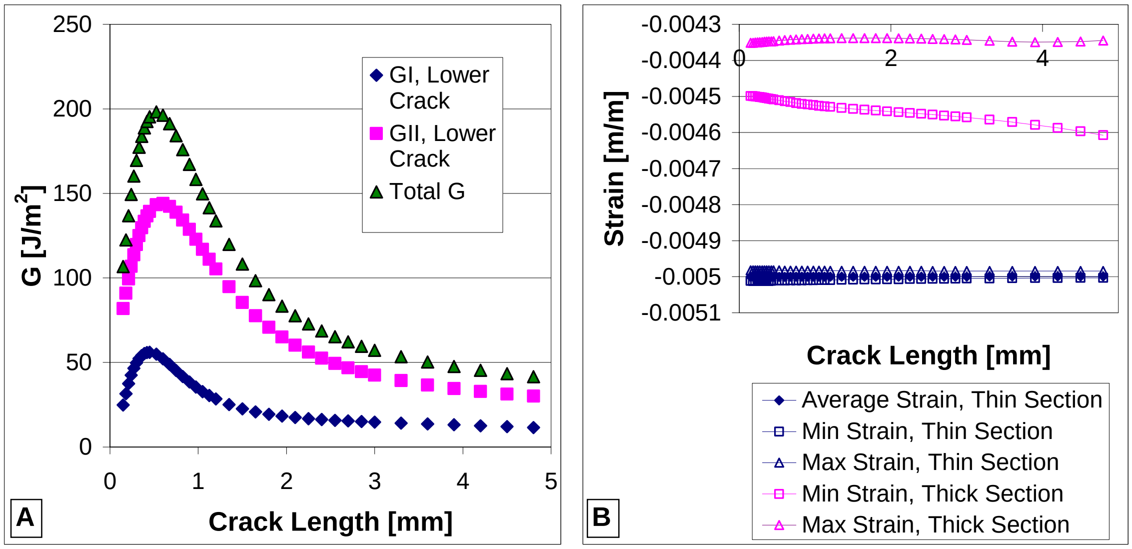

Figure 156: Internal Ply Drop, Glass, Compression, Upper Crack Suppressed. A: G vs. Crack Length; B: Strain vs. Crack Length.

	Maximum [J/m^2]	Crack Length at Maximum G [mm]	Average [J/m^2] (0.15 – 3.0 mm)
Total G	198.1	0.525	115.3
G_I, Lower Crack	56.0	0.45	27.8
G_{II}, Lower Crack	144.1	0.6	87.5

Table 62: Internal Ply Drop, Glass, Compression, Upper Crack Suppressed, Maximum and Average G.

Glass, Tension. Figure 157 and Figure 158 and Table 63, are results from the internal ply drop model, with glass 0’s, loaded in tension, with both cracks present.

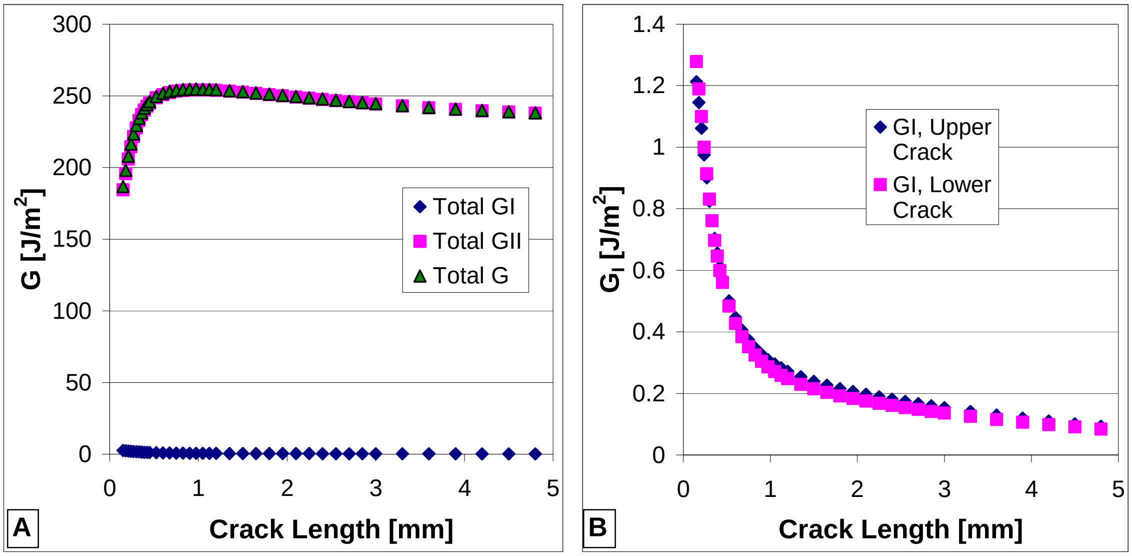

Figure 157: Internal Ply Drop, Glass, Tension, Both Cracks. A: Total G vs. Crack Length; B: G_I vs. Crack Length.

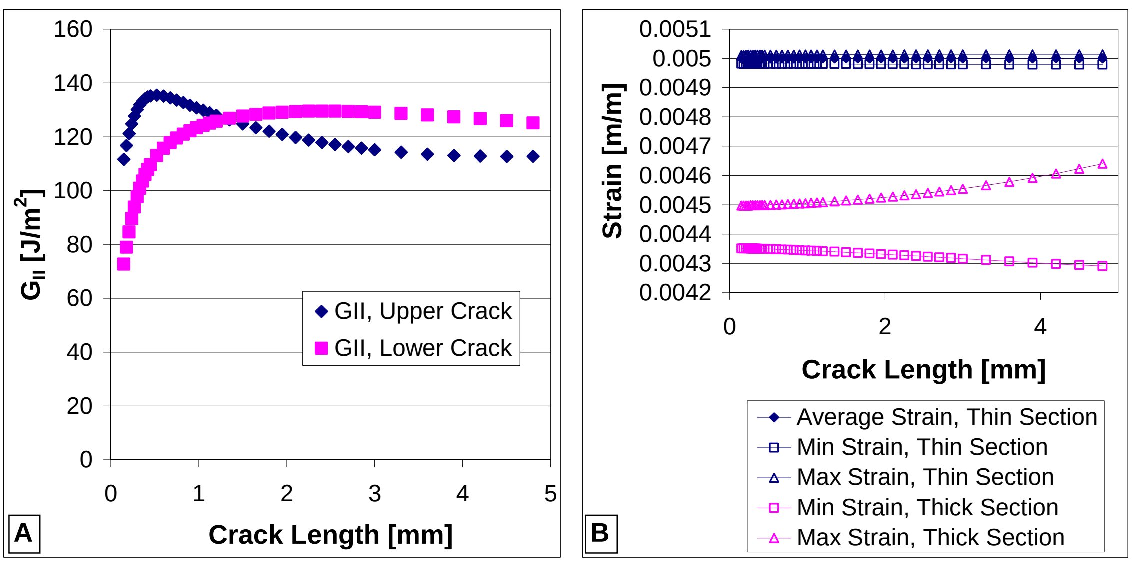

Figure 158: Internal Ply Drop, Glass, Tension, Both Cracks. A: G_{II} vs. Crack Length; B: Strain vs. Crack Length.

	Maximum [J/m^2]	Crack Length at Maximum G [mm]	Average [J/m^2] (0.15 – 3.0 mm)
Total G	254.7	0.975	247.9
G_I, Upper Crack	1.2	0.15	0.3
G_I, Lower Crack	1.3	0.15	0.3
G_{II}, Upper Crack	135.5	0.525	124.3
G_{II}, Lower Crack	129.5	2.4	122.9

Table 63: Internal Ply Drop, Glass, Tension, Both Cracks, Maximum and Average G.

Results from the internal ply drop model, with glass, loaded in tension, with the lower crack suppressed are given as Figure 159 and Table 64. The G_{II} values for this model are comparable to the G_{II} values for the internal ply drop model, with glass, loaded in compression, with the lower crack suppressed, as reported in Table 61.

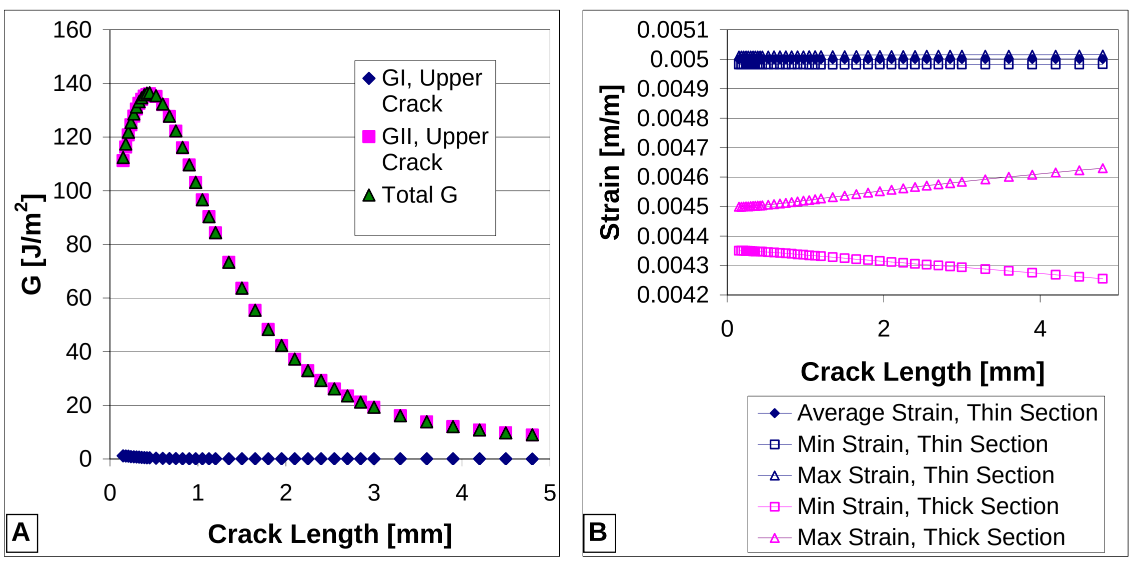

Figure 159: Internal Ply Drop, Glass, Tension, Lower Crack Suppressed. A: G vs. Crack Length; B: Strain vs. Crack Length.

	Maximum [J/m^2]	Crack Length at Maximum G [mm]	Average [J/m^2] (0.15 – 3.0 mm)
Total G	136.6	0.45	70.3
G_I, Upper Crack	1.2	0.15	0.2
G_{II}, Upper Crack	136.1	0.45	70.1

Table 64: Internal Ply Drop, Glass, Tension, Lower Crack Suppressed, Maximum and Average G.

Figure 160 and Table 65 are results from the internal ply drop model, with glass, loaded in tension, with the upper crack suppressed. Again, the G_{II} values match the G_{II} values from the corresponding model, loaded in compression.

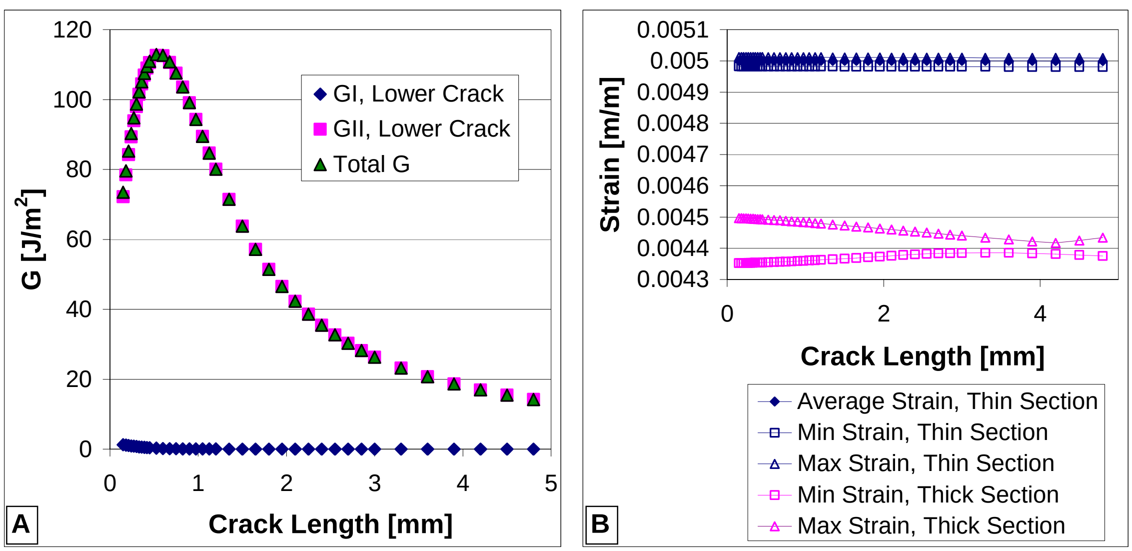

Figure 160: Internal Ply Drop, Glass, Tension, Upper Crack Suppressed. A: G vs. Crack Length; B: Strain vs. Crack Length.

	Maximum [J/m^2]	Crack Length at Maximum G [mm]	Average [J/m^2] (0.15 – 3.0 mm)
Total G	112.9	0.525	65.8
G_I, Lower Crack	1.2	0.15	0.1
G_{II}, Lower Crack	112.6	0.525	65.6

Table 65: Internal Ply Drop, Glass, Tension, Upper Crack Suppressed, Maximum and Average G.

External Ply Drop

Glass, Compression. Figure 161 and Table 66 show results from the external ply drop model, with glass, loaded in compression, with the lower crack suppressed. These results mirror those for the carbon in compression, though it is doubtful that the softening of the ±45's would have as great an effect, as the difference between the longitudinal and transverse stiffness of glass is much less than in carbon.

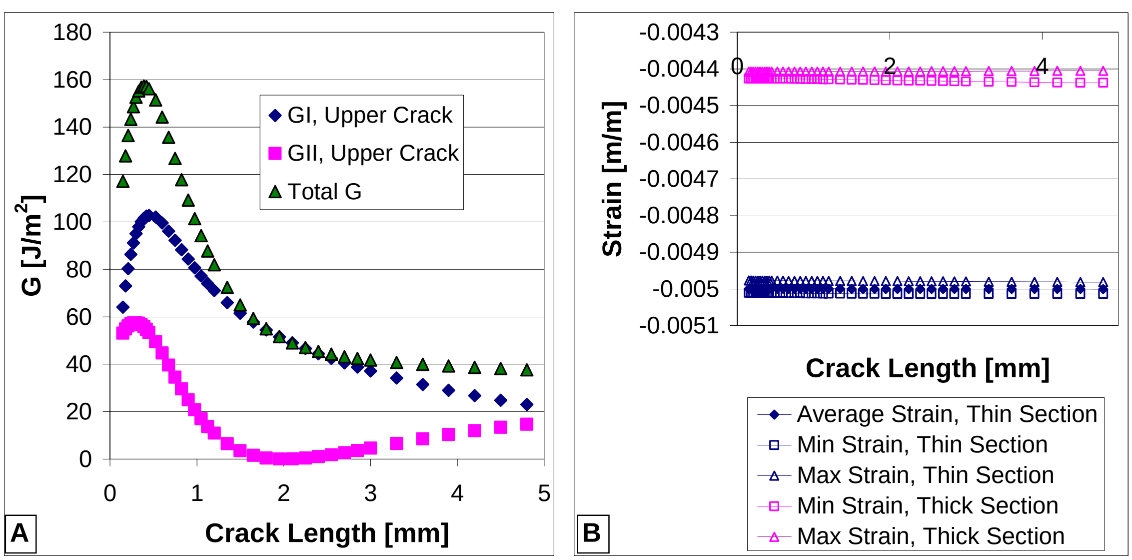

Figure 161: External Ply Drop, Glass, Compression, Lower Crack Suppressed. A: G vs. Crack Length; B: Strain vs. Crack Length.

	Maximum [J/m^2]	Crack Length at Maximum G [mm]	Average [J/m^2] (0.15 – 3.0 mm)
Total G	157.4	0.39	80.2
G_I, Upper Crack	102.7	0.45	64.7
G_{II}, Upper Crack	57.5	0.3	15.5

Table 66: External Ply Drop, Glass, Compression, Lower Crack Suppressed, Maximum and Average G.

Results shown in Figure 162 and Table 67 are for the external ply drop model, with glass, in compression, with the upper crack suppressed. These results show a greater influence of G_I than the same model run with carbon (Figure 99 and Table 33). Also, this model shows declining G values as the crack length increases, unlike the more constant values seen in the carbon model at longer crack lengths.

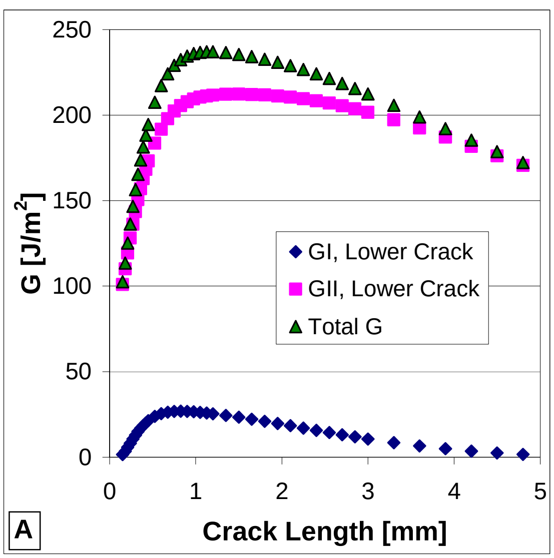

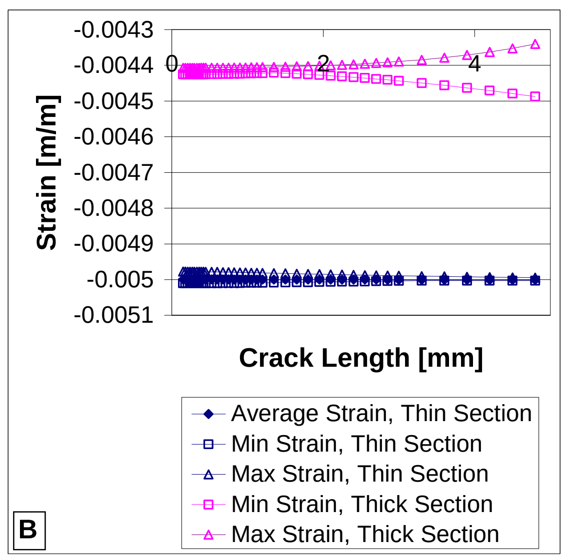

Figure 162: External Ply Drop, Glass, Compression, Upper Crack Suppressed. A: G vs. Crack Length; B: Strain vs. Crack Length.

	Maximum [J/m^2]	Crack Length at Maximum G [mm]	Average [J/m^2] (0.15 – 3.0 mm)
Total G	237.0	1.26	219.6
G_I, Lower Crack	26.9	0.825	19.6
G_{II}, Lower Crack	212.2	1.5	200.0

Table 67: External Ply Drop, Glass, Compression, Upper Crack Suppressed, Maximum and Average G.

Glass, Tension. Figure 163 and Table 68 are results from the external ply drop model, with glass 0's, loaded in tension, and with the lower crack suppressed. An interesting characteristic of these results, and those with the upper crack suppressed, is the G values drop off toward zero at longer crack lengths, unlike the model with both cracks, where values remain high at longer crack lengths.

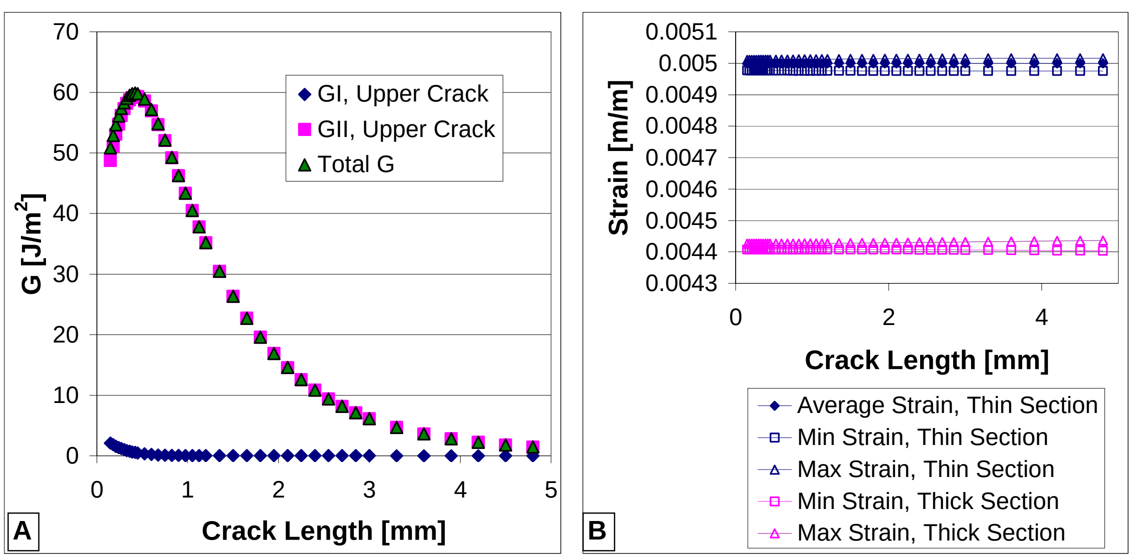

Figure 163: External Ply Drop, Glass, Tension, Lower Crack Suppressed. A: G vs. Crack Length; B: Strain vs. Crack Length.

	Maximum [J/m^2]	Crack Length at Maximum G [mm]	Average [J/m^2] (0.15 – 3.0 mm)
Total G	59.9	0.42	29.4
G_I, Upper Crack	2.1	0.15	0.2
G_{II}, Upper Crack	59.4	0.42	29.2

Table 68: External Ply Drop, Glass, Tension, Lower Crack Suppressed, Maximum and Average G.

Figure 164 and Table 69 are results from external ply drop model, run with glass, in tension, and with the upper crack suppressed. Similar to the carbon results for an upper crack suppressed model loaded in tension, the glass results show higher G_{II} levels.

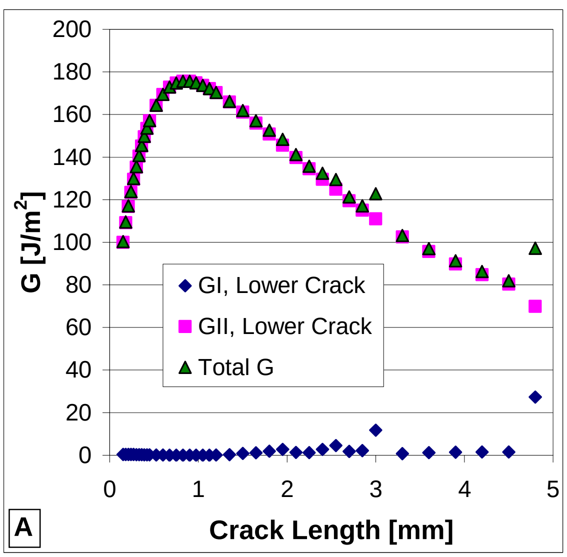

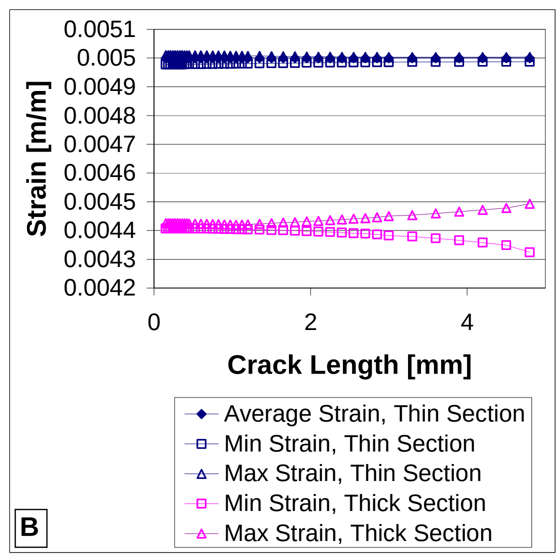

Figure 164: External Ply Drop, Glass, Tension, Upper Crack Suppressed. A: G vs. Crack Length; B: Strain vs. Crack Length.

	Maximum [J/m^2]	Crack Length at Maximum G [mm]	Average [J/m^2] (0.15 – 3.0 mm)
Total G	175.7	0.825	149.2
G_I, Lower Crack	27.3	4.8	1.4
G_{II}, Lower Crack	175.6	0.825	147.8

Table 69: External Ply Drop, Glass, Tension, Upper Crack Suppressed, Maximum and Average G.